5 September 2008 | $10

# Science

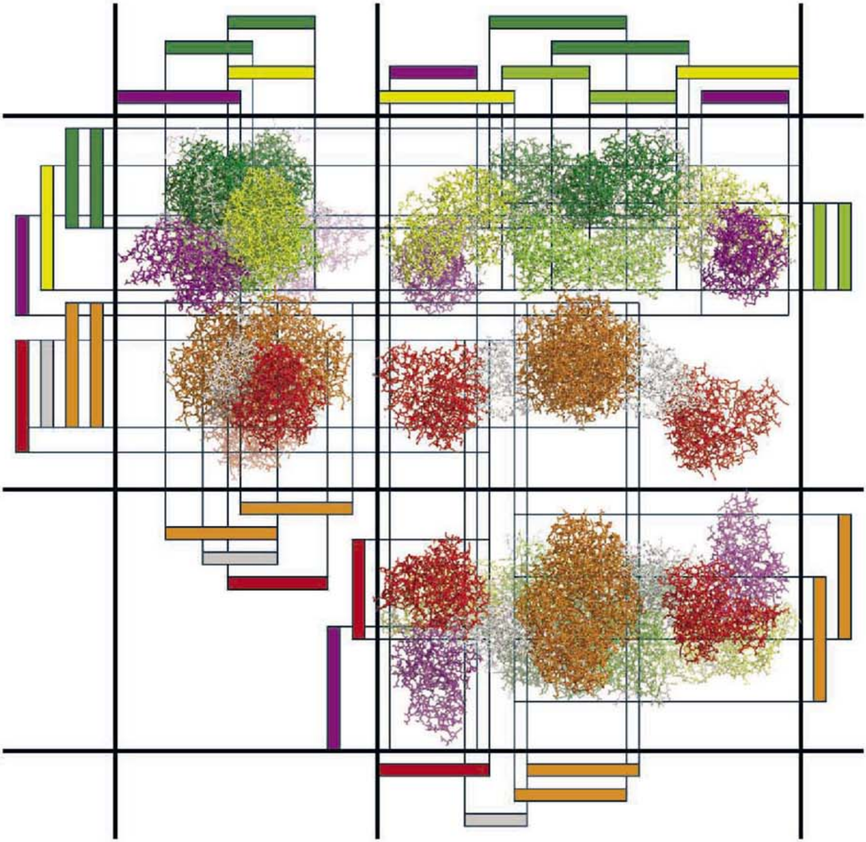

AAAS

## COVER

Mammalian fatty acid synthase, a multienzyme that catalyzes all steps of fatty acid biosynthesis. A blueprint of its atomic structure is shown in three views, and the extent of its functional domains is indicated by colored bars. The versatile segmental construction is also used in other members of this large family of multienzymes, which synthesize natural products such as antibiotics. See page 1315.

***Image: Marc Leibundgut and Timm Maier/ETH Zurich***

## DEPARTMENTS

## EDITORIAL

## NEWS OF THE WEEK

## NEWS FOCUS

1284

## LETTERS

## BOOKS *ET AL.*

1297

## POLICY FORUM

## PERSPECTIVES

**CONTENTS** continued >>

## SCIENCE EXPRESS

www.sciencexpress.org

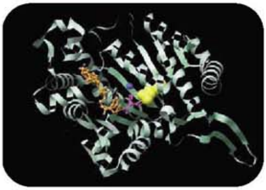

---

## TECHNICAL COMMENT ABSTRACTS

## REVIEW

## BREVIA

## RESEARCH ARTICLES

## REPORTS

**CONTENTS** continued >>

## REPORTS *CONTINUED...*

CHEMISTRY

**Identification of Active Gold Nanoclusters on Iron Oxide Supports for CO Oxidation** 1331

*A. A. Herzing* et al.

High-resolution microscopy showed that the most effective catalytic gold species on an iron oxide support were those forming bilayer clusters of just 10 atoms.

ASTRONOMY

**Laser Frequency Combs for Astronomical Observations** 1335

*T. Steinmetz* et al.

Accurate spectroscopy of the sun with a laser frequency comb shows that it can improve astronomical observations and may yield direct evidence of the universe's expansion.

>> *Perspective p. 1301*

PALEOCLIMATE

**Regional Synthesis of Mediterranean Atmospheric Circulation During the Last Glacial Maximum** 1338

*J. Kuhlemann* et al.

A three-dimensional reconstruction of atmospheric temperatures in the Mediterranean during glacial times is analogous to one of winter during the Little Ice Age.

CLIMATE CHANGE

**Kinematic Constraints on Glacier Contributions to 21st-Century Sea-Level Rise** 1340

*W. T. Pfeffer, J. T. Harper, S. O'Neel*

Evaluation of glacier dynamics implies that melting of the Greenland and Antarctic Ice Sheets could raise sea level by up to 2 meters by 2100, although a rise of 0.8 meters is more likely.

>> Science *Podcast*

IMMUNOLOGY

***Apobec3* Encodes *Rfv3*, a Gene Influencing Neutralizing Antibody Control of Retrovirus Infection** 1343

*M. L. Santiago* et al.

A resistance factor known to protect mice from retroviral infection is unexpectedly identified as *Apobec3*, a deoxycytidine deaminase that controls somatic hypermutation.

GENETICS

**Human-Specific Gain of Function in a Developmental Enhancer** 1346

*S. Prabhakar* et al.

When transferred to a mouse, a conserved regulatory element that has been positively selected in humans is robustly expressed at the base of its developing thumb and wrist.

>> *Perspective p. 1300; Brevia p. 1314*

CELL BIOLOGY

**Wnt3a-Mediated Formation of Phosphatidylinositol 4,5-Bisphosphate Regulates LRP6 Phosphorylation** 1350

*W. Pan* et al.

The interaction of the signaling molecule Wnt to its receptor triggers accumulation of a lipid regulator, which stimulates phosphorylation of the receptor and cellular responses.

BIOCHEMISTRY

**Helical Structures of ESCRT-III Are Disassembled by VPS4** 1354

*S. Lata* et al.

A protein responsible for the final separation of daughter cells or budding viruses forms heteromeric complexes on the inside of the membrane to regulate the abscission step.

MEDICINE

**A Neoplastic Gene Fusion Mimics Trans-Splicing of RNAs in Normal Human Cells** 1357

*H. Li, J. Wang, G. Mor, J. Sklar*

A chimeric messenger RNA generated in a tumor by a DNA rearrangement is also, unexpectedly, expressed in healthy cells, a result of splicing together two separate messenger RNAs.

>> *Perspective p. 1302*

MEDICINE

**Germline Allele-Specific Expression of *TGFBR1* Confers an Increased Risk of Colorectal Cancer** 1361

*L. Valle* et al.

In patients with colorectal cancer, one allele of the transforming growth factor–β gene produces less messenger RNA and thus less protein, a likely contributor to disease risk.

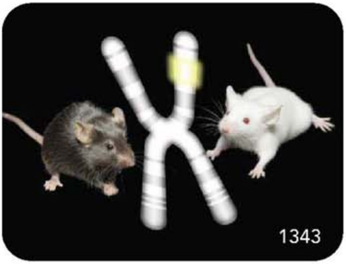

AAAS
ADVANCING SCIENCE, SERVING SOCIETY

**SCIENCE (ISSN 0036-8075) is published weekly on Friday, except the last week in December, by the American Association for the Advancement of Science, 1200 New York Avenue, NW, Washington, DC 20005.** Periodicals Mail postage (publication No. 484460) paid at Washington, DC, and additional mailing offices. Copyright © 2008 by the American Association for the Advancement of Science. The title SCIENCE is a registered trademark of the AAAS. Domestic individual membership and subscription (51 issues): $144 ($74 allocated to subscription). Domestic institutional subscription (51 issues): $770; Foreign postage extra: Mexico, Caribbean (surface mail) $55; other countries (air assist delivery) $85. First class, airmail, student, and emeritus rates on request. Canadian rates with GST available upon request, GST #1254 88122. Publications Mail Agreement Number 1069624. SCIENCE is printed on 30 percent post-consumer recycled paper. **Printed in the U.S.A.**

**Change of address:** Allow 4 weeks, giving old and new addresses and 8-digit account number. **Postmaster:** Send change of address to AAAS, P.O. Box 96178, Washington, DC 20090–6178. **Single-copy sales:** $10.00 current issue, $15.00 back issue prepaid includes surface postage; bulk rates on request. **Authorization to photocopy** material for internal or personal use under circumstances not falling within the fair use provisions of the Copyright Act is granted by AAAS to libraries and other users registered with the Copyright Clearance Center (CCC) Transactional Reporting Service, provided that $20.00 per article is paid directly to CCC, 222 Rosewood Drive, Danvers, MA 01923. The identification code for *Science* is 0036-8075. *Science* is indexed in the *Reader's Guide to Periodical Literature* and in several specialized indexes.

Printed on
30% post-consumer
recycled paper.

**CONTENTS** continued >>

Skeletal development requires the CaSR.

## SCIENCE **SIGNALING**

www.sciencesignaling.org

THE SIGNAL TRANSDUCTION KNOWLEDGE ENVIRONMENT

**EDITORIAL GUIDE: Seeing the Signaling Forest and the Trees**

*M. B. Yaffe*

*Science Signaling* launches primary research to meet the needs of the signal transduction community.

*Development*

**RESEARCH ARTICLE: The Extracellular Calcium-Sensing Receptor (CaSR) Is a Critical Modulator of Skeletal Development**

*W. Chang, C. Tu, T.-H. Chen, D. Bikle, D. Shoback*

**PERSPECTIVE: New Insights in Bone Biology—Unmasking Skeletal Effects of the Extracellular Calcium-Sensing Receptor**

*E. M. Brown and J. B. Lian*

The extracellular calcium-sensing receptor (CaSR) is essential for embryonic and postnatal skeletal development.

**RESEARCH ARTICLE: Linear Motif Atlas for Phosphorylation-Dependent Signaling**

*M. L. Miller, L. J. Jensen, F. Diella, C. Jørgensen, M. Tinti, L. Li, M. Hsiung, S. A. Parker, J. Bordeaux, T. Sicheritz-Ponten, M. Olhovsky, A. Pasculescu, J. Alexander, S. Knapp, N. Blom, P. Bork, S. Li, G. Cesareni, T. Pawson, B. E. Turk, M. B. Yaffe, S. Brunak, R. Linding*

Created with both in vitro and in vivo data, NetPhorest is an atlas of consensus sequence motifs for 179 kinases and 104 phosphorylation-dependent binding domains and reveals new insight into phosphorylation-dependent signaling.

**REVIEW: Alternative Wnt Signaling Is Initiated by Distinct Receptors**

*R. van Amerongen, A. Mikels, R. Nusse*

The traditional classification of Wnts into canonical or noncanonical proteins may be misleading.

## SCIENCE **ONLINE FEATURE**

**THE GONZO SCIENTIST: How Astronomers Have Fun (and Nearly Die Trying)**

In western Mongolia, a solar eclipse has mythic meaning (with audio slideshow).

*www.sciencemag.org/sciext/gonzoscientist/*

## SCIENCE**NOW**

www.sciencenow.org

HIGHLIGHTS FROM OUR DAILY NEWS COVERAGE

**Taking One for the Team**

Selflessness might be bad for the warrior but good for the tribe.

**Fancy Footwork Helps Flies Cheat Death**

High-speed videos reveal surprising sophistication in insect's escape response.

**Why Men Cheat**

Study chalks up promiscuous behavior to a single genetic change.

A particle physicist at the Large Hadron Collider.

## SCIENCE **CAREERS**

www.sciencecareers.org/career_development

FREE CAREER RESOURCES FOR SCIENTISTS

**Working in Industry: Taken for Granted—Fitting the Job Market to a 'T'**

*B. Benderly*

Scientists need more than bench expertise to find work in industry.

**Working in Industry: Mastering Your Ph.D.—Is Industry Right for You?**

*B. Noordam*

Research in industry differs from academic research in several ways.

**Triggermeister**

*C. Reed*

Particle physicist Bilge Demirkoz will make sure colleagues see what happens when CERN's Large Hadron Collider starts this month.

**September 2008 Funding News**

*J. Fernández*

Learn about the latest in research funding, scholarships, fellowships, and internships.

## SCIENCE**PODCAST**

www.sciencemag.org/about/podcast.dtl

FREE WEEKLY SHOW

Download the 5 September *Science* Podcast to hear about organizing memory in the hippocampus, ice loss and sea level rise, criminal psychopathy, and more.

***Separate individual or institutional subscriptions to these products may be required for full-text access.***

CREDITS: (TOP TO BOTTOM) W. CHANG/UCSF; COURTESY, B. DEMIRKOZ; K. KOLENBERG

## Toward Precision Astronomy >>

In a dynamical universe (one that is expanding), you would expect to see Doppler, or red shifts, of spectrograph lines of distant objects that are moving further and faster away from the observer, and for such shifts to drift in velocity over time. Determining the extent of velocity drift, however, requires a level of precision that has not been available—less than one centimeter per second per year. **Steinmetz *et al.*** (p. 1335; see the Perspective by **Lopez**) show how that situation may change using a laser frequency comb produced by an optic fiber. In a proof-of-principle experiment, they combine such a comb of equally spaced wavelengths with an astronomical observation (the Sun) to precisely measure and calibrate the wavelengths of the spectrogram.

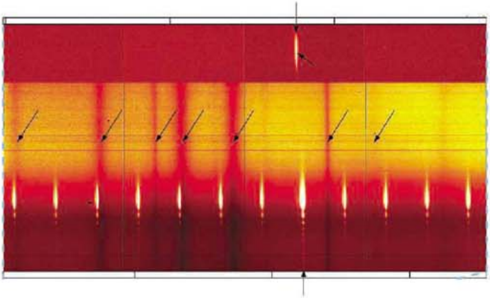

## Moderating Rainfall

Aerosols can either increase or decrease rainfall, so why do they act sometimes one way and sometimes another? **Rosenfeld *et al.*** (p. 1309) review the role of aerosols as moderators of precipitation, and propose a conceptual model to explain their apparently contradictory effects. Even small amounts of aerosols in very clean air prevent the development of long-lived clouds that can deliver large amounts of rain, whereas heavily polluted clouds evaporate much of their water before they can rain through a combination of microphysical and radiative effects. Thus, precipitation occurs most efficiently and abundantly at moderate aerosol concentrations.

## Back in Circulation

The climate of the Mediterranean region during the Last Glacial Maximum, between 23,000 and 19,000 years ago, is known to be much colder than today, but the atmospheric circulation patterns that prevailed remain poorly understood. **Kuhlemann *et al.*** (p. 1338, published online 31 July) synthesized a range of new and published data on the equilibrium line altitude of glaciers (the altitude at which ice covers the ground all year long), paleoflora, and regional sea surface temperatures, and reconstructed the three-dimensional temperature structure of the atmosphere. Atmospheric circulation was like that observed commonly in the winters of the Little Ice Age, roughly between 1500 and 1900.

## Putting Limits on Ice Loss

Ice loss from the margins of the Greenland and Antarctic ice sheets can occur through dynamically forced discharge from fast flowing ice streams and calving of marine-terminating glaciers. However, so little is known about ice sheet dynamics that models are unable to represent these processes accurately. Instead of trying to add up estimates of individual source contributions, **Pfeffer *et al.*** (p. 1340) calculated how much ice discharge from outlet glaciers in Greenland and Antarctica would be required to produce various rates of sea level rise, and then evaluate the plausibility of those discharge rates. Estimates of more than 2 meters of sea level rise by 2100 are highly unlikely—a more reasonable estimate is between 80 centimeters and 2 meters.

## Coding Space, Time, and Memory

Mental operations such as planning, free recall, and problem-solving are assumed to depend on the central nervous system's self-organized sequences of activity, which permit cognitive representations, in sequence, of the future or the past. Similar cognitive content should be represented by similar assembly sequences, and different content should be distinguished by distinctive sequences. Experimental verification of this hypothesis has had to wait for large-scale assembly recordings. **Pastalkova *et al.*** (p. 1322; see the News story by **Miller**) report that, during the delay period of a memory task when an animal is running in a running wheel, each time point is characterized by the firing of a particular constellation of hippocampal neurons that form a highly specific activity sequence across time. During learning, the temporal order of multiple external events is instrumental in selecting the appropriate neuronal representations, whereas, during free recall or action planning, the intrinsic dynamics of the hippocampal system determines sequence identity.

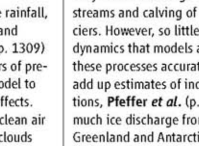

## Focus on Fatty Acid Synthase

Structural studies have led to an increased understanding of the large enzyme systems responsible for the synthesis of fatty acids, polyketides, and nonribosomal peptides. Now **Maier *et al.*** (p. 1315, see the cover and the Perspective by **Smith and Sherman**) report a structure of porcine fatty acid synthase (FAS) that includes five of seven catalytic domains, two nonenzymatic domains, and various linkers. The structure shows how the linker regions and catalytic domains are organized to provide the flexibility required for iterative fatty acid elongation. Like modular polyketide synthase, mammalian FAS acts as a "megasynthase" that can accommodate insertion or deletion of product modifying domains to allow generation of diverse products.

## Tracking Evolution of Transcription Regulation

Bioinformatic approaches are providing insight into the evolution of noncoding regulatory elements of genes that can drive different expression outcomes from similar sets of genes (see the Perspective by **Wray and Babbitt**). Several recent computational efforts have identified

CREDITS (TOP TO BOTTOM): STEINMETZ ET AL.; PASTALKOVA ET AL.

conserved noncoding sequences that have evolved rapidly in humans, but it is not known whether their functions might have changed during the evolution process. **Prabhakar *et al.*** (p. 1346) used such a noncoding element called human-accelerated conserved noncoding sequence 1 (HACNS1), as well as orthologs of the gene from nonhuman primates, to create transgenic mouse embryos. HACSN1, but not the nonprimate orthologs, drove expression of a reporter gene at the junction of the anterior developing hand and forearm, including the base of the developing thumb and wrist. Sequence changes were identified that could "humanize" the expression patterns of the chimpanzee enhancer. **Hong *et al.*** (p. 1314) searched for clusters of potential transcription factor binding sites, in this case for targets of regulation by the transcription factor Dorsal and known cofactors in the fruit fly. Some of the secondary, or "shadow," enhancers have patterns of gene expression that overlap those of primary enhancers, and may be able to evolve without disrupting core expression patterns.

## ESCRTing Membrane Scission

So-called ESCRT proteins have been implicated in catalyzing different cellular and pathological processes, including multivesicular body biogenesis, retrovirus budding, and cytokinesis. These processes involve topologically similar membrane events that require a common final abscission step to separate two newly formed membrane-enveloped structures. Little is known regarding how the budding steps, including membrane abscission, are catalyzed. Indirect evidence suggests that ESCRT-III plays an important role in the final step. Notably, dominant-negative CHMP3, a subunit of ESCRT-III, inhibits HIV-1 budding as well as cytokinesis. Because cytokinesis does not require vesicle formation, it would seem that ESCRT-III regulates steps in membrane abscission. **Lata *et al.*** (p. 1354, published online 7 August) provide structural evidence for the formation of distinct heteromeric ESCRT-III assemblies by electron microscopy. These structures could bind on the inside of the neck of a bud or at the midbody between dividing cells and regulate membrane abscission.

## The Normal Side of Trans-Splicing

Human tumors frequently display chromosomal rearrangements that fuse two distinct genes and result in the expression of chimeric messenger RNA (mRNA) transcripts whose protein products are oncogenic. **Li *et al.*** (p. 1357; see Perspective by **Rowley and Blumenthal**) suggest that the chimeric mRNAs generated by chromosomal rearrangements in tumors may sometimes represent constitutively expressed versions of chimeric mRNAs generated in healthy tissue by trans-splicing. Studying a *JAZF1-JJAZ1* chimeric transcript that is abundantly expressed in human endometrial stromal sarcomas with a (7;17) chromosomal translocation, the authors found unexpectedly that the same chimeric transcript was expressed in normal endometrial stromal cells, even though these cells lacked the chromosomal translocation. In normal cells, the chimeric transcript arose by trans-splicing between independently transcribed *JAZF1* and *JJAZ1* pre-mRNAs, and it was translated into a chimeric protein of unknown function. Trans-splicing is thought to be a rare event in mammalian cells, but these results suggest that other examples might be found by searching for normal RNA counterparts to the many chimeric mRNAs generated by chromosomal rearrangements in tumors.

## Quantity, Not Just Quality, Matters

Colorectal cancer is one of the leading causes of cancer-related deaths worldwide. Because 20 to 30% of cases occur in individuals with a family history of the disease, genetic factors are thought to be a substantial contributor to risk. **Valle *et al.*** (p. 1361, published online 14 August) now report that one of these factors is an inherited variation in the expression level of a gene encoding a key signaling protein previously implicated in colorectal cancer pathogenesis. Within a Caucasian population in the United States, individuals with colorectal cancer are 5 to 10 times more likely than controls to show germline allele-specific expression of the *TGFBR1* gene, which encodes the type I receptor for transforming growth factor–β. Allele-specific expression appears to result in a modest, but biologically meaningful, lifelong reduction in the expression of *TGFBR1*, which in turn confers an increased risk of colorectal cancer. Thus, it seems that the genetic contribution to disease risk includes not only mutations that abolish or modify the function of genes but also more subtle alterations that change the baseline expression levels of genes.

CREDIT: LATA ET AL.

Bruce Alberts is the Editor-in-Chief of *Science*.

# Scientific Publishing Standards

THIS WEEK MARKS THE LAUNCH OF A NEW, IMPROVED VERSION OF THE AAAS JOURNAL *Science Signaling*, which will now contain original research. Professor Michael Yaffe, its new chief scientific editor, has clearly articulated the ambitious goals for his journal.* Highly elaborate signaling mechanisms are essential for controlling the behavior of each cell in a multicellular organism—allowing each of the many billions of cells in our bodies to decide whether it will grow and proliferate, remain quiescent, kill itself, or change its behavior according to signals received from neighboring cells. Understanding how this complex system works represents a major challenge. Unraveling its many mysteries will require a great deal of ingenuity—and the collaboration of biologists, chemists, physicists, engineers, computer scientists, and mathematicians. We are confident that *Science Signaling* will set the highest standard for research in this important field, and that, through its Perspectives and Review articles, it will help to guide future researchers along highly productive paths.

The new journal began in 1999 as *Science*'s STKE (Signal Transduction Knowledge Environment), an online resource. The initial aim was to speed the generation of new knowledge by creating an Internet-based work environment that would provide "all practitioners in a field of endeavor access to all the knowledge within the field" and "speed identification of relevant information and encourage communication with others." The Web site flourished. As the next step in an ongoing evolution, *Science Signaling* has now added original peer-reviewed research papers to the myriad of resources provided at the site.

I want to take this propitious occasion to reflect briefly on the core purpose of scientific publishing, and to consider some guiding principles that we scientists, editors, and publishers need to keep in mind in our collective efforts to improve the scientific literature.

The publication of a scientific article is less a way for scientists to earn recognition and advance their careers than it is an engine for scientific progress. Science continually advances only because many cycles of independent testing by different scientists allow new knowledge to be built with confidence upon old knowledge, thereby creating a repository of reliable understandings about the world. The publications of those of us who are scientists explain what we have found in our investigations, and they lay out exactly what we have done to make each discovery. Clear, truthful presentations of data, results, and methods are essential for enabling the findings of one scientist to be confirmed, refuted, or extended in new ways by other scientists.

Scientists have an absolute obligation to honesty: They must accurately report how they arrived at their discoveries, as well as the discoveries themselves. Thus, our journals must insist on detailed descriptions of all of the methods used, so as to allow other scientists to reproduce the results in a straightforward manner. The appropriate place for most of this information is in the easily expandable Supplementary Materials that accompany each article. Authors, reviewers, and editors of scientific manuscripts should therefore constantly ask themselves whether the reader has been provided with everything needed to both understand and reproduce the results.

The increasingly large data sets produced in some studies present a different challenge; they require deposition in readily accessible, online archives, supported by stable public funding.

Last but not least, journals themselves can certainly set a higher bar for the clarity of presentation in the manuscripts that we publish. The problem is perhaps most obvious in the brief abstracts that authors write to introduce each article, which often seem to be written only for a handful of experts in the authors' subspecialty. Some abstracts, full of three-letter abbreviations and jargon, are incomprehensible to me even in my own field of cell biology. As scientists and as journal publishers, we can and we must do better. In this, as in many other areas, *Science Signaling* will aim for the same high standards that we strive for at *Science*.

**–Bruce Alberts**

10.1126/science.1165268

---

*Sci. Signal.* **1**, eg5 (2008).

PHYSICS

## Snapshot Magnetometry

In cold-atom chips, atoms are guided above tracks of wires that supply the magnetic field to keep them aloft. In applications ranging from quantum information processing to metrology, any deviation in the magnetic field from point to point over the chip could influence the delicate state of the atoms. Terraciano *et al.* introduce a technique that takes a snapshot image of the magnetic field landscape. Using a cloud of cold rubidium atoms, whose energy levels are sensitive to magnetic field, they let the cloud fall toward the chip and probe the atoms' state with a laser beam tuned to one of the magnetic transitions. The ability to take a two-dimensional snapshot image of magnetic field variations of 30 mG/cm above the atom chip over 5 mm with 250-μm resolution should prove useful in calibrating these chips for their envisioned applications. — ISO

*Opt. Express* **16**, 13062 (2008).

BIOCHEMISTRY

## Translation Translocations

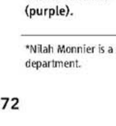

**EF4 (red) grabs the A-site tRNA (purple).**

Ribosomes translate mRNA into protein with the help of GTPases: the elongation factors (EFs). In prokaryotes, as each mRNA codon is presented in the A site of the ribosome, EF-Tu loads a complementary, amino acid–bearing tRNA into the A site. After peptide bond formation, EF-G translocates the ribosome along the mRNA strand by three nucleotides, moving the tRNA (now carrying the nascent polypeptide chain) into the neighboring P site and bringing the next codon into the A site. The GTPase EF4/LepA was recently found to promote backward translocation of the ribosome along the mRNA strand, moving the tRNA from the P site back into the A site. This function may allow the ribosome to recover from forward translocations of the wrong number of nucleotides. Connell *et al.* have visualized EF4 in complex with a ribosome and associated tRNAs using single-particle cryo–electron microscopy (EM). Fitting the crystal structure of EF4 into the cryo-EM reconstruction revealed that its C-terminal domain forms multiple contacts with a tRNA in the A site, suggesting that EF4 promotes back-translocation by stabilizing the A-site tRNA position over the P-site tRNA position. — NM*

*Nat. Struct. Mol. Biol.* **15**, 10.1038/nsmb.1469 (2008).

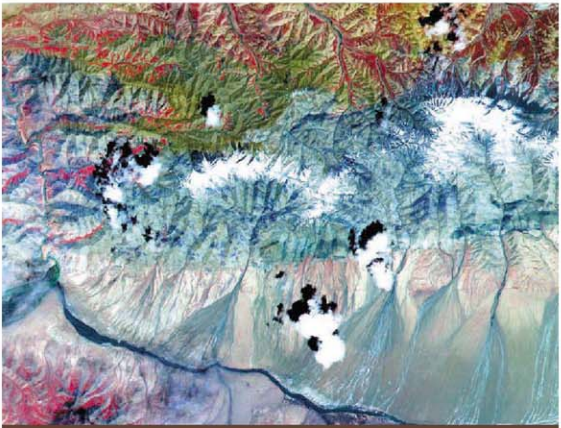

GEOPHYSICS

## Sensing Supershear

Recent observations, supported by experiments, have indicated that some earthquake ruptures transiently exceed the local speed of sound along the fault zone. This "supershear" can explain enhanced shaking from these quakes; thus, supershear ruptures are critical in assessing seismic risks. Many of the details of how ruptures accelerate to above the sound speed and then decelerate, in some cases repeatedly, as a rupture progresses are unclear, as most supershear ruptures have been inferred by data inversions. Vallée *et al.* were able to observe these dynamics more directly in the 2001 Kokoxili earthquake ($M = 7.8$)—which ruptured 400 km along the Kunlun fault in northern Tibet—thanks to an array of seismometers in Nepal that were nearly parallel to the rupture. Their data show that the earthquake, which began in the west, accelerated to above the shear wave velocity after ripping 175 km eastward, at a bend in the fault. Rupture speeds nearly reached the compressional (p) wave velocity before decelerating at another bend. Much of the high-frequency seismic energy from the quake was radiated during these transitions. — BH

*J. Geophys. Res.* **113**, B07305 (2008).

CLIMATE SCIENCE

## 1000 Years of Hurricanes

The natural variability of hurricane activity is poorly known, not least because the historic record for hurricanes extends back only about 130 years. As a result, there has been controversy over whether hurricane activity will change—or is already changing—as a result of global warming. Sediments may hold clues to hurricane activity over longer time scales, but few studies have yielded sedimentary records of hurricane activity at annual resolution. Besonen *et al.* have now obtained an annually resolved lake sediment record from Lower Mystic Lake in Boston, Massachusetts, that covers the past 1000 years. The record contains anomalous features—unusually thick layers in which coarse sediments and terrestrial, organic detritus are overlain by progressively finer sediments—that are indicative of strong flooding. Comparison with the historic record shows that 10 out of 11 of these features

CREDITS (TOP TO BOTTOM): NASA/GSFC/METI/ERSDAC/JAROS, AND U.S./JAPAN ASTER SCIENCE TEAM; CONNELL *ET AL.*, *NAT. STRUCT. MOL. BIOL.* 15, 10.1038/NSMB.1469 (2008)

---

*Nilah Monnier is a summer intern in *Science*'s editorial department.

occur in years when category 2-to-3 hurricanes struck Boston. The authors use this correlation to determine centennial-scale changes in hurricane frequency. Further records of this type from other locations will help to relate these patterns to other paleoclimate indicators. — JFU

*Geophys. Res. Lett.* **35**, L14705 (2008).

BIOCHEMISTRY

## Plasmid Propulsion

To be propagated stably in prokaryotes, low–copy number plasmids must be allocated actively during cell division. The R1 plasmid is maintained at four to six copies per cell by the *par* operon, which encodes the DNA-binding protein ParR and the actin-like ATPase ParM. ParR binds cooperatively as a dimer to 11–base pair repeats in *parC*; ParM undergoes ATP-dependent polymerization, but only grows into long parallel filaments that are capable of pushing replicated plasmids apart when capped by the ParR-*parC* complex. To understand how elongating filaments are stabilized, Salje and Lowe have used electron microscopy and biochemistry to determine the architecture of capped filaments. ParR-*parC* complexes have previously been shown to form a clamplike structure in which *parC* DNA wraps around a helical array of ParR dimers. Guided by biochemical mapping of the ParR-ParM interaction sites, they modeled the crystal structure of ParR onto the end of the double-helical ParM filament. The ParR-*parC* clamp wraps around the filament with the C-terminal regions of ParR bound to exposed loops of ParM. Each ParR-*parC* complex binds the end of a single filament, and the filament ends can be bound simultaneously. Unlike actin, ParM forms left-handed filaments, which allows ParM monomers access to the ends of protofilaments capped with right-handed ParR-*parC*. The authors suggest a model in which force is produced by the alternating addition of monomers to each protofilament accompanied by rocking of the ParR clamp from side to side, analogous to the model proposed for formin-assisted actin polymerization. — VV

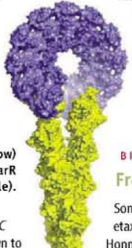

**ParM (yellow) capped by ParR (purple).**

*EMBO J.* **27**, 2230 (2008).

CREDIT: SALJE AND LOWE, EMBO J. 27, 2230 (2008)

BIOPHYSICS

## Molecular Cloaking

Natural products, such as latex rubber or beta-lactam antibiotics, have given rise to entire industries, and green fluorescent protein (GFP) has fought its way onto the list. A series of variants created in several laboratories have shifted the peak excitation and emission wavelengths (for multicolor imaging), improved the photostability (for time-lapse cinematography), and enhanced the quantum yields (lowering detection thresholds). Andresen *et al.* describe their latest entry—which has been christened Padron in recognition of its "reversed" behavior in comparison to its parent, Dronpa—and demonstrate how to implement multilabel, single-color imaging. Dronpa and its widely used descendant rsFastLime fluoresce when excited with blue light (488 nm), which also converts them from an "on" state to an "off" or nonfluorescent state, from which they can be switched on again by irradiation with ultraviolet (UV) light (405 nm). In contrast, Padron (differing at eight amino acid residues from Dronpa) is switched off by UV and on by blue light. As the emission of both proteins is centered at roughly 520 nm, and both exhibit very low off-state fluorescence, a single detection window can be used. — GJC

*Nat. Biotechnol.* **26**, 10.1038/nbt.1493 (2008).

BIOMEDICINE

## From Clinic to Lab and Back

Some breast cancer patients respond to docetaxel chemotherapy, but some do not. Honma *et al.* have marshaled converging evidence that ribophorin II (RPN2), a mammalian oligosaccharide transferase component, contributes to the development of resistance to docetaxel. Assessing gene expression levels in nonresponders versus responders yielded 85 genes expressed at higher levels in nonresponsive patients. Down-regulating these genes individually by applying small interfering RNAs (siRNAs) to a docetaxel-resistant breast cancer cell line winnowed the candidates to eight, with RPN2 knockdown strongly associated with the inhibition of cell growth (taxanes are antimitotic agents) and activation of apoptotic (programmed cell death) pathways; conversely, docetaxel-resistant cells displayed enhanced expression of *RPN2* and also of *MDR1*, which encodes a multidrug efflux pump. Translating these findings into two animal models—created by implanting two docetaxel-resistant breast cancer cell lines into mice—revealed that RPN2 siRNA delivery restored sensitivity to docetaxel and inhibited tumor growth; these effects were mediated by the diminished maturation and glycosylation of MDR1 and the accumulation of docetaxel within the orthotopic tumors. Finally, in a new, albeit small, set of breast cancer patients, RPN2 expression matched responsiveness to docetaxel treatment. — GJC

*Nat. Med.* **14**, 10.1038/nm.1858 (2008).

www.sciencemag.org

# Science

**1200 New York Avenue, NW**
**Washington, DC 20005**
Editorial: 202-326-6550, FAX 202-289-7562
News: 202-326-6581, FAX 202-371-9227
**Bateman House, 82-88 Hills Road**
**Cambridge, UK CB2 1LQ**
+44 (0) 1223 326500, FAX +44 (0) 1223 326501

**Subscription Services** For change of address, missing issues, new orders and renewals, and payment questions: 866-434-AAAS (2227) or 202-326-6417, FAX 202-842-1065. Mailing addresses: AAAS, P.O. Box 96178, Washington, DC 20090-6178 or AAAS Member Services, 1200 New York Avenue, NW, Washington, DC 20005

**Institutional Site Licenses** please call 202-326-6755 for any questions or information

**Reprints:** Author Inquiries 800-635-7181
Commercial Inquiries 803-359-4578

**Permissions** 202-326-7074, FAX 202-682-0816

**Member Benefits** AAAS/Barnes&Noble.com bookstore www.aaas.org/bn; AAAS Online Store http://www.apisource.com/aaas/ code MKB6; AAAS Travels: Betchart Expeditions 800-252-4910; Apple Store www.apple/eppstore/aaas; Bank of America MasterCard 1-800-833-6262 priority code FAA3YU; Cold Spring Harbor Laboratory Press Publications www.cshlpress.com/affiliates/aaas.htm; GEICO Auto Insurance www.geico.com/landingpage/go51.htm?logo=17624; Hertz 800-654-2200 CDP#343457; Office Depot https://bsd.officedepot.com/portalLogin.do; Seabury & Smith Life Insurance 800-424-9883; Subaru VIP Program 202-326-6417; VIP Moving Services http://www.vipmayflower.com/domestic/index.html; Other Benefits: AAAS Member Services 202-326-6417 or www.aaasmember.org.

| | |
|---|---|
| science_editors@aaas.org | (for general editorial queries) |
| science_letters@aaas.org | (for queries about letters) |
| science_reviews@aaas.org | (for returning manuscript reviews) |
| science_bookrevs@aaas.org | (for book review queries) |

Published by the American Association for the Advancement of Science (AAAS), *Science* serves its readers as a forum for the presentation and discussion of important issues related to the advancement of science, including the presentation of minority or conflicting points of view, rather than by publishing only material on which a consensus has been reached. Accordingly, all articles published in *Science*—including editorials, news and comment, and book reviews—are signed and reflect the individual views of the authors and not official points of view adopted by AAAS or the institutions with which the authors are affiliated.

AAAS was founded in 1848 and incorporated in 1874. Its mission is to advance science, engineering, and innovation throughout the world for the benefit of all people. The goals of the association are to: enhance communication among scientists, engineers, and the public; promote and defend the integrity of science and its use; strengthen support for the science and technology enterprise; provide a voice for science on societal issues; promote the responsible use of science in public policy; strengthen and diversify the science and technology workforce; foster education in science and technology for everyone; increase public engagement with science and technology; and advance international cooperation in science.

**Information for Authors**

See pages 634 and 635 of the 1 February 2008 issue or access www.sciencemag.org/about/authors

editor-in-chief **Bruce Alberts**
executive editor **Monica M. Bradford**
deputy editors
**R. Brooks Hanson, Barbara R. Jasny, Katrina L. Kelner**
news editor
**Colin Norman**

**Editorial supervisory senior editor** Phillip D. Szuromi; **senior editor/perspectives** Lisa D. Chong; **senior editors** Gilbert J. Chin, Pamela J. Hines, Paula A. Kiberstis (Boston), Marc S. Lavine (Toronto), Beverly A. Purnell, L. Bryan Ray, Guy Riddihough, H. Jesse Smith, Valda Vinson; **associate editors** Jake S. Yeston, Laura M. Zahn; **online editor** Stewart Wills; **associate online editors** Robert Frederick, Tara S. Marathe; **web content developer** Martyn Green; **book review editor** Sherman J. Suter; **associate letters editor** Jennifer Sills; **editorial manager** Cara Tate; **senior copy editors** Jeffrey E. Cook, Cynthia Howe, Harry Jach, Barbara P. Ordway, Trista Wagoner; **copy editors** Chris Filiatreau, Lauren Kmec, Peter Mooreside; **editorial coordinators** Carolyn Kyle, Beverly Shields; **publications assistants** Ramatoulaye Diop, Joi S. Granger, Jeffrey Hearn, Lisa Johnson, Scott Miller, Jerry Richardson, Jennifer A. Seibert, Brian White, Anita Wynn; **editorial assistants** Carlos L. Durham, Emily Guise, Patricia M. Moore; **executive assistant** Sylvia S. Kihara; **administrative support** Maryrose Madrid

**News deputy news editors** Robert Coontz, Eliot Marshall, Jeffrey Mervis, Leslie Roberts; **contributing editors** Elizabeth Culotta, Polly Shulman; **news writers** Yudhijit Bhattacharjee, Adrian Cho, Jennifer Couzin, David Grimm, Constance Holden, Jocelyn Kaiser, Richard A. Kerr, Eli Kintisch, Andrew Lawler (New England), Greg Miller, Elizabeth Pennisi, Robert F. Service (Pacific NW), Erik Stokstad; **interns** Rachel Zelkowitz, Andrea Lu, Fayana Richards; **contributing correspondents** Jon Cohen (San Diego, CA), Daniel Ferber, Ann Gibbons, Mitch Leslie, Charles C. Mann, Virginia Morell, Evelyn Strauss, Gary Taubes; **copy editors** Linda B. Felaco, Melvin Gatling; **administrative support** Scherraine Mack, Fannie Groom; **bureaus** New England: 207-549-7755, San Diego, CA: 760-942-3252, FAX 760-942-4979, Pacific Northwest: 503-963-1940

**Production director** James Landry; **senior manager** Wendy K. Shank; **assistant manager** Rebecca Doshi; **senior specialists** Steve Forrester, Chris Redwood; **specialist** Anthony Rosen; **Preflight director** David M. Tompkins; **manager** Marcus Spiegler; **specialist** Jessie Mudjitaba

**Art director** Yael Kats; **associate art director** Aaron Morales; **illustrators** Chris Bickel, Katharine Sutliff; **senior art associates** Holly Bishop, Laura Creveling, Preston Huey, Nayomi Kevitiyagala; **associate** Jessica Newfield; **photo editor** Leslie Blizard

***Science* International**

**Europe** (science@science-int.co.uk) **editorial: international managing editor** Andrew M. Sugden; **senior editor/perspectives** Julia Fahrenkamp-Uppenbrink; **senior editors** Caroline Ash, Stella M. Hurtley, Ian S. Osborne, Peter Stern; **editorial support** Deborah Dennison, Rachel Roberts, Alice Whaley; **administrative support** John Cannell, Janet Clements, Louise Smith; **news: europe news editor** John Travis; **deputy news editor** Daniel Clery; **contributing correspondents** Michael Balter (Paris), John Bohannon (Vienna), Martin Enserink (Amsterdam and Paris), Gretchen Vogel (Berlin); **intern** Lauren Cahoon

**Asia** Japan Office: Asca Corporation, Eiko Ishioka, Fusako Tamura, 1-8-13, Hirano-cho, Chuo-ku, Osaka-shi, Osaka, 541-0046 Japan; +81 (0) 6 6202 6272, FAX +81 (0) 6 6202 6271; asca@os.gulf.or.jp; **asia news editor** Richard Stone (Beijing: rstone@aaas.org); **contributing correspondents** Dennis Normile (Japan: +81 (0) 3 3391 0630, FAX +81 (0) 3 5936 3531; dnormile@gol.com); Hao Xin (China: +86 (0) 10 6307 4439 or 6307 3676, FAX +86 (0) 10 6307 4358; cindyhao@gmail.com); Pallava Bagla (South Asia: +91 (0) 11 2271 2896; pbagla@vsnl.com)

**Africa** Robert Koenig (contributing correspondent, rob.koenig@gmail.com)

executive publisher **Alan I. Leshner**
publisher **Beth Rosner**

**Fulfillment Systems and Operations** (membership@aaas.org); **director** Waylon Butler; **senior systems analyst** Jonny Blaker; **customer service supervisor** Pat Butler; **specialists** Latoya Casteel, LaVonda Crawford, Vicki Linton; **data entry supervisor** Cynthia Johnson; **specialist** Tarrika Hill

**Business Operations and Administration director** Deborah Rivera-Wienhold; **assistant director, business operations** Randy Yi; **manager, business analysis** Michael LoBue; **manager, business operations** Jessica Tierney; **financial analysts** Benjamin Aronin, Priti Pamnani; **rights and permissions: administrator** Emilie David; **associate** Elizabeth Sandler; **marketing director** John Meyers; **marketing manager** Allison Pritchard; **marketing associates** Aimee Aponte, Alison Chandler, Mary Ellen Crowley, Marcia Leach, Julianne Wielga, Wendy Wise; **international marketing manager** Wendy Sturley; **marketing executive** Jennifer Reeves; **marketing/member services executive** Linda Rusk; **site license sales director** Tom Ryan; **sales manager** Russ Edra; **sales and customer service** Iquo Edim, Kiki Forsythe, Catherine Holland, Ilese Ominsky, Phillip Smith, Philip Tsolakidis; **electronic media: manager** Lizabeth Harman; **project manager** Trista Snyder; **assistant manager** Lisa Stanford; **senior production specialists** Christopher Coleman, Walter Jones; **production specialists** Nichele Johnston, Kimberly Oster

**Advertising director, worldwide ad sales** Bill Moran

**Product** (science_advertising@aaas.org); **midwest** Rick Bongiovanni: 330-405-7080, FAX 330-405-7081; **west coast/w. canada** Teola Young: 650-964-2266; **east coast/e. canada** Laurie Faraday: 508-747-9395, FAX 617-507-8189; **uk/europe/asia** Tracy Holmes: +44 (0) 1223 326525, FAX +44 (0) 1223 326532; **japan** Mashy Yoshikawa: +81 (0) 3 3235 5961, FAX +81 (0) 3 3235 5852; **senior traffic associate** Delandra Simms

**Commercial Editor** Sean Sanders: 202-326-6430

**Project Director, Outreach** Brianna Blaser

**Classified** (advertise@sciencecareers.org); **us: recruitment sales manager** Ian King: 202-326-6528, FAX 202-289-6742; **inside sales manager: midwest/canada** Daryl Anderson: 202-326-6543; **inside sales representative** Karen Foote: 202-326-6740; **key account manager** Joribah Able; **northeast** Alexis Fleming: 202-326-6578; **southeast** Tina Burks: 202-326-6577; **west** Nicholas Hintibidze: 202-326-6533; **sales coordinators** Erika Foard, Rohan Edmonson, Shirley Young; **international: sales manager** Tracy Holmes: +44 (0) 1223 326525, FAX +44 (0) 1223 326532; **sales** Marium Hudda, Alex Palmer, Alessandra Sorgente; **sales assistant** Louise Moore; **japan** Mashy Yoshikawa: +81 (0) 3 3235 5961, FAX +81 (0) 3 3235 5852; **advertising production operations manager** Deborah Tompkins; **senior production specialists** Robert Buck, Amy Hardcastle; **senior traffic associate** Christine Hall; **publications assistant** Mary Lagnaoui

**AAAS Board of Directors retiring president, chair** David Baltimore; **president** James J. McCarthy; **president-elect** Peter C. Agre; **treasurer** David E. Shaw; **chief executive officer** Alan I. Leshner; **board** Lynn W. Enquist, Susan M. Fitzpatrick, Alice Gast, Linda P. B. Katehi, Nancy Knowlton, Cherry A. Murray, Thomas D. Pollard, Thomas A. Woolsey

AAAS
ADVANCING SCIENCE, SERVING SOCIETY

## RUN, TOAD, RUN

Cane toad races are a barroom pastime in parts of northern Australia. Now the pestiferous amphibians are racing for science.

Researchers led by zoologist Michael Kearney at the University of Melbourne have been trying to predict the potential range of the country's plague of cane toads, which were first introduced in the 1930s to attack sugar cane beetles in Queensland.

The toads have been expanding their range roughly at a rate of 60 kilometers a year. To see how far south the population could extend, the scientists tried to gauge how far the animals can hop under various temperature conditions. They tested 89 toads on a 2-meter course, measuring hopping speed at five temperatures ranging from 15° to 35°C. Hopping speeds ranged from a molasses-like 300 meters per hour at 15°C to a brisk 2.2 km at 30°C, they report in the August issue of *Ecography*.

Combining data on toad movements with information on reproductive needs (ponds for eggs and larvae) and climate, the researchers predicted that, contrary to some previous analyses, the toads won't be invading major cities such as Sydney and Melbourne. Even with predicted climate change, they say, adults would be too slowed down by cool, dry weather to spawn or find enough to eat. Biologist A. Marm Kilpatrick of the University of California, Santa Cruz, who does research on the West Nile virus, calls it a "neat" study that "offers a bottom-up mechanistic way to look at an animal's distribution" by combining data on climate, physiology, and behavior.

## The Emperor's Toes

This 80-centimeter-long foot—in what archaeologists describe as "exquisitely carved army boots covered with a lion skin and decorated with tendrils and Amazon shields"—is part of a 5-meter-tall statue of the Roman emperor Marcus Aurelius, who ruled from 161 to 180 C.E. The fragments were found last month in the rubble of a huge bath complex in the Turkish town of Sagalassos by a team led by Marc Waelkens of the Catholic University of Leuven, Belgium. The baths were destroyed by an earthquake about 600 C.E., according to carbon dating of owl pellets at the site.

The statue was part of a gallery of 2nd century emperors that the scientists believe stood in niches around the cross-shaped, mosaic-covered frigidarium, into which people plunged for cold baths. Last year, the team uncovered chunks from a giant statue of Hadrian, who ruled from 117 to 138 C.E., that are currently on display in the British Museum in London.

## The Right Note

Perfect pitch is thought to be a rare capacity, possessed by about one in 10,000 people. But researchers at the University of Rochester's Eastman School of Music in New York state have developed a way to test nonmusicians for perfect pitch that they hope will yield a more accurate estimate.

The usual test—playing a note and seeing if a person can identify it by the sound—can be done only with subjects who know musical notation. Betsy Marvin, a musical theorist, and Elissa Newport, a neuroscientist, devised a test in which people listen to a three-note motif played repeatedly for 20 minutes. Then they hear either those notes again or the same motif transposed to a different key and are asked to identify the original notes. The researchers first validated the test with music students, comparing results with the results of the traditional pitch test. Then they tried it on 24 volunteers with little or no musical training. Six of those proved to be as accurate or almost as accurate in recognizing pitches as the music students with perfect pitch. That suggests perfect pitch is more common than has been thought, says Marvin, who presented preliminary results last week at the International Conference of Music Perception and Cognition in Sapporo, Japan.

Peter Gregersen, a geneticist at the North Shore–Long Island Jewish Health System in New York who studies absolute pitch, says such a test could help in determining if people are born with perfect pitch or if learning plays a role.

## Chinese Emissions

Economic modelers are having a hard time keeping up with the Chinese industrial juggernaut. Based on recalibrated modeling and the latest economic data, a new working paper from the Electric Power Research Institute (EPRI) in Palo Alto, California, forecasts that by 2030 China's energy sector will be emitting about 4 billion tons of carbon—twice as much as estimated in a 2005 International Energy Agency (IEA) projection. "Growth in China is so rapid that it is difficult to predict emissions just 2 years from now," says the unpublished paper by Geoffrey J. Blanford and colleagues at EPRI and the Centre for Energy Policy and Economics in Zürich, Switzerland.

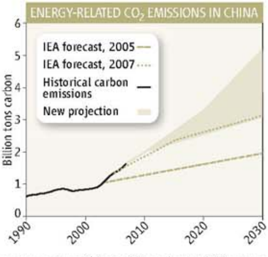

CREDITS: BEN PHILLIPS; SOURCE: G. BLANFORD; SAGALASSOS ARCHAEOLOGICAL RESEARCH PROJECT

# NEWSMAKERS

EDITED BY YUDHIJIT BHATTACHARJEE

## LHC

The world's most expensive particle physics experiment will get under way on 10 September when CERN's Large Hadron Collider (LHC) goes online (see p. 1291). Thousands will be watching as the first beams of protons are sent through the collider. But the search for the Higgs boson also has a human side. Here are a few of their stories.

So, on the big day, who will be sitting in the Captain Kirk chair ready to push the start button? **Roger Bailey**, head of the beam commissioning team, isn't letting on. "It'll be me or one or two colleagues," he says. "We'll decide over the next couple of days."

Bailey has assembled a 30-person team that will operate the accelerator round the clock over the next few months in hopes of ironing out the kinks that come with the first collisions. "It's going to be pretty stressful between now and Christmas," he says.

Bailey was there in the control room in 1989 at the opening bell for CERN's previous big machine, the Large Electron-Positron collider. "Half the lab was crammed in there," he recalls. His goal for 10 September is clear, if not simple: Get streams of protons to circumnavigate both rings. "If we can do that, we'll know we have something we can work with."

If the Large Hadron Collider (LHC) reveals the Higgs boson—the famed God particle—then CERN officials have a detailed protocol to announce the discovery at a specially convened seminar. However, CERN spokesperson **James Gillies** concedes that word will probably leak out prematurely. "People are excited about [LHC], and they want to talk," he says. "I think it's pretty likely that if there's solid evidence of the Higgs, it will come out." Still, Tejinder "Jim" Virdee, leader of the team working with the massive CMS particle detector, says that he expects his collaborators—all 2900 of them—"to follow the protocol, no ifs or buts."

## Q&A

Three months after the Large Hadron Collider (LHC) is turned on, former CERN particle physicist **Rolf-Dieter Heuer** will rejoin the lab as its new director general. Currently research director for particle and astroparticle physics at DESY, Germany's particle physics lab in Hamburg, Heuer says that it's time for CERN "to change back to analysis mode" after spending more than a decade building the $5.5 billion machine.

**Q: CERN still has debts to repay on the LHC. What will be their impact?**

[Repayments] will certainly limit our activities, but after 2010–11 we will have some maneuvering space to fund new initiatives.

**Q: Will these include non-LHC areas, such as antimatter and neutrino physics, that were scaled down during construction?**

These have continued on a minimal level, but we do need to maintain diversity. If I want to ramp these up, proposals must be scientifically high-class. One should be able to convince funding agencies.

**Q: Funders seem cool about pushing ahead with the International Linear Collider. Would a delay give CERN's emerging CLIC accelerator technology a new opportunity over the design already on the table?**

Between 2010 and 2012, the LHC will tell us the next energy range of interest. Once we know the energy range, we can decide on which technology.

**Q: Should countries such as the United States and Japan, which don't pay for the collider or for operating costs, start paying a share of CERN's annual running expenses?**

There has to be a discussion of the role of CERN as a European lab in a global partnership, and the issue of contributions will come up naturally. We must be proactive: Already next year, we should start to define how that partnership would look.

## In Other News ...

### AWARDS

Three European scientists last week received honors for their efforts to communicate science to the public. **Chris Smith**, a virology lecturer at the University of Cambridge, U.K., received the Royal Society's $4500 Kohn award for his popular radio show, *The Naked Scientists*, which aims to "strip science down to its bare essentials" through interviews with researchers. Evolutionary biologist **Axel Meyer** of the University of Konstanz, Germany, took home $7300 as winner of the European Molecular Biology Organization's (EMBO's) annual communications award for his articles in mainstream newspapers and magazines and his radio and television appearances. EMBO also awarded a special prize of $4700 to another successful science communicator: zoologist **Jürgen Tautz** of the University of Würzburg, Germany, who authored a popular book on honey bees last year.

## THEY SAID IT

**"Science, science, science, and science."**

—House Speaker Nancy Pelosi (D–CA), at a 26 August breakfast meeting during the Democratic National Convention in Denver, when asked about her plans for the first 100 days if Barack Obama is elected president. A spokesperson says the speaker's "innovation agenda" also includes "21st century jobs and biomedical research."

CREDITS (TOP TO BOTTOM): ©CERN; ©CERN; ©CERN

The genetics of two aggressive cancers
1280

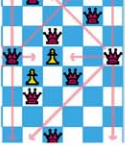

MathFest: By the numbers
1282

GENETIC PRIVACY

# Whole-Genome Data Not Anonymous, Challenging Assumptions

Last week, scientists learned that a type of genetic data that is widely shared and often posted online can be traced back to individuals who proffered up their DNA for research. The revelation, in a paper published in *PLoS Genetics*, prompted the National Institutes of Health (NIH) in Bethesda, Maryland, and the Wellcome Trust in the United Kingdom to strip some genetic data from their publicly accessible Web sites, and NIH to recommend that other institutions do the same.

The concern is with studies in which researchers pool genetic data from hundreds of people to look for broad patterns of genetic inheritance. Because the pool consists of DNA from so many people, the assumption has been that it would be impossible to identify any one individual's DNA. The new study suggests that's not the case. NIH officials and others agree that the likelihood of a breach of privacy is low, largely because the pooled data must be matched against a particular person's isolated DNA—something that, currently, only researchers generally have access to.

But the discovery that these DNA pools don't protect anonymity is still troubling, especially because no one had considered that a possibility. The first response to the results "is, 'You're crazy,' " says David Craig, a geneticist at the Translational Genomics Research Institute in Phoenix, Arizona, who conducted the work. Less than 9 months ago, NIH was so confident in the anonymity of pooled genetic data that it recommended it be made public for all researchers to use.

Craig found this confidence misplaced, for a simple reason: Geneticists now routinely examine hundreds of thousands of DNA variants, called single-nucleotide polymorphisms (SNPs), at a time, instead of hundreds as they did just a few years ago. As a result, they're gathering enough information about the pattern of SNPs in a pooled sample that it's feasible to deduce whether a particular individual, with her own unique SNP blueprint, is represented in a much bigger pool of DNA—even if that person's DNA was less than 1% of the mix. Craig and his colleagues managed to do this by ascertaining the distribution pattern of every single SNP—essentially, asking the same question 500,000 times. They were successful because, it turns out, every individual shifts a genetic pool subtly in certain directions, and studying enough SNPs unveils the pattern of those shifts. The biggest chance of error comes from false positives from relatives whose DNA may also appear in the pool, says Craig.

**Faceless no more.** A new study shows that individuals can be pinpointed in pooled DNA.

NIH officials were startled when Craig notified them of his findings about 2 months ago; they had their own statisticians repeat the experiments. "They said, 'Yup, this works,' " says Elizabeth Nabel, head of NIH's Heart, Lung, and Blood Institute. "We still consider the risk to the individual relatively low," she continues, but "there's a window of vulnerability."

The greatest concern is that identifying an individual this way could reveal sensitive health information. Genome-wide association studies compare data from people with and without a particular disease, so knowing which pool a person falls into can convey whether they have, say, cancer, or diabetes, or multiple sclerosis. "We have a false sense of security with pooled data," says Pablo Gejman, a psychiatric geneticist at Northwestern University in Evanston, Illinois. "There is sensitive information" here.

The Wellcome Trust has pulled data on about a dozen common diseases, and NIH has pulled data from nine genetic studies off two sites, dbGaP, which includes genome-wide association studies, and CGEMS, a site for cancer genetics work. The seven affected studies on dbGaP had been downloaded by about 1000 people all told, says James Ostell, who oversees that and other NIH databases.

NIH officials are informing geneticists about the policy change through e-mails and their Web site; the Broad Institute in Cambridge, Massachusetts, has followed suit and removed pooled data from its site. This is "a logical choice, a necessary choice," says Michael Boehnke, a statistical geneticist at the University of Michigan, Ann Arbor, whose data from a diabetes study was taken down from NIH.

Nabel says that NIH is considering a new policy in which the pooled data will be released to researchers who apply, as is now the case with data traditionally considered much more sensitive.

Still, Ostell and others say the current privacy risk is minimal. It could be of more concern 5 or 10 years from now, as genetic information proliferates. One possible scenario is that law enforcement agencies might turn to pooled data to determine whether their suspect is present—and even demand that the researcher help them identify him.

Craig's work could help future forensic investigators in another way: Currently, they're unable to identify a suspect's DNA in a mixed sample—say, a sample of blood from several people—if the suspect's blood is less than 10% of the total. "A lot of forensic crime samples do have small contributions from people of interest, [and] right now we can do essentially nothing," says Bruce Weir, a biostatistician who studies genetics and forensics at the University of Washington, Seattle.

**–JENNIFER COUZIN**

CREDIT: CHAD BAKER/RYAN MCVAY/GETTY IMAGES

FOCUS

The psychopathic brain
1284

Particle physics's new frontier
1287

PLANT SCIENCE

# China Plans $3.5 Billion GM Crops Initiative

**BEIJING**—Confronted with land degradation, chronic water shortages, and a growing population that already numbers 1.3 billion, China is looking to a transgenic green revolution to secure its food supply. Later this month, the government is expected to roll out a $3.5 billion research and development (R&D) initiative on genetically modified (GM) plants. "The new initiative will spur commercialization of GM varieties," says Xue Dayuan, chief scientist on biodiversity at the Nanjing Institute of Environmental Science of the Ministry of Environmental Protection.

A central aim is to help China catch up with the West in the race to identify and patent plant genes "of great value," says Huang Dafang, former director of the Biotechnology Research Institute of the Chinese Academy of Agricultural Sciences in Beijing. Once intellectual property rights are in place, says Huang, transgenic technology could transform Chinese farming "from high-input and extensive cultivation to high-tech and intensive cultivation."

In the decade since China first allowed commercial planting of four GM crops, the government has moved cautiously, granting only two further approvals for small-market species: poplar trees and papaya (see table). Currently, just one GM crop—insect-resistant cotton—is now planted widely, says Xue. China has balked at commercializing GM versions of staples such as rice, corn, and soybeans.

That may change, as China's leadership has thrown its weight fully behind GM. "To solve the food problem, we have to rely on big science and technology measures, rely on biotechnology, rely on GM," Premier Wen Jiabao told academicians last June at the annual gathering of the Chinese Academy of Sciences (CAS) and the Chinese Academy of Engineering. China's State Council, which Wen leads, approved the GM initiative in July.

Details of the new initiative, including which crops will gain initial support, are being hammered out, scientists say. Some funds will go to R&D on transgenic livestock, an area that has lagged behind GM crops. By 2006, the Chinese government had granted permits for 211 field trials of 20 GM crops, including the six approved for commercial production. As in other countries, the varieties that China has commercialized so far are equipped with genes to resist pests, tolerate herbicides, or stay fresh longer—not genes that directly boost yields.

CHINA'S TRANSGENIC PLANTS

| PLANT | YEAR COMMERCIALIZED |
|---|---|
| Cotton | 1997 |
| Petunia | 1997 |
| Tomato | 1998 |
| Sweet pepper | 1998 |
| Poplar trees | 2005 |
| Papaya | 2006 |

**Slim pickings.** Of the six plants that China has approved for commercialization, only cotton is grown widely. A new initiative could pave the way for GM versions of the biggest prize of all: rice.

Proponents note that China's cautious embrace of transgenic technology has yielded a major success story: GM cotton. Introduced into commerce in 1997, 64 varieties of pest-resistant cotton are now grown on 3.7 million hectares, or about 70% of the area devoted to commercial cotton, averting the use of 650,000 tons of pesticides, says Huang.

The big prize is GM rice. Three years ago, Huang Jikun, director of CAS's Center for Chinese Agricultural Policy in Beijing, and colleagues reported that field trials of GM rice in China were going well—boosting yields and reducing pesticide use on plots—and predicted that the varieties were on the threshold of commercialization (*Science*, 29 April 2005, p. 688). But the Chinese government is reluctant to tinker with the country's most important crop and has put off commercialization. The new initiative might break the logjam, says Huang Jikun. "I hope the commercialization of GM rice will come within a couple of years," he says.

Although the central government has not released a budget figure for the new initiative, a spokesperson for the Ministry of Agriculture told *Science* that it would cost $3.5 billion over 13 years. Half is expected to come from local governments on whose land GM crops will be grown and from agricultural biotechnology companies. "It's a new way to support a big science project in China," says Huang Dafang. Another departure from other R&D initiatives, he says, is that each funded program is expected to produce an economic payoff.

One component of the initiative will be to educate the public about GM crops, says Huang Jikun. Although China is unlikely to see the sort of protests that have derailed field trials and commercialization in Europe, there are currents of disquiet in the general population. "For consumers, the safety of GM crops is the biggest worry. Just like some people are afraid of ghosts, some people are afraid of GM crops," says Zeng Yawen of the Biotechnology and Genetic Resources Institute of the Yunnan Academy of Agricultural Sciences in Kunming. Although Zeng believes that GM food safety will be demonstrated adequately, he worries that the new initiative will push China to "move too fast to commercialize GM varieties."

But with questions mounting about China's ability to feed itself, others contend that not pushing ahead with GM varieties could be more detrimental than any theoretical hazard. "Any kind of new technology may have risk," says Huang Dafang. But legitimate concerns, he says, should not be overshadowed by scare tactics designed to "mislead the public in the name of environmental protection." With the country's leaders firmly behind GM crops, it's unlikely that any protests would get very far.

**–RICHARD STONE**

With reporting by Chen Xi and Jia Hepeng.

PHOTO CREDITS: USDA/ARS

CANCER GENETICS

## A Detailed Genetic Portrait of the Deadliest Human Cancers

Three studies published this week have given researchers their most detailed look so far at the genetic mutations that underlie the deadliest of human cancers: pancreatic cancer and the brain tumor glioblastoma. They have firmed up the role of key genes and also found that scores of aberrant genes are involved in relatively few cell signaling pathways. One study also unearthed a gene never before linked to cancer that is mutated in a substantial fraction of glioblastoma tumors. "It shows we can still be surprised" by the biology of cancer, says Michael Stratton, who oversees a cancer gene sequencing project at the Sanger Institute in Hinxton, U.K.

These studies are all based on the premise that information gleaned from systematically cataloging the main mutations in tumors will be worth the high cost. Three years ago, when genome sequencer Eric Lander of the Broad Institute in Cambridge, Massachusetts, proposed spending $1.5 billion on what is now called The Cancer Genome Atlas (TCGA), skeptics helped persuade the U.S. National Institutes of Health to start with a 3-year, $100 million pilot project. One of the glioblastoma studies is the first fruit of that effort.

Meanwhile, a team led by Bert Vogelstein, Kenneth Kinzler, and Victor Velculescu at Johns Hopkins University in Baltimore, Maryland, had begun a private cancer genome project, starting with breast and colorectal cancer (*Science*, 8 September 2006, p. 1370). Now this team and collaborators have sequenced the coding regions of 20,700 genes—nearly all the known genes in the human genome—in 22 glioblastoma and 24 pancreatic cancer samples. They also looked for abnormalities in gene copy number and gene expression.

In two papers published online by *Science* this week (www.sciencemag.org/cgi/content/abstract/1164382 and -1164368), they report finding hundreds of genes that were mutated in these two cancers. There were an average of 63 altered genes in each pancreatic tumor and 60 per glioblastoma. The mutations varied from tumor to tumor, but the most important tended to fall in the same cell pathways. For example, 12 specific pathways were disrupted in at least 70% of pancreatic tumors. "It points to a new way of looking at cancer," says Vogelstein, who suggests that treatments should target these pathways, not the products of single genes.

One of the altered genes found in the glioblastoma study, *IDH1*, appeared in 12% of tumors, and more often in younger patients and those with secondary tumors, the Johns Hopkins team reported. A change in an amino acid of the encoded protein seems to help patients with this mutation live longer than others with glioblastoma.

The third study, published online by *Nature*, analyzed more than 200 glioblastoma samples. It surveyed all the samples for genetic alterations such as changes in copy number and probed about half the samples for mutations in 600 genes already implicated in cancer, says co-leader Lynda Chin of the Dana-Farber Cancer Institute in Boston (*Science*, 4 July, p. 26). The study found many of the same aberrant

NEUROSCIENCE

## Hippocampal Firing Patterns Linked to Memory Recall

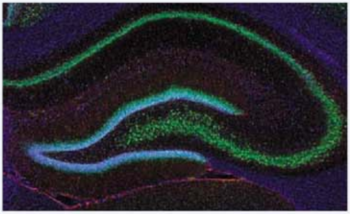

**Memory aid.** A rat's hippocampus (*above*) generates sequences of neural firing that may help it remember what to do next.

CREDIT: NEAL MELVIN/2007 OLYMPUS BIOSCAPES COMPETITION (HONORABLE MENTION)

The hippocampus, tucked deep inside the temporal lobes of the brain, has been intensely studied for its role in recording memories. Now two studies—one with rats and one with people undergoing surgery for intractable epilepsy—suggest that patterns of neuron firing in the hippocampus are also involved in recalling past experiences.

"The two papers are significant because they point directly to reactivation of neural activity sequences as a mechanism for memory recall," says Edvard Moser, a neuroscientist at the Norwegian University of Science and Technology in Trondheim. Such a mechanism may underlie several functions attributed to the hippocampus, Moser says, including navigation, memory, and planning future actions.

In the rat study, researchers led by Eva Pastalkova and György Buzsáki of Rutgers University in Newark, New Jersey, simultaneously recorded the activity of scores of hippocampal neurons as rodents ran through a maze shaped like a squared-off figure eight. The rats always started the maze by running down the middle of the three arms and then chose to continue down either the left or the right arm. The researchers trained them to alternate between the right and left arms each time they ran the maze. In between runs, the rats spent 10 to 20 seconds on a running wheel.

During this delay period, neurons in the hippocampus fired in sequences that predicted which arm the rat would run next, the researchers report on page 1322. Even in the few cases when a rat goofed and went the wrong way, the preceding firing sequence predicted its mistake.These sequences—which resemble sequences that occur as a rat actually runs through a maze—likely represent the brain's internal mechanism for planning (or reminding itself) what it has to do next, Buzsáki says.

The findings confirm a decade-old prediction that the hippocampus might generate such firing sequences to maintain important information during a delay in a task, says David Redish, a neuroscientist at the University of Minnesota, Minneapolis. Redish notes that consistent patterns of activity emerged only when the rat had something to remember. "When the rat is just running on

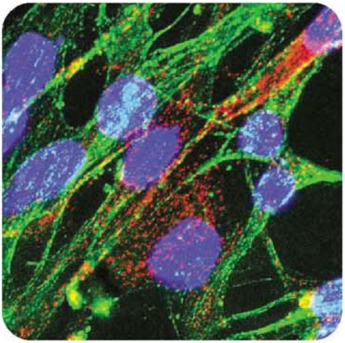

**Probing a killer.** Two new studies tally genetic glitches that cause the brain tumor known as glioblastoma, orange in this image of brain cells.

CREDIT: R. BICK, B. POINDEXTER, UT MEDICAL SCHOOL/PHOTO RESEARCHERS, INC.

genes that the Johns Hopkins team uncovered—but not *IDH1*, which was not among the genes the team sequenced. Their larger sample set will serve as a reliable reference on how frequently mutations occur in glioblastoma, including several genes for which the evidence was limited until now, says Chin. Having methylation data and samples from patients who received treatment also allowed the team to finger mutations in DNA repair genes that may help explain why tumors that initially respond to temozolomide, the main drug for glioblastoma, can become resistant to subsequent therapies.

TCGA is preparing follow-on papers, for example on using the molecular data to classify subsets of tumors, Chin notes. It will also expand the search: The project, which is also studying lung and ovarian cancers, will use new technologies to sequence thousands of genes in each tumor.

"I see them [the public and private glioblastoma studies] as wonderfully complementary," says pathologist Paul Mischel of the University of California, Los Angeles, who studies glioblastoma. Other researchers who hope to use the findings to improve cancer treatment agree. "This is a start and a wonderful start," says Santosh Kesari, a neurooncologist at Dana-Farber.

**–JOCELYN KAISER**

a wheel for the heck of it in its home cage, they don't see it."

In the human study, published online this week in *Science* (www.sciencemag.org/cgi/content/abstract/1164685), researchers led by Hagar Gelbard-Sagiv of the Weizmann Institute of Science in Rehovot, Israel, and Itzhak Fried of the University of California, Los Angeles, recorded from hundreds of neurons in and around the hippocampus of 13 epilepsy patients undergoing operations in which surgeons introduced electrodes into the brain to locate the source of their seizures. The patients watched several 5- to 10-second video clips that depicted a variety of landmarks, people, and animals. A few minutes later, the researchers asked the patients to freely recall the clips they'd just seen and call them out as they came to mind. (Most subjects easily remembered almost all of the clips.) The first time the patients saw the clips, many neurons in the hippocampus and a nearby region, the entorhinal cortex, responded strongly to certain clips and weakly to others—preferring a clip from *The Simpsons*, say, to ones showing Elvis or Michael Jordan. Later, each neuron began firing strongly a second or two before the subject reported recalling that neuron's preferred clip, but not when the subject recalled another clip.

"Previous work [with animals] has shown that such reactivation occurs during sleep as well as during certain behaviors where memory is needed, but it has remained unclear whether reactivation actually reflects recall of the memory," say Moser. Fried's findings are exciting because they provide the first direct link between reactivation of hippocampal neurons and conscious recall of a past experience, says neuroscientist Matthew Wilson of the Massachusetts Institute of Technology in Cambridge.

Both studies have implications for an ongoing debate about the relationships among various functions attributed to the hippocampus, says Lynn Nadel, a neuroscientist at the University of Arizona in Tucson. Nadel says that the findings fit with his view that the neural mechanisms underlying spatial navigation, episodic memory, and action planning may be one and the same. "One might say at this point that the available data suggest that the hippocampus is critical for 'navigating' through space not only in the present but also in the past, to retrieve memories, and in the future, to predict the results of actions," Nadel says.

**–GREG MILLER**

# SCIENCESCOPE

## Japanese Budget Rollout

**TOKYO**—Japan's education ministry last week optimistically called for boosting fiscal 2009 science spending a hefty 13.4% year-on-year to $24.1 billion. The ministry wants to add $20 million, a 12.4% increase, for academic research grants and 11% more—for a total of $1.2 billion—to advance big science projects, including $41 million for Japan's contribution to the international Atacama Large Millimeter Array in Chile. Applied research fared even better. The ministry wants to increase one such grant category, for example, by 42%, to $4.5 million. The proposed budget faces scrutiny from the budget-minded finance ministry. "Negotiations will be tough, but we'll do our best," says Shinichiro Izumi of the education ministry. The budget, which takes effect in April, will be finalized by January.

**–DENNIS NORMILE**

## Taleyarkhan Weighs Suit

Rusi Taleyarkhan, the Purdue University nuclear engineer deemed guilty of research misconduct, isn't going quietly. Last week, Purdue stripped him of his named professorship. Now, Taleyarkhan and his attorney are considering filing a grievance with Purdue, a lawsuit against the school, or both. "The process and the manner in which Purdue has carried itself … is testimony for the need to resort to the court system," Taleyarkhan wrote in an e-mail to *Science*. In 2002, Taleyarkhan and colleagues reported that a tabletop device generated nuclear fusion inside collapsing bubbles. But in July, an investigation organized by Purdue concluded that later reports aimed at replicating the work involved research misconduct. Taleyarkhan's attorney says the scientist will continue to investigate bubble fusion. **–ROBERT SERVICE**

## Your Local Library

The U.S. National Institutes of Health (NIH) has chosen nine screening centers in the second phase of its Molecular Libraries program (*Science*, 8 August, p. 764). NIH wants to test biological assays submitted by researchers against 300,000 chemicals in hopes of finding research probes and drug leads. Four major centers will receive a total of $208 million over 4 years—the Burnham Institute for Medical Research and The Scripps Research Institute, both in San Diego, California; NIH's intramural center in Rockville, Maryland; and the Broad Institute in Cambridge, Massachusetts. NIH will also support five smaller centers.

**–JOCELYN KAISER**

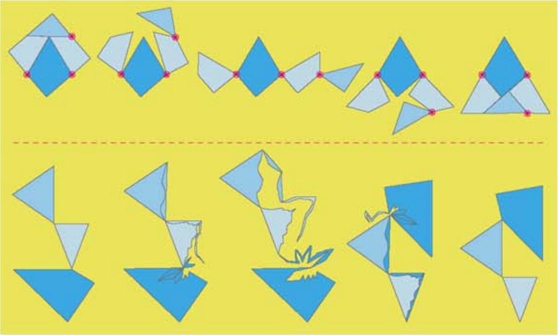

**Location, location, location.** A square can become an equilateral triangle without ever falling apart (*top*). The same is true for other pairs of polygons. The proof starts with a trick that, in effect, moves hinges around (*bottom*).

# Shapeshifting Made Easy

Mathematicians aren't squeamish about doing dissections, but they do often come unhinged. Now computational geometers at the Massachusetts Institute of Technology (MIT) in Cambridge have proven it's possible to do mathematical dissections without falling to pieces.

The victims in this case are not frogs but polygons: simple geometric shapes bounded by straight sides. In the early 19th century, mathematicians proved that any two polygons with the same area can be cut into a finite number of matching pieces. For example, it's possible to cut a square into four pieces and rearrange them into an equilateral triangle.

About 100 years ago, the English mathematician and puzzle designer Henry Dudeney added an extra wrinkle to the dissection challenge: He showed that the rearrangement from square to equilateral triangle can be done with pieces connected by hinges (see figure, above). Dissection enthusiasts have since devised many more hinged transformations.

In 1997, Greg Frederickson, a computer scientist and geometric-dissection buff at Purdue University in West Lafayette, Indiana, asked whether what Dudeney did for the square and triangle can be done for any two polygons. The question caught the attention of Erik Demaine, then beginning graduate work in computer science. A decade later, Demaine, now a professor at MIT, has the answer: in a word, yes.

Demaine returned to Frederickson's problem last fall with his father, Martin Demaine, and four students in a problem-solving seminar: Timothy Abbott of MIT, Zachary Abel and Scott Kominers of Harvard University, and David Charlton of Boston University. The group came up with a general procedure for turning an arbitrary dissection into a hinged dissection. Demaine described their proof at MathFest. "It was a surprising result to me, because I thought it was false," he says.

Their proof starts with an idea "so crazy that we never thought of it," Demaine says. That idea is simply to take an unhinged dissection of one polygon and arbitrarily add hinges, then subdivide the pieces and add additional hinges until the polygon can contort into its equal-area partner. The key step is to show that judicious subdivision can, in effect, take a hinge that connects, say, piece A to piece B and move it to connect A to C (see figure).

"The movement is magical," Frederickson says. On the other hand, he notes, "you don't get very pretty dissections this way."

The construction works on three-dimensional (3D) dissections as well, which could help guide the design of reconfigurable robots—modular machines that rearrange their parts like real-life Transformers. In 3D, unfortunately, equal volume doesn't guarantee the existence of a dissection. But when dissections do exist, the MIT group's construction shows that they can be refined into hinged dissections. The results are an encouraging first step toward applications, Demaine says: "Now the optimization begins."

# Sweet Inspiration

Geometers find ideas everywhere. Take Mozartkugel, the famously spherical chocolate confections from Austria. Erik Demaine, his father, Martin, and colleagues John Iacono at the Polytechnic Institute of New York University and Stefan Langerman at Université Libre de Bruxelles have worked out a more efficient way to wrap them.

As mapmakers know from trying to go the other way, flattening a globe invariably distorts areas on its surface. Conversely, wrapping a globe with an inflexible wrapper (such as foil) crinkles the wrapper with infinitely many tiny folds. As a result, the area of any wrapper must exceed the surface area of the chocolate ball ($4\pi$ square units for a ball with a radius of 1).

One popular brand of Mozartkugel comes in a square foil of side length $\pi\sqrt{2}$ ($\pi$ times the square root of 2). Another comes in a $\pi \times 2\pi$ rectangular wrapper. In each case, the wrapper's area is $2\pi^2$—some 57% greater than the surface area of the sphere. Demaine and crew set out to see if they could do better.

The computational chocolatiers found that they could achieve a 0.1% savings over current practice with an equilateral triangle whose area turns out to be approximately $1.9986\pi^2$. (The exact value for 1.9986 … is a messy formula involving, for no obvious reason, the square root of 57.) But in fact, all that really covers the kugel is a three-leaf petal inside the triangle (see figure). That means the tips of the triangle can be cut off, leaving a wrapper of area $1.8377\pi^2$.

The clipped triangular wrapper offers another advantage: The length of its perimeter, $5.3503\pi$, is shorter than that of any other shape the researchers have found. (The square wrapper has a perimeter of $5.6569\pi$; the rectangular one, $6\pi$.) So a trefoil wrapper would not only save foil, Demaine and colleagues conclude, it would also be cheaper to

CREDITS (TOP TO BOTTOM): E. DEMAINE ET AL.; A. MORALES/SCIENCE

cut. The potential reduction in the carbon footprint associated with Mozartkugel materials and manufacturing, they joke, "partially solves the global-warming problem and consequently the little-reported but equally important chocolate-melting problem."

## A Royal Squeeze

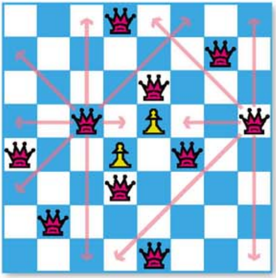

**Vivat regina.** Adding pawns makes a classic chessboard problem even more queenly.

In 1850, the great German mathematician Carl Friedrich Gauss took a shine to a funky little counting problem: How many ways can eight queens be placed on a chessboard so that no two queens attack one another (i.e., line up horizontally, vertically, or diagonally)? It's not obvious it can be done at all, but it turns out there are 92 solutions. Gauss didn't spot them all, proof in itself that the problem is a bit of a poser.

Modern computers can easily find all 92, but mathematicians have upped the ante so that even Deep Blue would scratch its silicon head, mainly by making the board larger. There are, for example, 2,207,893,435,808,352 ways of placing 25 nonattacking queens on a $25 \times 25$ chessboard, a computation completed 3 years ago at INRIA.

"There's a lot of interesting theory behind these questions," notes Loren Larson, a chessboard problem expert in Northfield, Minnesota. "They're also nice programming exercises. They're good examples of backtracking algorithms," also known as depth-first searches.

In a talk at MathFest, Doug Chatham of Morehead State University (MSU) in Kentucky described a variant he and collaborators have explored, in which pawns are allowed on the chessboard. The pawns interrupt the queens' line of sight, making it possible for more queens to fit on the board. How many more queens, they wondered, do the pawns make possible?

Chatham and crew—MSU colleagues Gerd Fricke and R. Duane Skaggs, Maureen Doyle of Northern Kentucky University in Highland Heights, Matthew Wolff of Pyramid Controls Inc. in Cincinnati, Ohio, and MSU student Jon Reitmann—have proved that each additional pawn permits an extra queen, provided the board is large enough. For example, with two pawns, it's possible to get 10 queens on a standard $8 \times 8$ board (see figure). In the current proof, fitting an extra $k$ queens using $k$ pawns on an $N \times N$ board requires $N$ to be greater than $25k$, Chatham notes, but adds, "We believe the actual minimum sizes are much smaller."

There are no immediate applications for the queens-and-pawns problem, Chatham says, but the original nonattacking-queens problem has found uses in computer science for parallel memory schemes and in statistical physics for particle models with long-range interactions. "We hope to find similar applications for our problem," he says. **–BARRY CIPRA**

## Taking the Edge Off

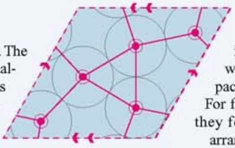

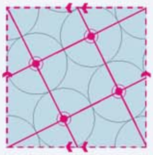

Math has a lot to say about packing things together. The abstract problem of cramming, for example, equal-sized circles into a larger square has applications as far-flung as error-correcting codes for digital communications and the physics of granular materials such as sand. But what if the square has no edges? A quartet of researchers has shown how packing works in such a borderless space.

The space in question is a torus, a shape like the surface of an inner tube. To topologists, a torus is equivalent to a parallelogram with its opposite edges glued together. On the unfurled, flattened-out torus map, anything leaving on one side immediately reenters from the other, as in many video games. William Dickinson of Grand Valley State University in Allendale, Michigan, and undergraduates Daniel Guillot of Louisiana State University, Baton Rouge, Anna Castelaz of the University of North Carolina, Asheville, and Sandi Xhumari of Grand Valley have spent the past two summers studying circle packings in tori.

Because a torus has no boundary, the circles are constrained only by one another—just as they would be on a patch of regularly repeating patterned wallpaper. Dickinson and students classified the graphs that can result when lines are drawn connecting centers of tangent circles (red lines in the figure, below), then set to work analyzing which ones lead to the densest packings (i.e., packings with circles of the largest possible radius). For five circles—the first truly challenging case—they found 20 different ways the circles could be arranged on the torus.

They applied the theory to two particular tori: the "square" torus formed by connecting opposite edges of a square, and the "triangular" torus, which starts from a rhombus with a 60-degree angle. Guillot and Castelaz found the best five-circle packing for the triangular torus last summer (2007), and Xhumari did the same for six circles this summer. Together, the ideas they developed enabled Dickinson to nail down the densest packing for five circles on the square torus. It occupies $\pi/4$ or 78.5% of the square torus, as compared with 71.1% on the triangular torus (see figure).

"In general, it is very difficult to prove that a particular packing is optimal," says Ronald Graham, a circle-packing expert at the University of California, San Diego. Working without boundaries may make proofs easier to come by, he thinks, "but that is just an impression." **–B.C.**

**Unwrapped.** To cover a torus with circles, researchers studied how to pack them into a square or rhombus whose opposite edges are connected.

CREDITS (TOP TO BOTTOM): D. CHATHAM ET AL.; J. NEWFIELD/SCIENCE; SOURCE: W. DICKINSON ET AL.

# Investigating the Psychopathic Mind

**With a mobile brain scanner and permission to work with inmates in New Mexico state prisons, Kent Kiehl hopes to understand what goes awry in the brains of psychopathic criminals**

**ALBUQUERQUE, NEW MEXICO—**Kent Kiehl remembers his first conversation with a psychopath as if it were yesterday. Kiehl had just started a graduate program in psychology, and he intended to study the criminal mind by interviewing prisoners. His first subject was a thief who'd made a fortune robbing banks in North America and lived the high life for years, renting luxury apartments across Europe and—if he did say so himself—enjoying a great deal of success with the fairer sex. "Have you ever had 15 women in one night?" he asked Kiehl.

The man was behind bars not because of a heist gone wrong but because one of his girlfriends was cheating on him. He tracked her down at a motel room and burst in with his gun drawn. He shot her lover, but the man managed to get away. The woman later testified against him in court. If he could do it all over again, he told Kiehl, he would have killed them both. Such stories fascinate Kiehl, now an associate professor of psychology and neuroscience at the University of New Mexico and director of Mobile Imaging Core and Clinical Cognitive Neuroscience at the Mind Research Network (MRN) in Albuquerque. "The other 300 or so psychopaths I've interviewed are just as interesting," he says.

Online
**sciencemag.org**
Podcast interview with the author of this article.

At age 38, Kiehl is embarking on a project he hopes will unravel the neural basis of psychopathy, a suite of personality and behavioral traits that is far more common in violent criminals than in the general population and is a strong predictor of repeat offenses. Given the crime and other societal costs caused by psychopathic individuals, Kiehl says, this group has been woefully understudied. He intends to change that. With a custom-built mobile magnetic resonance imaging (MRI) scanner—roughly $2.3 million of equipment packed into a 15-meter-long trailer—and permission from the New Mexico governor to work in all 12 state prisons, Kiehl aims to scan 1000 inmates a year.

"We'll have to see if he gets that much done, but if anybody can do it, Kent can," says Joseph Newman, a psychologist at the University of Wisconsin, Madison. "He has big ideas, and he pursues them energetically."

Kiehl's team conducts hours of interviews with each subject to assess them for psychopathy, substance abuse, and other mental health problems. In addition to functional MRI (fMRI) experiments to investigate neural activity during various tasks, they're also collecting anatomical images of the brain and DNA samples that could eventually be used to search for genetic risk factors—all with the prisoners' full consent and cooperation and all to be used solely for research. Kiehl's research is funded by four R01 grants from the National Institutes of Health, which pay about $900,000 a year in direct costs; MRN paid for the scanner.

Depending on what he finds, Kiehl's work could raise a host of legal and ethical questions. Could brain scans or blood tests one day improve on the personality profiles and other low-tech methods now used to assess the degree of risk a prisoner poses to society? If so, how should they be used? Could a better understanding of the psychopathic brain alter the way we think about the culpability of certain criminals? Could it point the way to interventions that prevent recidivism?

We'll never know unless we do the research, Kiehl says: "We just have no idea how their brains are different, how they got that way, and how we might be able to treat the condition."

### Local boy does bad

Kiehl's interest in psychopathy goes back to his childhood. He grew up in a middle-class neighborhood in Tacoma, Washington, not

CREDIT: MCDAVID HENDERSON

far from the boyhood home of serial killer Ted Bundy. While Kiehl was in grade school, Bundy was on a nationwide rampage, killing dozens of young women. Kiehl's father was a newspaper editor at the time, and Bundy's exploits were a common topic of discussion at the family dinner table.

Bundy exhibited several defining traits of psychopathy. He was cunning and manipulative, often donning disguises or feigning injury to lure women into a vehicle, and his preferred method of killing—crowbar blows to the head—as well as his proclivity for sex with his dead victims suggest a stunning lack of empathy. "Why would someone from my neighborhood end up being so bad?" Kiehl remembers wondering at the time.

By the time Bundy was executed in Florida in 1989, Kiehl was fantasizing about becoming a professional athlete. He entered the University of California (UC), Davis, that year after being recruited to play on the football team. Solidly built at 6'2", Kiehl still exudes an athlete's self-confidence. On a recent afternoon, he collected on a $100 bet with his lab manager over how far he could hit a golf ball. "I bet I could hit a ball farther than Tiger Woods," he boasted.

When a knee injury forced Kiehl to reconsider his life goals, he recalled his fascination with Bundy and began getting more interested in neuroscience. He rotated through the laboratories of several UC Davis neuroscientists, setting his sights on graduate work with psychologist Robert Hare at the University of British Columbia (UBC) in Vancouver, Canada. Hare is a preeminent psychopathy researcher who in 1980 published the first version of what has become the main tool for diagnosing psychopathy. In its current incarnation, the Psychopathy Checklist-Revised (PCL-R) scores subjects on 20 traits indicative of psychopathy, including callousness, impulsivity, and a history of behavioral problems. People in the general population typically score a four or five on the 40-point scale, Hare says. A score of 30 is widely used as a benchmark for psychopathy.

Psychopathy is not listed in the American Psychiatric Association's *Diagnostic and Statistical Manual of Mental Disorders*, 4th ed. (*DSM-IV*). The *DSM-IV* diagnosis of antisocial personality disorder captures some of the external manifestations of psychopathy, including impulsivity and antisocial behavior, but ignores personality traits such as glibness, callousness, and lack of remorse that are scored by the PCL-R. Studies with prison populations have found that roughly 20% (slightly more or less, depending on the security level of the prison) of inmates qualify as psychopaths. Incarcerated psychopaths have committed an average of four violent crimes by the age of 40, Kiehl says. More than 80% of those who are released from prison commit another crime, usually a violent one, within 3 years, compared with 50% for the overall prison population. "Psychopathy is the single best predictor of violent recidivism," says Kiehl, who hoped to collaborate with Hare to study the brains of psychopathic criminals.

But Hare wasn't interested in taking him on. "I had a lot of really outstanding students applying to work in my lab, and his grades weren't particularly great," Hare says. Not one to give up easily, Kiehl launched a campaign that included a barrage of recommendation letters from UC Davis faculty members; he also drove through a snowstorm from Tacoma to Vancouver to hand-deliver a few bottles of California wine that he knew Hare would appreciate. "That did it," says Hare. "He wore me down."

## An emotional problem?

Long before fMRI scanners came along, researchers suspected that psychopathy springs from a defect in emotional processing in the brain. Several of the disorder's signature traits hint at this, as do early studies that found blunted physiological responses—by measures such as heart rate and skin conductance—to emotionally evocative photographs in psychopaths.

Such abnormalities cast obvious suspicion on the amygdala, the hub of emotion in the brain. In the first fMRI study of psychopathy, published in 2001 in *Biological Psychiatry*, Kiehl and UBC colleagues found reduced amygdala activity in psychopathic criminals compared with nonpsychopathic criminals in response to emotionally charged words. A malfunctioning amygdala is likely to be one crucial factor in psychopathy, says James Blair, a cognitive neuroscientist at the National Institute of Mental Health in Bethesda, Maryland. Human and animal studies have shown that the amygdala is essential for learning to avoid behaviors with unwanted outcomes, he notes. By preventing children from learning to avoid actions that harm other people, faulty wiring in the amygdala could derail normal social development and contribute to the callous, unemotional traits seen in psychopaths, he proposes. In the June issue of *The American Journal of Psychiatry*, his research group reports that children with callous, unemotional traits have less amygdala activity than other children when viewing photos of fearful facial expressions.

Other researchers question whether the amygdala is really the source of the problem, however. Newman, for example, has long argued on the basis of behavioral evidence that deficits in regulating attention may be the central issue for psychopaths. "Once they start paying attention to some goal they want, they ignore cues that would otherwise activate the amygdala," he says.

Kiehl takes an even broader view. He suspects that psychopathy involves disruptions to a network of "paralimbic" regions in the brain's temporal and frontal lobes that contribute to emotion, attention, decision-

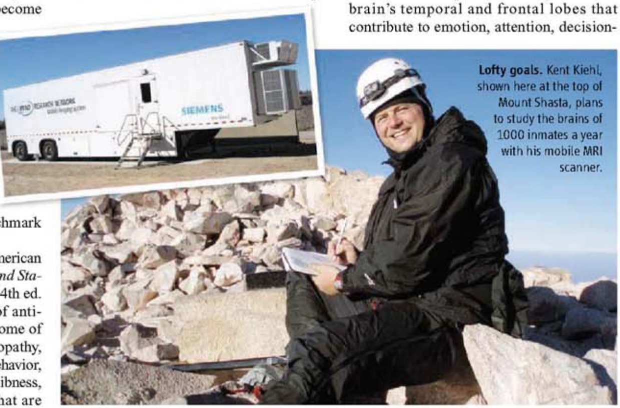

**Lofty goals.** Kent Kiehl, shown here at the top of Mount Shasta, plans to study the brains of 1000 inmates a year with his mobile MRI scanner.

CREDITS (TOP TO BOTTOM): COURTESY OF KENT KIEHL; STEVE RICHTER

making, and other cognitive functions. Resolving some of the confusion about which cognitive processes—and which brain regions—are dysfunctional in psychopathy is a major goal of his neuroimaging work in New Mexico.

But neuroimaging has limitations (*Science*, 13 June, p. 1412). The behaviors that can be studied inside an fMRI scanner, for example, are necessarily simplified and artificial. Proving that any given neural abnormality that shows up in imaging actually contributes to psychopathic traits and behavior in real life is never easy, says Adrian Raine, a clinical neuroscientist at the University of Pennsylvania. And then there's the chicken-and-egg problem. "Is it leading a violent, psychopathic way of life that causes the structural and functional impairments we find, or is it the other way around?" Raine asks. "It's going to be hard to answer that very important question."

### Prison-bound

On a blazing hot day in late July, Kiehl's mobile scanner was parked inside the gates topped with razor wire at the Youth Diagnostic and Development Center in Albuquerque. From the outside, the mobile resembles any trailer you'd see on an 18-wheeler, albeit cleaner than most. Kiehl spent a year working with engineers at Siemens to design it and ensure that the scanner's magnetic field would remain stable in different locations. Inside, the mobile looks like an ultra-high-tech recreational vehicle. The scanner sits at one end, its magnetic cylinder a pale blue doughnut extending from floor to ceiling. Flat-screen monitors adorn the walls in the adjacent control room, and next to that a small sitting room contains a stack of magazines for the benefit of a corrections officer who waits here while a juvenile prisoner gets scanned.

All experiments are off-limits to the media, in part because of concerns about the privacy of prisoners but largely because of a bad experience Kiehl had in Canada. A television network broadcast an interview with one of his research subjects that was edited to make the guy seem even scarier than he was, Kiehl says. When the inmate was denied parole a short time later, he threatened to kill any other inmates who participated in Kiehl's research; he also threatened to hit Kiehl with a chair. Now Kiehl says he won't jeopardize his staff by allowing the media to watch experiments or interview inmates.

Despite the nature of some of their subjects' crimes, Kiehl's students and postdocs say that they've never felt threatened. "They tend to really like us," says postdoc Matthew Shane. "They enjoy any excuse to talk with someone from outside the prison."

In one of the first studies using the mobile scanner, Kiehl's postdoc Carla Harenski and colleagues investigated how the brains of adult male prisoners respond to morally charged photographs, such as an image of a man holding a knife to a woman's throat. The inmates also rated the severity of the "moral violation" depicted in the photographs on a five-point scale. Those who gave high scores, suggesting greater sensitivity to moral violations, tended to have more activity in the superior temporal sulcus, a region implicated in previous studies of moral judgments, the researchers reported at an April meeting of the Cognitive Neuroscience Society. The team has subsequently scanned a bigger sample of prisoners and is investigating whether activity in this and other brain regions differs between those who are psychopathic and those who aren't.

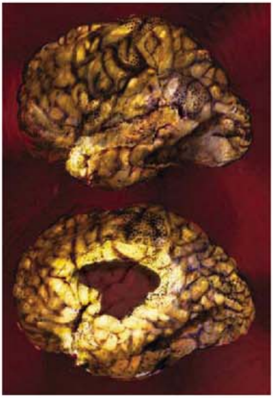

**Neural roots.** Kiehl suspects that disruptions to paralimbic brain regions (light areas) underlie psychopathy.

### Into the courtroom?

Such differences in brain activity within prison populations could potentially prove useful in assessing the risk posed by individual criminals, perhaps as a supplement to the PCL-R, Kiehl says. That checklist is currently used in dozens of countries. Depending on the jurisdiction, PCL-R scores are considered during sentencing and parole hearings. Some prisons use them, along with other factors, to determine security measures and treatment options.

Whether brain scans will ever prove useful in such settings depends on whether they add any predictive power, says Walter Sinnott-Armstrong, a philosopher at Dartmouth College and co-director of the MacArthur Foundation's Law and Neuroscience Project in Hanover, New Hampshire. Not everyone is optimistic. "It's not some sort of crystal ball that's going to tell you who's going to reoffend in 5 years' time," says Essi Viding, a cognitive neuroscientist at University College London. She also questions the practicality of the approach, given that MRI scans cost $1000 or more apiece and require substantial technical expertise. Even so, research on the neural basis of psychopathy could have important legal implications, says Sinnott-Armstrong. For example, he says, if future research points to a diminished moral capacity due to a neurodevelopmental defect, that could be relevant in court, where a defendant's understanding of the wrongfulness of his actions has a bearing on the verdict.

Kiehl gets impatient with such hypotheticals. For him, the ultimate question is how best to intervene—ideally, early in life before psychopathic traits become ingrained. The conventional wisdom is that psychopathy is untreatable, but that's based "more on clinical lore than solid research," says Michael Caldwell, a psychologist at the Mendota Juvenile Treatment Center and the University of Wisconsin, Madison. One widely cited study found that psychopaths who participated in a treatment program in the 1970s actually did worse than those who didn't, Caldwell says. But given that the treatment regimen involved nude encounter groups and LSD, those findings should perhaps be taken with several grains of salt. Kiehl says he's been buoyed by a recent series of papers by Caldwell and colleagues that suggest that targeted interventions, including cognitive behavioral therapy and family counseling, with juvenile offenders with psychopathic traits can prevent future crimes.

Caldwell, Newman, and other veteran psychopathy researchers say that they're encouraged to see Kiehl's project getting off the ground because public support and funding for psychopathy research has been hard to come by in the past. "If someone is cruel and always out for himself, it's not something that engenders sympathy, concern, and the desire to understand it," says Newman. "My view is that it's a really important disorder that needs to be understood." Kiehl says he couldn't agree more.

**–GREG MILLER**

CREDIT: MCDAVID HENDERSON

**Ring of fire.** The new machine will smash particles at energies seven times the previous record.

# The Overture Begins

**Next week, physicists at the European particle physics lab, CERN, will fire up the world's biggest atom smasher. Expectations are skyhigh, but discoveries may still be years away**

Fourteen years ago, scientists at the European particle physics laboratory, CERN, near Geneva, Switzerland, had only plans for a new highest energy particle smasher. Now, thanks to the efforts of thousands of people, they have a gargantuan machine, the $5.5 billion Large Hadron Collider (LHC), which stretches through a 27-kilometer ring of tunnel between Lake Geneva to the east and France's Jura Mountains to the west (*Science*, 23 March 2007, p. 1652). "It seemed like an enormous mountain to climb, that's for sure, back when we didn't have even a single magnet," says CERN's Lyndon Evans, who has led the project since its inception.

Evans says he's had moments of despair. In 2004, a manufacturing error forced workers to rip out and rebuild 3 kilometers of the high-tech plumbing that carries frigid liquid helium to the accelerator's superconducting magnets. In 2002, cost overruns led officials to delay the completion of the LHC by a year. But now, as researchers test the LHC's myriad subsystems, "it really feels like an old friend," Evans says. "It acts exactly like it is supposed to act." Physicists around the world hope their *ami*, the most complex scientific apparatus ever built, continues to behave next week when, for the first time—provided that lawsuits do not force a delay (see sidebar, p. 1291)—researchers try to circulate particles through its twin rings.

CREDITS: © CERN

In the quest to unravel the universe's inner workings, the 10 September start-up of the LHC marks the beginning of a new age of exploration. The collider should bag the long-sought Higgs boson, the missing link in physicists' "standard model" of the known particles and the one thought to give the others their mass. It could glimpse a slew of new particles, such as those predicted by a scheme called supersymmetry, or even reveal new dimensions of space. Other colliders hammered out how the standard model is structured; the LHC should answer deeper questions about why the model is as it is, says Gordon Kane, a theorist at the University of Michigan, Ann Arbor. "The LHC is a 'why' machine," he says.

But answers most likely won't come right away, cautions CERN's Peter Jenni, spokesperson for the 2500-member team working with the 25-meter-tall, 45-meter-long ATLAS particle detector—one of four big detectors the LHC will feed. "People should definitely not take it for granted that big things will happen immediately," he says. If all goes well, the LHC will start smashing particles in October, and oddities could jump out right away. More likely, it will take a few years for the LHC to clinch the discovery of the Higgs or something even stranger. Still, after 3 decades in which the standard model has answered every question asked at particle accelerators, physicists are eager to see something really new.

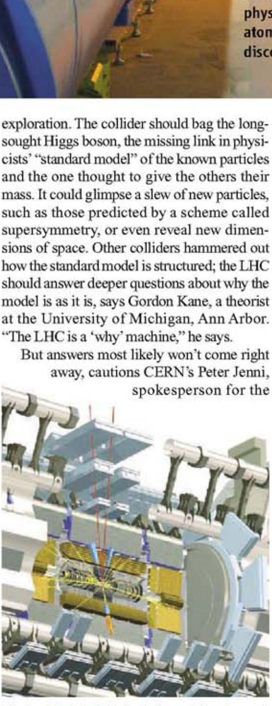

**What a blast!** In this simulation, a Higgs boson is born and decays inside the ATLAS particle detector.

### First off, look for something old

Like all colliders, the LHC aims to produce fleeting bits of matter not seen in the everyday world. As Einstein noted, energy and mass are equivalent. So physicists can generate heavier exotic particles by smashing known ones together with sufficient energy. Blasting protons into protons at energies seven times as high as the previous record, the LHC could cough up new particles more than 1000 times as massive as a proton. But first, researchers will simply search for familiar standard-model particles.

Ordinary matter consists of particles called "up quarks" and "down quarks," which combine to make the protons and neutrons in atomic nuclei; the electrons that make up the rest of the atom; and wispy particles called neutrinos that emerge in a particular type of nuclear decay. This first family of particles is

## Researchers, Place Your Bets!

The days before the start-up of the Large Hadron Collider (LHC) should be filled with quiet contemplation and reverence for the adventure to come, says physicist Maria Spiropulu. "Now is not the time to speculate," says the experimenter at the European particle physics lab, CERN, near Geneva, Switzerland. "We should be silent and respectful and wait for the data to come."

Or not. Many physicists seem to think that now is precisely the time to guess at what CERN's great particle smasher might find. And some are even willing to put their money where their favorite theoretical models are and wager on their expectations.

**High rollers.** Tommaso Dorigo (below) wagers that the LHC will see nothing new. Jacques Distler disagrees and expects to pocket $750 of Dorigo's money.

Tommaso Dorigo, an experimenter at the University of Padua in Italy, doubts that the LHC will find evidence of supersymmetry, a theoretical scheme that predicts a massive "superpartner" for every known particle in physicists' current "standard model." In the past 10 or 15 years, extremely precise measurements of standard-model particles have indirectly undermined the viability of the notion, Dorigo says. "I realized I don't believe in the thing," he says. Dorigo has bet $1000 with two other physicists that, after the LHC has accumulated a certain amount of data, it will see no sign of supersymmetry.

More precisely, Dorigo has bet that the LHC will see no clear deviations from the standard model of any kind, explains Jacques Distler, a theorist at the University of Texas, Austin, who has $750 of the action. Like a calculating professional gambler, Distler says he took the bet because it is so open-ended that he likely can't lose. "History has always been, you explore a new energy range and you see something new," he says.

For some, *not* having a bet bespeaks the strength of their predictions. Gordon Kane, a theorist at the University of Michigan, Ann Arbor, says he would gladly wager that the LHC will find supersymmetry, but "nobody I know will bet against it." Stuart Raby, a theorist at Ohio State University in Columbus, also says he can't find anyone who will take such a bet. To which Distler says, "I wonder how hard they tried."

The general public can get into the game, too. Online gambling sites and prediction exchanges such as Intrade.com, Hubdub.com, and NewsFutures.com are taking bets on when the Higgs boson will be discovered, whether the Tevatron collider at Fermi National Accelerator Laboratory in the United States will see it first, and related questions. **–A.C.**

flanked by two sets of heavier, unstable relatives. That means there are also strange and charm, top and bottom quarks; the electron has beefier cousins called the muon and the tau lepton; and there are two more "flavors" of neutrinos. Still other particles convey forces: Photons carry the electromagnetic force, the massive W and Z bosons convey the weak nuclear force, and gluons make up the strong nuclear force that binds protons and neutrons.

Tracking such familiar particles will enable experimenters to calibrate their immensely complex devices, says Tejinder "Jim" Virdee, a physicist at Imperial College London and spokesperson for the 2900-member team working with the 12,500-ton CMS particle detector, ATLAS's rival. (The LHC's two other detectors, ALICE and LHCb, won't search directly for new particles but will do more specialized work.) For example, a Z boson can decay into a muon and an antimuon, so by studying Z's physicists can measure how well they spot those particles.

Such studies also set the baselines from which to search for something new, Virdee says. "If you see something [unusual], the first question everyone is going to ask is, 'Do you also see the other things you expect?'" he says. "You have to be able to say 'yes' before you can claim anything new." The LHC should produce a smidgen of data between October and December, when it will shut down for the winter, and experimenters will use it primarily to "rediscover" the standard model.

### The Higgs: Wait a couple of years

Of course, experimenters will also keep an eye out for new things, such as the elusive Higgs boson. That oddball particle solves a serious problem with the standard model: The theory goes mathematically haywire unless particles have no mass. The "Higgs mechanism" sidesteps that problem by generating mass through the interactions of the otherwise massless particles themselves. It assumes that empty space is filled with a field a bit like an electric field that drags on particles to give them inertia, the essence of mass. Just as an electric field is made up of photons, the Higgs field consists of particles—Higgs bosons—that can be ripped out of the vacuum.

But finding the Higgs may not be easy. It all depends on how much the particle weighs, says Karl Jakobs, a physicist at the University of Freiburg in Germany and physics coordinator for ATLAS. The standard model does not predict how heavy the Higgs should be. If it weighs between about 200 and 500 times as much as a proton, then it should stick out fairly clearly. In that case, experimenters might collect enough data to find it by the end of 2009, Jakobs says, although analyzing the data could take months longer. But previous searches and indirect inferences suggest that the Higgs is lighter—definitely more than 121 times as massive as a proton but probably less than 170 as massive as that benchmark. If the Higgs is that light, then it could take until 2012 or later to find it.

The difference is that if the Higgs is heavy enough, it should decay in a distinctive way—into two hefty Z's that both decay into a muon and an antimuon. But if the Higgs is too light for that, then researchers will have to look for it decaying into combinations such as a pair of photons. So many photons will be produced in a typical LHC collision that sifting out the Higgs's signal from the clutter will take lots of data.

Most physicists say that they are sure to find the Higgs or something even weirder, because without it the standard model again breaks down mathematically at the energies the LHC will reach. Ironically, finding *only* the Higgs boson would disappoint many, as it would leave physicists nothing to puzzle over. "The worst scenario for me is that you start running and you see no evidence of deviations from the standard model, and after 2 or 3 years you see evidence of a standard-model Higgs and nothing else," Jakobs says. The Higgs would be the last brick in the standard model. It alone would leave physicists facing a conceptual wall and could signal the end of the field.

### Spotting signs and nailing discoveries

Most physicists expect to find much more at the energies the LHC will explore. New forces might emerge, or quarks themselves could turn out to consist of other particles. More speculatively, space may have additional curled-up dimensions that might be pried open, or the

CREDITS (LEFT TO RIGHT): COURTESY OF TOMMASO DORIGO; COURTESY OF JACQUES DISTLER

LHC might make tiny black holes, which would tie together the realms of quantum mechanics and gravitational physics.

Perhaps the most favored idea is supersymmetry, a scheme that posits a heavier, unobserved "superpartner" for every particle in the standard model. Seemingly profligate in its complexity, supersymmetry would help solve a number of fundamental, albeit esoteric, problems in the standard model. For example, it helps unify the three forces in the theory, a prerequisite to formulating a theory in which all forces, including gravity, are different manifestations of a single master force. Supersymmetry might also provide the mysterious dark matter whose gravity holds the galaxies together, as the least massive superpartner would be a heavy particle that would interact with ordinary matter essentially only through its gravity.

Supersymmetry might be very easy to see at the LHC, some say. "We predict a signature that they could see with five events," says Michigan's Kane. "They could see it in the first week of running in October." Generally, collisions producing the undetectable least massive supersymmetric particle would look lopsided, with a spray of ordinary particles shooting out one side of the particle detector and the supersymmetric particle zipping out the other side without leaving a trace.

But although spotting those events may be easy, proving that they're evidence of supersymmetry and not something else may be tough, says CERN's Paraskevas Sphicas, physics coordinator for CMS: "The catch is that the signature is so complex that we would have to do a lot of analysis to understand it." In fact, clinching the case for supersymmetry could take several years.

First, however, physicists must get the machine up and running. Researchers have already succeeded in injecting protons into each of its countercirculating rings. On 10 September, they'll try to coax the beams all the way around the rings at a very low energy. They'll then aim to increase the beam energy to 70% of the ultimate goal and the beam intensity to 1/1000 the design standard before beginning collisions in several weeks' time. Next year, the LHC should smash a billion particles each second at full energy.

The first collisions will mark the beginning of the real fun for experimenters. Some say that, although they have some pretty good ideas, they don't really know what to expect. "I want surprises," says CERN's Maria Spiropulu, an experimenter working on CMS. She may well get them, although she and her colleagues may have to wait just a bit longer. **–ADRIAN CHO**

---

# Bracing for a Maelstrom of Data, CERN Puts Its Faith in the Grid

**Researchers have hammered out new networking tools to store the LHC's instrument readings and make them available to physicists worldwide**

After the Large Hadron Collider (LHC) powers up next week, the physicists and engineers who built the machine and its detectors won't be the only ones nervously waiting for its two beams to collide for the first time. Just as anxious will be the researchers charged with taking the flood of data that the LHC will produce and processing it, storing it, and making it available for physicists to study the world over. The LHC is expected to produce 15 petabytes (15 million gigabytes) of data every year. Dedicated fiber-optic lines have been laid down to whisk the data away from CERN to some 250 other physics labs in 50 countries worldwide, where about 100,000 PC processors are ready and waiting to receive them.

At the beginning of this decade, CERN's information technology (IT) department decided to handle the LHC's torrent of data using a novel computer architecture known as a grid. A grid is a way of using the Internet, just as the World Wide Web and e-mail are. But the technology has not developed as fast as particle physicists had expected. CERN researchers believe they have ironed the wrinkles out of their system, dubbed the LHC Computing Grid (LCG), but nagging doubts remain.

"By an order of magnitude, this is the biggest grid [yet assembled]," says John Gordon, deputy director of GridPP, the United Kingdom's contribution to the LCG. "I'm reasonably confident that the grid is ready for data." But Les Robertson, head of the LCG project from its inception in 2001 until the beginning of this year, adds a note of caution: "It's very difficult. There's no real data, and real users are not active. A live test will only come when [real] data starts to flow." He adds: "This is what we will use. There's no fallback."

Fifteen petabytes is an enormous amount of data. To store it all on CDs would require a stack of disks 20 kilometers high—more than four times the height of Mont Blanc, Europe's tallest mountain. When CERN's IT experts began planning how to handle data from the LHC in the late 1990s, they soon realized that it would not be feasible to do it all at CERN. It wasn't clear that Geneva's electricity supply could power enough computers to do the job,

**First stop.** CERN's computers form the central node in a global data-sharing network.

CREDIT: EMERIK MALANDAIN © CERN

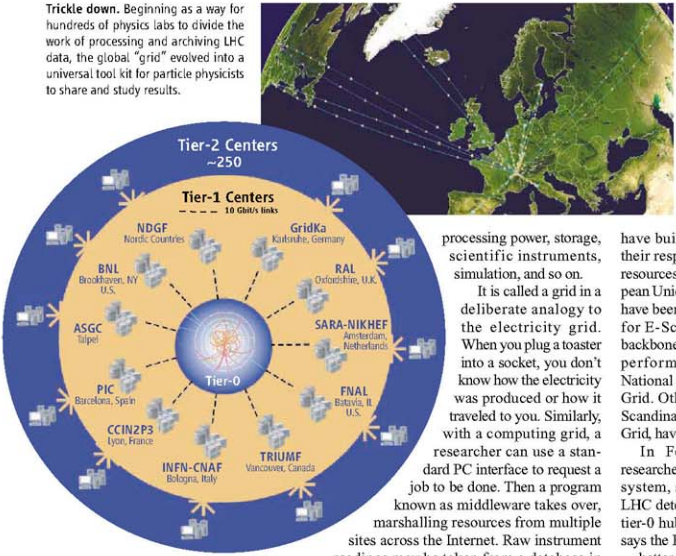

**Trickle down.** Beginning as a way for hundreds of physics labs to divide the work of processing and archiving LHC data, the global "grid" evolved into a universal tool kit for particle physicists to share and study results.

and in any event, CERN couldn't afford them: All of the LHC budget was being spent on the machine itself. "It was easier to get resources that were already available at computer centers," says Robertson.

At first, the CERN team set about designing an architecture in which, as the LHC detectors churn out data, the information would be archived in its raw state at CERN while simultaneously being streamed out to 10 or so large physics labs elsewhere in the world. At these tier-1 centers, some processing of the data would be done; then it would be archived again and some data would be farmed out from each tier-1 center to 10 or 20 tier-2 centers. In this way, the work of processing and archiving data is shared among particle physics labs around the world. The scheme would have worked, but it lacked flexibility, and the researchers soon heard about something better.

In the mid-1990s, Ian Foster and Steven Tuecke of Argonne National Laboratory in Illinois and Carl Kesselman of the California Institute of Technology in Pasadena had devised the idea of a grid. Whereas the Web is essentially a system for moving data around with limited processing for tasks such as searching, a grid aims to share everything: processing power, storage, scientific instruments, simulation, and so on.

It is called a grid in a deliberate analogy to the electricity grid. When you plug a toaster into a socket, you don't know how the electricity was produced or how it traveled to you. Similarly, with a computing grid, a researcher can use a standard PC interface to request a job to be done. Then a program known as middleware takes over, marshalling resources from multiple sites across the Internet. Raw instrument readings may be taken from a database in Europe and processed by a supercomputer in the United States; the manipulated data may be stored in China and then put through a visualization program in Japan before being returned to the researcher—who sees only the results, not the journey that got them there.

A major difficulty in setting up a grid arises from the "firewalls" that institutions erect to protect their computers from unauthorized access. It's a challenge getting the differing architectures and security arrangements of all the institutions in a grid to work together and trust one another. Each job travels around with "certificates" confirming that the user who requested the job has the authority to use the resources. To make grids work, there are "many hurdles, social, political, and technical," says particle physicist David Britton of the University of Glasgow in the U.K.

As particle physicists learned more about grids, the CERN team decided that the approach offered a more flexible way to handle the LHC's mountain of data, says Robertson. Although the same basic layout of tier-1 and tier-2 centers remains, it is no longer a rigid structure like the spokes of a wheel, with users tied to their local tier-1 center. The production process of disseminating the LHC data is handled by the grid, and researchers can get hold of the data they want without knowing where they are or what passwords they need to get access to them.

Since that decision was made in 2001, dedicated high-speed fiber-optic lines have been built between CERN (tier-0) and the tier-1 centers. Beyond that, the normal Internet provides the infrastructure. Particle physicists in each participating country have built up the LCG with funding from their respective governments for computer resources to add to the grid. Within the European Union, national grid efforts for research have been linked to form the Enabling Grids for E-Science (EGEE), which forms the backbone of the LCG in Europe. That role is performed in the United States by the National Science Foundation's Open Science Grid. Other smaller grids, such as GridPP, Scandinavia's NorduGrid, and Italy's INFN Grid, have also been woven into the LCG.

In February and May this year, researchers carried out two major trials of the system, sending simulated data from the LHC detectors themselves through CERN's tier-0 hub out to tier-1s and tier-2s. Britton says the February test was "quite successful, … better than we hoped," although they managed only a couple of days running data from all four detectors simultaneously. Much fine-tuning was done before the May dry run, and as a result they ran the four detectors together for the entire month. "We tested the whole chain, and most things stood up," says Gordon. Some bits of software didn't behave as expected, he says. In addition, the tier-1 center at Amsterdam had trouble keeping its computers cool, while the U.K. tier-1 at Rutherford Appleton Laboratory near Oxford suffered a small power failure. "But it was successful because we caught up," Gordon says.

Researchers say that almost all the computing resources needed for full LHC operation are now in place, and they are confident that the production side of the operation—transmitting, processing, and storing LHC data as it's produced—will go as planned. The thing that still gives them the odd sleepless night is what will happen when the LHC starts producing some interesting physics. Suddenly, thousands of physicists across the globe who have patiently waited years for these data will log onto the grid and request jobs. Grid experts refer to such use as "chaotic" because of its unpredictability. "It's definitely an unknown still," says

CREDITS: © CERN

## Is the LHC a Doomsday Machine?

Even for a car ad, the pitch on the radio was hard to ignore: an "end-of-the-world sale," offering a 30% discount and $1000 cash back on new automobiles. "Buy yourself something really frivolous," it urged. The reason: Miniature black holes created by the Large Hadron Collider (LHC) might soon touch off an unstoppable chain reaction that would blow up Earth.

Brad Benson, the New Jersey Hyundai dealer behind the ad, isn't really worried about the fate of the planet. "I'm a *National Geographic* kind of a guy," he told *Science*. "I love reading about this kind of stuff." But as the $5.5 billion particle smasher prepares to carry its first beam next week, some people see the machine as a threat. A handful of physicists and others have proposed an array of dangerous entities that could be created in the minuscule fireball of a particle collision—including microscopic black holes, strange matter that is more stable than normal matter, magnetic monopoles, a different quantum-mechanical vacuum, and even thermonuclear fusion triggered by a stray beam. Discussion forums on the World Wide Web sizzle with rants against arrogant scientists who meddle with nature and put us all at risk. And a few groups have sued to stop the LHC.

In March, Walter Wagner, a nuclear physicist based in Hawaii, and Luis Sancho filed for a restraining order and injunction against the LHC in the U.S. District Court of Hawaii. This week, Wagner is due to appear to fight a motion from the U.S. Department of Energy to dismiss the case.

Meanwhile, late in August a European group filed a complaint with the European Court of Human Rights (ECHR) for an emergency injunction to halt the switch-on. On 29 August, after 3 days of deliberation, the court declined to grant the injunction. An ECHR spokesperson says the plaintiffs can continue to pursue the complaint, but given the number of cases on the court's files it may take as long as 3 years to decide on its admissibility alone. "The only serious solution is not even to start the [LHC] project," says Markus Goritschnig, spokesperson for the ECHR complaint. "We will continue the case," he adds.

ILLUSTRATION FROM THAT PESKY TOASTER, 1995 BEN HILLMAN

The LHC is not the first particle collider to face campaigns over its safety. In 1999, Wagner sued to stop the Relativistic Heavy Ion Collider (RHIC) at Brookhaven National Laboratory in Upton, New York. The case was dismissed in 2000, and RHIC began operating the same year. To forestall similar campaigns against the LHC, which part of the time will collide heavy ions at even higher energies, CERN commissioned five independent physicists and one CERN staffer to assess the dangers of the new machine. Their conclusion, published in 2003: "We find no basis for any conceivable risk." A second panel, the LHC Safety Assessment Group (LSAG), came to the same conclusion in a report published this June.

The doom mongers do have one thing right: The LHC just might create black holes. According to Einstein's theory of general relativity, energy warps space and time. So by smashing protons together with unprecedented vigor, the LHC might cram enough energy into a small enough volume to create pinholes in the universe—miniature black holes. If space has three dimensions, even the energies reached by the LHC will be about a million billion times too low. However, string theory—which assumes that every fundamental particle is in fact an infinitesimal vibrating string—predicts that space has more dimensions curled into tiny loops. If some of them are curled loosely enough, then the energy threshold may tumble to within the LHC's reach, some theorists have argued.

But such tiny black holes should quickly evaporate into ordinary particles. At the least, they must be able to decay back into the particles that created them. They should also decay through "Hawking radiation," which comes about when, thanks to quantum uncertainty, a particle-antiparticle pair pops out of the vacuum and one partner falls in the hole while the other shoots outward.

LHC opponents point out that no one has ever observed Hawking radiation, and they fear that the black holes will grow and gobble up more and more matter. German physicist Rainer Plaga, in a paper cited in the ECHR complaint, theorizes that black holes could both grow and radiate intensely, doing as much damage through radiation as they do by eating everything in sight. In another cited paper, Otto Rössler, a theoretical chemist at the University of Tübingen in Germany, begins with an unusual—and, physicists say, wrong—interpretation of general relativity to argue that minuscule black holes should be stable and may form tiny radiation-spewing quasars.

All those scenarios are based on dodgy reasoning, says Jonathan Ellis, a theorist at CERN. Besides, he says, Earth, the sun, and other celestial bodies are constantly bombarded by cosmic particles with energies far higher than the LHC will reach. As the LSAG noted in its report: "This means that Nature has conducted the equivalent of about a hundred thousand LHC experimental programmes on the Earth already—and the planet still exists."

Physicists may have unwittingly helped foment panic by talking too glibly about black holes, Ellis notes. "Maybe we should be more careful with our rhetoric," he says. "For example, we talk about recreating the big bang, and people think, 'Oh my God, they're going to recreate the big bang!' " Of course, physicists don't aim to literally return the universe to its fiery birth, just to mimic those conditions in fleeting particle collisions. Alas, that less sexy line isn't going to catch anyone's attention, as any good car salesman can tell you.

**–D.C. AND A.C.**

---

Gordon. Britton agrees. "It will be a challenge to the grid because there will be a large number of less expert users," he says. "We'll have to learn how to help users in this type of environment."

LCG researchers were surprised that it has been this hard to develop the grid. At the outset, they expected it to evolve as the World Wide Web did: After CERN invented it, industry took the ball and now provides the Web as a service to researchers and the public alike. Although some companies, including Amazon, are starting to provide gridlike services commercially—the buzz phrase is "cloud computing"—the LCG researchers had to develop much of the new system as they went along. "We hoped the grid would be a service by now, but it hasn't happened," says Tony Cass, head of fabric infrastructure and operations in CERN's IT department.

Britton acknowledges that it was a risk going down the grid route, but he says the particle physics community looked at the technology, assumed it would develop, and assumed they could make it work in the time available—just as they did with the rest of the LHC. "That's exactly what particle physicists have to do: push things beyond the current envelope."

**–DANIEL CLERY**

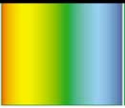

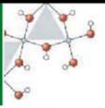

# LETTERS

*edited by Jennifer Sills*

## Reading Between the Number Lines

IN THEIR REPORT "LOG OR LINEAR? DISTINCT INTUITIONS OF THE number scale in Western and Amazonian indigene cultures" (30 May, p. 1217), S. Dehaene *et al.* investigate how Mundurucu Indians of the Amazon map numerosity judgments on a line segment. They conclude that the concept of a linear number line is a product of culture and formal education and that "the mapping of numbers onto space is a universal intuition and that this initial intuition of number is logarithmic." While I fully agree with the former statement—which I have defended elsewhere (*1*)—I disagree with the latter.

First, if the intuition of mapping numbers onto space is as fundamental as the authors claim, we should expect ubiquitous manifestations of number lines—linear or logarithmic—in early arithmetic in Mesopotamia, Egypt, China, and Mesoamerica. But no such evidence exists. Indeed, 4000-year-old clay tablets show that Babylonians developed a sophisticated knowledge of arithmetical bases, fractions, and operations apparently without the slightest reference to number lines (see photograph) (*2*). The number line is a complex idea that appears to have been introduced as late as 1685 by John Wallis (*3*). Second, if humans' initial intuition of "number" is logarithmic, we wouldn't have had to wait until the 17th century to see the invention of logarithms through Napier's painstaking work. These late inventions are inconsistent with the authors' claim that "mathematical" objects may find their ultimate origin in basic intuitions internalized through millions of years of evolution. The Report seems to be less about mathematical concepts and more about the role a line segment can play in reporting a person's impressions of numerosity.

**Ancient math.** By providing insight into the math used in ancient cultures, artifacts such as this 4000-year-old clay tablet can help to distinguish learned mathematical concepts from those that are intuitive.

CREDIT: BILL CASSELMAN, YALE BABYLONIAN COLLECTION. IMAGES AVAILABLE AT WWW.MATH.UBC.CA/PEOPLE/FACULTY/CASS/EUCLID/YBC/YBC.HTML

**RAFAEL E. NÚÑEZ**

Department of Cognitive Science, University of California, San Diego, La Jolla, CA 92093, USA.

### References

1. G. Lakoff, R. Núñez, *Where Mathematics Comes From* (Basic Books, New York, 2000).
2. K. Menninger, *Number Words and Number Symbols* (MIT Press, Cambridge, MA, 1969).
3. J. Wallis, *Treatise on Algebra* (1685), chapter LXVI.

---

### Response

WE AGREE WITH NÚÑEZ THAT THE MUNDURUCU do not master the formal properties of number lines and logarithms, but as the term "intuition" implies, they spontaneously experience a logarithmic mapping of number to space as natural and "feeling right."

Contrary to Núñez's claims, mappings of numbers onto space are omnipresent in ancient mathematics. Systems of measurement in which numbers are applied in a systematic linear manner to measure lengths (as well as a variety of physical continua) date back at least to the third or fourth millennia BCE in Egypt, Mesopotamia, and the Indus Valley (*1*). Babylonians were engaged in the measurement of lengths, as illustrated, for example, by a clay tablet giving the length of the diagonal of the square up to the sixth decimal (see photograph) (*2*); the realization that the diagonal and the side of the square were incommensurate led to a major and fruitful crisis in Pythagorician mathematics. We did not find a precise date for the introduction of formalized number lines, but writings from the 17th century indicate that mathematicians had conceptualized number lines by that time (*3*). Wallis's *Treatise on Algebra*, cited by Núñez, was written years after the introduction of coordinate systems in 1637 by Descartes and Fermat. Wallis only uses a number line metaphor to set the ground for the notion of negative numbers, en route to introducing complex numbers.

The logarithmic scale for mapping numbers onto space is highly resistant to change, as we observed the production of logarithmic scales even among educated Mundurucus, who were proficient in Portuguese. U.S. children of European ancestry show a similar behavior, both with the present task (*4*) and in a slightly different version in which they were instructed to divide a rectangle in a given number of parts, which should have favored a linear scale (*5*). This resistance could explain the late introduction of formal linear number lines in mathematics, despite a solid intuition for number-space mapping. In the absence of a formalized concept of logarithms, a logarithmically compressed scale presents limited computational utility, in contrast to a linear scale, which embodies properties of addition and subtraction and can be used as a ruler. Initially, only linearly scaled number lines were pursued by mathematicians, yet introducing these linear scales required overcoming the robust logarithmically shaped intuition that numbers should be mapped onto space based on their ratio similarity. Today, the universal use of logarithmic axes, even in newspaper graphs, and the extraordinary spread of slide rules before the advent of calculators testify to the status of the logarithm as both an abstract mathematical concept and an intuitive mental tool.

**VÉRONIQUE IZARD,[1,2,3,4]**
**STANISLAS DEHAENE,[1,2,3,5]**
**PIERRE PICA,[6] ELIZABETH SPELKE[4]**

[1]INSERM, Cognitive Neuro-imaging Unit, IFR 49, Gif-sur-Yvette, France. [2]CEA, NeuroSpin center, IFR 49, Gif-sur-Yvette, France. [3]Universite Paris-Sud, IFR 49, F-91191 Gif-sur-Yvette, France. [4]Department of Psychology, Harvard University, Cambridge, MA 02138, USA. [5]Collège de France, Paris, France. [6]Unité Mixte de Recherche 7023, Formal Structure of Language, CNRS and Paris VIII University, Paris, France.

**References and Notes**

1. H. A. Klein, *The World of Measurements: Masterpieces, Mysteries and Muddles of Metrology* (Simon & Schuster, New York, 1974).
2. Images of a clay tablet from the Yale Babylonian collection (www.math.ubc.ca/people/faculty/cass/Euclid/ybc/ybc.html).
3. R. Descartes, *La Géométrie*, D. E. Smith and M. L. Lantham, Transl., Eds. (Dover, New York, 1954).
4. R. S. Siegler, J. E. Opfer, *Psych. Sci.* **14**, 237 (2003).
5. P. Gréco, A. Morf, *Structures Numériques Elémentaires: Etudes d'Epistémologie Génétique* (Presses Universitaires de France, Paris, 1962), vol. 13.

## The Risks of Pigging Out on Antibiotics

THE NEWS STORY "THE BACTERIA FIGHT BACK" by G. Taubes (Special Section on Drug Resistance, 18 July, p. 356) highlights the growing health threat from antibiotic-resistant bacteria, especially methicillin-resistant *Staphylococcus aureus* (MRSA), and the need to rein in medical uses of antibiotics to curb resistance.

But reining in health care uses alone is insufficient to address the resistance epidemic. As recommended by the Institute of Medicine (*1*), World Health Organization (*2*), American Academy of Pediatrics (*3*), and other health organizations, routine and widespread use of medically important antibiotics in animal agriculture also must be ended to effectively address resistance. Recent evidence showing that some human MRSA infections are associated with animal agriculture underscores this point.

In Europe, MRSA has been shown to be transmitted from pigs to farmers and their families, veterinarians, and hospital staff (*4*, *5*). One MRSA strain, once found only in pigs, is associated with serious human illness, including skin, wound, lung, and heart infections (*6*, *7*). This new pig strain is linked to more than 20% of human MRSA infections in the Netherlands (*8*).

Researchers have only begun to examine MRSA from North American livestock. Both Canadian pig farmers and swine are commonly colonized by MRSA (*9*). A recent study found that 70% of the tested pigs in Iowa and Illinois carried MRSA (*10*).

Extensive use of antibiotics in livestock operations can select for resistant bacteria such as MRSA, just as in health care settings. By one estimate, more than 70% of all antibiotics and related drugs used in the United States are used as feed additives for livestock (*11*). Dutch pig farms that routinely use antibiotics are more likely to have MRSA than farms with limited antibiotic use (*12*).

According to the World Health Organization, "Our grandparents lived during an age without antibiotics. So could many of our grandchildren" (*13*). Overuse of antibiotics in agriculture as well as in human medicine could result in this frightening outcome.

**REBECCA GOLDBURG,[1]* STEVEN ROACH,[2]**
**DAVID WALLINGA,[3] MARGARET MELLON[4]**

[1]Environmental Defense Fund, New York, NY 10010, USA. [2]Food Animals Concerns Trust, Chicago, IL 60614, USA. [3]Institute for Agriculture and Trade Policy, Minneapolis, MN 55404, USA. [4]Union of Concerned Scientists, Washington, DC 20006, USA.

*To whom correspondence should be addressed. E-mail: bgoldburg@edf.org

**References**

1. M. S. Smolinski, M. A. Hamburg, J. Lederberg, Eds., *Microbial Threats to Health: Emergence, Detection, and Response* (National Academy of Sciences, Washington, DC, 2003).
2. World Health Organization, *WHO Global Principles for the Containment of Antimicrobial Resistance in Animals Intended for Food* (WHO Publication WHO/CDS/CSR/APH/2000.4, 2000); http://whqlibdoc.who.int/hq/2000/who_cds_csr_aph_2000.4.pdf.
3. K. M. Shea, *Pediatrics* **114**, 862 (2004).
4. X. W. Huijsdens *et al.*, *Ann. Clin. Microbiol. Antimicrob.* **5**, 26 (2006).
5. A. Voss, F. Loeffen, J. Bakker, L. Klaasen, M. Wulf, *Emerging Infect. Dis.* **11**, 1965 (2005).
6. M. B. Ekkelenkamp, M. Sekkat, N. Carpaij, A. Troelstra, M. J. Bonten, *Ned. Tijdschr. Geneeskd.* **150**, 2442 (2006).
7. W. Witte, B. Strommenger, C. Stanek, C. Cuny, *Emerging Infect. Dis.* **13**, 255 (2007).
8. I. van Loo *et al.*, *Emerging Infect. Dis.* **13**, 1834 (2007).
9. T. Khanna, R. Friendship, C. Dewey, J. S. Weese, *Vet. Microbiol.* **128**, 298 (2007).
10. T. C. Smith *et al.*, paper presented at the 2008 International Conference on Emerging Infectious Diseases, Centers for Disease Control and Prevention, Council of State and Territorial Epidemiologists, Atlanta, GA, 16 to 19 March 2008.
11. M. Mellon, C. Benbrook, K. L. Benbrook, *Hogging It! Estimates of Antimicrobial Abuse in Livestock* (UCS Publishing, Cambridge, MA, 2001).
12. E. van Duijkeren *et al.*, *Vet. Microbiol.* **126**, 383 (2007).
13. World Health Organization, *World Health Organization Report on Infectious Diseases 2000: Overcoming Antimicrobial Resistance* (WHO Publication, 2000); www.who.int/infectious-disease-report/2000/index.html.

### Letters to the Editor

Letters (~300 words) discuss material published in *Science* in the previous 3 months or issues of general interest. They can be submitted through the Web (www.submit2science.org) or by regular mail (1200 New York Ave., NW, Washington, DC 20005, USA). Letters are not acknowledged upon receipt, nor are authors generally consulted before publication. Whether published in full or in part, letters are subject to editing for clarity and space.

## Battle of the Bugs

IN THE NEWS STORY "THE BACTERIA FIGHT back" (Special Section on Drug Resistance, 18 July, p. 356), G. Taubes describes the ongoing war between bacteria and antibiotics, which the bacteria appear to be winning. Against this backdrop, scientists are struggling to uncover viable therapeutic alternatives to these erstwhile wonder drugs.

One such alternative, probiotic therapy, has become the focus of considerable research effort in recent times (*1*). Indeed, several clinical trials have attributed impressive health-promoting effects to probiotics—so-called "good bugs"— including effective antagonistic activities against a variety of microbial pathogens by competitive exclusion and bacteriocin production (*2*).

Furthermore, a new generation of probiotics termed "designer probiotics" has been engineered to express proteins that mimic cell surface receptors, which adsorb toxins and specifically target enteric infections by blocking ligand-receptor interactions between pathogen and host cells (*3*). Blocking bacterial adherence reduces infection, while toxin neutralization ameliorates symptoms until the pathogen is eventually overcome by the immune system.

Indeed, McFarland (*4*), in her seminal review on the control of antibiotic-resistant *Clostridium difficile*, proposed that effective treatment must "reduce the burden of *C. difficile* and its toxins in the intestine, restore the normal colonic microflora and assist the host's immune system." Designer probiotics, satisfying all of these criteria, provide an ideal alternative for the treatment of not only *C. difficile* but also other multidrug-resistant pathogens.

Perhaps the only hope of winning the war against "bad bugs" will be achieved by recruiting "good bugs" as our allies.

**ROY D. SLEATOR* AND COLIN HILL**

Alimentary Pharmabiotic Centre, University College Cork, College Road, Cork, Ireland.

*To whom correspondence should be addressed. E-mail: r.sleator@ucc.ie

**References**

1. R. D. Sleator, C. Hill, *Lett. Appl. Microbiol.* **46**, 143 (2008).
2. S. C. Corr *et al.*, *Proc. Natl. Acad. Sci. U.S.A.* **104**, 7617 (2007).

3. A. W. Paton, R. Morona, J. C. Paton, *Nat. Rev. Microbiol.* **4**, 193 (2006).
4. L. V. McFarland, *J. Med. Microbiol.* **54**, 101 (2005).

## DOE Should Keep Education in Mind

I BELIEVE A. CHO'S NEWS OF THE WEEK STORY "Two U.S. labs vie for long-delayed exotic nuclei source" (18 July, p. 328) misses a few important points about the competition between Michigan State University (MSU) and Argonne National Laboratory (ANL) to build the Department of Energy–funded Facility for Rare Isotope Beams (FRIB). I know both institutions, having received a Ph.D. in nuclear physics from MSU in 1967 and having worked as a contractor during the 1970s at ANL, where I taught courses on the assay of nuclear materials to members of the International Atomic Energy Commission.

Cho frames this issue as a David-versus-Goliath contest, comparing the size of MSU's existing nuclear science facility, the National Superconducting Cyclotron Laboratory (NSCL), with ANL in its entirety. A more apt, apples-to-apples comparison would have considered the relative scale of MSU ($1.7 billion annual budget, 11,700 employees) and ANL ($530 million annual budget, 2,800 employees) (*1*). Clearly, both institutions are capable of managing large, complex operations. And of the two, only MSU, the nation's eighth largest university, is host to a lab designated as one of the nation's flagship nuclear physics facilities by the Nuclear Science Advisory Committee (*2*).

However, size is not the critical issue in this competition. Although the national labs provide many training opportunities, education is of primary importance only in a university setting. MSU has the second-best U.S. nuclear physics graduate program (behind MIT) and trains 10% of the nation's nuclear physics Ph.D.'s (*3*). The MSU lab is currently training about 100 graduate and undergraduate students.

Cho points out that the MSU lab might close if FRIB lands elsewhere. So, as the competition proceeds, decision-makers must consider whether expanding our national lab complex at the expense of jeopardizing a successful university-based educational and scientific center is in the national interest.

**LORENZ A. KULL**

Former President and Chief Operating Officer, Science Applications International Corporation (SAIC), 274 Pearl Lane, Silverthorne, CO 80498, USA.

**References**

1. 2007 Michigan State University Data Digest, p. 3 (http://opbweb.opb.msu.edu/).
2. The Frontiers of Nuclear Science: A Long Range Plan, DOE/NSF Nuclear Science Advisory Committee, 2007, p. 3 (www.sc.doe.gov/np/nsac/docs/Nuclear-Science.Low-Res.pdf).
3. U.S. News & World Report, "America's Best Graduate Schools," 2009 edition (http://grad-schools.usnews.rankingsandreviews.com/grad/phy/nuclear).

## Call for an Objective DOE Decision

AFTER READING A. CHO'S NEWS OF THE WEEK story "Two U.S. labs vie for long-delayed exotic nuclei source" (18 July, p. 328), I can't help but wonder: How can anyone be sure that the U.S. Department of Energy (DOE) will make this decision objectively? Our National Laboratories have outlived the reasons for which they were established, and, as would any large and aging organization, they are vying to find a new raison d'être.

Our universities are hurting for American students, particularly in technical fields. Universities, not national labs, have been a fountain of fresh, competent, and cost-effective personnel that will provide leadership and allow us to regain our technological edge in the coming decades. Support for universities is sorely needed at this time, and DOE must bear this in mind when they make their decision, particularly when the facts point them in a direction that is against their own interests.

**CONSTANTINE CASSAPAKIS**

President and CEO, L'Garde, Inc., 15181 Woodlawn Avenue, Tustin, CA 92780, USA.

## CORRECTIONS AND CLARIFICATIONS

**News of the Week:** "Full-genome sequencing paved the way from spores to a suspect" by M. Enserink (15 August, p. 898). The affiliation of microbial genomicist Claire Fraser-Liggett should have been the University of Maryland School of Medicine in Baltimore.

**Table of Contents:** (25 July, p. 457). In the description of the Report "Did cooling oceans trigger Ordovician biodiversification? Evidence from conodont thermometry" by J. A. Trotter *et al.*, the time of the cooling trend through the Early Ordovician was incorrect. The sentence should read: "About 470 million years ago, ocean temperatures dropped to values near those of today after being much higher for many millions of years, coeval with a sharp jump in biodiversity."

**Reports:** "Did cooling oceans trigger Ordovician biodiversification? Evidence from conodont thermometry" by J. A. Trotter *et al.* (25 July, p. 550). In the References and Notes, reference 27, which is a duplicate of reference 4, should have been deleted. References and notes 28 to 39 should have been renumbered 27 to 38. The citations to these references are correct. In the Fig. 3 legend, the citation to Chen *et al.* should be 29 (not 31).

**Perspectives:** "Tracking corrosion cracking" by A. Stierle (18 July, p. 349). The last sentence on p. 349 incorrectly stated that "King *et al.* have found that the grain boundaries in stainless steel … are more sensitive to carbon segregation and the formation of chromium carbides, which makes them more sensitive to corrosion." Instead, the sentence should state that "King *et al.* have found that the grain boundaries in stainless steel … are more sensitive to corrosion, which might be related to enhanced carbon segregation at these grain boundaries and the formation of chromium carbides."

**Reviews:** "Rise of the Andes" by C. N. Garzione *et al.* (6 June, p. 1304). A minus sign was missing from an equation in the second paragraph of the third column on p. 1305. The correct equation should read "$h = -472.5\delta^{18}O_{\text{rainfall}} - 2645$."

**Reports:** "Hidden neotropical diversity: Greater than the sum of its parts" by M. A. Condon *et al.* (16 May, p. 928). The first sentence of the main text included a misplaced reference citation. The sentence should read: "The diversity of neotropical herbivorous insects, ranging in number from 3 million to 30 million species (*1*), has been hypothesized to be a function of plant diversity (*2*), but the degree to which specialization shapes that function is contentious (*3*)."

## TECHNICAL COMMENT ABSTRACTS

### COMMENT ON "Fire-Derived Charcoal Causes Loss of Forest Humus"

**Johannes Lehmann and Saran Sohi**

Wardle *et al.* (Brevia, 2 May 2008, p. 629) reported that fire-derived charcoal can promote loss of forest humus and belowground carbon (C). However, C loss from charcoal-humus mixtures can be explained not only by accelerated loss of humus but also by loss of charcoal. It is also unclear whether such loss is related to mineralization to carbon dioxide or to physical export.

Full text at www.sciencemag.org/cgi/content/full/321/5894/1295c

### RESPONSE TO COMMENT ON "Fire-Derived Charcoal Causes Loss of Forest Humus"

**David A. Wardle, Marie-Charlotte Nilsson, Olle Zackrisson**

We find the suggestion that substantial charcoal loss occurred in the humus-charcoal mixtures implausible and discuss why complexing of soluble carbon released from the mixtures by underlying mineral soil should be minor. This exchange highlights our limited knowledge about charcoal effects on native soil carbon, indicating that strong advocacy for charcoal addition to offset $CO_2$ emissions remains premature.

Full text at www.sciencemag.org/cgi/content/full/321/5894/1295d

PUBLIC HEALTH

# The Tobacco Strategy Entrenched

**Carl F. Cranor**

**Doubt Is Their Product**
How Industry's Assault on Science Threatens Your Health
***by David Michaels***
Oxford University Press, Oxford, 2008. 384 pp. $27.95, £14.99. ISBN 9780195300673.

Ever wonder why it has been so slow and difficult to reduce the health risks from tobacco, secondhand smoke, lead, beryllium, or chromium? David Michaels's excellent *Doubt Is Their Product* provides part of the explanation, showing numerous ways in which "the product defense industry" uses scientific (and pseudoscientific) arguments to undermine public health protections, corrupt the scientific record, and mislead the public.

The book's title announces its central theme. A tobacco industry strategy memo argues, "Doubt is our product since it is the best means of competing with the 'body of fact' that exists in the minds of the general public. It is also the means of establishing a controversy." (*1*) The aim: to sow doubt in the minds of the public, judges, and even regulatory scientists (if they are susceptible) about the scientific basis for greater public health or environmental protections (think global warming) or tort law actions. Because of the tobacco industry's success in obfuscating, slowing, reducing, and blocking regulatory actions, its approach has been adopted by others, has become institutionalized in presidential administrations, and has been used as talking points by some politicians. Fostering doubt and controversy and demanding high degrees of certainty postpone legal actions, keep products in commerce longer, and perhaps delay improved protections indefinitely. They can also leave the public or work force at risk.

As Michaels (an epidemiologist at George Washington University) explains, this clever strategy permits people to oppose public health rules without arguing the policy point and without being labeled anti–public health. It also uses a common science term that might resonate with some in the scientific community. Scientific articles usually note uncertainties about the research subject and the need for further studies.

Industries and their supporters have also demanded "proof" (more at home in mathematics than science) before agencies can increase public health protections or plaintiffs can successfully receive tort law compensation for injuries suffered. However, even though scientists may not understand all aspects of a problem, public health agencies need to act on the weight of the best science available at the time.

The doubt strategy is most at home in postmarket legal contexts. Public health agencies face the burden of establishing scientific and legal cases that will withstand appellate court scrutiny before they can successfully provide increased health and environmental protections or withdraw drugs or pesticides from the market. Companies that emphasize scientific uncertainties appear to be scientific angels; they only seek to preserve the integrity and certainty of the relevant fields against hasty regulatory action based on incomplete science.

Tort plaintiffs face similar burdens. They must show that the defendant's products or actions more likely than not can and did cause injuries from which the plaintiff suffers. The U.S. Supreme Court's *Daubert* decision requires judges to review the scientific basis of expert testimony; they may bar litigants from trial if the science is insufficient (*2*). Fostering doubt may sway judges, who are typically less informed about science than are regulatory scientists. The product defense industry has also helped to persuade some judges that they should review and exclude scientific studies individually without reviewing the total body of relevant evidence on which scientists rely, a most unscientific way to review the basis of expert testimony.

The book presents examples of product defense experts who have accepted funding to reach predetermined conclusions, misrepresented scientific claims, hidden their affiliations, written articles while using others' names, or had scientific papers ghost-written by lawyers.

What should be done? Among the author's recommendations is to require the testing of chemicals before workers and the public are exposed. If all products were subject to premarket testing for safety and impartial agency review before commercialization, this removes some incentives to raise doubt about the science. Drug and pesticide manufacturers rarely point out that their science is too uncertain to permit their products into the market. Michaels might have said more about additional legal changes that would reduce the influence of the doubt and uncertainty arguments, e.g., shifting legal burdens to the manufacturer once its product's safety was called into question.

Michaels also recommends a number of disclosures: of any and all research sponsors,

**Desire for doubt.** In April 1994, the CEOs of several tobacco companies told a committee of the U.S. House of Representatives that "Cigarette smoking is not addictive." In January 1998, their successors (shown) would only admit "Under some definitions cigarette smoking is addictive."

CREDIT: CEDENO KEN/CORBIS SYGMA

---

The reviewer, the author of *Toxic Torts: Science, Law, and the Possibility of Justice*, is at the Department of Philosophy, University of California Riverside, 900 University Avenue, Riverside, CA 92521, USA. E-mail: carl.cranor@ucr.edu

of what manufacturers know about the toxicity of their product (with penalties for covering up or lying), and of hazards in the public's midst (like community right-to-know laws). These recommendations are not panaceas but make good first steps.

In addition, *Doubt Is Their Product* reminds one of deeper risks that threaten scientific fields and democratic deliberation. When science affects commercial interests, there are substantial temptations for researchers or their employers to substitute the ethics of the marketplace for the ethics of careful, objective evaluation of the data to understand the world, environmental threats, and health risks. Such substitution can result in the corruption of the scientific literature and the breaking of incremental links in chains of evidence on which researchers and the public depend, and it also tends to undermine properly informed political and judicial decisions. The scientific community and the public need to be on guard against such abuses; Michaels's history of these events sounds an alert that must not be ignored.

**References**

1. Brown and Williamson Tobacco Company, *Smoking and Health Proposal* (Brown and Williamson document no. 680561778–1786, 1969); http://legacy.library.ucsf.edu/tid/nvs40f00.
2. *Daubert* v. *Merrell Dow Pharm., Inc.*, 509 U.S. 579 (1993).

10.1126/science.1162339

## THE GONZO SCIENTIST

# Chasing the Biggest Shadow of All

Choosing which extreme sport to pursue in one's life is difficult. Most people are content with the likes of bungee jumping, ice climbing, or street luge, but not scientists. In addition to thrills, they want their sport to produce useful data. I tried out an extreme scientific sport last month: eclipse chasing. The objective is to take very sensitive equipment to very remote locations, very punctually.

**Online**
**sciencemag.org**
For more on this episode, go to www.gonzoscientist.org

The roots of the sport go back to ancient China, where astronomers experienced, in the words of the late television anchorman Jim McKay, both "the thrill of victory" (prestige in the emperor's court) and "the agony of defeat" (beheading for miscalculation). Eclipse chasing has come a long way since then (more data, less beheading)—and made headlines around the world in 1919. On 29 May that year, after struggling with biting insects and tropical storms on a volcanic island, a British team recorded starlight bent around the eclipsed Sun by gravity, an observation that was widely trumpeted as confirming Albert Einstein's theory of relativity.

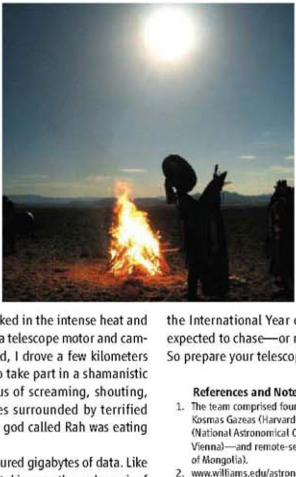

CREDIT: RAY JAYAWARDHANA

For my first taste of eclipse chasing, I joined a team of scientists (*1*) hoping for a rendezvous with an eclipse 1 August in the wild west of Mongolia. To get to the site, we made a night trek over the Altai Mountains, which nearly killed us when our driver nodded off at the wheel. On the day itself, we worked in the intense heat and dust of the Gobi desert, which actually did kill a telescope motor and camera. But just as the eclipse was getting started, I drove a few kilometers away with astrophysicist Ray Jayawardhana, to take part in a shamanistic ritual that involved a hundreds-strong chorus of screaming, shouting, and clapping at the sky. We found ourselves surrounded by terrified Mongolian locals convinced that a monstrous god called Rah was eating the Sun. But that is another story.

While Rah captured the Sun, our team captured gigabytes of data. Like astro-paparazzi, we harvested hundreds of digital images through a pair of telescopes—a refractor and a reflector fixed to a motor-driven astrograph built by team member Kosmas Gazeas—during the 2 hours of partial and 2 minutes of total eclipse. And we weren't the only ones ogling the darkened sky. A team led by Jay Pasachoff, an astrophysicist at Williams College, Massachusetts, was observing to the north in Siberia (*2*). And to the south, *Science*'s Beijing correspondent, Richard Stone, was watching in western China with researchers from the National Astronomical Observatories, Chinese Academy of Sciences, and other institutions (*3*).

But how useful are all those data? With orbiting telescopes like Hinode trained on the Sun—and capable of creating their own eclipse anytime by simply occluding the Sun's photosphere with a metal disk, can ground-based observation add anything? "I get that question all the time," comments Pasachoff. In fact, he says, data produced by earthly eclipse chasers are more valuable than ever. The space telescopes, put in place at enormous cost, provide only part of the picture. By design, "the spacecraft can't observe a huge region around the Sun, the whole inner and middle corona." Studying the dynamics of these superhot solar gases should lead to better modeling of solar wind and answer a nagging riddle: Why is the corona hundreds of times hotter than the Sun's surface? Not only are the eclipse chasers equipped with "more modern and efficient" charge-coupled device cameras, explains Pasachoff, but "the resolution on the corona that we get by processing eclipse images is finer than that obtainable by any spacecraft." To understand the Sun, astronomers still need the Moon to cover it.

Pasachoff, who has seen 47 solar eclipses, wants to rename the sport. Rather than a chaser, "I am an eclipse preceder," he says. After all, successfully predicting and getting to the site of an eclipse is the name of the game. For next year's eclipse, a blockbuster event in the International Year of Astronomy (*4*), record numbers of people are expected to chase—or rather, precede—the 22 July solar eclipse in Asia. So prepare your telescopes and book your tickets now.

**References and Notes**

1. The team comprised four astrophysicists—Ray Jayawardhana (University of Toronto), Kosmas Gazeas (Harvard-Smithsonian Center for Astrophysics), Kazuhiro Sekiguchi (National Astronomical Observatory, Japan), and Katrien Kolenberg (University of Vienna)—and remote-sensing researcher Tuvjargal Norovsambuu (National University of Mongolia).
2. www.williams.edu/astronomy/eclipse/eclipse2008.
3. R. Stone, *Science* **321**, 759 (2008).
4. www.astronomy2009.org.

**–JOHN BOHANNON**

10.1126/science.1164877

MEDICINE

# Life Cycle of Translational Research for Medical Interventions

From the initial discovery of a medical intervention to a highly cited article is a long road, and even this is not the end of the journey.

**Despina G. Contopoulos-Ioannidis,[1] George A. Alexiou,[2] Theodore C. Gouvias,[2] John P. A. Ioannidis[2,3,4]***

Despite a major interest in translational research (*1*–*3*), development of new, effective medical interventions is difficult. Of 101 very promising claims of new discoveries with clear clinical potential that were made in major basic science journals between 1979 and 1983, only five resulted in interventions with licensed clinical use by 2003 and only one had extensive clinical use (*4*). Drug discovery faces major challenges (*5*–*8*). Moreover, for several interventions supported by high-profile clinical studies, subsequent evidence from larger and/or better studies contradicts their effectiveness or shows smaller benefits (*9*). The problem seems to be even greater for nonrandomized studies (*9*). Here, we present the results of an empirical evaluation of the life-cycle phases of translational research for selected medical interventions.

We examined key milestones in the life cycle of translational research for all the interventions claimed to be effective in at least one study that received over 1000 citations in the literature in 1990–2004, on the basis of the Web of Science. These are the most-cited papers in the literature of medical interventions (*10*). Because they have received the greatest attention, they provide easily identifiable scientific milestones. Citation counts are a widely accepted coinage of recognition. Of course, several blockbusters may go through an industrial discovery–testing–production process that does not involve any particular highly cited paper in the peer-reviewed literature. In these cases, it is not as clear-cut to isolate one or a few studies that are indisputable milestones in the translational process.

Of 49 articles with >1000 citations, we excluded articles where the intervention was ineffective, as well as those assessing management strategies rather than specific interventions, and we selected only the earliest article whenever two or more highly cited studies with >1000 citations had been published on the same intervention and indication. Thirty-two interventions for specific indications were thus evaluated, and we could place the milestone of when their first highly cited clinical study was published showing effectiveness (tables S1 and S2). We considered this an important time point in the translational process and estimated how long a time ("translation lag") it had taken from the initial discovery of each intervention to reach that point. Highly cited status does not necessarily mean that these interventions continue to be considered as effective as proposed in the original highly cited papers. By the end of 2006, the effectiveness of 19 interventions had been replicated by other subsequent studies ($n = 14$) or had remained unchallenged ($n = 5$), whereas the other 13 had been either contradicted ($n = 5$) or found to have had initially stronger effects ($n = 8$) when larger or better controlled subsequent studies were performed (table S1).

### Translation Lag

To place each discovery in time, we identified the year when the earliest journal publication on preparation, isolation, or synthesis appeared or the earliest patent was awarded (whichever occurred first). Overall, the median translation lag was 24 years (interquartile range, 14 to 44 years) between first description and earliest highly cited article (see the chart, page 1299). This was longer on average (median 44 versus 17 years) for those interventions that were fully or partially "refuted" (contradicted or having initially stronger effects) than for nonrefuted ones (replicated or remaining unchallenged) ($P = 0.004$).

In a secondary analysis, we defined the time of discovery as the first description (publication or awarded patent) of any agent in the wider intervention class (those with similar characteristics and mode of action). Early translational work may be performed with different agents in the same class compared with those that eventually get translated into postulated high-profile clinical benefits. Analyses using information on the wider class of agents showed even longer translation lag, with median of 27 (interquartile range, 21 to 50) years and similar prolongations of the translation lag for refuted interventions.

Among the 18 nonrefuted interventions that had a highly cited randomized trial to support them, the median translation lag was 16.5 years (range 4 to 50 years) in the main analysis [22 years (range 6 to 50 years) considering the wider class]. The fastest successful translation occurred for indinavir (as part of triple antiretroviral therapy) and abciximab, both of which took only 4 years from their patenting to the publication of a highly cited randomized trial. Both of these fast successes involved multidisciplinary work spanning molecular to clinical research on protease inhibitors and integrins, respectively.

We also tried to identify the first published article that described the use of each intervention in humans and the first published article that described the use of each intervention in humans for the specific intervention described eventually in the highly cited study (*11*). There was a very large variability in the timing of the first human study and of the first human study for the specific indication (see the chart, page 1299). The range for the time from first discovery to first human use was 0 to 28 years. The range for the time from first discovery to first specific human use was 0 to 221 years.

We observed that most highly cited claims that were eventually refuted had a very slow translation history preceding them [e.g., flavonoids, vitamin E, and estrogens were already available for many decades before observational (nonrandomized) studies claimed implausibly large survival benefits in the 1990s]. We conclude that claims for large benefits from old interventions require extra caution as they are likely to be exaggerated. Given the considerable refutation rate of even the most highly cited interventions, extensive replication and confirmation of proposed treatment benefits are indicated. New drug discovery is probably essential for common diseases where the existing drug armamentarium has been already extensively screened. Conversely, for uncommon and neglected diseases, the existing drug options may remain largely untested, and old drugs may find interesting new uses (*12*–*14*).

---

[1] Department of Pediatrics, University of Ioannina School of Medicine, Ioannina, 45110, Greece, and Department of Pediatrics, George Washington University School of Medicine and Health Sciences, Washington, DC 20037, USA. [2] Clinical Trials and Evidence-Based Medicine Unit, Department of Hygiene and Epidemiology, University of Ioannina School of Medicine, Ioannina, 45110, Greece. [3] Department of Medicine, Tufts Medical Center, and Institute for Clinical Research and Health Policy Studies, Tufts University School of Medicine, Boston, MA 02111, USA. [4] Biomedical Research Institute, Foundation for Research and Technology–Hellas, Ioannina 45110, Greece.

*Author for correspondence (at the address in footnote 2). E-mail: jioannid@cc.uoi.gr; john.pa.ioannidis@gmail.com

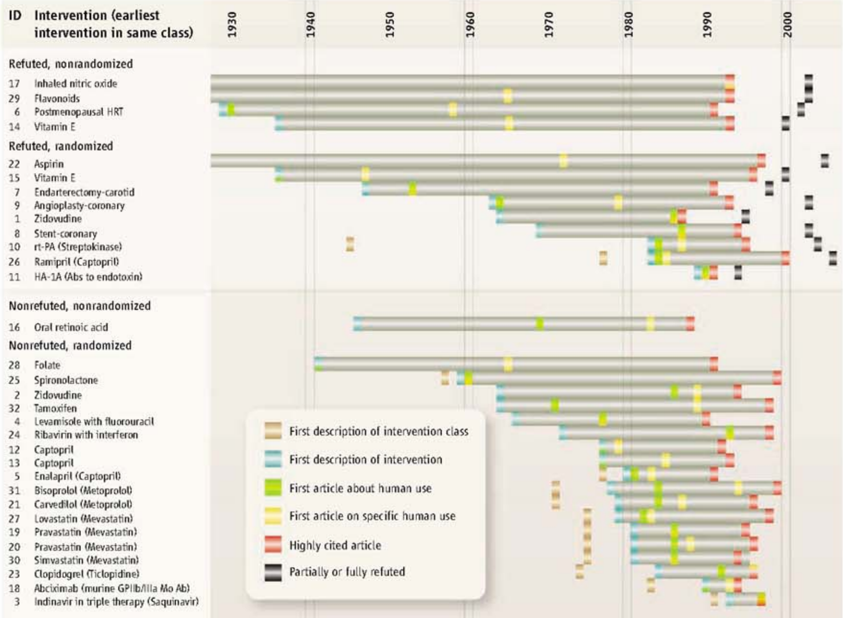

**Milestones for the 32 interventions.** First description of agent in wider class, tan box (when the agent used in the highly cited article is not the same as the first described in its class); first description, cyan box; first human-use article, green box; first specific–human use article, yellow box; earliest highly cited publication, red box; realization of full or partial refutation (for contradicted or initially stronger effects), black box. Whenever two or more milestones coincide in the same year, the respective colors are superimposed on that box. Folate, flavonoids, and vitamin E were already in human use at the time of first description. Extending beyond the illustrated time range were the first description for nitric oxide in 1772 and its first human use in 1800; and the first description of flavonoids in 1898, aspirin in 1853, and of the wider class of antiendotoxins in 1896. Details for these interventions can be found in tables S1 to S5, listed by the ID number. Ab, antibody; GP, glycoprotein; HA-1A, human IgM monoclonal antibody against endotoxin A; HRT, hormone replacement therapy; mo Ab, monoclonal antibody; rt-PA, recombinant tissue plasminogen activator.

### Recommendations for the Future

Our analysis documents objectively show the long length of time that passes between discovery and translation. As scientists, we should convey to our funders and the public the immense difficulty of the scientific discovery process. Successful translation is demanding and takes a lot of effort and time even under the best circumstances; making unrealistic promises for quick discoveries and cures may damage the credibility of science in the eyes of the public. The following are some recommendations for improving the system, based on our analyses:

- Discovery of new substances and interventions remains essential, but proper credit and incentives should be given to accelerate the testing of these applications in high-quality, unbiased clinical research and the replication of claims for effectiveness.
- Multidisciplinary collaboration with focused targets and involving both basic and clinical sciences should be encouraged.
- Proof of effectiveness for new interventions requires large, robust randomized clinical trials.
- Translational efforts for common diseases should focus more on novel agents and new cutting-edge technologies; for these ailments, it is unlikely that genuine major benefits from interventions already known for a long time have gone unnoticed.

#### References and Notes

1. E. A. Zerhouni, *JAMA* **294**, 1352 (2005).
2. F. M. Marincola, *J. Transl. Med.* **1**, 1 (2003).
3. J. P. Ioannidis, *J. Transl. Med.* **2**, 5 (2004).
4. D. G. Contopoulos-Ioannidis, E. Ntzani, J. P. Ioannidis, *Am. J. Med.* **114**, 477 (2003).
5. P. Cuatrecasas, *J. Clin. Invest.* **116**, 2837 (2006).
6. G. Duyk, *Science* **302**, 603 (2003).
7. B. Booth, R. Zemmel, *Nat. Rev. Drug Discov.* **3**, 451 (2004).
8. D. G. Hackam, D. A. Redelmeier, *JAMA* **296**, 1731 (2006).
9. J. P. Ioannidis, *JAMA* **294**, 218 (2005).
10. Methods and details for the collection and analysis of data are available as supporting material on *Science* Online along with its supplementary tables S1 to S5. These interventions included 18 drugs, two monoclonal antibodies, one hormonal therapy, four vitamins or food products, and three surgical or device interventions. Three drugs and one vitamin appear two times each in the list, as they were used for two different indications. For more information and references, see tables S1 and S2.
11. For more details, see Methods in the supporting online material and tables S3 to S5
12. C. R. Chong, D. J. Sullivan, *Nature* **448**, 645 (2007).
13. S. Zhu *et al.*, *Nature* **417**, 74 (2002).
14. J. D. Rothstein *et al.*, *Nature* **433**, 73 (2005).

10.1126/science.1160622

**Supporting Online Material**
www.sciencemag.org/cgi/content/full/321/5894/1298/DC1

GENETICS

# Enhancing Gene Regulation

Bioinformatic approaches reveal functional changes and the evolution of regulatory sequences that control gene expression.

**Gregory A. Wray and Courtney C. Babbitt**

Nearly half a century has passed since François Jacob and Jacques Monod demonstrated that specific noncoding sequences are required to activate genes that metabolize lactose in the bacterium *Escherichia coli* (*1*). In a prescient observation, they noted that mutations in these regulatory sequences might play a role in the evolution of organismal traits. They further argued that gene function is not only based on the biochemical activity of its product but also on how the gene's expression is regulated. This idea was expanded in 1975 in an influential paper by Mary-Claire King and Alan Wilson (*2*), who proposed that trait differences between humans and chimpanzees are primarily due to regulatory changes in gene expression. Decades elapsed, however, before it was feasible to begin testing these ideas in detail. Two papers in this issue, by Prabhakar *et al.* on page 1346 (*3*), and by Hong *et al.* on page 1314 (*4*), demonstrate the power of combining bioinformatic approaches with experimental tests to characterize such regulatory regions.

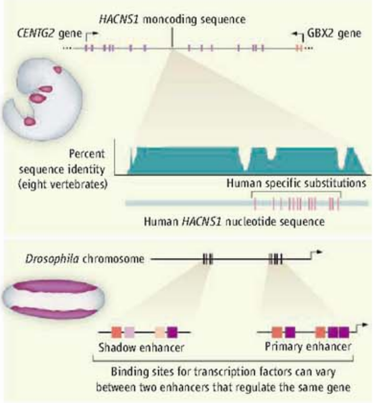

**Identification of enhancer elements.** (**Top**) *HACNS1* is a noncoding region of conservation (percent identity) among eight vertebrate species, with 13 human-specific substitutions (vertical red lines). *HACNS1* drives the expression of a reporter gene (purple) in the limbs of a developing mouse embryo. (**Bottom**) Primary enhancers (red and purple boxes) near a gene are conserved relative to more distant "shadow" enhancers, which appear to be less functionally constrained (pink and light purple boxes). These enhancers drive gene expression (purple) in the *Drosophila* embryo.

CREDIT: ADAPTED BY P. HUEY/SCIENCE

A major impediment to studying the evolutionary importance of mutations in regulatory regions is simply knowing where to look. DNA sequences that regulate the transcription of genes occupy no fixed position relative to coding DNA regions and are often diffuse and widely dispersed. Even when the position of a regulatory element is known, there is the added challenge of identifying which mutations have functional consequences. Within coding sequences, the genetic code imposes familiar regularities: Mutations that change protein structure can be identified exhaustively and unambiguously. By contrast, identifying functional mutations within regulatory regions requires experimental tests of putative regulatory elements from different species or individuals—a costly and time-consuming process. Bioinformatic methods offer a way to identify promising functional noncoding regions and to narrow the focus for experimental tests.

One approach is to search genomes for highly conserved blocks of noncoding sequence (on the assumption that conservation implies function) and then scan for instances of rapid sequence divergence on just one branch of a phylogeny (which implies a functional change in a single species) (*5*). Prabhakar *et al.* use this approach to identify a noncoding region they call *human-accelerated conserved noncoding sequence 1* (*HACNS1*) (see the figure). To test the function of this region, they genetically engineered mouse embryos to express a construct composed of human *HACNS1*, the promoter element of a heat shock gene, and a reporter gene. Their results show that human *HACNS1* drives expression in the mesenchyme of the early developing forelimb, and later developing hindlimb, in these mouse embryos. A comparison of expression patterns driven by macaque, chimpanzee, and human orthologs of *HACNS1* revealed that consistently strong forelimb expression is a unique property of the human version. By testing various combinations of human and chimpanzee *HACNS1* sequences, the authors narrowed down the relevant functional mutations to an 81–base pair region containing 13 substitutions that arose during human evolution. This concentration of substitutions is highly unusual relative to the genome as a whole, implying positive selection on this region during human origins.

What genes does *HACNS1* regulate? This conserved region lies within an intron of *CENTG2*, which encodes a guanosine triphosphatase activating protein that regulates endosomes (membrane-bound vesicles that transport materials into a cell). It is also ~300 kb downstream of the next nearest gene, *GBX2*, which encodes a transcription factor that is expressed, among other locations, in developing limbs. If *GBX2* is indeed the target of *HACNS1* regulation, the implications are fascinating. Because of *GBX2*'s role in limb development, the authors note that changes in its expression could have altered human limb anatomy—producing, for instance, specializations of the hand that facilitate tool use, or modifications of the foot associated with bipedalism.

Another bioinformatic approach to identifying regulatory elements is to search for clusters of potential transcription factor binding sites (*6*). Hong *et al.* examined data from chromatin immunoprecipitation combined with microarray technology—so-called ChIP-chip analysis—from the fruit fly (*Drosophila melanogaster*) genome for targets of regulation by the transcription factor Dorsal and known cofactors (*4*). Surprisingly, they found that many target genes of Dorsal contain not one but two clusters of transcription factor binding sites, implying the presence of multiple regulatory regions with similar function (see the figure). Although most experimentally verified enhancers lie within a few kilobases of the gene they regulate, some of the

---

Department of Biology and Institute for Genome Science and Policy, Duke University, Box 90338, Durham, NC 27708, USA. E-mail: gwray@duke.edu

secondary enhancers lie tens of kilobases away. The authors used transgenic flies to show that both nearby and more distant clusters of binding sites drive similar patterns of reporter gene expression for two genes, *brk* and *sog*.

The evolutionary role of these "shadow enhancers" is unclear. One possibility suggested by Hong *et al.* is that they provide an opportunity for natural selection to tinker with regulatory sequences, while the primary enhancers maintain essential gene function. Consistent with this hypothesis, the sequences of "shadow enhancers" evolve more rapidly than those of primary enhancers, which suggests that they operate under fewer functional constraints. The intriguing possibility that "shadow enhancers" more commonly confer expression differences among species could be tested with the type of comparative experimental approach that Prabhakar and colleagues applied to *HACNS1*.

Although identifying functional changes in regulatory sequences remains a serious challenge, these two papers demonstrate the power of combining bioinformatics and experimental tests. However, most regulatory elements are neither highly conserved among species nor composed of clusters of the same binding motif. Indeed, few of the well-documented cases connecting noncoding mutations to trait evolution in humans and flies (*7–9*) involve regions that would have been identified as functional on the basis of sequence conservation or motif clustering.

The challenge now is to develop methods that can recognize functional changes within a much greater proportion of regulatory elements. As phylogenetic sampling of sequenced genomes grows denser, it is becoming possible to carry out unbiased surveys of regulatory change based on genome-scale functional assays (*10*), quantitative genetics (*11*), and tests for positive selection (*12*). Decades after Jacob and Monod first speculated about the evolutionary importance of regulatory mutations, we are in a position to begin testing their ideas in earnest.

**References**

1. F. Jacob, J. Monod, *J. Mol. Biol.* **3**, 318 (1961).
2. M. C. King, A. C. Wilson, *Science* **188**, 107 (1975).
3. S. Prabhakar *et al.*, *Science* **321**, 1346 (2008).
4. J.-W. Hong, D. A. Hendrix, M. S. Levine, *Science* **321**, 1314 (2008).
5. S. Prabhakar, J. P. Noonan, S. Pääbo, E. M. Rubin, *Science* **314**, 786 (2006).
6. M. Markstein, P. Markstein, V. Markstein, M. S. Levine, *Proc. Natl. Acad. Sci. U.S.A.* **99**, 763 (2002).
7. N. Gompel, B. Prud'homme, P. J. Wittkopp, V. Kassner, S. B. Carroll, *Nature* **433**, 481 (2005).
8. N. S. Enattah *et al.*, *Nat. Genet.* **30**, 233 (2002).
9. M. T. Hamblin, A. Di Rienzo, *Am. J. Hum. Genet.* **66**, 1669 (2000).
10. A. P. Boyle *et al.*, *Cell* **132**, 311 (2008).
11. E. E. Schadt *et al.*, *Nature* **422**, 297 (2003).
12. R. Haygood, O. Fedrigo, B. Hanson, K. D. Yokoyama, G. A. Wray, *Nat. Genet.* **39**, 1140 (2007).

10.1126/science.1163568

---

ASTRONOMY

# The Universe Measured with a Comb

A technique for wavelength calibration promises to revolutionize observational astrophysics, in areas including planet searches and cosmology.

**Sebastian Lopez**

In 1962, Allan Sandage predicted that an expanding universe should cause a drift in the redshift of cosmological objects, but noted: "With present optical techniques there is apparently no hope of detecting such small changes in redshifts for time intervals smaller than $10^7$ years" (*1*). Future extremely large telescopes (with diameters of 30 to 40 m), equipped with powerful spectrometers, could in principle enable such a measurement. However, measuring a systematic change in radial velocity of only 1 cm s$^{-1}$ per year over the course of about 20 years—a measurement referred to as the Sandage-Loeb experiment (*2–4*)—would still be impossible if it were not for the recent development of a new and exquisite wavelength calibration technique called "laser frequency combs" (*5*). On page 1335 of this issue, Steinmetz *et al.* apply this technique for the first time to an astrophysical experiment (*6*), and the results look promising.

The Doppler effect provides astronomers with a precise method to measure radial velocities of stars and galaxies using the observed shift in wavelength (or frequency) of their spectral features relative to laboratories on Earth: The higher the radial velocity, the stronger the effect. And when the light entering the spectrometer comes from distant objects like galaxies or quasars—thus crossing cosmological distances to reach the telescope—their spectra provide information about the geometry and history of the universe as a whole.

Because the universe expands, distant objects can always be assigned with a redshift, a quantity that cosmologists relate to distance and time by fitting various parameters to cosmological models. The past decade has seen a series of breakthroughs in cosmology. The Wilkinson Microwave Anisotropy Probe (WMAP) mission delivered images of the cosmic microwave background that support a

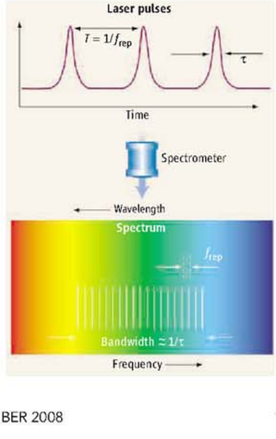

**The basics of a laser frequency comb.** A mode-locked laser creates femtosecond pulses at gigahertz frequencies, $f_{\mathrm{rep}}$ **(top)**, that are synchronized with an atomic clock. A spectrum of the pulses **(bottom)** is composed of many modes that are uniformly spaced in wavelength (or frequency) and cover a spectral bandwidth given roughly by the inverse of the pulse duration. Each mode's wavelength (or frequency) does not have to be measured, but instead is given by a mathematical relation that includes $f_{\mathrm{rep}}$, known a priori with very high accuracy. Laser frequency combs could therefore become the perfect wavelength calibration technique for astrophysical experiments that require high accuracy and long-term stability.

CREDIT: ADAPTED BY P. HUEY/SCIENCE

---

Departamento de Astronomía, Universidad de Chile, Casilla 36-D, Santiago, Chile. E-mail: slopez@das.uchile.cl

flat universe, and studies measuring distances to Type Ia supernovae or the large-scale distribution of galaxies, among others, have established that the universe not only expands, but that the expansion is accelerating—presumably due to the effect of an unknown component in the mass-energy budget of the universe called "dark energy." Many projects aim to elucidate what dark energy really is, but all of them rely on a given cosmological model; only the Sandage-Loeb experiment could track the history of the expansion directly, without any previous assumption on the geometry of the universe.

What has been the impediment to fully exploiting present instrument capabilities? Traditional spectral calibration techniques use a crowd of emission or absorption lines at known laboratory wavelengths as reference to map the detector pixels into wavelengths. However, calibration units are subject to uncertainties that unavoidably degrade the wavelength solution: Lines are not evenly distributed in the spectral range of interest, have a wide range of intensities, and sometimes appear blended. These systematic effects become the perennial stumbling block for precision spectroscopy. They limit the capabilities of current high-resolution spectrometers and hinder experiment repeatability, crucial for any long-term monitoring.

The recently developed laser frequency combs (*3*, *6*–*9*) may offer the solution. Such a comb is the spectrum of a femtosecond "mode-locked" laser that delivers pulses at repetition rates $f_{\mathrm{rep}}$ of ~1 GHz (determined by the round-trip time in the laser cavity). When these pulses pass through a spectrometer, a regular train of modes is produced in the frequency domain, each of them evenly separated by $f_{\mathrm{rep}}$ (see the figure) and spanning a spectral bandwidth given by the inverse of the pulse duration. Because time—and thus frequency—is the most accurately measured quantity in physics thanks to atomic clocks, each mode's frequency (or wavelength) is accurately known a priori and can be used as a perfect ruler to calibrate astronomical spectra.

Steinmetz *et al.* now report the first astronomical spectrum (of the Sun) calibrated with a laser frequency comb. Besides slightly outperforming current best standards of accuracy using just a small bandwidth, the team was also able to characterize the stability of the instrument in an unprecedented fashion. Use of larger bandwidths should allow wavelengths to be measured with a stable precision of 1 part in 10 billion, opening a new era in astronomical spectroscopy.

Full implementation of laser frequency combs in large telescopes will require coverage of the entire optical range. Once this challenge is overcome, at least two other astrophysical experiments besides the future Sandage-Loeb test should benefit from the use of this technique.

First, some astronomers have wondered whether the atomic physics responsible for the redshifted absorption lines seen in the spectra of distant quasars has remained the same over cosmological times. The values of fundamental constants or combinations of constants—like the proton-to-electron mass ratio or the fine-structure constant—determine the relative positions of the lines in the quasar spectra. Thus, one could in principle compare the value of those constants then ("at high redshift") and now (on Earth) to determine whether they have remained constant. By choosing particular methods and sets of lines, different groups have arrived at diverging conclusions. After a decade of research, the debate is now centered on the systematic effects inherent to the observations. Laser frequency combs could help to identify the origin of these systematic effects.

Second, the precision and stability offered by laser frequency combs could greatly help astronomers looking for exoplanets (which orbit stars other than the Sun). Such planets imprint small changes on the radial velocity of their solar system, and monitoring the radial velocities of bright stars has thus become the most reliable way of finding planets. However, the smaller the planet, the smaller the drift in radial velocity. Discovering Earth-like planets orbiting solar-like stars in the "habitable zone" (where life could exist) requires a precision of about $5\ \mathrm{cm\ s}^{-1}$ and a stability of about 1 year. This should be an easy task for this new technique.

### References and Notes

1. A. Sandage, *Astrophys. J.* **136**, 319 (1962).
2. A. Loeb, *Astrophys. J.* **499**, L111 (1998).
3. M. T. Murphy *et al.*, *Mon. Not. R. Astron. Soc.* **380**, 839 (2007).
4. J. Liske *et al.*, *Mon. Not. R. Astron. Soc.* **386**, 1192 (2008).
5. T. W. Hänsch and J. L. Hall received the 2005 Nobel Prize in Physics "for their contributions to the development of laser-based precision spectroscopy, including the optical frequency comb technique."
6. T. Steinmetz *et al.*, *Science* **321**, 1335 (2008).
7. Th. Udem, R. Woltzwarth, T. W. Hänsch, *Nature* **416**, 233 (2002).
8. C. Araujo-Hauck *et al.*, *Messenger* **129**, 24 (2007).
9. C.-H Li *et al.*, *Nature* **452**, 610 (2008).

10.126/science.1163194

---

MEDICINE

# The Cart Before the Horse

**Janet D. Rowley[1] and Thomas Blumenthal[2]**

Chimeric RNAs, transcribed from malignancy-associated chromosomal translocations, can also arise from RNA trans-splicing in normal cells.

Since the identification of specific regions in human chromosomes that undergo recurring structural rearrangements (translocations) and cloning of the associated breakpoint genes, the fusion of genes has been viewed as a unique event in abnormally growing, usually malignant, cells (*1*, *2*). However, the study by Li *et al.* on page 1357 in this issue (*3*) indicates quite the contrary, turning at least one paradigm of cancer cytogenetics on its head.

Li *et al.* report that in normal human endometrial tissue, there is a low amount of a messenger RNA (mRNA) that corresponds to sequences from two genes, *JAZF1* on chromosome band 7p15 and *JJAZ1/SUZ12* on chromosome band 17q21. Moreover, this chimeric mRNA is identical to that seen in 50% of human endometrial stromal sarcomas, in which there is a 7;17 chromosomal translocation that results in a gene fusion, even though no translocation is detected in normal endometrial cells. The product encoded by the chimeric mRNA is a fusion protein that is expressed in cultured cells, and consequently, could confer cellular resistance to programmed cell death and increased growth (under conditions where expression of the endogenous *JJAZ1* gene was suppressed). Further, this fusion mRNA is expressed in a cyclical manner in normal endometrial cells, most readily detected at the beginning and end of the menstrual cycle when concentrations of estrogen and progesterone are low.

How is this fusion mRNA made in the absence of a corresponding gene fusion?

---

[1] Department of Medicine, University of Chicago, 5841 South Maryland Avenue, MC 2115, Chicago, IL 60637, USA. E-mail: jrowley@medicine.bsd.uchicago.edu [2] Department of Molecular, Cellular and Developmental Biology, University of Colorado, Boulder, CO 80309, USA. E-mail: tom.blumenthal@colorado.edu

Li *et al.* propose that the fusion mRNA is produced by trans-splicing of RNA (see the figure) in which nucleotides at the 3′ end of *JAZF1*-encoding precursor mRNA are replaced with those of *JJAZ1*-encoding precursor mRNA. A different form of trans-splicing is common in several lower animal phyla (*4*), and a few mRNAs have been shown to be assembled from separate transcripts in insects (*5*). And although trans-splicing in mammalian cells has been reported, the resulting chimeric RNAs do not perform obvious functions and are usually not present in large enough amounts to do so.

It has not been clear how two separate mRNAs are spliced together (*6*). Perhaps they are brought together through the pairing of nucleotides within noncoding sequences (introns) between two transcripts, or maybe each contains a binding site for proteins that can form dimers or higher-order multimers. Although sloppiness by the spliceosome—the cellular machine that removes introns from precursor RNA—could be an explanation, only specific pairs of precursor mRNAs engage in trans-splicing. Perhaps RNAs from different genes are trans-spliced because they are transcribed in the same geographic location. Alternatively, trans-splicing could occur more frequently than we realize, but most cases go undetected.

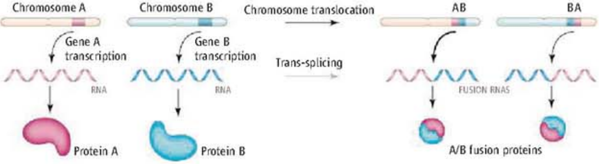

**Fusion RNAs.** Either chromosome translocation or RNA trans-splicing can give rise to fusion mRNAs and proteins. Some chromosomal translocations produce two hybrid genes that may produce mRNAs containing the 5′ end of one gene and the 3′ end of the other. Both may encode fusion proteins. Alternatively, normal mRNAs corresponding to both genes can recombine by trans-splicing that may produce equivalent fusion mRNAs and proteins. Only one of the possible fusion mRNAs and proteins is examined by Li *et al.*

CREDIT: ADAPTED BY P. HUEY/SCIENCE

What makes the study by Li *et al.* especially interesting is that trans-splicing is clearly regulated. The mRNA fusion appears only in cells from endometrial tissue. Its expression is increased by hormones and hypoxia, with much higher expression in late secretory and early proliferative stages of the menstrual cycle. The key question is whether the chimeric RNA is transcribed from some undetected rearranged copies of the two genes. However, Li *et al.* show that there is no such gene rearrangement in cells producing the trans-spliced mRNA and that this trans-splicing event can be duplicated in vitro. In addition, they show that a nontransformed human endometrial stromal cell line had no rearranged DNA or visually abnormal chromosomes.

Given the absence of any detectable rearranged DNA in cells producing the chimeric RNA, the obvious explanation is rearrangement at the RNA level. To demonstrate that trans-splicing could account for the chimera, Li *et al.* made extracts from a human endometrial stromal cell line and from a rhesus monkey fibroblast cell line so that they could detect trans-spliced products by a sequence difference between the RNA from the two species. The authors demonstrated in vitro trans-splicing of the rhesus *JAZF1* exons (coding regions of DNA) to human *JJAZ1* exons. Treatment of the rhesus RNA with deoxyribonuclease (to cleave any DNA that might be present) did not prevent formation of the chimeric RNA, confirming that chimeric RNA arose from trans-splicing.

Is it a coincidence that the same RNA occurs in normal cells by trans-splicing and in tumor cells of the same type by DNA rearrangement? The authors suggest the intriguing possibility that whatever leads to the trans-splicing could also lead to the genomic rearrangement. This could occur by at least three general mechanisms. The same sequences could pair at the RNA level to result in trans-splicing and at the DNA level to result in genomic rearrangement. However, sequence analyses of translocation breakpoints in leukemia reveal large deletions and duplications as well as precise nucleotide base-pairing (*7*). Alternatively, genomic rearrangement could be a direct result of the trans-splicing event if genes involved in the rearrangement are brought into close proximity during the RNA trans-splicing process. This idea is consistent with recent reports on the existence of "factories" for transcription and RNA processing (*8–10*). Finally, the RNA created by trans-splicing could act as a guide RNA to facilitate the genomic rearrangement, an idea for which there is precedent (*11*). In this case, the trans-spliced RNA would anneal to regions of both of the chromosomes and guide them in a DNA recombination event. Indeed, it is possible that other genomic rearrangements could be guided by cellular RNAs.

If fusion mRNA is widespread, it could explain the conundrum that has long perplexed cancer geneticists: why fusion mRNAs can be detected in apparently normal tissues of healthy people. Such fusions involve common translocations seen in neoplastic hematopoietic cells, but never in solid tumors. If fusion mRNAs are part of normal cell function, then finding fusions of the immunoglobulin heavy chain gene (*IGH*) to the *BCL2* gene in normal spleens, which usually reflects the presence of a t(14;18) translocation in lymphomas, would not be unexpected (*12*). Given that *IGH* and the *MYC* genes frequently colocalize in transcription factories (*9*), this geography could provide a mechanism for having nascent RNAs in juxtaposition; moreover, the genes themselves would be close together. Translocations involving the *IGH* and *IGK/L* genes and the genes encoding T cell receptors (*TCRs*) in lymphoid malignancies are exceptions in that they do not lead to a fusion mRNA, but rather to altered regulation of the apparently normal target protein (*13*). Presumably all translocations are mediated by DNA recombination enzymes, but could this process be guided by RNA produced by trans-splicing? The study by Li *et al.* also raises questions relevant to clinical practice. Potent therapies targeting fusion mRNA and proteins may disrupt critical pathways of normal cell function. Increasingly sensitive methods to determine the presence of a few translocation-bearing cells leads one to question whether translocations or normal cell products are being detected. This is a critical issue because the search for minimal residual disease is in high gear, especially for chronic myeloid leukemia that responds to the drug imatinib, as a "cure" seems within reach (*14*). Many patients suffering from this cancer are translocation-negative on standard cytogenetic analysis, but show a gene fusion (*BCR-ABL*) by reverse transcriptase polymerase chain reaction. For these patients, especially the ones with very low amounts of fusion, it is unclear whether what is being detected is a malignant cell or a trans-splicing event.

As the search for fusions in normal cells will likely be fast-paced for the next few years, two points should be considered, given the findings of Li *et al*: cell specificity and regulation of the trans-splicing event. So choose the fusion to be investigated, mindful of these constraints.

### References

1. J. D. Rowley, *Nat. Rev. Cancer* **1**, 245 (2001).
2. F. Mitelman, B. Johansson, F. Mertens, *Nat. Genet.* **36**, 331 (2004).
3. H. Li, J. Wang, G. Mor, J. Sklar, *Science* **321**, 1357 (2008).
4. T. Blumenthal, in *Wormbook*, The *C. elegans* Research Community, Ed.; Wormbook, 10.1895/wormbook.1.5.1, www.wormbook.org.
5. R. Dorn, G. Reuter, A. Loewendorf, *Proc. Natl. Acad. Sci. U.S.A.* **98**, 9724 (2001).
6. T. Takahara *et al.*, *Mol Cell.* **18**, 245 (2005).
7. Y. Zhang, J. D. Rowley, *DNA Repair (Amst)*. **5**, 1282 (2006).
8. S. McCracken *et al.*, *Nature* **385**, 357 (1997).
9. C. S. Osborne *et al.*, *PLoS Biol.* **5**, e192 (2007).
10. J. A. Mitchell, P. Fraser, *Genes Dev.* **22**, 20 (2008).
11. M. Nowacki *et al.*, *Nature* **451**, 153 (2008).
12. S. Janz, M. Potter, C. S. Rabkin, *Genes Chromosome Cancer* **36**, 211 (2003).
13. T. W. McKeithan, *Semin Oncol.* **17**, 30 (1990).
14. A. Hochhaus *et al.*, *Blood* **111**, 1039 (2008).

10.1126/science.1163791

---

BIOCHEMISTRY

# An Enzyme Assembly Line

Fatty acid synthases and related megaenzymes are highly adaptable to new functions as a result of their modular architecture.

**Janet L. Smith[1,2] and David H. Sherman[1,3]**

The fundamental polymers of biology—proteins, DNA, and RNA—are products of repetitive condensation of simple amino acid or nucleotide building blocks and are comparatively easy to assemble. However, other biomolecules require additional reactions beyond condensation of building blocks. Examples are the fatty acids and the polyketide and nonribosomal peptide secondary metabolites. These molecules are produced by complex enzyme assembly lines that include multiple catalytic domains. Two new crystal structures—one reported recently (*1*), the other by Maier *et al.* on page 1315 of this issue (*2*)—enrich our understanding of how these mega-enzymes function as efficient factories to produce a remarkable range of metabolic products.

Maier *et al.* study the fatty acid synthase (FAS-I) responsible for de novo fatty acid synthesis in the cytosol of animal cells. FAS-I is homologous in sequence and architecture with the very large family of modular polyketide synthases (PKSs), which produce a wide variety of natural products with potential medicinal value. In 2006, the authors reported the structure of FAS-I from a 4.5 Å electron density map, in which most domains could be assigned but no details were visible (*3*). Their new structure provides sufficient detail to understand the fold and the connectivity of six of its eight domains; however, the flexibly tethered acyl carrier protein (ACP) and thioesterase (TE) domains remain invisible. The other structure, reported by Tanovic *et al.* (*1*), is of an intact module of a nonribosomal peptide synthetase (NRPS). Except for the peptidyl carrier protein (PCP), the primary NRPS domains are not related to those of the FAS and PKS systems, but the assembly-line approach is similar.

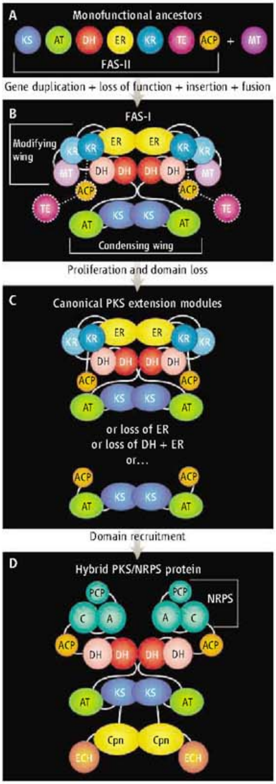

**Assembly-line proliferation.** The dissociated FAS-II **(A)** evolved into the homodimeric FAS-I **(B)** [dotted lines outline disordered parts of the FAS-I structure (*2*); lighter shades indicate inactivated DH, KR, and MT domains]. Duplication of an ancestral FAS-I gene, followed by selective deletion, yielded the canonical extension modules of modern PKS pathways **(C)**. An even richer diversity of polyketides arose by domain recruitment. For example, the CurF protein of the hybrid PKS/NRPS for curacin A (*10*) includes decarboxylase (ECH), cyclopropanase (Cpn), and NRPS domains **(D)**.

All data indicate that the ancestor of FAS-I was a set of monofunctional enzymes, presumably resembling the dissociated FAS (type II, FAS-II) that catalyzes fatty acid biosynthesis in modern bacteria and plant plastids (see the figure, panel A). Gene duplication, loss of function, and gene fusion gave rise to the 270-kD polypeptide that functions as the homodimeric FAS-I in mammals (see the figure, panel B). A different mega-enzyme fusion of monofunctional ancestors evolved in fungi (*4*). Of these two assembly-line architectures for fatty acid synthesis, the mammalian FAS-I proved the more adaptable, and it now exists not only for fatty acid biosynthesis but throughout the eubacterial and fungal world for synthesis of polyketides. Indeed, high-resolution structures of PKS components (*5*, *6*) provide critical corroboration for the mammalian FAS structure.

Two key features of the FAS-I architecture explain its remarkable adaptability. First, the structure is segregated into two wings: a selection/condensing wing for addition of new building blocks, and a modifying wing for chemical processing of chain elongation intermediates (see the figure, panel B). The heart of the assembly line is the condensing wing, where an acyltransferase (AT) domain selects

---

[1] Life Sciences Institute, University of Michigan, Ann Arbor, MI 48109, USA. [2] Department of Biological Chemistry, University of Michigan, Ann Arbor, MI 48109, USA. [3] Departments of Medicinal Chemistry, Chemistry, and Microbiology and Immunology, University of Michigan, Ann Arbor, MI 48109, USA. E-mail: janetsmith@umich.edu; davidhs@umich.edu

a building block and a ketosynthase (KS) domain adds it to the growing chain. The dimeric KS also contributes most of the dimer contacts in the complex.

The second key architectural feature is an open and flexible design that is ideal for insertion or deletion of catalytic domains, especially in the modifying wing. Each two-carbon addition (via malonate) to a fatty acid chain is followed by three reactions—keto reduction (KR), dehydration (DH), and enoyl reduction (ER)—carried out in the modifying wing of the FAS-I. A major source of chemical diversity in polyketides arises from deletion or inactivation of one or more of these modifying domains (see the figure, panel C), providing the chemical variation that is lacking in fatty acids.

In FAS-I and most fungal PKSs, the assembly line is used for iterative synthesis: Each enzyme domain performs the same reaction at each extension step on the growing substrate. In contrast, in most bacterial PKSs, polyketide synthesis is sequential: Each extension step is carried out by an individual FAS-I–like "module," offering the possibility to vary the building block identity and modification chemistry at each step. This scheme greatly expands genetic and protein complexity. Several modules (up to 20 or more) are required to build a complex polyketide, and specific interactions of sequential modules must be faithfully maintained by fusion or by docking domains (*7*, *8*).

A big surprise of the new FAS structure is a vestigial methyltransferase (MT) domain at the periphery of the dimer, following the DH in the polypeptide sequence. Thus, the mega-enzyme ancestor of FAS-I appears to have had a methylation reaction as part of its fatty acid biosynthetic cycle. Was there a prokaryotic methyl branched-chain fatty acid, unknown to us today? The MT domain lost its function in FAS-I, was deleted from most PKS systems, but exists in some PKSs as an active methyltransferase. And herein lies a conundrum; the ubiquity of PKS pathways in bacteria and elsewhere strongly argues that the original FAS-I evolved in a prokaryote. However, other than *Mycobacterium tuberculosis* and related species that generate unusual fatty acids, we know of no modern prokaryote that uses a FAS-I for normal membrane lipid fatty acid biosynthesis (*9*).

In many PKS modules, the open FAS-I architecture has been augmented with a variety of other catalytic domains, such as *S*-acetyltransfer, halogenase, cyclopropanase, decarboxylase, and even entire NRPS modules (see the figure, panel D) (*10*, *11*). The new structure of the terminal module of the surfactin NRPS (*1*) shows how it, too, is highly adaptable. Like FAS-I, the NRPS has a solid platform for condensation, including an adenylation (A) domain to select the amino acid building block and a condensation (C) domain to form a peptide link to the growing chain (*1*). The monomeric C-A didomain (analogous to KS-AT in the FAS-I condensing wing) is fused to a PCP and a terminal TE domain. As in the FAS-I structure, the PCP is flexibly linked to the synthetase by tethers long enough for it to deliver substrate to the active sites of all catalytic domains. Unlike the FAS-I structure, the PCP and TE domains are well ordered in the NRPS module.

The three assembly line types use homologous domains (ACP or PCP) to carry the growing fatty acid, polyketide, or peptide via a pantetheine-linked thioester. The common thioester chemistry and the adaptable architecture have resulted in the proliferation of hybrid PKS-NRPS and even PKS-FAS-I pathways found in phylogenetically diverse bacteria (*9*, *12*). The rich diversity of PKS, NRPS, and hybrid systems demonstrates that nature has not employed a Henry Ford–like assembly line, from which the customer could have any color car so long as it was black. Rather, we see a modular assembly line that is easily copied, modified, and adapted to new function; this is the secret to its success.

### References

1. A. Tanovic, S. A. Samel, L.-O. Essen, M. A. Marahiel, *Science* **321**, 659 (2008); published online 26 June 2008 (10.1126/science.1159850).
2. T. Maier, M. Leibundgut, N. Ban, *Science* **321**, 1315 (2008).
3. T. Maier, S. Jenni, N. Ban, *Science* **311**, 1258 (2006).
4. S. Jenni, M. Leibundgut, T. Maier, N. Ban, *Science* **311**, 1263 (2006).
5. A. T. Keatinge-Clay, R. M. Stroud, *Structure* **14**, 737 (2006).
6. Y. Tang, C. Y. Kim, I. I. Mathews, D. E. Cane, C. Khosla, *Proc. Natl. Acad. Sci. U.S.A.* **103**, 11124 (2006).
7. M. Thattai, Y. Burak, B. I. Shraiman, *PLoS Comput. Biol.* **3**, 1827 (2007).
8. J.-P. Nougayrède *et al.*, *Science* **313**, 848 (2006).
9. R. S. Gokhale, P. Saxena, T. Chopra, D. Mohanty, *Nat. Prod. Rep.* **24**, 267 (2007).
10. Z. Chang *et al.*, *J. Nat. Prod.* **67**, 1356 (2004).
11. L. Gu *et al.*, *Science* **318**, 970 (2007).
12. M. A. Fischbach, C. T. Walsh, J. Clardy, *Proc. Natl. Acad. Sci. U.S.A.* **105**, 4601 (2008).

10.1126/science.1163785

---

MICROBIOLOGY

# How to Infect a Mimivirus

Large DNA viruses such as the giant Mimivirus can be infected by smaller viruses.

**Hiroyuki Ogata and Jean-Michel Claverie**

The giant DNA "Mimivirus" (*Acanthamoeba polyphaga* mimivirus, or APM) was initially mistaken for a bacterium, until La Scola *et al.* classified it as a virus in 2003 (*1*). This highly unusual virus has more genes than many bacteria (*2*), forms the most complex known virus particle (*3*), has a unique DNA delivery system (*4*), and encodes aminoacyl-tRNA synthetases (*5*), normally restricted to cellular organisms. As a possible "missing link" between the cellular and the viral world, APM's discovery revived theories that link DNA viruses to the emergence of the eukaryotic nucleus (*6*). Large viruses closely related to APM are abundant in the sea (*7*) and may play important roles in the geochemical fluxes that regulate Earth's climate. La Scola *et al.* now report in *Nature* (*8*) that the APM family has another unusual property: It is susceptible to infection by another virus, named Sputnik (after "traveling companion" in Russian).

Sputnik—a small icosahedral virus with a DNA genome encoding 21 genes—was isolated with a new strain of APM from a cooling tower in Paris. Attempts to culture Sputnik alone in amoeba cells were not successful. However, when amoebae were inoculated with the two viruses, both Sputnik and APM virions multiplied. La Scola *et al.* (*8*) show that Sputnik reproduces in the "virus factory," the replication and assembly center built by APM in amoeba cells during their lytic infection. The virus factory is a DNA-rich cytoplasmic compartment that appears 4 hours after APM infection and grows to several micrometers in diameter. Sputnik virions reproduce faster than do APM virions; 6 hours after infection, Sputnik virions start to emerge from the virus factory, while the new generation of APM virions only appears after 8 hours. Infection with both viruses decreases the yield of infective APM virions

---

Structural and Genomic Information Laboratory, CNRS-UPR 2589, IFR-88, Université de la Méditerranée, Parc Scientifique de Luminy, FR-13288 Marseille, France. E-mail: ogata@igs.cnrs-mrs.fr; jean-michel.claverie@univmed.fr

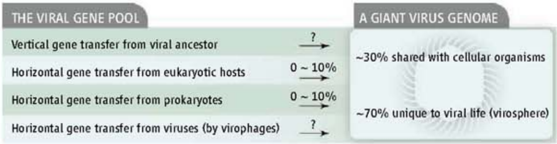

**Origin of genes in large eukaryotic viruses.** The distribution of sequence database matches suggests diverse origins for the genes of large DNA viruses. Horizontal gene transfer may occur through exposure to host or prokaryotic DNA. The many genes unique to viruses are vertically or horizontally transferred between viruses—a process in which the newly discovered virophages may play a key role.

and results in "sick" APM virions with aberrant morphologies. Sputnik thus behaves as a true parasite with a detrimental effect on APM reproduction.

Small viruses requiring other larger viruses for their reproduction have previously been documented. These "satellite viruses" lack essential functions for multiplication, for which they exploit their "helper viruses." La Scola *et al.* (*8*) argue that Sputnik is more than a satellite virus, because it uses its partner's virus factory and impairs its fitness. They therefore call Sputnik a "virophage."

What is the origin of the Sputnik virophage? The authors provide evidence suggesting the existence of related virophages in the oceans (*8*). Marine virologists have reported small viruses occurring with larger ones in marine protist populations (*9*, *10*). During recurrent infection of a cell by the two viruses, one virus may begin to benefit from the other. Like Sputnik, the small marine viruses multiply faster than the larger ones. If the viral genomes can physically interact, genes can be exchanged, and the two viruses may evolve into various states of dependency, from mutualisms to parasitism. In this context, it is worth noting that Sputnik has an integrase (an enzyme that inserts pieces of DNA from one DNA molecule into another). The genome of a marine virus, infecting the planktonic species *Emiliania huxleyi* contains a strange 176-kb central segment (*11*): Genes in this segment lack homologs in other viruses, but harbor a unique promoter. This segment is expressed much earlier than the rest of the viral genome and may be the integrated genome of an unknown virophage.

The genes in giant eukaryotic viruses have multiple origins (see the figure). The APM genome contains eukaryotic- or prokaryotic-like genes. Recent horizontal gene transfers from its eukaryotic hosts or prokaryotic organisms partially account for these genes. However, giant viral genomes also contain genes that are unique to viruses, the origin of which is hotly debated (*6*, *12*, *13*). Do these genes originate in vertical gene transfer from a very old viral common ancestor? The small number of genes shared among modern viruses argues against this possibility. Viral genome mosaicism is also suggested by the occurrence of very similar genes in different viruses (*14*). Furthermore, a substantial amount of horizontal gene transfer may occur between viruses. The Sputnik virophage now provides a new potential vehicle for such horizontal gene transfers. In fact, the Sputnik genome encodes several genes that may originate in vastly different viruses.

Assessing the proportions of vertical gene transfer and virus-virus horizontal gene transfer now appears crucial for understanding the evolution of giant viruses, refining the concept of virus lineage, and elucidating gene flow in the virosphere. The unusual features of the giant Mimivirus revived the popular, yet unresolved question: "Are viruses alive?" The discovery that some of them can get sick adds a new twist to this old debate.

**References**

1. B. La Scola *et al.*, *Science* **299**, 2033 (2003).
2. D. Raoult *et al. Science* **306**, 1344 (2004).
3. P. Renesto *et al. J. Virol.* **80**, 11678 (2006).
4. N. Zauberman *et al. PLoS Biol.* **6**, e114 (2008).
5. C. Abergel *et al.*, *J. Virol.* **81**, 12406 (2007).
6. J.-M. Claverie, *Genome Biol.* **7**, 110 (2006).
7. A. Monier, J.-M. Claverie, H. Ogata, *Genome Biol.* **9**, R106 (2008).
8. B. La Scola *et al.*, *Nature* 10.1038/nature07218 (2008).
9. K. Nagasaki, *J. Microbiol.* **46**, 235 (2008).
10. C. P. Brussaard *et al.*, *Virology* **319**, 280 (2004).
11. M. J. Allen *et al.*, *J. Virol.* **80**, 7699 (2006).
12. H. Ogata, J.-M. Claverie, *Genome Res.* **17**, 1353 (2007).
13. E. V. Koonin, W. Martin, *Trends Genet.* **21**, 647 (2005).
14. K. Nagasaki *et al.*, *Appl. Environ. Microbiol.* **71**, 3599 (2005).

10.1126/science.1164839

---

PHYSICS

# An End to the Drought of Quantum Spin Liquids

Patrick A. Lee

After decades of searching, several promising examples of a new quantum state of matter have now emerged.

Electrons possess magnetic behavior through the quantum mechanical property of spin. The magnetic properties of materials then arise from the collective interaction of electrons on atoms within the crystal. Below a transition temperature, the electron spins of normal magnets "freeze" into an ordered array of magnetic dipoles. Whether the ordering is ferromagnetic (all the dipoles point in the same direction) or antiferromagnetic (the dipoles on adjacent sites point in opposite directions) is determined by the sign and strength of the interaction between the electrons. Early theoretical work has indicated a departure from these ordered states, suggesting that quantum mechanical fluctuations of the spin could be so strong that ordering would be suppressed and the spin ensemble would remain in a liquid-like state, even down to the lowest temperatures. Experimental evidence, which has until recently remained elusive, is emerging in favor of this long-predicted state of quantum matter.

To understand the controversy surrounding this exotic quantum spin liquid state, it is instructive to go back to the description of antiferromagnetism. Soon after the invention of quantum mechanics, Heisenberg pointed out that electron spins on neighboring atoms can have short-range interaction due to quantum mechanical exchange. Louis Néel

**Ordered spins. (Left)** Néel's picture of antiferromagnet ordering with an alternate spin-up–spin-down pattern across the lattice. **(Right)** Quantum fluctuations lead to mutual spin flips, which Landau argued would disorder Néel's state.

---

Department of Physics, Massachusetts Institute of Technology, Cambridge, MA 02139, USA. E-mail: palee@mit.edu

showed that a negative exchange interaction results in an antiparallel arrangement of neighboring spins, and that at low temperatures the spins order in an alternating up-down pattern (see the first figure, left panel) (*1*). This antiferromagnetic, or Néel, state was initially greeted with skepticism—Lev Landau was among the doubters (*2*).

Landau did not publish his objection, but on the basis of Friedel's comments (*2*) we can surmise that his argument was that the correct application of quantum mechanics to such a system would lead to fluctuations (see the first figure, right panel), which may completely randomize the spin order. It was not until 1949, when antiferromagnetic order was directly observed by neutron scattering, that Néel was fully vindicated. In fact, Néel's theory was far more successful than he had the right to expect: For 70 years the Néel state has prevailed.

In 1973, Philip W. Anderson reasoned that the best chance to defeat Néel ordering came in the form of "frustrated" spin systems (*3*), with the special example of spins on a triangular lattice. This lattice is "frustrated" because if an up- and down-spin occupy two corners of a triangle, the spin on the third corner does not know which way to point to obtain the lowest-energy configuration. Instead of a Néel state, Anderson proposed a ground state made up of a quantum mechanical superposition of singlet pairs that cover the lattice. He called this a resonating valence bond (RVB) state, an explicit example of a quantum spin liquid. Unfortunately, it was soon shown that neighboring spins in a triangular lattice manage to order at a 120° angle, and Néel once again won out.

The field of quantum spin liquids languished until 1987, when high-temperature superconductivity was discovered. Anderson pointed out a connection between the RVB spin liquid and the Cooper pairs of a superconductor (*4*). Attempts to justify the RVB theory of superconductivity led to rapid developments of the spin liquid theory. It is now understood that the spin liquid (defined as having an odd number of electron spins on each lattice unit cell) is a new state of matter with properties we have never encountered before. For example, the excited states may be spinons—charge-neutral objects that possess magnetic properties. Depending on the type of spin liquid, the spinon may obey Fermi or Bose statistics and there may or may not be an energy gap. Furthermore, these spinons cannot live by themselves but are generally accompanied by gauge fields, just as electrons are always accompanied by electromagnetic gauge fields (*5*). This is a dramatic example of emergent phenomena, where new particles and fields emerge at low-energy scales but are totally absent in the Hamiltonian that describes the initial system.

CREDIT: S. OKUBO/HFM2006 ORGANIZING COMMITTEE

Confirmation of the existence of the spin liquid state has been elusive, and only recently have several promising examples surfaced. The first is an organic solid called $\kappa$-$(ET)_2Cu_2(CN)_3$ (*6*, *7*) in which the active ingredients are dimers of an organic molecule, ET [bis(ethylenedithio) - tetrathiafulvalene]. A single electron is localized on each dimer, which forms layers of approximately triangular lattices. Despite an exchange energy of ~250 K, no magnetic order was detected down to 30 mK. This material is an insulator but becomes a superconductor (critical temperature $T_c = 3.5$ K) and then a metal under pressure. It is believed that the proximity to an insulator-to-metal transition implies that the spins interact with a more complicated Hamiltonian than the Heisenberg model and allows the spin liquid state to form (*8*, *9*). Remarkably, the spin susceptibility goes to a constant at low temperatures and the specific heat is linear in temperature (*7*). These properties are normally associated with metals, being consequences of the electron Fermi surface. The linear specific heat is particularly unusual for an insulator that is relatively defect-free. Furthermore, the ratio of magnetic susceptibility to the linear temperature coefficient of the specific heat is close to that of free fermions. These observations strongly suggest that the excitations are indeed fermionic spinons that form a Fermi sea, and thus offer strong evidence for a spin liquid ground state.

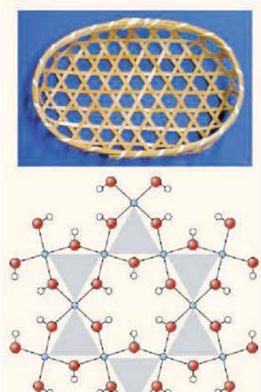

**Meeting with frustration.** **(Top)** A Kagome basket. **(Bottom)** Structure of $ZnCu_3(OH)_6Cl_2$ (*10*) showing that the Cu ions (blue) occupy a Kagome lattice; O-H is red-white.

Last year an entirely different class of spin liquid was discovered. It has long been suspected that spins on a Kagome lattice support a spin liquid ground state. Kagome is the Japanese name for the weave pattern of a basket (see the second figure, top panel). The structure consists of corner-sharing triangles and is even more frustrated than the triangular lattice considered by Anderson. Last year saw the synthesis of such a solid-state Kagome system: $ZnCu_3(OH)_6Cl_2$, where a single electron spin resides on the Cu (*10*) (see the second figure, bottom panel). Although the exchange energy is ~200 K, this material does not show any magnetic ordering down to millikelvin temperatures. The magnetic excitations are apparently gapless, but unlike the organic compound, the large specific heat at low temperatures is sensitive to magnetic field, which suggests that the low-temperature properties may be dominated by a few percent of local moment defects.

Spin liquids are not limited to two-dimensional systems. A newly synthesized material, $Na_4Ir_3O_8$, has Ir ions that form a three-dimensional network of corner-sharing triangles, termed a hyper-Kagome structure (*11*). Despite an exchange energy of ~300 K, no magnetic order was found down to 1 K and below.

It is an exciting time in the history of antiferromagnetism. After decades of searching, three examples of the defeat of Néel order by quantum fluctuations have been discovered in quick succession. There are good reasons to believe that fermionic spinons will emerge as the low-energy excitations, but more work will be needed to confirm this. An even more intriguing question is whether their partner, the emergent gauge field, can make its presence felt as well. We can be optimistic that even more exciting discoveries lie ahead.

### References

1. L. Néel, *Ann. Phys.* **5**, 232 (1936).
2. J. Friedel, *Phys. Today* **54**, 88 (October 2001).
3. P. W. Anderson, *Mater. Res. Bull.* **8**, 153 (1973).
4. P. W. Anderson, *Science* **235**, 1196 (1987).
5. P. A. Lee *et al.*, *Nat. Rev. Mod. Phys.* **78**, 17 (2006).
6. Y. Shimizu, K. Miyagawa, K. Kanoda, M. Maesato, G. Saito, *Phys. Rev. Lett.* **91**, 107001 (2003).
7. S. Yamashita *et al.*, *Nat. Phys.* **4**, 459 (2008).
8. O. Motrunich, *Phys. Rev. B* **72**, 045105 (2005).
9. S.-S. Lee, P. A. Lee, *Phys. Rev. Lett.* **95**, 036403 (2005).
10. J. Helton *et al.*, *Phys. Rev. Lett.* **98**, 107204 (2007).
11. Y. Okamoto *et al.*, *Nat. Phys. Rev. Lett.* **99**, 137207 (2007).

10.1126/science.1163196

# Flood or Drought: How Do Aerosols Affect Precipitation?

Daniel Rosenfeld,[1]* Ulrike Lohmann,[2] Graciela B. Raga,[3] Colin D. O'Dowd,[4] Markku Kulmala,[5] Sandro Fuzzi,[6] Anni Reissell,[5] Meinrat O. Andreae[7]

Aerosols serve as cloud condensation nuclei (CCN) and thus have a substantial effect on cloud properties and the initiation of precipitation. Large concentrations of human-made aerosols have been reported to both decrease and increase rainfall as a result of their radiative and CCN activities. At one extreme, pristine tropical clouds with low CCN concentrations rain out too quickly to mature into long-lived clouds. On the other hand, heavily polluted clouds evaporate much of their water before precipitation can occur, if they can form at all given the reduced surface heating resulting from the aerosol haze layer. We propose a conceptual model that explains this apparent dichotomy.

Cloud physicists commonly classify the characteristics of aerosols and clouds into "maritime" and "continental" regimes, where "continental" has become synonymous with "aerosol-laden and polluted." Indeed, aerosol concentrations in polluted air masses are typically one to two orders of magnitude greater than in pristine oceanic air (Fig. 1) (*1*). However, before humankind started to change the environment, aerosol concentrations were not much greater (up to double) over land than over the oceans (*1*, *2*). Anthropogenic aerosols alter Earth's energy budget by scattering and absorbing the solar radiation that energizes the formation of clouds (*3*–*5*). Because all cloud droplets must form on preexisting aerosol particles that act as cloud condensation nuclei (CCN), increased aerosols also change the composition of clouds (i.e., the size distribution of cloud droplets). This, in turn, determines to a large extent the precipitation-forming processes.

Precipitation plays a key role in the climate system. About 37% of the energy input to the atmosphere occurs by release of latent heat from vapor that condenses into cloud drops and ice crystals (*6*). Reevaporation of clouds consumes back the released heat. When water is precipitated to the surface, this heat is left in the atmosphere and becomes available to energize convection and larger-scale atmospheric circulation systems.

The dominance of anthropogenic aerosols over much of the land area means that cloud composition, precipitation, the hydrological cycle, and the atmospheric circulation systems are all affected by both radiative and microphysical impacts of aerosols, and are likely to be in a different state relative to the pre-industrial era.

## The Opposing Effects of Aerosols on Clouds and Precipitation

The radiative effects of aerosols on clouds mostly act to suppress precipitation, because they decrease the amount of solar radiation that reaches the land surface, and therefore cause less heat to be available for evaporating water and energizing convective rain clouds (*7*). The fraction of radiation that is not reflected back to space by the aerosols is absorbed into the atmosphere, mainly by carbonaceous aerosols, leading to heating of the air above the surface. This stabilizes the low atmosphere and suppresses the generation of convective clouds (*5*). The warmer and drier air thus produces circulation systems that redistribute the remaining precipitation (*8*, *9*). For example, elevated dry convection was observed to develop from the top of heavy smoke palls from burning oil wells (*10*). Warming of the lower troposphere by absorbing aerosols can also strengthen the Asian summer monsoon circulation and cause a local increase in precipitation, despite the global reduction of evaporation that compensates for greater radiative heating by aerosols (*11*). In the case of bright aerosols that mainly scatter the radiation back to space, the consequent surface cooling also can alter atmospheric circulation systems. It has been suggested that this mechanism has cooled the North Atlantic and hence pushed the Intertropical Convergence Zone southward, thereby contributing to the drying in the Sahel (*12*, *13*).

Aerosols also have important microphysical effects (*14*). Added CCN slow the conversion of cloud drops into raindrops by nucleating larger number concentrations of smaller drops, which are slower to coalesce into raindrops or rime onto ice hydrometeors (*15*, *16*). This effect was shown to shut off precipitation from very shallow and short-lived clouds, as in the case of

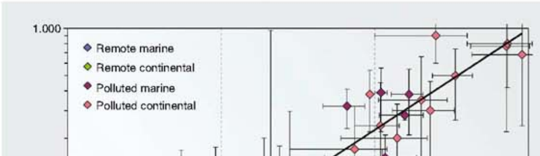

**Fig. 1.** Relations between observed aerosol optical thickness at 500 nm and CCN concentrations at supersaturation of 0.4% from studies where these variables have been measured simultaneously, or where data from nearby sites at comparable times were available. The error bars reflect the variability of measurements within each study (standard deviations or quartiles). The equation of the regression line between aerosol optical thickness (*y*) and $CCN_{0.4}$ (*x*) is given by the inset expression; *R* is the correlation coefficient. The aerosols exclude desert dust. [Adapted from (*1*)]

---

[1]Institute of Earth Sciences, Hebrew University of Jerusalem, Jerusalem 91904, Israel. [2]Institute for Atmospheric and Climate Science, ETH Zürich, 8092 Zürich, Switzerland. [3]Universidad Nacional Autónoma de México, Mexico City 04510, Mexico. [4]School of Physics and Centre for Climate and Air Pollution Studies, Environmental Change Institute, National University of Ireland, Galway, Ireland. [5]Department of Physics, University of Helsinki, Post Office Box 64, Helsinki 00014, Finland. [6]Istituto di Scienze dell'Atmosfera e del Clima–CNR, Bologna 40129, Italy. [7]Biogeochemistry Department, Max Planck Institute for Chemistry, Post Office Box 3060, D-55020 Mainz, Germany.

*To whom correspondence should be addressed. E-mail: daniel.rosenfeld@huji.ac.il

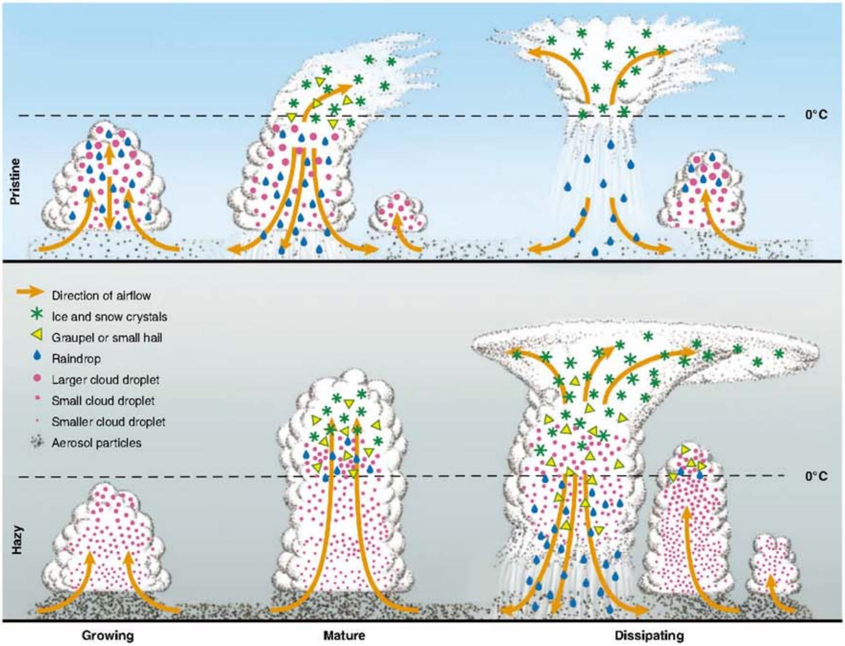

**Fig. 2.** Evolution of deep convective clouds developing in the pristine (top) and polluted (bottom) atmosphere. Cloud droplets coalesce into raindrops that rain out from the pristine clouds. The smaller drops in the polluted air do not precipitate before reaching the supercooled levels, where they freeze onto ice precipitation that falls and melts at lower levels. The additional release of latent heat of freezing aloft and reabsorbed heat at lower levels by the melting ice implies greater upward heat transport for the same amount of surface precipitation in the more polluted atmosphere. This means consumption of more instability for the same amount of rainfall. The inevitable result is invigoration of the convective clouds and additional rainfall, despite the slower conversion of cloud droplets to raindrops (*43*).

smoke from ship smokestacks in otherwise pristine clouds over the ocean (*17*). This created the expectation that polluted areas would suffer from reduced rainfall. On the other hand, it was expected that accelerating the conversion of cloud water to precipitation (i.e., increasing the autoconversion rate) by cloud seeding would enhance rainfall amounts. It turns out, however, that polluted areas are not generally drier, and rain enhancement by cloud seeding remains inconclusive (*18*, *19*).

With the advent of satellite measurements, it became possible to observe the larger picture of aerosol effects on clouds and precipitation. (We exclude the impacts of ice nuclei aerosols, which are much less understood than the effects of CCN aerosols.) Urban and industrial air pollution plumes were observed to completely suppress precipitation from 2.5-km-deep clouds over Australia (*20*). Heavy smoke from forest fires was observed to suppress rainfall from 5-km-deep tropical clouds (*21*, *22*). The clouds appeared to regain their precipitation capability when ingesting giant (>1 μm diameter) CCN salt particles from sea spray (*23*) and salt playas (*24*). These observations were the impetus for the World Meteorological Organization and the International Union of Geodesy and Geophysics to mandate an assessment of aerosol impact on precipitation (*19*). This report concluded that "it is difficult to establish clear causal relationships between aerosols and precipitation and to determine the sign of the precipitation change in a climatological sense. Based on many observations and model simulations the effects of aerosols on clouds are more clearly understood (particularly in ice-free clouds); the effects on precipitation are less clear."

A recent National Research Council report that reviewed "radiative forcing of climate change" (*25*) concluded that the concept of radiative forcing "needs to be extended to account for (1) the vertical structure of radiative forcing, (2) regional variability in radiative forcing, and (3) nonradiative forcing." It recommended "to move beyond simple climate models based entirely on global mean top of the atmosphere radiative forcing and incorporate new global and regional radiative and nonradiative forcing metrics as they become available." We propose such a new metric below.

## How Can Slowing the Conversion of Cloud Droplets to Raindrops Enhance Rainfall?

A growing body of observations shows that submicrometer CCN aerosols decrease precipitation from shallow clouds (*17*, *20*, *21*, *26*–*28*) and invigorate deep convective rain clouds with warm (> ~15°C) cloud base (*29*–*33*), although the impact on the overall rainfall amount is not easily detectable (*34*, *35*). These observations are supported by a large number of cloud-resolving model studies (*36*–*43*). The simulations also show that adding giant CCN to polluted clouds accelerates the autoconversion, mainly through nucleating large drops that rapidly grow into precipitation particles by collecting the other smaller cloud droplets (*44*). However, the autoconversion rate is not restored to that of pristine clouds (*42*).

Fundamentally, the amount of precipitation must balance the amount of evaporation at a global scale. Therefore, the consequence of aerosols suppressing precipitation from shallow clouds must be an increase in precipitation from deeper clouds. Such compensation can be accomplished not only at the global scale (*45*) but also at the cloud scale; that is, the clouds can grow to heights where aerosols no longer impede precipitation (*46*). All of this is consistent with the conceptual model shown in Fig. 2. This model suggests that slowing the rate of cloud droplet coalescence into raindrops (i.e., autoconversion) delays the precipitation of the cloud water, so that more water can ascend to altitudes where the temperature is colder than 0°C. Even if the total rainfall amount is not decreased by the increase in aerosols, delaying the formation of rain is sufficient to cause invigoration of cloud dynamics. By not raining early, the condensed water can form ice precipitation particles that release the latent heat of freezing aloft (*6*, *29*, *30*) and reabsorb heat at lower levels where they melt after falling.

The role of ice melting below the 0°C isotherm level in invigoration has been successfully modeled (*47*), although models also predict invigoration through increased aerosol loads even without ice processes (*43*). These model simulations suggest that the delay of early rain causes greater amounts of cloud water and rain intensities later in the life cycle of the cloud. The enhanced evaporative cooling of the added cloud water, mainly in the downdrafts, provides part of the invigoration by the mechanism of enhanced cold pools near the surface that push upward the ambient air. The greater cooling below and heating above lead to enhanced upward heat transport, both in absolute terms and normalized for the same amount of surface precipitation. The consumption of more convective available potential energy (CAPE) for the same rainfall amount would then be converted to an equally greater amount of released kinetic energy that could invigorate convection and lead to a greater convective overturning, more precipitation, and deeper depletion of the static instability (*6*). Simulations have shown that greater heating higher in the troposphere enhances the atmospheric circulation systems (*48*).

In clouds with bases near or above the 0°C isotherm, almost all the condensate freezes, even if it forms initially as supercooled raindrops in a low-CCN environment. Moreover, the slowing of the autoconversion rate by large concentrations of CCN can leave much of the cloud droplets airborne when strong updrafts thrust them above the homogeneous ice nucleation level of ~ –38°C, where they freeze into small ice particles that have no effective mechanism to coagulate and fall as precipitation. This phenomenon was observed by aircraft (*49*) and simulated for convective storms in west Texas (*50*) and the U.S. high plains (*51*). When the same simulation (*50*) was repeated with reduced CCN concentrations, the calculated rainfall amount increased substantially. The same model showed that adding small CCN aerosols in warm-base clouds has the opposite effect to that of cold-base clouds: increasing the precipitation amount by invigorating the convective overturning, while keeping the precipitation efficiency (i.e., surface precipitation divided by total cloud condensates) lower (*52*).

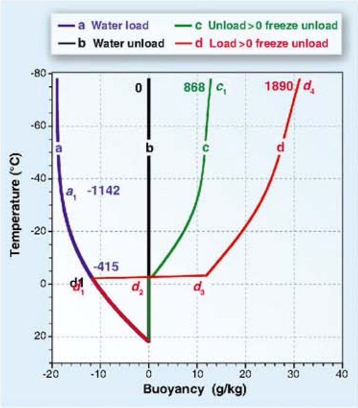

**Fig. 3.** The buoyancy of an unmixed adiabatically raising air parcel. The zero-buoyancy reference is the standard parcel: liquid water saturation, immediately precipitating all condensates without freezing (vertical line *b*). Cloud base is at 22°C and 960 hPa. The buoyancy of the following scenarios is shown: (*a*) suppressing rainfall and keeping all condensed water load, without freezing; (*b*) precipitating all condensed water, without freezing; (*c*) precipitating all condensates, with freezing at $T < -4$°C; (*d*) Suppressing precipitation until $T = -4$°C, and then freezing and precipitating all condensed water above that temperature. The released static energy (J $\text{kg}^{-1}$) with respect to reference line *b* is denoted by the numbers.

The invigoration due to aerosols slowing the autoconversion can be explained according to fundamental theoretical considerations of the pseudo-adiabatic parcel theory (Fig. 3). The CAPE measures the amount of moist static energy that is available to drive the convection. Its value is normally calculated with reference to a pseudo-adiabatic cloud parcel that rises while precipitating all its condensate in the form of rain, even at subfreezing temperatures.

Consider the case of a tropical air parcel that ascends from sea level with initial conditions of cloud base pressure of 960 hPa and temperature of 22°C. When not allowing precipitation, all the condensed water remains in the parcel and requires 415 J $\text{kg}^{-1}$ to rise to the height of the –4°C isotherm (point $d_1$ in Fig. 3), which is the highest temperature at which freezing can practically occur in the atmosphere. Freezing all the cloud water would warm the air and add thermal buoyancy by an amount that would almost exactly balance the condensate load ($d_2$). When the ice hydrometeors precipitate from a parcel, it becomes more positively buoyant because of its reduced weight ($d_3$), so that the released convective energy at the top of the cloud ($d_4$) is the largest. Specifically, it is greater by ~1000 J $\text{kg}^{-1}$ relative to the case where cloud water is precipitated as rain below the –4°C isotherm and as ice above that level ($c_1$). However, further delaying the conversion of cloud water into precipitation to greater heights above the 0°C level weakens the convection. In the extreme case of extending the suppression from the –4°C to the –36°C isotherm level ($a_1$), additional energy of 727 J $\text{kg}^{-1}$ is invested in lifting the condensates. There is no effective mechanism for precipitating cloud water that glaciated homogeneously into small ice particles. This would prevent the unloading of the parcel, taking up even more convective energy and further suppressing the convection and the precipitation. In reality, cloud parcels always mix with the environment, but this applies equally to all the scenarios in Fig. 3, so that qualitatively the contrasting aerosol effects remain the same. Although the idealized calculations here are useful to establish the concepts, the exact calculations require running three-dimensional models on the full life cycle of convective cloud systems, followed by validation with detailed observations.

The importance of the aerosol control of the released convective energy by adding as much as 1000 J $\text{kg}^{-1}$ can be appreciated by considering that CAPE averages ~1000 to 1500 J $\text{kg}^{-1}$ in the Amazon (*30*). Simulations of aerosols invigorating peak updrafts by 20% (*37*, *52*) are consistent with an increase of released convective energy by nearly 50%.

### Role of Radiative Versus Microphysical Aerosol Effects

Until now, the radiative and microphysical impacts of aerosols on the climate system have been considered separately and independently; their various, often conflicting, influences have not been amenable to quantitative weighting on the same scale. Given the opposing microphysical and radiative effects on the vigor and rainfall amounts of deep warm-base convective clouds, there is a need to assess the combined effects of these two factors (*25*).

A quantitative comparison between the strengths of the radiative and microphysical effects of the aerosols is presented in Fig. 4. Because optically active aerosols are larger than 0.05 μm in radius, and because mature pollution aerosols of this or larger size can act as CCN (*53*), CCN concentrations generally increase with aerosol optical thickness (AOT) (Fig. 1). The empirical relationship between AOT and CCN is shown in Fig. 4 by $\mathrm{AOT} = 0.0027 \times (\mathrm{CCN}_{0.4})^{0.64}$ (*1*), where $\mathrm{CCN}_{0.4}$ is the concentration of CCN active at a supersaturation of 0.4%. The cloud droplet concentration $N_c$ is proportional to $(\mathrm{CCN}_{0.4})^k$, where $k$ is typically smaller than 1. Using $k = 0.825$ relates 2000 cloud drops $\mathrm{cm}^{-3}$ to $10^4$ $\mathrm{CCN}_{0.4}$ $\mathrm{cm}^{-3}$, which corresponds to AOT = 1. The value of $k$ was inferred from Ramanathan *et al.* (*7*), although Freud *et al.* (*54*) imply that $k$ is closer to 1. In turn, $N_c$ was shown to be related to the depth above cloud base ($D$) required for onset of rain (*54*). This depth determines the thermodynamic track of the rising parcel (Fig. 3) and hence the vigor of the convection and the extent of convective overturning, which determines the rainfall amount produced by the cloud system throughout its life cycle. The cloudy parcel ascends along curve *a* in Fig. 3 as long as the cloud top has not reached $D$, and shifts to a track between curves *c* and *d* according to the amount of condensed water at that height.

The dependence of $D$ on CCN is obtained by a compilation of aircraft measurements (*27*, *54*, *55*) that provides an approximate relation of $D = 80 + (4 \times \mathrm{CCN}_{0.4})$. According to this relation, $\mathrm{CCN}_{0.4}$ should reach ~1200 $\mathrm{cm}^{-3}$ for preventing rainout from typical tropical clouds before reaching the practical freezing temperature of −4°C, which is at $D \approx 5$ km. At this point the invigoration effect is at its maximum, where the cloud parcel follows curve *d* in Fig. 3. Adding CCN beyond this point suppresses the vigor of the convection by shifting the cloud parcel gradually from curve *d* to curve *a* in Fig. 3. This means that the microphysical effect on invigorating the convection has a maximum at moderate CCN concentrations. This maximum becomes smaller for cooler-base clouds, where the distance to the freezing level is shorter, so that fewer CCN are sufficient to suppress the onset of rain up to that level.

At the point of strongest microphysical invigoration, AOT is still at the modest value of ~0.25. Added aerosols increase the AOT and reduce the flux of solar energy to the surface, which energizes convection. As a result, with increasing aerosol loads beyond the optimum, the weakening of the microphysical invigoration is reinforced by the suppressive effect of reduced surface heating.

The interplay between the microphysical and radiative effects of the aerosols may explain the observations of Bell *et al.* (*33*), who showed that the weekly cycle of air pollution aerosols in the southeastern United States is associated with a weekday maximum and weekend minimum in the intensity of afternoon convective rainfall during summer. This was mirrored by a minimum in the midweek rainfall over the adjacent sea areas, reflecting an aerosol-induced modulation of the monsoonal convergence of air and its rising over land with return flow aloft to the ocean. This is a remarkable finding, as it suggests that the microphysical impacts of aerosols on invigorating warm-base deep clouds are not necessarily at the expense of other clouds in the same region, but can lead to changes in regional circulation that lead to greater moisture convergence and regional precipitation.

This weekly cycle emerged in the late 1980s and strengthened through the 1990s, along with the contemporary reversal of the dimming trend of solar radiation reaching the surface, which took place until the 1980s (*56*). This was likely caused by the reversal in the emissions trends of sulfates and black carbon (*57*). It is possible that the weekly cycle emerged when the overall aerosol levels decreased to the range where the microphysical impacts are dominant, as shown in Fig. 4.

### Measuring Radiative and Microphysical Aerosol Effects with the Same Metric

The precipitation and the radiative effects of the aerosols (both direct and cloud-mediated) can be integrally measured when considering the combined changes in the energy of the atmosphere and the surface. The commonly used metrics are the radiative forcing at the top of the atmosphere (TOA) and at the BOA (bottom of the atmosphere, i.e., Earth's surface), measured in W $\mathrm{m}^{-2}$. The atmospheric radiative forcing is the difference between TOA and BOA forcing (*7*). Here we propose a new metric, the aerosol thermodynamic forcing (TF) (*58*), representing the aerosol-induced change in the atmospheric energy budget that is not radiative in nature. In contrast to TOA radiative forcing, TF does not change the net Earth energy budget, but rather redistributes it internally; hence, TF can affect temperature gradients and atmospheric circulation. The main source of TF is the change in the amount of latent heat released by aerosol-induced changes in clouds and precipitation. It can be expressed as a change in latent heat flux (in units of W $\mathrm{m}^{-2}$) in the atmospheric column.

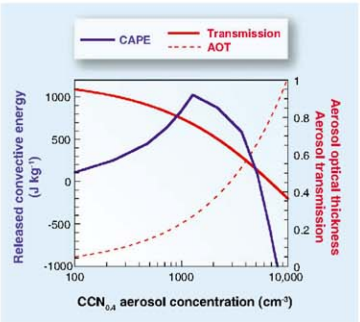

**Fig. 4.** Illustration of the relations between the aerosol microphysical and radiative effects. The aerosol optical thickness (AOT) is assumed to reach 1 at $\mathrm{CCN}_{0.4} = 10^4$ $\mathrm{cm}^{-3}$ (dashed red line), which corresponds to nucleation of 2000 cloud drops $\mathrm{cm}^{-3}$. The related transmission of radiation reaching the surface is shown by the solid red line. The vigor of the convection is shown by the blue line, which provides the released convective available potential energy (CAPE) of a cloud parcel that ascends to the cloud top near the tropopause. The calculation is based on the scheme in Fig. 3, with respect to curve *c* as the zero reference. Note that a maximum in CAPE occurs at $\mathrm{CCN}_{0.4} \approx 1200$ $\mathrm{cm}^{-3}$, which corresponds to the maximum cloud invigoration according to curve *d* of the scheme in Fig. 3. The AOT corresponding to the $\mathrm{CCN}_{0.4}$ at the microphysical optimum is only 0.25. Adding aerosols beyond this point substantially decreases the vigor of the cloud because both microphysical and radiative effects work in the same direction: smaller release of convective energy aloft and less radiative heating at the surface.

The vertical distribution of the atmospheric heating is critically important because it determines the vertical lapse rate and hence the CAPE, which quantifies the ability to produce convective clouds and precipitation. Atmospheric radiative heating due to absorbing aerosols tends to reduce CAPE and thereby suppress the development of convective clouds, whereas the microphysical effects of aerosols allow a deeper exploitation of CAPE and hence invigoration of convection and associated precipitation.

All the components of the aerosol radiative (direct and cloud-mediated) and thermodynamic forcing and the resulting changes in CAPE can now be quantified as energy flux perturbations in units of $W\ m^{-2}$. Consider the example of smoke changing tropical convection from thermodynamic path *c* to path *d* in Fig. 3. At the end of the convective cycle, an additional $1000\ J\ kg^{-1}$ are depleted from CAPE relative to convection under pristine conditions. The resultant increased convective overturning is likely to produce more rainfall and increase the temperature by converting more latent heat into sensible heat, at a rate of $29\ W\ m^{-2}$ for each added millimeter of rainfall during 24 hours. This can be considered as a cloud-mediated TF of aerosols, which works to enhance rainfall and accelerate the hydrological cycle, resulting in a positive sign for TF. On the other hand, if the smoke becomes very thick, its radiative impact would be to reduce surface latent and sensible heating and warm the mid-troposphere. For example, an AOT of 1 induces a BOA forcing of $-45\ W\ m^{-2}$ in the Amazon (*5*). This stabilization of the atmosphere would cause less convection and depletion of CAPE, less rainfall, and a resulting deceleration of the hydrological cycle (*7*). Furthermore, too much aerosol can suppress the precipitation-forming processes to the extent of changing from thermodynamic path *d* to path *a* in Fig. 3 (see also Fig. 4), hence reversing the cloud-mediated TF of aerosols from positive to negative, adding to the negative radiative forcing.

Thermodynamic forcing can occur even without changing the surface rainfall: The energy change when polluted clouds develop along track *d* in Fig. 3, with respect to the pristine reference state shown in track *c*, would be defined as TF. In this case, the TF solely due to added release of latent heat of freezing is $2.44\ W\ m^{-2}\ mm^{-1}\ day^{-1}$ of heating above the freezing level and the same amount of cooling due to melting below the melting level. This is a net vertical redistribution of latent heat. For an area-average rainfall of $20\ mm\ day^{-1}$, the TF scales to $48.8\ W\ m^{-1}$. In addition, we should consider the thermodynamic consequences of the aerosol-induced added rainfall due to increased convective overturning. This would convert latent heat to sensible heat at a rate of $29\ W\ m^{-2}\ mm^{-1}\ day^{-1}$. Such deeper consumption of CAPE would require a longer time for the atmosphere to recover for the next convective cycle, representing a temporal redistribution of heating and precipitation.

### Concluding Thoughts

The next challenge will be to map the radiative and cloud-mediated thermodynamic forcing of the aerosols in the parameter space of AOT versus CCN. The good correlation between AOT and CCN means that, at least at large scales, the radiative and microphysical effects of aerosols on cloud physics are not free to vary independently (*1*), and hence mainly the diagonal of the parameter space is populated.

According to Fig. 4, there should be an optimum aerosol load in the tropical atmosphere that should lead to the most positive aerosol thermodynamic forcing, manifested as the most vigorous convection. This optimum probably occurs at $AOT \approx 0.25$ and $CCN_{0.4} \approx 1200\ cm^{-3}$. Remarkably, these fundamental considerations for $AOT \approx 0.25$ for optimal cloud development were matched recently by observations in the Amazon (*59*).

This hypothesis reconciles the apparent contradictory reports that were reviewed in two major assessments (*18, 19*) as impeding our overall understanding of cloud-aerosol impacts on precipitation and the climate system. The main cause for the previous uncertainties was the nonmonotonic character of competing effects, which is inevitable in a system that has an optimum. The new conceptual model outlined here improves our understanding and ability to simulate present and future climates. It also has implications for intentional weather and climate modification, which are being considered in the context of cloud seeding for precipitation enhancement and geoengineering. Testing this hypothesis is planned within the Aerosol Cloud Precipitation Climate (ACPC) initiative (*60, 61*).

### References and Notes

1. M. O. Andreae, *Atmos. Chem. Phys. Discuss.* **8**, 11293 (2008).
2. M. O. Andreae, *Science* **315**, 50 (2007).
3. U. Lohmann, J. Feichter, *Atmos. Chem. Phys.* **5**, 715 (2005).
4. V. Ramanathan *et al.*, *Proc. Natl. Acad. Sci. U.S.A.* **102**, 5326 (2005).
5. I. Koren, Y. J. Kaufman, L. A. Remer, J. V. Martins, *Science* **303**, 1342 (2004).
6. D. Rosenfeld, *Space Sci. Rev.* **125**, 149 (2006).
7. V. Ramanathan, P. J. Crutzen, J. T. Kiehl, D. Rosenfeld, *Science* **294**, 2119 (2001).
8. S. Menon, J. Hansen, L. Nazarenko, Y. F. Luo, *Science* **297**, 2250 (2002).
9. C. Wang, *J. Geophys. Res.* **109**, D03106 (2004).
10. Y. Rudich, A. Sagi, D. Rosenfeld, *J. Geophys. Res.* **108**, 10.1029/2003JD003472 (2003).
11. R. L. Miller, I. Tegen, J. Perlwitz, *J. Geophys. Res.* **109**, D04203 (2004).
12. L. D. Rotstayn, U. Lohmann, *J. Geophys. Res.* **107**, 10.1029/2002JD002128 (2002).
13. I. M. Held, T. L. Delworth, J. Lu, K. L. Findell, T. R. Knutson, *Proc. Natl. Acad. Sci. U.S.A.* **102**, 17891 (2005).
14. W. Cotton, R. Pielke, *Human Impacts on Weather and Climate* (Cambridge Univ. Press, Cambridge, 2007).
15. R. Gunn, B. B. Phillips, *J. Meteorol.* **14**, 272 (1957).
16. P. Squires, *Tellus* **10**, 256 (1958).
17. L. F. Radke, J. A. Coakley Jr., M. D. King, *Science* **246**, 1146 (1989).
18. National Research Council, *Critical Issues in Weather Modification Research* (National Academies Press, Washington, DC, 2003).
19. Z. Levin, W. Cotton, *Aerosol Pollution Impact on Precipitation: A Scientific Review. Report from the WMO/IUGG International Aerosol Precipitation Science Assessment Group (IAPSAG)* (World Meteorological Organization, Geneva, Switzerland, 2007).
20. D. Rosenfeld, *Science* **287**, 1793 (2000).
21. D. Rosenfeld, *Geophys. Res. Lett.* **26**, 3105 (1999).
22. D. Rosenfeld, W. L. Woodley, in *Cloud Systems, Hurricanes, and the Tropical Rainfall Measuring Mission (TRMM)*, W.-K. Tao, R. Adler, Eds. (American Meteorological Society, Boston, 2003), pp. 59–80.
23. D. Rosenfeld, R. Lahav, A. Khain, M. Pinsky, *Science* **297**, 1667 (2002); published online 15 August 2002 (10.1126/science.1073869).
24. Y. Rudich, O. Khersonsky, D. Rosenfeld, *Geophys. Res. Lett.* **29**, 10.1029/2002GL016055 (2002).
25. National Research Council, *Radiative Forcing of Climate Change: Expanding the Concept and Addressing Uncertainties* (National Academies Press, Washington, DC, 2005).
26. D. Rosenfeld, Y. J. Kaufman, I. Koren, *Atmos. Chem. Phys.* **6**, 2503 (2006).
27. D. Rosenfeld *et al.*, *J. Geophys. Res.* **113**, D15203 (2008).
28. M. O. Andreae *et al.*, *Science* **303**, 1337 (2004).
29. J. Molinié, C. A. Pontikis, *Geophys. Res. Lett.* **22**, 1085 (1995).
30. E. Williams *et al.*, *J. Geophys. Res.* **107**, 10.1029/2001JD000380 (2002).
31. I. Koren, Y. J. Kaufman, D. Rosenfeld, L. A. Remer, Y. Rudich, *Geophys. Res. Lett.* **32**, L14828 (2005).
32. J. C. Lin, T. Matsui, R. A. Pielke Sr., C. Kummerow, *J. Geophys. Res.* **111**, D19204 (2006).
33. T. L. Bell *et al.*, *J. Geophys. Res.* **113**, D02209 (2008).
34. D. M. Schultz, S. Mikkonen, A. Laaksonen, M. B. Richman, *Geophys. Res. Lett.* **34**, L22815 (2007).
35. T. Bell, D. Rosenfeld, *Geophys. Res. Lett.* **35**, L09803 (2008).
36. A. Khain, A. Pokrovsky, M. Pinsky, A. Seifert, V. Phillips, *J. Atmos. Sci.* **61**, 2963 (2004).
37. A. Khain, D. Rosenfeld, A. Pokrovsky, *Q. J. R. Meteorol. Soc.* **131**, 2639 (2005).
38. B. H. Lynn *et al.*, *Mon. Weather Rev.* **133**, 59 (2005).
39. C. Wang, *J. Geophys. Res.* **110**, D21211 (2005).
40. S. C. van den Heever, G. G. Carrió, W. R. Cotton, P. J. DeMott, A. J. Prenni, *J. Atmos. Sci.* **63**, 1752 (2006).
41. A. Seifert, K. D. Beheng, *Meteorol. Atmos. Phys.* **92**, 67 (2006).
42. A. Teller, Z. Levin, *Atmos. Chem. Phys.* **6**, 67 (2006).
43. W. K. Tao *et al.*, *J. Geophys. Res.* **112**, D24S18 (2007).
44. D. B. Johnson, *J. Atmos. Sci.* **39**, 448 (1982).
45. U. Lohmann, *Atmos. Chem. Phys.* **8**, 2115 (2008).
46. E. R. Graber, Y. Rudich, *Atmos. Chem. Phys.* **6**, 729 (2006).
47. V. T. J. Phillips, A. Pokrovsky, A. Khain, *J. Atmos. Sci.* **64**, 338 (2007).
48. M. W. DeMaria, *J. Atmos. Sci.* **42**, 1944 (1985).
49. D. Rosenfeld, W. L. Woodley, *Nature* **405**, 440 (2000).
50. A. P. Khain, D. Rosenfeld, A. Pokrovsky, *Geophys. Res. Lett.* **28**, 3887 (2001).
51. Z. Cui, K. S. Carslaw, Y. Yin, S. Davies, *J. Geophys. Res.* **111**, D05201 (2006).
52. A. P. Khain, N. BenMoshe, A. Pokrovsky, *J. Atmos. Sci.* **65**, 1721 (2008).
53. U. Dusek *et al.*, *Science* **312**, 1375 (2006).
54. E. Freud, D. Rosenfeld, M. O. Andreae, A. A. Costa, P. Artaxo, *Atmos. Chem. Phys.* **8**, 1661 (2008).
55. M. C. VanZanten, B. Stevens, G. Vali, D. H. Lenschow, *J. Atmos. Sci.* **62**, 88 (2005).
56. M. Wild *et al.*, *Science* **308**, 847 (2005).
57. D. G. Streets, Y. Wu, M. Chin, *Geophys. Res. Lett.* **33**, L15806 (2006).
58. The term "thermodynamic aerosol effect" was first mentioned in (*25*), but in a more restrictive context.
59. I. Koren, J. V. Martins, L. A. Remer, H. Afargan, *Science* **321**, 946 (2008).
60. B. Stevens, *iLEAPS Newsletter* **5**, 10 (2008).
61. The Aerosol Cloud Precipitation Climate (ACPC) initiative is a joint initiative by the International Geosphere/Biosphere Programme (IGBP) core projects Integrated Land Ecosystem/Atmosphere Process Study (iLEAPS) and International Global Atmospheric Chemistry (IGAC) and the World Climate Research Programme (WCRP) project Global Energy and Water Cycle Experiment (GEWEX).
62. This paper resulted from discussions held during an ACPC workshop hosted and supported by the International Space Science Institute, Bern, Switzerland, through its International Teams Program.

10.1126/science.1160606

# Shadow Enhancers as a Source of Evolutionary Novelty

Joung-Woo Hong, David A. Hendrix, Michael S. Levine*

The dorsal-ventral patterning of the early *Drosophila* embryo is controlled by a sequence-specific transcription factor, Dorsal, which is related to mammalian NF-κB (*1*). Dorsal works in concert with two additional transcription factors, Twist and Snail, to regulate gene expression in the early embryo. Chromatin immunoprecipitation (ChIP)–chip assays identified a few hundred binding clusters for Dorsal, Twist, and Snail scattered throughout the *Drosophila* genome (*2*). Over 35 of these clusters function as authentic enhancers when tested in transgenic embryos.

ChIP-chip assays predicted that many of the Dorsal target genes contain two separate enhancers for the same or similar expression pattern. This prediction was experimentally confirmed for *vnd* and *miR-1* (*2*). *vnd* contains two enhancers that mediate expression in the presumptive neurogenic ectoderm, whereas *miR-1* contains at least two enhancers for expression in the ventral mesoderm. In both cases, the secondary enhancers map within 5 kb of the transcription start site.

However, some of the potential secondary enhancers identified by the ChIP-chip assays are predicted to map quite far from Dorsal target genes. For example, *brinker* (*brk*) is regulated by a known enhancer located in the 5′ flanking region (*3*). A potential secondary enhancer maps within the intron of a neighboring gene, *Atg5*, located ~13 kb downstream of the *brk* transcription start site. A ~1-kb genomic DNA fragment encompassing the *Atg5* intron was tested for enhancer activity in transgenic embryos (Fig. 1A). It directs broad lateral stripes of lacZ reporter gene expression, similar to the endogenous *brk* expression pattern that is recapitulated by the previously identified 5′ enhancer.

A similar situation is seen for the Dorsal target gene, *sog*. Bioinformatics methods identified an intronic enhancer that recapitulates the normal *sog* expression pattern in the presumptive neurogenic ectoderm (*3*). ChIP-chip assays identified this enhancer, as well as a second cluster of Dorsal, Twist, and Snail binding sites located 20 kb 5′ of the *sog* transcription start site, downstream of a neighboring gene (Fig. 1B). The newly identified binding cluster generates broad lateral stripes of gene expression in transgenic embryos, similar to those produced by the intronic enhancer. The secondary enhancers identified in this study are almost certainly dedicated to the regulation of *brk* and *sog* transcription units because the associated genes, *Atg5* and *CG8117*, respectively, are not significantly expressed in the early embryo (Fig. 1 and fig. S1).

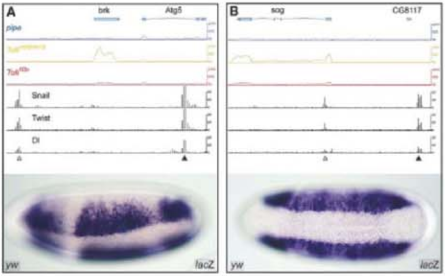

**Fig. 1.** Identification of shadow enhancers. **(A)** Genome browser showing the *Brinker* locus (*brk*) and neighboring gene *Atg5* (http://flybuzz.berkeley.edu/cgi-bin/gbrowse/fly4_3/). The first three lines from the top—blue, yellow, and red—show the levels of steady-state RNAs in the *pipe*, *Toll*$^{rm9/rm10}$, and *Toll*$^{10b}$ mutants, respectively (*7*). *brk* transcripts are absent in *pipe* and *Toll*$^{10b}$ mutants but present in *Toll*$^{rm9/rm10}$ mutants. *Atg5* is inactive in all mutants, suggesting that the intronic enhancer is dedicated to *brk* regulation. The last three lines show the distributions of Snail, Twist, and Dorsal (Dl) based on whole-genome ChIP-chip assays (*2*). The leftmost cluster (open arrowhead) coincides with the known, primary enhancer in the 5′ flanking region. A second cluster (solid arrowhead) is detected 13 kb downstream of the *brk* transcription start site within *Atg5*. An ~1-kb genomic DNA fragment encompassing the 3′ binding cluster (shadow enhancer) was tested in transgenic embryos (solid arrowhead). The 5′ enhancer was tested previously (*3*). Both fragments function as authentic enhancers to generate lateral stripes of gene expression in the neurogenic ectoderm. **(B)** Same as (A) except that the *sog* locus is shown. *sog* transcripts are predominantly detected in *Toll*$^{rm9/rm10}$ mutants where the gene is fully active (see the blue, yellow, and red lines, which show the results of the whole-genome tiling arrays). ChIP-chip assays identify two clusters of Dorsal, Twist, and Snail binding sites within intron 1 and 3′ of the neighboring gene, *CG8117*. Both genomic DNA fragments function as authentic enhancers to direct lateral stripes of gene expression. Gene prediction models are displayed above each graphical presentation. Each 3′ end is indicated by a triangle.

ChIP-chip assays suggest that as many as one-third or even one-half of all Dorsal target genes might be regulated by secondary enhancers (*2*). We propose the term "shadow enhancer" for remote secondary enhancers mapping far from the target gene and mediating activities overlapping the primary enhancer. Phylogenetic comparisons suggest that the *brk* and *sog* shadow enhancers are evolving more rapidly than the primary enhancers mapping within or near the two genes (figs. S2 and S3). Despite these different rates of divergence, the overall structures of the shadow enhancers are clearly related to their respective primary enhancers (fig. S4). Given the conservation of the shadow enhancers in all 12 sequenced drosophilids, it is likely that they are essential for fitness.

Why are Dorsal target genes regulated by shadow enhancers? They might help ensure precise and reproducible patterns of gene expression during embryogenesis. It is possible that shadow enhancers are pervasively used in animal development. For example, the mouse *sonic hedgehog* gene is regulated in the floorplate of the embryonic neural tube by two separate enhancers with slightly distinct activities (*4*). Shadow enhancers can explain why deletions of well-defined enhancers sometimes produce no apparent mutant phenotypes [e.g., (*5*)]. We suggest that shadow enhancers might arise from duplication, comparable to the duplication and divergence of protein-coding sequences.

The evolution of cis-regulatory DNAs is a major mechanism of animal diversity [e.g., (*6*)]. However, there is the potential problem that such change could compromise essential genetic activities. Shadow enhancers have the potential to evolve novel binding sites and achieve new regulatory activities without disrupting the core patterning functions of critical developmental control genes.

### References and Notes

1. A. Stathopoulos *et al.*, *Cell* **111**, 687 (2002).
2. J. Zeitlinger *et al.*, *Genes Dev.* **21**, 385 (2007).
3. M. Markstein *et al.*, *Proc. Natl. Acad. Sci. U.S.A.* **99**, 763 (2002).
4. Y. Jeong *et al.*, *Development* **133**, 761 (2006).
5. N. Xiong, C. Kang, D. H. Raulet, *Immunity* **16**, 453 (2002).
6. S. Jeong *et al.*, *Cell* **132**, 783 (2008).
7. F. Biemar *et al.*, *Proc. Natl. Acad. Sci. U.S.A.* **103**, 12763 (2006).
8. This study was funded by the NIH (GM46638) and the Moore Foundation.

### Supporting Online Material

www.sciencemag.org/cgi/content/full/321/5894/1314/DC1
Materials and Methods
Figs. S1 to S4
Tables S1 to S3
References and Notes

19 May 2008; accepted 2 July 2008
10.1126/science.1160631

---

Department of Molecular and Cell Biology, Division of Genetics, Genomics, and Development, Center for Integrative Genomics, University of California, Berkeley, CA 94720, USA.

*To whom correspondence should be addressed. E-mail: mlevine@berkeley.edu

# The Crystal Structure of a Mammalian Fatty Acid Synthase

Timm Maier, Marc Leibundgut, Nenad Ban*

**Mammalian fatty acid synthase is a large multienzyme that catalyzes all steps of fatty acid synthesis. We have determined its crystal structure at 3.2 angstrom resolution covering five catalytic domains, whereas the flexibly tethered terminal acyl carrier protein and thioesterase domains remain unresolved. The structure reveals a complex architecture of alternating linkers and enzymatic domains. Substrate shuttling is facilitated by flexible tethering of the acyl carrier protein domain and by the limited contact between the condensing and modifying portions of the multienzyme, which are mainly connected by linkers rather than direct interaction. The structure identifies two additional nonenzymatic domains: (i) a pseudo-ketoreductase and (ii) a peripheral pseudo-methyltransferase that is probably a remnant of an ancestral methyltransferase domain maintained in some related polyketide synthases. The structural comparison of mammalian fatty acid synthase with modular polyketide synthases shows how their segmental construction allows the variation of domain composition to achieve diverse product synthesis.**

Fatty acids fulfill a variety of vital functions: They are central constituents of biological membranes, serve as energy storage compounds, and act as second messengers or as covalent modifiers governing the localization of proteins. In bacteria and plants, fatty acid biosynthesis is accomplished by a series of monofunctional proteins in a dissociated type II fatty acid synthase (FAS) system (*1*). In contrast, the type I FASs of fungi and animals are huge multifunctional polypeptides that integrate all steps of fatty acid synthesis into large macromolecular assemblies. Fungal FAS is a 2.6-MD $\alpha_6\beta_6$-heterododecamer with the catalytic domains distributed over two polypeptides (*2*–*4*), whereas mammalian FAS (mFAS) consists of a 270-kD polypeptide chain (comprising all seven required domains) that assembles into homodimers for enzymatic activity (*5*, *6*).

Despite this variation in structural organization, all organisms employ a conserved set of chemical reactions for fatty acid biosynthesis (*1*, *6*–*8*). Stepwise elongation of precursors is achieved by cyclic decarboxylative condensation of acyl-coenzyme A (CoA) with the elongation substrate malonyl-CoA, initiated by the starter substrate acetyl-CoA. In the priming step, the acetyl transferase loads acetyl-CoA onto the terminal thiol of the phosphopantheteine cofactor of the acyl carrier protein (ACP), which passes the acetyl moiety over to the active site cysteine of the β-ketoacyl synthase (KS). Malonyl transferase (MT) transfers the malonyl group of malonyl-CoA to ACP, and the KS catalyzes the decarboxylative condensation of the acetyl and malonylmoieties to an ACP-bound β-ketoacyl intermediate. The β-carbon position is then modified by sequential action of the NADPH (the reduced form of nicotinamide adenine dinucleotide, $NADP^+$)–dependent β-ketoreductase (KR), a dehydratase (DH), and the NADPH-dependent enoyl reductase (ER) to yield a saturated acyl product elongated by two carbon units. This acyl group functions as a starter substrate for the next round of elongation, until the growing fatty acid chain reaches a length of 16 to 18 carbon atoms and is released from ACP. In mFAS, the malonyl and acetyl transferase reactions are catalyzed by a single bifunctional protein domain, the malonyl-acetyl transferase (MAT), and the products are released from ACP as free fatty acids by a thioesterase (TE) domain (*6*).

Humans eating a typical Western diet take in a surplus of fatty acids. Consequently, de novo fatty acid biosynthesis and FAS activity are low in most body tissues. However, FAS is overexpressed in many cancer cells, and its expression level is correlated with tumor malignancy (*9*). FAS inhibitors have demonstrated anti-tumor activity in vivo and in vitro, and in recent years FAS has emerged as an important drug target for the treatment of human cancer (*10*, *11*). The medical use of FAS inhibitors has been hampered by off-target activities. Recently, more specific inhibitors of type I FAS have been described (*12*) and remain to be tested.

Currently, high-resolution structures are known for all components of bacterial (*1*) and fungal FAS (*2*, *4*, *13*), whereas the structural information for mFAS is limited to high-resolution structures for the isolated MAT [Protein Data Bank (PDB) entry 2jfd], ACP (*14*, *15*), and TE domains (*16*, *17*) and a domain architecture model based on a 4.5 Å resolution x-ray crystallographic map (*5*). Structure determination of KS–acyl transferase didomain fragments and KR domains of polyketide synthases (PKS) (*18*–*21*)—large modular megasynthases involved in the microbial synthesis of a number of bioactive compounds and drugs—has confirmed the anticipated close structural relation between mFAS and PKS modules (*6*, *22*). Here, we present the crystal structure of mFAS in its free and $NADP^+$-bound states, in which the flexibly tethered C-terminal ACP/TE domains (*23*) remain unresolved.

## Overall Structure and Topology

The crystal structures of natively purified mFAS from pigs, free and in complex with the cofactor $NADP^+$, have been determined at 3.2 and 3.3 Å resolution and refined to $R/R_{\text{free}}$ values of 0.22/0.26 and 0.19/0.24, respectively (where $R/R_{\text{free}}$ are $\Sigma|F_{\text{obs}}(h) - F_{\text{calc}}(h)|\Sigma F_{\text{obs}}(h)$ calculated for the working/test set of reflections). Diffraction data were affected by anisotropy with one weaker direction of reciprocal space (*24*). mFAS assembles into an intertwined dimer approximating an "X" shape (Fig. 1A). This structure agrees well with our previous architectural model at intermediate resolution (*5*) and additionally provides the connectivities of domains, the detailed features of active sites, and the nature of linking sequences outside the conserved core domains. mFAS is segregated into a lower condensing portion, containing the condensing KS and the MAT domains, and an upper portion including the DH, ER, and KR domains responsible for β-carbon modification (Fig. 1, A and B). Two additional nonenzymatic domains are located at the periphery of the modifying part. The first of these domains is homologous to the methyltransferase family and is thus named "pseudo-methyltransferase" (ΨME). The second represents a truncated KR fold dimerizing with the catalytic KR domain and is referred to as "pseudo-ketoreductase" (ΨKR). The condensing and modifying parts of mFAS are loosely connected and form only tangential contacts. The structural organization of domains deviates dramatically from their linear arrangement in sequence (Fig. 1, A and C).

The two polypeptides dimerize through an extended contact area of 5400 $Å^2$, which involves more than 150 residues per chain (table S2). The main contributions to this interface arise from homophilic interactions of the KS and ER domains, with areas of ~2600 and 1600 $Å^2$, which resemble the dimer organization of monofunctional homologs (*25*, *26*). Additional dimer contacts (800 $Å^2$) are provided by the DH domain through homophilic interactions between the double "hot dog" folds via a loop around residue 941. The remaining interactions are formed by the C-terminal part of the linker region between the MAT and DH domains (residues 846 to 860) with the KS domain of the other chain (400 $Å^2$).

## Interdomain Linking and Interaction

The characteristics of multienzyme complexes are to a great degree determined by the nature of

---

Institute of Molecular Biology and Biophysics, ETH Zurich, 8092 Zurich, Switzerland.

*To whom correspondence should be addressed. E-mail: ban@mol.biol.ethz.ch

the interactions and linking of functional subunits. Notably, animal FAS invests only ~9% of its total sequence for linkers (Fig. 2, A to E) and an additional 16% for the lateral noncatalytic ΨME and ΨKR domains (Fig. 1A). No scaffolding insertions are found in the catalytic cores. This is in contrast to the fungal FAS, the other megasynthase for which a high-resolution structure is available (*2*, *4*, *13*). In that multienzyme, almost 50% of the total sequence forms a complex structural matrix of numerous inter- and intradomain insertions, which define the spatial organization of the catalytic domains. The only structured linker domain in mFAS connects the KS and MAT domains [KS-MAT linker domain (Fig. 2A)] and is composed of amino acids 420 to 490 between KS and MAT and of residues 809 to 837 joining MAT and DH. It includes two short α-helices facing the KS and a three-stranded antiparallel β sheet on the MAT side and acts as an adapter, preventing any direct interaction between the KS and MAT domains. Similar linker domains were recently found in the KS–acyl transferase didomain structures of two PKS modules (*18*, *21*). Although an additional helix is inserted in the PKS linker domains (fig. S1), the relative positions of the transferase and KS domains remain essentially the same in mFAS and PKS (fig. S2).

The connection between the condensing and modifying part of mFAS is provided by residues 838 to 858 between the KS-MAT linker domain and the DH domain (Fig. 2, D and E). Again, the conformation and position of this linker closely resembles those observed in KS-acyl transferase didomain structures from PKS modules, even though these didomains are derived from modules with a considerably different sequence context, containing only KR domains for β-carbon modification (*18*, *21*). Besides the linker itself, only very limited contacts are formed between the condensing and modifying parts of mFAS (with an interaction area of 230 Å$^2$). It is even possible that some percentage of molecules in the crystal have an alternative connectivity between the two parts (equivalent to a rotation of the upper portion of the molecule), which would escape detection by crystallographic methods (figs. S3 and S4).

The KR domain acts as a central connector for the modifying part of mFAS and interacts with the DH, ER, and noncatalytic ΨME and ΨKR domains (Fig. 3, A and B, and table S3). In contrast, neither the DH nor the ER domain interacts with either of the noncatalytic domains, and the contact between the DH and ER domains is very weak. The KR domain interacts with the second hot dog subdomain of DH, forming an 800 Å$^2$ interface. The contact between KR and ER is less intricate and extends over an area of 400 Å$^2$. About 10% (or 1100 Å$^2$) of the KR surface is involved in a contact with the ΨKR domain, mimicking one of the two major dimerization interfaces observed in the tetrameric KR of bacteria (fig. S5). The ΨME, which has the highest mobility based on atomic displacement parameter analysis (fig. S6), protrudes from the mostly planar body of mFAS. It is docked via interactions with the KR and the ΨKR domain, the former providing 20% (200 Å$^2$) and the latter 80% (800 Å$^2$) of the docking area.

Most of the linker regions in the modifying domains are solvent exposed (Fig. 2). An important exception is β strand–forming regions at the N terminus of the ΨKR-ER linker (residues 1513 to 1518) and the C terminus of the DH2-ΨME linker (residues 1117 to 1123). These are buried between the KR, ΨKR, and ΨME domains and have an important structural role, as discussed in the next paragraph (Fig. 2C).

### The Nonenzymatic Domains

The KR character of the mFAS ΨKR domain, which has approximately half the size of the active KR domain, is maintained only in the

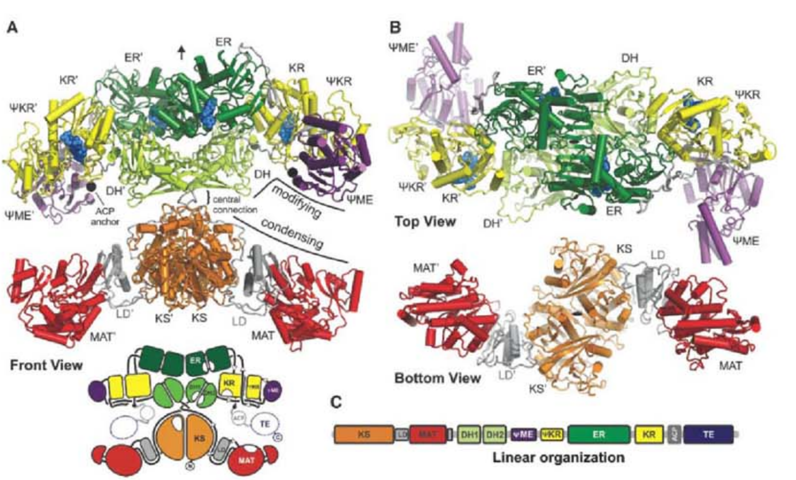

**Fig. 1.** Structural overview. **(A)** Cartoon representation of mFAS, colored by domains as indicated. Linkers and linker domains are depicted in gray. Bound NADP$^+$ cofactors and the attachment sites for the disordered C-terminal ACP/TE domains are shown as blue and black spheres, respectively. The position of the pseudo-twofold dimer axis is depicted by an arrow; domains of the second chain are indicated by an appended prime. The lower panel (front view) shows a corresponding schematic diagram. **(B)** Top (upper panel) and bottom (lower panel) views, demonstrating the "S" shape of the modifying (upper) and condensing (lower) parts of mFAS. The pseudo-twofold axis is indicated by an ellipsoid. **(C)** Linear sequence organization of mFAS, at approximate sequence scale.

conserved dimerization interface. Because of extensive truncation of its core, it has lost the ability to bind NADPH. Consequently, the ΨKR domain functions mainly to support the integrity of the active site of the catalytic KR domain. The KR/ΨKR arrangement closely resembles the structure of a KR-ΨKR domain derived from 6-deoxyerythronolide B synthase (DEBS) PKS module 1 (*19*) (Fig. 3A). The mFAS ΨKR domain lacks the two N-terminal sheet-helix windings of the DEBS1 ΨKR, which itself is already shorter than the catalytically active KR fold (Fig. 3A). Because of the insertion of the ER and ΨME domains into the KR-ΨKR fold, two β strands originally formed by the linkers flanking the KR and ΨKR domains are no longer directly adjacent to these two domains in the mFAS sequence. Rather, they are provided by amino acid stretches leading from the DH2 into the ΨME domain, 300 amino acids upstream of the ΨKR, and the linker between ΨKR and ER, separated by 360 residues from the KR domain (Fig. 3C).

The ΨME domain is structurally closely related to *S*-adenosyl-methionine (SAM)–dependent methyltransferases, in spite of low sequence homology (fig. S7A and table S4). The core of these enzymes consists of a seven-stranded β sheet with three helices on each side and the C-terminal strand in anti-parallel orientation (*27*). The methyltransferase fold of mFAS carries an additional short β strand and three helices at its N terminus (residues 1125 to 1224). At its C terminus, a short linker (residues 1407 to 1413) leads directly into the adjacent ΨKR fold. Such a topology is characteristic of small-molecule (including lipid) methyltransferases (*27*). Nevertheless, the D/ExGxGxG motif involved in SAM cofactor binding (*27*) is not conserved in any of the metazoan FAS sequenced so far (fig. S8). In FAS of mammals, this motif is changed to ExLxGxG, which probably prevents cofactor binding, in agreement with the absence of methyltransferase activity and methylated products in mFAS systems. Notably, this motif is strictly conserved in several iterative and modular PKSs found in fungi and bacteria that share a related overall domain organization with FAS but are able to methylate their polyketide substrate with an intrinsic C-methyltransferase activity (fig. S7B) (*28*–*30*). Thus, the ΨME domain of FAS most likely represents an inactive version of a previously functional enzyme in a common precursor of mFAS and PKSs.

### Catalytic Domains and Cofactor Binding

*Ketoacyl synthase.* The KS enzymes of all systems for fatty acid or modular polyketide synthesis share a common fold and chemical mechanism, but their substrate specificities differ considerably (*1*, *6*). In the bacterial systems, which lack an acetyltransferase, KASIII (FabH) directly accepts acetyl-CoA as starter substrate. Further acyl chain extensions from C4 to C14 and from C14 to C16 are carried out by KASI (FabB) and KASII (FabF), respectively. Modular PKS contain specialized KS with some specificity for the β-carbon status but accept a wide range of substrate lengths (*6*). In the fungal type I FAS, only a single KS (which accepts C2 to C16 primers) is required for fatty acid synthesis. Likewise, mFAS has a single KS domain for all steps of fatty acid elongation. In contrast to PKS KS, mFAS KS is highly specific for saturated acyl chains and does not accept β-ketoacyl, β-enoyl- or β-hydroxyacyl substrates (*6*, *31*). On the basis of structural alignments, mFAS KS is closely related to KS domains from the DEBS I PKS system [1.3 Å root mean square deviation (RMSD)] but is structurally also very similar to fungal KS (RMSD 1.8 Å). It is more closely related to bacterial KASI and KASII (1.8 Å/1.6 Å RMSD) than to KASIII (2.9 Å RMSD), reflecting its ability to elongate long ACP-bound acyl chains.

Despite the pronounced structural similarity between the KS domains of mFAS and PKS, the selectivity of FAS for saturated acyl chains can be explained by a considerable constriction at the base of the active site phosphopantetheine binding pocket leading into the large acyl chain substrate binding tunnel, which connects both active sites of the KS dimer (Fig. 4, A and B). A number of residues lining this narrow tunnel are highly conserved in mFAS but are substituted with smaller residues in all DEBS PKS modules (Fig. 4B), resulting in a wider, more permissive tunnel in the KS of DEBS.

*Malonyl-acetyl transferase.* The acyl transferases of FAS and PKS systems are composed of an α/β-hydrolase core fold and a ferredoxin-like subdomain, which together create the active site cleft (*32*). In mFAS, the MAT domains of the two monomers have slightly different relative orientations of the two subdomains, probably selected by crystal-packing interactions. The structurally closest relatives are acyl transferases from DEBS didomain structures (2.0 Å/2.2 Å RMSD), the human mitochondrial MT (2.2 Å), and the *Escherichia coli* FAS MT (FabD) (2.3 Å RMSD) (table S4). All members of this family share a conserved active site with a catalytic Ser-His dyad. MTs are distinguished from acetyl transferases by the presence of a conserved active site arginine (*2*), which forms a bidentate salt bridge with the malonyl carboxylate (*33*). The mFAS MAT and related MTs display a rather

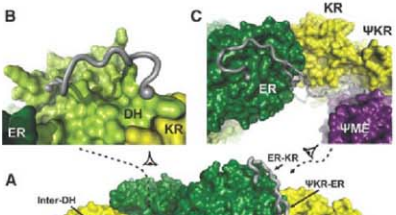

**Fig. 2.** Interdomain linkers. **(A)** Surface representation of individual mFAS domains (front view), colored as in Fig. 1. Linking regions are shown as tubes. **(B to E)** Close-up views of individual linkers. The direction of view is indicated by arrowheads in (A). (B) Linker connecting the two subdomains of the DH domain only loosely interacts with the main body of the double hot dog fold. (C) Linkers in the KR/ER region are wrapped around the domains with close interactions to the domain surfaces and pronounced linker-linker contacts; they mediate interactions between the KR, ΨKR, and ΨME domains. (D) Modifying upper and condensing lower parts of FAS are only in tangential contact in the region of the central connection. Few residues besides the connecting linkers mediate the sparse interactions via a small interface area. (E) MAT-DH linker meanders through a groove on the surface of the KS domain.

broad specificity for malonyl-CoA derivatives (e.g., propionyl-CoA and methylmalonyl-CoA). However, only mFAS MAT uses both acetyl-CoA and malonyl-CoA with equal efficiency (*6*). A structural comparison with bacterial and PKS MTs reveals three candidate residues for this specificity (Fig. 4C). Phe$^{682}$ replaces a serine in most PKS and bacterial homologs, whereas Phe$^{553}$ and Met$^{499}$ substitute for conserved glutamine residues. Together, these three substitutions create a considerably more hydrophobic active site. The two phenylalanines form a hydrophobic cavity, which may allow Met$^{499}$ to flip onto the methyl group of an acetyl substrate. Thus, the dual specificity of mFAS MAT appears to result from the combined presence of the conserved arginine for salt-bridging malonyl substrates and the more hydrophobic nature of the active site. The double specificity can be changed by mutating the arginine to alanine, which then transforms the MAT into an acetyl transferase (*34*).

*Ketoreductase*. The NADPH-dependent KR domain belongs to the family of short-chain dehydrogenases/reductases (SDRs) (*35*)—single-domain proteins that have a characteristic Rossmann fold and a substrate binding extension inserted before the last helix. mFAS KR is structurally closely related to both the tetrameric bacterial KR (FabG, 2.0 Å RMSD) and ER (FabI, 2.2 Å RMSD) and to the fungal KR domain (2.6 Å RMSD) (table S4). As for the KS and MAT domains, the closest structural homology is observed with the KR domains from modular PKS (RMSDs of 1.5 Å for tylosin PKS KR and 1.6 Å for DEBS KR). The arrangement of residues in the active site of the mFAS KR domain is consistent with a proton-relay mechanism described for bacterial FabG (*36*). However, two residues of the proton-wire, Asn$^{2038}$ and Lys$^{1995}$, have swapped positions (Fig. 4D), as previously observed in PKS KR domains (*19*, *20*). Loops in the vicinity of the active site cleft are disordered in the apo form of mFAS and become stabilized upon cofactor binding. This includes residues 1975 to 1990, corresponding to the $\beta 4/\alpha 4$ loop in FabG, that are presumably stabilized by interactions of Met$^{1973}$ with the active site Lys$^{1995}$, and part of the substrate binding extension (residues 2072 to 2075). The direction of substrate entry into the active site can be inferred from the stereospecificity of mFAS KR, which produces an *R*-hydroxyl group (*6*, *20*). The substrate approaches the NADPH cofactor from above the nicotinamide ribose, as observed for the structurally related mycobacterial ER InhA (*37*, *38*).

*Dehydratase*. The mFAS DH domain adopts a pseudodimeric double hot dog fold (Fig. 5A). The subdomain arrangement is more similar to

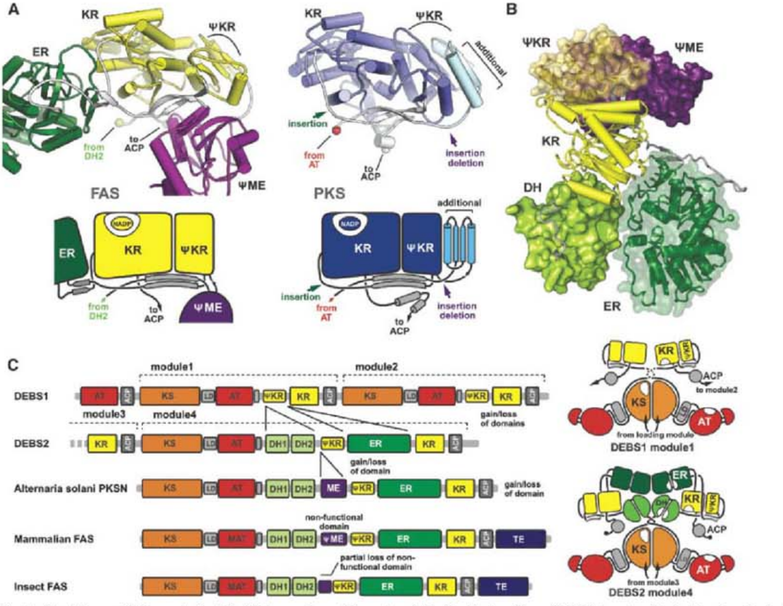

**Fig. 3.** Modularity of the modifying part of mFAS. **(A)** Comparison of the KR/ΨKR arrangement in mFAS (at left) and a related polyketide synthase, DEBS1 (*19*) (at right). The lower panels provide a schematic overview. The only modifying domain present in DEBS1 PKS includes KR-ΨKR, which is N- and C-terminally extended compared with mFAS KR/ΨKR. The additional ER and DH domains are integrated into mFAS without disturbing the path of the KR/ΨKR linker compared with PKS, leaving the N and C termini in identical positions. **(B)** KR interacts with all other domains in the modifying part of mFAS, whereas no direct interactions occur between either of the nonenzymatic domains and DH or ER. **(C)** Schematic sequence diagram depicting the integration and removal of additional domains in the modifying parts of PKS, mFAS, and insect FAS, on the basis of structural and sequence alignments (at left). The putative domain topologies of DEBS modules 1 and 4 are shown schematically on the right.

the functional DH dimers of bacterial FabA/Z than to the pseudodimeric fungal DH (fig. S9 and table S4) (*39*, *40*). Each mFAS pseudodimer contains a single composite active site formed by residues His$^{878}$ from the N-terminal hot dog fold and Asp$^{1033}$ and His$^{1037}$ from the C-terminal fold (Fig. 5B). The catalytic importance of these amino acids in mFAS has been demonstrated by mutagenesis and is further corroborated by a topologically similar arrangement in the active centers of bacterial DHs (Fig. 5B) (*39*–*42*). This also suggests a similar two-base reaction mechanism, as proposed for *E. coli* FabA, with His$^{878}$ and Asp$^{1033}$ participating in substrate protonation and deprotonation (*39*). The histidine at position 1037 is only present in the active site of chicken and pig FAS, whereas in all other sequenced mFAS the corresponding amino acid is a glutamine (fig. S10). The equivalence of a histidine and a glutamine at this position has been verified by mutagenesis (*42*). In the mFAS structure, His$^{1037}$ is positioned toward Asp$^{1033}$ at hydrogen-bonding distance, indicating a stabilizing function similar to those of the glutamine in other mFAS and bacterial DHs (*40*).

A hydrophobic substrate binding tunnel starts at the pseudodimer interface, stretches through the C-terminal hot dog domain, and has an open end that points toward the top of the FAS assembly (Fig. 5A). In contrast to type II DHs, which harbor two equivalent active sites in each homodimer, the second catalytic site is inactive in mFAS: The loop harboring the second catalytic histidine in bacteria is reduced to a short turn, and the corresponding accessory catalytic residues located in the central helix of the fold are replaced by tryptophane and lysine (Fig. 5A). The hydrophobic tunnel is entirely absent, and the domain is truncated by 30 residues at the N terminus.

*Enoylreductase.* In contrast to all other functional domains of the fatty acid elongation cycle, the mFAS ER has a different fold from its functional analogs in the bacterial type II FAS system, where the ERs are either SDR [FabI, FabL, FabV (*43*–*45*)] or TIM barrel proteins (FabK)—the latter also found as an ER domain in fungal type I FAS (*2*, *46*). Instead, the mammalian ER establishes a subfamily of medium-chain dehydrogenases/reductases (MDRs) (*47*) that is structurally related to bacterial quinone oxidoreductase (table S4). The mFAS ER contains two subdomains, a nucleotide binding Rossmann-fold (residues 1651 to 1794) and a substrate binding portion (residues 1530 to 1650 and 1795 to 1858). It binds the NADP$^+$ cofactor in an open extended conformation between the two subdomains (Fig. 5C). Our structure identifies Lys$^{1771}$ and Asp$^{1797}$ as candidate donor residues for substrate protonation after hydride transfer from NADPH (Fig. 5D). These two residues are in close proximity to the hydride-donating nicotinamide C4, in a similar position as the suggested active site tyrosines in other MDR subfamilies (e.g., the mitochondrial ER) (*48*–*50*). The two residues are strictly conserved in mFAS (fig. S11), and a corresponding lysine/aspartate pair is observed in the apo-form structure of the nucleotide binding subdomain of a related type I PKS ER domain (PDB entry 1pqw). The active site of ER is located in a narrow crevice created in part by the bound nucleotide cofactor, very different from the substrate binding groove in the related quinone reductase (*50*). Substrate entry probably occurs through a tunnel along the cofactor toward the nicotinamide ring. The tunnel continues through a constriction toward the back of the ER domain, where an opening would allow exit of long acyl chains (Fig. 5C).

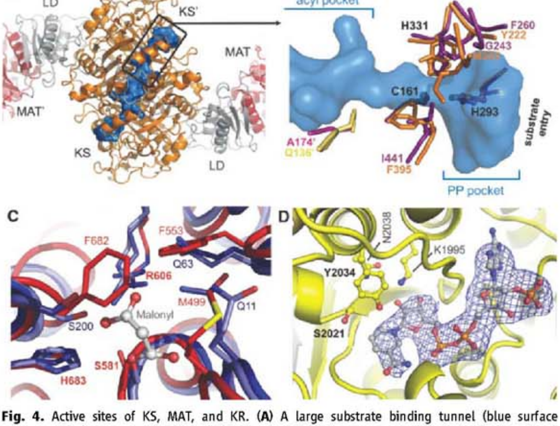

**Fig. 4.** Active sites of KS, MAT, and KR. (**A**) A large substrate binding tunnel (blue surface representation) traverses the dimeric KS domain. The substrate entry site of the KS domains is oriented toward the MAT domain of the other chain. (**B**) A narrow constriction in the substrate binding tunnel of the KS domain adjacent to the conserved active site residues (labeled in black) prevents the entry of larger modified substrates. Four residues involved in the formation of the constriction (orange for one subunit and yellow for the second one) are conserved in mFAS and replaced with smaller residues in the more permissive KS domains of PKS, as exemplified by KS of DEBS module 5 (purple for one subunit and pink for the second) (*18*). (**C**) MAT active site of mFAS (red) compared to bacterial MT, with and without bound substrate (light and dark blue, respectively) (*32*, *33*). Conserved active site residues in mFAS are indicated in bold. Two phenylalanines and a methionine characteristic for the acetyl-CoA/malonyl-CoA double-specific mFAS create a more hydrophobic binding groove and may close onto the methyl group of an acetyl moiety to promote efficient binding. (**D**) Active site of KR with bound NADP$^+$ and a 3.3 Å unbiased simulated annealed omit electron density map for the cofactor, contoured at $2.7\sigma$. The proton-donating tyrosine is in equivalent position to bacterial homologs, but the asparagine (N$^{2038}$) and lysine (K$^{1995}$) involved in proton replenishment are swapped.

### Structural Relation to PKS

The structural information presented here provides extensive evidence for the evolutionary relationship between mFAS and bacterial and fungal PKSs. (i) All catalytic mFAS domains are most closely related to PKS domains at the sequence level. Notably, the domains of mFAS are more similar to PKS domains than to the bacterial FAS counterparts, despite the differences in their substrate specificities. (ii) The structure of mFAS demonstrates that the similarity to PKSs extends to the linkers and the overall architecture—e.g., those in the KS/MAT or the KR/ΨKR regions—despite very low sequence conservation. (iii) Finally, an additional piece of evidence is provided by the existence of the nonfunctional ΨME domain, which can be considered a remnant of a catalytically active domain present in a common evolutionary ancestor of mFAS and PKS that is still preserved in several PKSs (*28*–*30*).

Functionally, modular PKSs differ from FAS by their non-iterative mode of action, where each module carries out a single precursor elongation step equivalent to one round of chain elongation by mFAS (*51*). The modules are concatenated into large polypeptides, several of which may assemble into production lines with more than 10 modules. This allows the synthesis of a variety of structurally diverse compounds. Based on the structural similarity discussed above, mFAS can be considered as a single PKS module specialized for iterative fatty acid synthesis.

Individual PKS modules contain substrate loading and condensing domains and variations of domains involved in β-carbon processing that control the chemical structure of the produced polyketide. Overall comparison of the PKS DEBS module 1 KR-ΨKR, which is the only β-carbon–modifying domain in this module, with the corresponding parts of mFAS reveals the structural basis for the notable modularity of modifying domains in megasynthases: Mediated by short linking sequences emanating from conserved secondary structure elements, the full ER domain is inserted between the ΨKR and KR domain, whereas the ΨME domain is integrated into the linker leading into the N terminus of the ΨKR domain (Fig. 3, A and C). As a consequence of this architectural solution, the insertions do not affect the core folds of the ΨKR and KR domains. Furthermore, because of a very flexible mode of interaction between KS and DH and weak contacts between KR and either DH or ER (table S3) of the mFAS, it is relatively easy to envision the architecture of some representative PKS modules (Fig. 3C). For example, the minimal PKS module, such as module 1 of DEBS1, which includes only the KR of the possible β-carbon–processing domains, would have this domain linked to KS with a short 10–amino acid linker, similar to the linker connecting KS to DH in mFAS. Other truncated variants of the mFAS architecture are also detectable at the sequence level. In the case of the closely related insect FAS, the ΨME domain lacks the N-terminal extension (Fig. 3C and fig. S8), whereas there is no methyltransferase in DEBS module 4 (Fig. 3C) (*19*, *52*). Short extensions may substitute for missing domain interactions, as indicated by a C-terminal addition of two helices to the KR-ΨKR of DEBS 1 (*19*) (Fig. 3A), which covers the region of the ΨKR surface occupied by the ΨME in mFAS.

These results also imply that the iterative mode of elongation (in which ACP shuttles substrates within one module) and a noniterative elongation (where substrates are passed between modules) can be accomplished with a similar overall architecture of the molecules. Notably, compared to the mFAS structure, no supplementary elements with a potential role in oligomerization are observed in the PKS structures available so far, except for a single helix in the KS-MAT linker domain (fig. S1) and a small C-terminal extension of the KR domain (Fig. 3A). Apparently, the N- and C-terminal docking domains (*53*, *54*) are sufficient to determine the higher-order assembly of PKS modules and polypeptides.

The architecture and the fold of mFAS and of the related PKSs are extremely versatile. This is in contrast to fungal FAS, which forms a barrel-shaped 2.6 MD $\alpha_6\beta_6$-heterododecameric assembly with three full sets of active sites enclosed in each of the two reaction chambers (*2*, *13*). The scaffold of the cage-forming fungal FAS appears less tolerant toward product modifying domain insertions and excisions because of symmetry constraints and the tight embedding of catalytic domains. Consistently, no naturally occurring fungal type I FAS with an altered domain composition has been detected, and all fungal FAS and most of their homologs produce only saturated fatty acid products (*8*).

### Substrate Shuttling by the ACP Domain

The entry sites to the active centers of the mFAS enzymatic domains are grouped around the two lateral clefts. In each cleft, the entry sites of MAT, DH, and ER are oriented toward one face of mFAS, and those of KS and KR toward the other face (Fig. 6). The flexibly tethered ACP and the following TE domains are not visualized in the structure. However, the structure defines the anchor point of ACP at residue 2113 in the center of the upper portion of the lateral clefts of mFAS. Together with recent structures of closely related rat and human ACP (*14*, *15*), which define the first ordered ACP residue at positions 2125 to 2127 (porcine FAS numbering), the flexible KR-ACP linker is composed of 12 to 14 amino acids, corresponding to a maximum length of ~40 Å. With a length of 23 to 26 residues, the ACP-TE linker is substantially longer and could span up to an 80 Å distance, as deduced from the corresponding isolated domain structures (*14*–*17*). In contrast to the fungal ACP linkers, which have a high Pro/Ala content that can increase their stiffness (*55*), the tethers flanking mFAS ACP have no unusual amino acid composition (Fig. 6). Whereas the motion of fungal ACP is constrained by double-tethering, no second anchor point is apparent for mFAS ACP, because the subsequent TE domain is not located at a defined position relative to the body of mFAS. Still, the TE domain may influence the motion of the tethered ACP either by transiently interacting with other domains or by steric effects.

Confining the path of the ACP may be one role of the protruding noncatalytic ΨME domain. This domain is docked to the body of mFAS in the vicinity of the ACP anchor point (Fig. 1, A

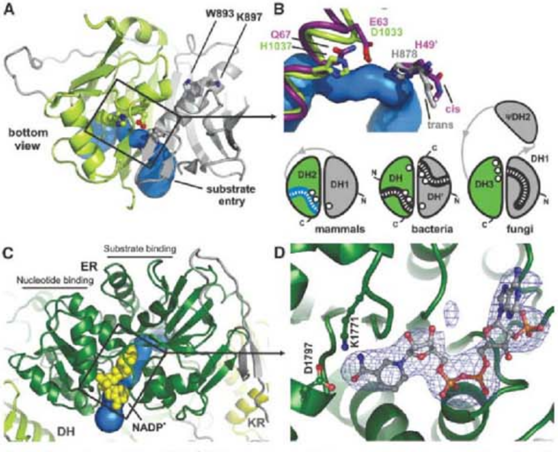

**Fig. 5.** Active sites of DH and ER. **(A)** Pseudo-dimeric DH domain only harbors a single active site and substrate binding tunnel with an open end. Active site residues are shown in ball-and-stick representation. These residues are not conserved in the corresponding position of the second subdomain ($Trp^{893}$ and $Lys^{897}$). **(B)** Close-up view of the DH active site topology (top) and schematic comparison to bacterial and fungal FAS (bottom). The mFAS active site residues (green) have their functional groups in similar positions as their bacterial FabZ counterparts (*40*) (purple), despite the exchange of two amino acids and the loss of an unusual non-proline cis peptide bond at $H^{878}$. **(C)** Open-ended substrate binding tunnel (blue) of the ER domain of mFAS shown in the presence of the bound $NADP^+$ cofactor (yellow spheres). **(D)** Two amino acids, $Asp^{1797}$ and $Lys^{1771}$, are candidate proton donor residues for enoyl reduction based on the positioning of their functional groups at ~4.2 Å distance to the C4 of the $NADP^+$ nicotinamide ring. A 3.3 Å unbiased simulated annealed omit electron density map for the bound $NADP^+$ cofactor, contoured at 3.3σ, is shown.

and B) and narrows the accessible region along the MAT, KS, DH, and ER substrate entry sites to a rim that is just slightly wider than the ACP (Fig. 6 and fig. S7C). The discrete ACPs of bacterial-type FAS (*56*–*58*) sequester fully saturated fatty acyl chains within their hydrophobic core. In contrast, mFAS ACP does not bury the acyl chain inside its core (*14*), raising the question whether other parts of the molecule may have taken over this function (for instance, by providing hydrophobic rims for a sliding motion of ACP-tethered acyl chains on the surface of mFAS). However, mapping of conservation or electrostatic potential on the mFAS surface did not reveal such regions.

The linker length, together with the steric constraints of the mFAS structure, allows ACP to reach a full set of active sites in one cleft but no active sites from the other cleft. During the elongation cycle (Fig. 6), the ACP is first loaded with substrates at the lateral MAT domain. ACP then has to deliver the substrates to the KS entry pocket on the opposite face of mFAS. The shortest route would lead directly through the cleft (path 1 in Fig. 6), which is just sufficiently open to allow the passage of ACP. After condensation at the KS, the ACP must reach the KR on the same face as the KS active site (path 2) before crossing the cleft again to approach the DH domain (path 3). From here, ACP proceeds toward the nearby ER (path 4) and finally delivers the fully saturated substrate to the KS active center before being reloaded at the MAT for the next cycle. During this cycle, the ACP interacts with the MAT and the β-carbon–processing domains of one chain, but it also interacts with the KS of the second polypeptide chain in the FAS dimer. Notably, the partially preserved active site cleft of the catalytically inactive ΨME domain could easily be accessed by ACP from the reaction chamber, as required in PKSs that display methyltransferase activity (fig. S7C) (*28*, *30*).

The requirement for ACP to shuttle back and forth through the cleft does not appear to be the most favorable solution for efficient substrate transfer and catalysis by mFAS. An alternative is suggested by considering the properties of the junction between the lower condensing and the upper modifying part of mFAS: They are joined only via the MAT-DH linkers, which are expected to mediate a flexible junction between the two halves of ~200 kD molecular mass each (*59*). Moreover, the pseudosymmetry-related DH/KS contacts on either side of the joint are not identical as would be expected for a stable interaction in solution. Consequently, the flexible connection of the mFAS halves may allow rotational motion around the dimer axis or a certain degree of tilting. Such motion would drag the ACP between the two faces of FAS and may contribute considerably to productive substrate shuttling. Mutant complementation and cross-linking studies have demonstrated that the vast majority of sub-

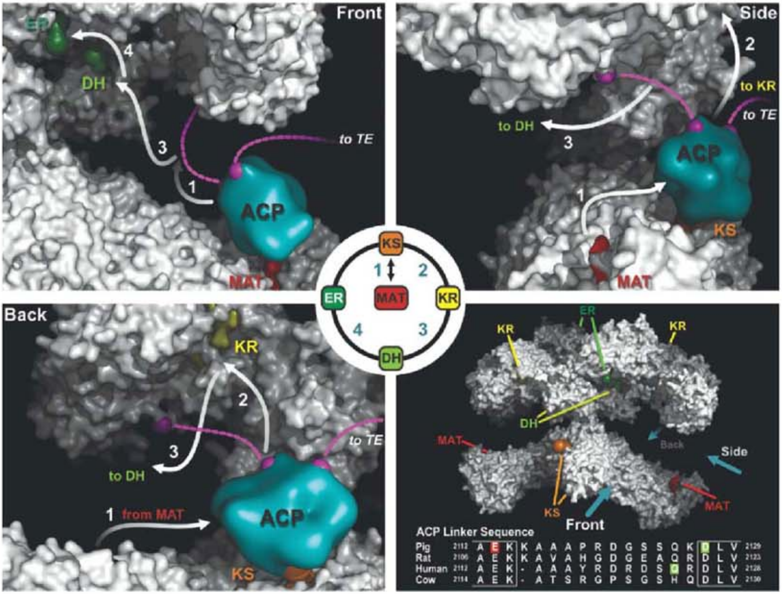

**Fig. 6.** Substrate shuttling by the ACP in mFAS. After substrate loading at the MAT on one side of the reaction chamber, the flexibly linked ACP has to shuttle the substrates to the other side for condensation at the KS and reduction at the KR (paths 1 and 2). To reach the DH and ER domain, ACP has to cross the cleft a second time (paths 3 and 4) before the saturated acyl chain can be back-transferred to KS to serve as primer for the next elongation cycle. The flexible linkers of ACP are depicted by dashed lines (pink). The precise length of the KR-ACP linker is defined by the KR and ACP domain borders in the current and previously solved structures (*14*, *16*, *17*) (bottom right, red and green). A schematic representation of the mFAS ACP domain based on experimentally determined structures (*14*, *15*) was positioned to the active site clefts by superposition with fungal ACP bound to the KS domain (*13*) and by orienting it according to residual electron density observed in the active site cleft of MAT (fig. S12).

strates are processed in mFAS by individual full sets of active sites, according to the path of ACP described above. However, these studies have also shown that a minority of substrates can be shuttled between the two sets of active sites, either by ACP serving both MAT domains or by direct interaction of ACP with both KS domains (*6*, *60*–*62*). In light of the large 135 Å distance between the ACP anchor point located in one catalytic cleft and the MAT in the other, the most plausible explanation for the minor mode-of-domain interaction is a large-scale rotation of the upper portion of mFAS, relative to the lower portion (fig. S4).

The molecular description of active sites in mFAS should stimulate the development of improved inhibitors as anticancer drug candidates. As demonstrated by structural homology, this structure is also a good template for the organization of PKS modules; it agrees with and extends present theoretical models of PKS architecture (*19*, *22*). Furthermore, the structure of mFAS paves the way for structure-based experiments to answer remaining questions on the dynamics and substrate shuttling mechanism in megasynthases.

### References and Notes

1. S. W. White, J. Zheng, Y. M. Zhang, C. O. Rock, *Annu. Rev. Biochem.* **74**, 791 (2005).
2. S. Jenni *et al.*, *Science* **316**, 254 (2007).
3. S. Jenni, M. Leibundgut, T. Maier, N. Ban, *Science* **311**, 1263 (2006).
4. I. B. Lomakin, Y. Xiong, T. A. Steitz, *Cell* **129**, 319 (2007).
5. T. Maier, S. Jenni, N. Ban, *Science* **311**, 1258 (2006).
6. S. Smith, S. C. Tsai, *Nat. Prod. Rep.* **24**, 1041 (2007).
7. F. Lynen, *Eur. J. Biochem.* **112**, 431 (1980).
8. E. Schweizer, J. Hofmann, *Microbiol. Mol. Biol. Rev.* **68**, 501 (2004).
9. F. P. Kuhajda *et al.*, *Proc. Natl. Acad. Sci. U.S.A.* **91**, 6379 (1994).
10. J. A. Menendez, R. Lupu, *Nat. Rev. Cancer* **7**, 763 (2007).
11. F. P. Kuhajda, *Cancer Res.* **66**, 5977 (2006).
12. H. Orita *et al.*, *Clin. Cancer Res.* **13**, 7139 (2007).
13. M. Leibundgut, S. Jenni, C. Frick, N. Ban, *Science* **316**, 288 (2007).
14. E. Ploskon *et al.*, *J. Biol. Chem.* **283**, 518 (2008).
15. G. Bunkoczi *et al.*, *Chem. Biol.* **14**, 1243 (2007).
16. B. Chakravarty, Z. Gu, S. S. Chirala, S. J. Wakil, F. A. Quiocho, *Proc. Natl. Acad. Sci. U.S.A.* **101**, 15567 (2004).
17. C. W. Pemble IV, L. C. Johnson, S. J. Kridel, W. T. Lowther, *Nat. Struct. Mol. Biol.* **14**, 704 (2007).
18. Y. Tang, C.-Y. Kim, I. I. Mathews, D. E. Cane, C. Khosla, *Proc. Natl. Acad. Sci. U.S.A.* **103**, 11124 (2006).
19. A. T. Keatinge-Clay, R. M. Stroud, *Structure* **14**, 737 (2006).
20. A. T. Keatinge-Clay, *Chem. Biol.* **14**, 898 (2007).
21. Y. Tang, A. Y. Chen, C.-Y. Kim, D. E. Cane, C. Khosla, *Chem. Biol.* **14**, 931 (2007).
22. C. Khosla, Y. Tang, A. Y. Chen, N. A. Schnarr, D. E. Cane, *Annu. Rev. Biochem.* **76**, 195 (2007).
23. A. K. Joshi, A. Witkowski, H. A. Berman, L. Zhang, S. Smith, *Biochemistry* **44**, 4100 (2005).
24. Materials and methods are available as supporting material on *Science* Online.
25. J. G. Olsen, A. Kadziola, P. von Wettstein-Knowles, M. Siggaard-Andersen, S. Larsen, *Structure* **9**, 233 (2001).
26. J. M. Thorn, J. D. Barton, N. E. Dixon, D. L. Ollis, K. J. Edwards, *J. Mol. Biol.* **249**, 785 (1995).
27. J. L. Martin, F. M. McMillan, *Curr. Opin. Struct. Biol.* **12**, 783 (2002).
28. I. Fujii, N. Yoshida, S. Shimomaki, H. Oikawa, Y. Ebizuka, *Chem. Biol.* **12**, 1301 (2005).
29. I. Molnar *et al.*, *Chem. Biol.* **7**, 97 (2000).
30. D. J. Edwards *et al.*, *Chem. Biol.* **11**, 817 (2004).
31. A. Witkowski, A. K. Joshi, S. Smith, *Biochemistry* **36**, 16338 (1997).
32. L. Serre, E. C. Verbree, Z. Dauter, A. R. Stuitje, Z. S. Derewenda, *J. Biol. Chem.* **270**, 12961 (1995).
33. C. Oefner, H. Schulz, A. D'Arcy, G. E. Dale, *Acta Crystallogr. D Biol. Crystallogr.* **62**, 613 (2006).
34. V. S. Rangan, S. Smith, *J. Biol. Chem.* **272**, 11975 (1997).
35. B. Persson, Y. Kallberg, U. Oppermann, H. Jornvall, *Chem. Biol. Interact.* **143-144**, 271 (2003).
36. A. C. Price, Y. M. Zhang, C. O. Rock, S. W. White, *Structure* **12**, 417 (2004).
37. D. A. Rozwarski, C. Vilcheze, M. Sugantino, R. Bittman, J. C. Sacchettini, *J. Biol. Chem.* **274**, 15582 (1999).
38. T. J. Sullivan *et al.*, *Am. Chem. Soc. Chem. Biol.* **1**, 43 (2006).
39. M. Leesong, B. S. Henderson, J. R. Gillig, J. M. Schwab, J. L. Smith, *Structure* **4**, 253 (1996).
40. M. S. Kimber *et al.*, *J. Biol. Chem.* **279**, 52593 (2004).
41. A. K. Joshi, S. Smith, *J. Biol. Chem.* **268**, 22508 (1993).
42. S. Pasta, A. Witkowski, A. K. Joshi, S. Smith, *Chem. Biol.* **14**, 1377 (2007).
43. C. Baldock, J. B. Rafferty, A. R. Stuitje, A. R. Slabas, D. W. Rice, *J. Mol. Biol.* **284**, 1529 (1998).
44. R. J. Heath, N. Su, C. K. Murphy, C. O. Rock, *J. Biol. Chem.* **275**, 40128 (2000).
45. R. P. Massengo-Tiasse, J. E. Cronan, *J. Biol. Chem.* **283**, 1308 (2008).
46. J. Saito *et al.*, *Protein Sci.* **17**, 691 (2008).
47. E. Nordling, H. Jornvall, B. Persson, *Eur. J. Biochem.* **269**, 4267 (2002).
48. T. T. Airenne *et al.*, *J. Mol. Biol.* **327**, 47 (2003).
49. T. Hori *et al.*, *J. Biol. Chem.* **279**, 22615 (2004).
50. Y. Shimomura, Y. Kakuta, K. Fukuyama, *J. Bacteriol.* **185**, 4211 (2003).
51. D. A. Hopwood, D. H. Sherman, *Annu. Rev. Genet.* **24**, 37 (1990).
52. C. D. Richter *et al.*, *FEBS J.* **274**, 2196 (2007).
53. C. D. Richter, D. Nietlispach, R. W. Broadhurst, K. J. Weissman, *Nat. Chem. Biol.* **4**, 75 (2008).
54. K. J. Weissman, *ChemBioChem* **7**, 485 (2006).
55. R. N. Perham, *Biochemistry* **30**, 8501 (1991).
56. A. Roujeinikova *et al.*, *Structure* **10**, 825 (2002).
57. A. Roujeinikova *et al.*, *J. Mol. Biol.* **365**, 135 (2007).
58. G. A. Zornetzer, B. G. Fox, J. L. Markley, *Biochemistry* **45**, 5217 (2006).
59. S. Jones, J. M. Thornton, *Proc. Natl. Acad. Sci. U.S.A.* **93**, 13 (1996).
60. S. Smith, A. Witkowski, A. K. Joshi, *Prog. Lipid Res.* **42**, 289 (2003).
61. A. K. Joshi, V. S. Rangan, A. Witkowski, S. Smith, *Chem. Biol.* **10**, 169 (2003).
62. V. S. Rangan, A. K. Joshi, S. Smith, *Biochemistry* **40**, 10792 (2001).
63. All data were collected at the Swiss Light Source (SLS, Paul Scherrer Institute, Villigen). We thank C. Schulze-Briese, S. Gutmann, R. Bingel-Erlenmeyer, S. Russo, A. Pauluhn, and T. Tomizaki for their outstanding support at the SLS; S. Jenni and M. Sutter for critically reading the manuscript and all members of the Ban laboratory for suggestions and discussions; R. Grosse-Kunstleve, P. Afonine, and P. Adams for support with the PHENIX software; and A. Jones for support with the program O. This work was supported by the Swiss National Science Foundation (SNSF) and the National Center of Excellence in Research Structural Biology program of the SNSF. Structure factors and atomic coordinates of the porcine FAS in the apo- and NADP$^+$-bound form have been deposited in the Protein Data Bank with accession codes 2vz8 and 2vz9.

**Supporting Online Material**

www.sciencemag.org/cgi/content/full/321/5894/1315/DC1
Materials and Methods
Figs. S1 to S15
Tables S1 to S4
References

3 June 2008; accepted 31 July 2008
10.1126/science.1161269

---

# Internally Generated Cell Assembly Sequences in the Rat Hippocampus

**Eva Pastalkova, Vladimir Itskov,* Asohan Amarasingham, György Buzsáki†**

**A long-standing conjecture in neuroscience is that aspects of cognition depend on the brain's ability to self-generate sequential neuronal activity. We found that reliably and continually changing cell assemblies in the rat hippocampus appeared not only during spatial navigation but also in the absence of changing environmental or body-derived inputs. During the delay period of a memory task, each moment in time was characterized by the activity of a particular assembly of neurons. Identical initial conditions triggered a similar assembly sequence, whereas different conditions gave rise to different sequences, thereby predicting behavioral choices, including errors. Such sequences were not formed in control (nonmemory) tasks. We hypothesize that neuronal representations, evolved for encoding distance in spatial navigation, also support episodic recall and the planning of action sequences.**

A prominent theory states that the hippocampal system primarily serves spatial navigation (*1*, *2*); a component of this theory is that the place-dependent activity of neurons [place cells (*1*, *2*)] in the hippocampus arises from external serially ordered environmental stimuli (*3*–*7*). Place cells are thought to embody the representation of a cognitive map, enabling flexible navigation. However, neural theories of other cognitive processes that may depend on the hippocampus, such as episodic memory and action planning, draw on the activity of hypothetical internally organized cell assemblies (*8*–*13*).

---

Center for Molecular and Behavioral Neuroscience, Rutgers, The State University of New Jersey, 197 University Avenue, Newark, NJ 07102, USA.

*Present address: Center for Neurobiology and Behavior, Columbia University, 1051 Riverside Drive, New York, NY 10032, USA.

†To whom correspondence should be addressed. E-mail: buzsaki@axon.rutgers.edu

Several observations have refined the navigation theory. Hippocampal neurons can predict where the animal is coming from, or its destination (*14*–*17*); the sequential activity of place cells during locomotion is replicated within single cycles of the theta oscillation (8 to 12 Hz) (*18*–*20*); furthermore, the temporal recruitment of active neurons in the population bursts of rest and sleep also reflects, again on a faster time scale, their sequential activity as place cells during locomotion (*21*–*23*). Thus, the sequential activation of hippocampal neurons can be disengaged from external landmarks (*24*, *25*). However, internally generated assembly sequences operating at the time scale of behavior have not yet been reported.

The frameworks of environment-controlled versus internally generated assembly sequences give rise to distinct predictions. Imagine that a rat is frozen in position during its travel (and yet the theta oscillation is maintained). According to the navigation theory, a subset of landmark-controlled place cells should then display sustained activity, and other neurons would remain suppressed (*2*–*6*). In contrast, if assembly sequences were generated by internal mechanisms, neurons might rather display continually changing activity. We tested these predictions by examining the activity of hippocampal neurons while a rat was running in a wheel at a relatively constant speed (*26*, *27*) during the delay of a hippocampus-dependent alternation memory task.

**Internally generated cell-assembly sequences.** Rats were trained to alternate between the left and right arms of a figure-eight maze [Fig. 1A and supporting online material (SOM) text]. During the delay period between maze runs (10 s for rat 1; 20 s each for rats 2 and 3), the animals were trained to run steadily in the same direction in a wheel (Fig. 1A). To confront the predictions of the navigation theory with those of the internal sequence-generation hypothesis, we compared

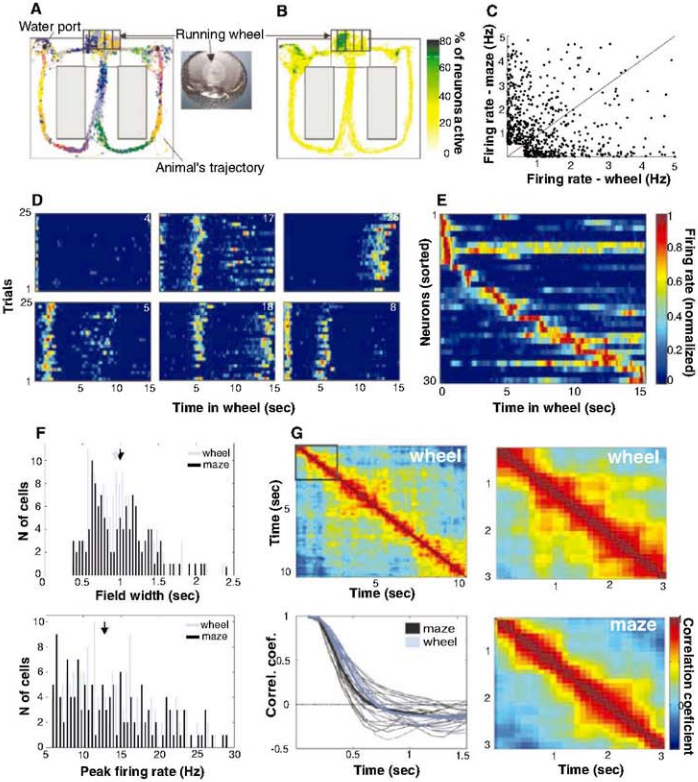

**Fig. 1.** Episode fields in the wheel and place fields in the maze are similar. (**A**) Color-coded spikes (dots) of simultaneously recorded hippocampal CA1 pyramidal neurons. The rat was required to run in the wheel facing to the left during the delay between the runs in the maze. (**B**) Percent of neurons firing >0.2 Hz within each pixel. The highest percentage of neurons was active when rats were running in the wheel. (**C**) Relationship between firing rate of neurons active in rats running the wheel and the maze ($r_s = -0.3$, $P < 0.0001$, 681 neurons, three rats, 17 sessions). (**D**) Normalized firing rate of six simultaneously recorded neurons during wheel running (each line shows the color-coded activity on single trials turning to the left arm). The episode fields occurred at specific segments of the run. (**E**) Normalized firing rate of 30 simultaneously recorded neurons during wheel running, ordered by the latency of their peak firing rate. (**F**) Width (top) and peak firing rate (bottom) of episode and place fields (wheel, $n = 135$ neurons; maze, $n = 162$ neurons). Arrows indicate medians. (**G**) Population vector cross-correlation matrix (SOM text). The width of the diagonal stripe indicates the rate at which neuronal assemblies transition. (Lower left) The decay of the population vector correlation during wheel running and maze traversal. Thin lines, individual sessions; thick lines, group means.

the firing patterns of CA1 hippocampal neurons in rats running the wheel and the maze.

We analyzed the activity of ~500 pyramidal cells recorded in the wheel and ~600 neurons in the maze (mean firing rate >0.5 Hz) (Fig. 1A). Pyramidal neurons were transiently active in rats running both the maze [place cells (*1*)] and the wheel. Although the position and direction of the rat's head were stationary during wheel running (fig. S1), the percentage of neurons active in the pixels occupied by the head during wheel running was three to four times greater than in any area of comparable size in the maze (Wilcoxon rank sum test, $P < 0.0001$) (Fig. 1B). Thus, if pyramidal neurons were solely activated by environmental cues (*2–6*), this finding would reflect several-fold–stronger neuronal representation of the animal's position within the wheel. Many individual pyramidal cells were active both in rats running the wheel and rats running the maze, but the sequential order of their activation in rats in the wheel was unrelated to that of rats in the maze, and their firing rates in these two areas were inversely correlated [Spearman correlation coefficient ($r_s$) = –0.3, $P < 0.0001$, $n = 681$ neurons (Figs. 1C and 4B); contrast this with the population of interneurons, $r_s = 0.85$, $P < 0.0001$, $n = 125$ interneurons (fig. S2)]. The average proportion of pyramidal neurons simultaneously active [firing at least a single spike in 100-ms windows (averaging over 100-ms windows)] was similar in the wheel (10.75 ± 3.97%) and the maze (12.56 ± 4.32%) (fig. S3).

Pyramidal neurons typically fired transiently, and reliably in successive trials, at specific times of wheel running (episode fields), and most cells had multiple peaks of varying sizes (Fig. 1D). Typically, and reminiscent of a synfire chain (*11*), at least one episode cell was active at every moment of a wheel run (Fig. 1E).

Were episode cells in rats in the wheel generated by the same mechanism as place cells in rats in the maze? We looked for evidence of differing mechanisms by comparing several measures of the firing of episode and place cells. First, we calculated the duration of activity (field width) (Fig. 1F) of single cells [including only fields with a peak firing rate of ≥6.0 Hz and ≥4.5 SD above the mean firing rate (SOM text)]. The temporal and spatial extent of the field was determined as those times and positions at which firing rates were at least 10% that of the peak firing rate (in the wheel or maze) (*19, 28*). By these criteria, 32% of the neurons recorded in the wheel and 22% in the maze had at least one field. Neither the distribution of field widths (medians were 0.94 and 1.0 s, respectively; Wilcoxon test, $P = 0.44$) nor peak firing rates (medians were 13.08 and 12.8 Hz, respectively; $P = 0.61$) differed significantly between the episode and place fields (Fig. 1F). Second, to measure the average lifetime of assembly activity for a population, we determined the maximal time lag at which the autocorrelation of the population's activity was above 0.5 (*29*) and again found no significant difference, with respect to the median, between the populations of episode and place cells (medians were 0.83 and 0.75 s, respectively; $P = 0.32$) (Fig. 1G). Third, we compared the relationship between spikes and the local field potential in episode and place cells. On linear tracks, sequentially generated spikes of a place cell gradually shift to earlier and earlier phases of the theta oscillation as the rat passes through the place field (phase precession), and there is a systematic relationship between the phase of spikes and the animal's position (*3, 18–20, 28, 30, 31*). The navigation theory predicts that the phase of spikes will remain fixed if environmental inputs do not change (*3, 26, 27*). In contrast, episode cells displayed phase precession during wheel running (Fig. 2A). Similarly to place cells, the theta frequency oscillation of episode cells was higher than that of the field theta rhythm (Fig. 2B), and the slope of the phase precession was inversely related to the length of the episode field (Fig. 2, A and D) (*3, 19, 20, 28, 30, 31*).

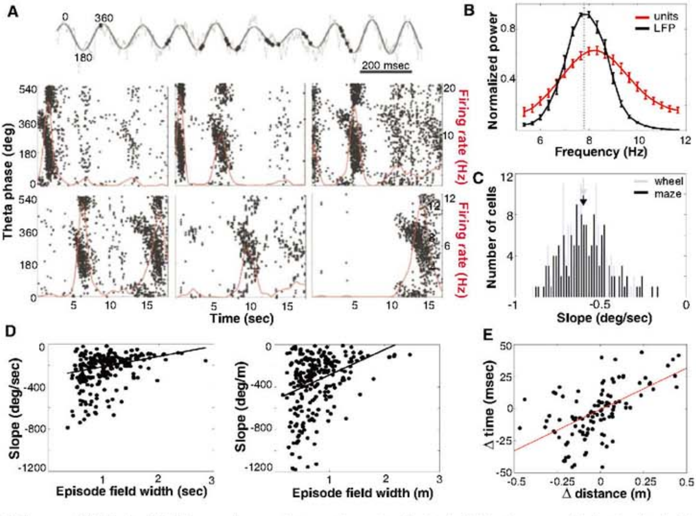

**Fig. 2.** Episode neurons in the wheel display theta phase precession and temporal compression. **(A)** (Top) Unfiltered (light gray) and filtered (4 to 10 Hz) (dark gray) traces of LFP and phase advancement of action potentials (dots). (Bottom) Activity of six example neurons from the same session. Each dot is an action potential, displayed as a function of theta phase and time from the beginning of wheel running from all trials. One and a half theta cycles are shown (*y* axis). Red line, smoothed firing rate. **(B)** Power spectra of spike trains generated during wheel running ($n = 283$ pyramidal neurons) and the simultaneously recorded LFP. Faster oscillation of neurons occurs relative to LFP. **(C)** Slope of theta phase precession within episode fields in the wheel and within place fields in the maze. **(D)** Relationship between phase precession slope and episode length (left, $r_s = 0.46$, $P < 0.0001$) and episode field width (right, $r_s = 0.52$, $P < 0.0001$), respectively. **(E)** Temporal compression of spikes sequences. Correlation of the distance between the peaks of episode fields of neuron pairs in the wheel with the temporal offset of the pair's cross-correlogram peaks is shown. Each dot represents a neuron pair ($n = 105$ eligible pairs; three rats; $r_s = 0.59$; $P < 0.0001$).

Furthermore, the slopes correlated more strongly with the length of the episode field ($r_s = 0.52$, $P < 0.0001$) than with the time it took the rat to run through the same field ($r_s = 0.46$, $P < 0.0001$) (Figs. 2D and 3) because of the variability of the rat's running speed (*28*). The distributions of phase precession slopes for the episode and place fields were also similar (medians were –0.6°/s and –0.6°/s, respectively; $P = 0.6$) (Fig. 2C). Finally, we compared the spike timing relationships among neurons. During maze traversals, the distance between the place-field peaks of a neuronal pair was correlated with the temporal offset between its spikes within the theta cycle, a phenomenon known as distance-time compression (SOM text) (*18*, *19*). Analogously, the distance between peaks of the episode fields of neuron pairs (episode fields with peak firing rate >5 Hz and >3 SD above the mean firing rate were included in this analysis; $n = 105$ pairs) was correlated with the temporal offsets between the spikes at the theta time scale ($r_s = 0.59$, $P < 0.0001$) (Fig. 2E). These findings indicate that the mechanisms generating place and episode fields are similar.

**Body cues are not sufficient to generate assembly sequences.** It has been suggested that in addition to generating a cognitive map of the environment (*2*), the hippocampus and its associated structures integrate self-motion–induced information (*7*, *32*, *33*). Were the episode cell sequences generated by idiothetic self-motion cues? We examined population firing patterns in two control (nonmemory) tasks. In the first task (control 1), the animals (rats 3 and 4) were required to run in the wheel for a water reward available in an adjacent box (*26*). In the second task (control 2), the animals (rats 2 and 3) had continuous access to a wheel adjacent to their home cage, and recordings were made during spontaneous wheel-running episodes. Transient firing patterns, consistent across trials, were rarely observed during the control tasks. Rather, the majority of active neurons exhibited relatively sustained firing throughout the wheel-running

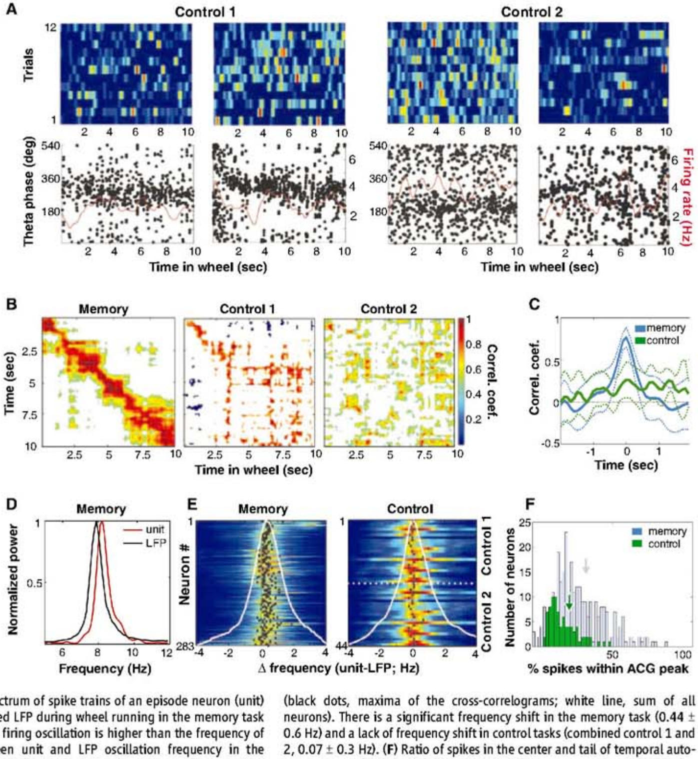

**Fig. 3.** Firing patterns during wheel running depend on the context of the task. **(A)** (Top) Activity of representative single neurons (color-coded) during wheel running in control tasks 1 and 2 (compare with Fig. 1D). (Bottom) Unit discharges (dots) from all trials within a session as a function of theta phase, plotted against time from the beginning of a wheel run. Red line, smoothed mean firing rate. Relatively steady firing rates and a steady theta phase occur in both control tasks. **(B)** Cross-correlation matrices in three different tasks (memory and control 2 are from the same rat). In the memory task, trials with the same future choices [left (L)–trials$_n$ versus L-trials$_{n+1}$ and right (R)–trials$_n$ versus R-trials$_{n+1}$) were cross-correlated, whereas in control tasks trials$_n$ and trials$_{n+1}$ were cross-correlated. Only pixel values significantly different from chance are shown (Spearman rank correlation, $P < 0.01$). **(C)** Population-vector correlation coefficient values in the memory task ($n = 17$ sessions) and control tasks ($n = 8$ sessions) (mean ± SD). **(D)** Power spectrum of spike trains of an episode neuron (unit) and simultaneously recorded LFP during wheel running in the memory task (*30*). The frequency of unit firing oscillation is higher than the frequency of LFP. **(E)** Difference between unit and LFP oscillation frequency in the memory (left) and control (right) tasks. Each line is a color-coded normalized cross-correlogram between power spectra of a pyramidal neuron and simultaneously recorded LFP. A shift of the maximal correlation values to the right indicates that unit theta oscillation is faster than LFP theta oscillation (black dots, maxima of the cross-correlograms; white line, sum of all neurons). There is a significant frequency shift in the memory task (0.44 ± 0.6 Hz) and a lack of frequency shift in control tasks (combined control 1 and 2, 0.07 ± 0.3 Hz). **(F)** Ratio of spikes in the center and tail of temporal autocorrelograms (SOM text). High values indicate compact episode fields; low values indicate spikes scattered throughout the time of wheel running (memory task, $n = 287$ neurons; control tasks, $n = 85$ neurons; rank sum test, $P < 0.0001$). Arrows indicate medians.

periods (Fig. 3A and fig. S4) (*5*, *26–27*). During runs of opposite direction in the wheel, different populations of neurons were active (fig. S5) (*26*), arguing for the importance of distant cues (*2*, *20*) and against a critical role of idiothetic inputs (*26*). In addition, the temporal organization of cell assemblies in control tasks was less precise, as reflected by much weaker correlations between temporally adjacent populations during the control tasks than during the memory task (Fig. 3, B and C), despite the similarity in firing rates during all tasks (fig. S6). As another contrast to the memory task, neurons recorded during the control tasks fired throughout the trial, with spikes locked to a similar phase of the theta cycle (Fig. 3A). Consistent with these observations, neurons in the rats performing the memory task oscillated faster than the local field potential (LFP) [difference (Δ) = 0.44 ± 0.6 Hz] (Figs. 2B and 3, D and E), an indication of phase precession (*19*, *20*, *29*, *30*), whereas during the control tasks, the power spectra of the units and LFP were similar (Δ = 0.07 ± 0.3 Hz) (Fig. 3E). Finally, to quantify differences in temporal clustering of spikes, we examined an autocorrelogram of each neuron. We applied (after filtering, 0.2 to 2 Hz) the same definition for the peak region boundaries that we used for the episode field detection boundary of the episode field (the 10% boundary) and then compared, for each neuron, the ratio of the number of spikes that fell within the peak region boundary to those that fell outside. These ratios were significantly larger during the memory task and reflected the temporal compactness of firing during the memory task as opposed to the control tasks (Fig. 3F). Thus, the indicators of temporally precise sequential activity in neuronal populations were absent during the control tasks, despite indistinguishable motor characteristics across all tasks.

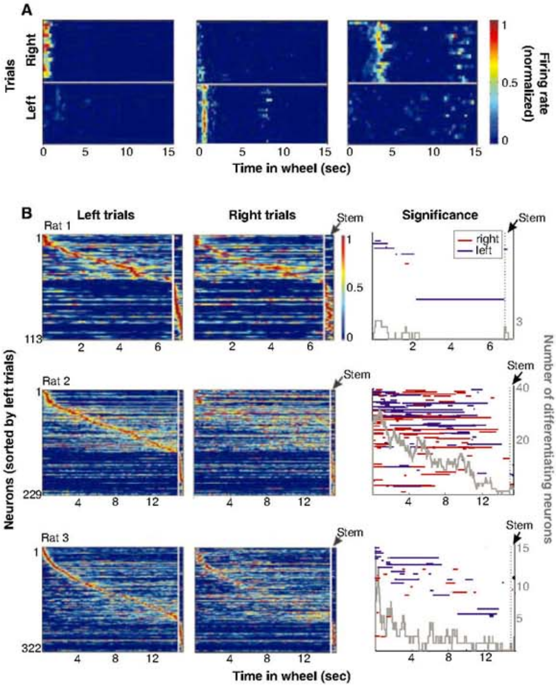

**Fig. 4.** Cell-assembly activity in the wheel predicts the future choice of the rat in the maze. **(A)** Examples of three neurons that strongly differentiated between wheel-running trials preceding right and left choices (fig. S7 and movie S1). **(B)** Normalized firing rate profiles of neurons during wheel running and in the stem of the maze, ordered by the latency of their peak firing rates during left trials (each line is a single cell; cells are combined from all sessions). White line, time gap between the end of wheel running and the initiation of maze stem traversal. (Middle) Normalized firing rates of the same neurons during right trials. (Right) Time periods of significant differences ($P < 0.05$) in firing rates between left and right trials for respective neurons (red line, R > L; blue line, L > R). Gray line, number of neurons discriminating between left and right trials as a function of wheel-running time.

**Assembly sequences depend on memory load.** What is the behavioral function of internally generated cell-assembly sequences? Temporarily inactivating neuronal circuits in the dorsal hippocampus, we found that performance in the delayed alternation task depends on the integrity of the hippocampus (fig. S7) (*17*). Thus, we hypothesized that information about choice behavior is reflected in assembly sequences (*34*). All correctly performed trials were sorted according to the rat's future choice of arm (left or right), and choice-specific firing effects were identified by comparing the firing patterns of single neurons with those of surrogate spike trains created by shuffling the left and right labels (Fig. 4, A and B, and SOM text) (*34*). Some neurons were active exclusively before either the left or right choice, whereas others showed differential firing rates and/or fired at different times after the beginning of wheel running (Fig. 4A, figs. S8 to S10, and movie S1). The largest proportion of neurons exhibiting choice-predictive activity was at the beginning of the run; this proportion decreased as a function of time during the delay and in the stem of the maze (Fig. 4B), suggesting a critical role for initial conditions in specifying the sequences (fig. S11). In addition, we designed a probabilistic model of the relationship between neuronal firing patterns and the animal's choices (SOM text). Using this model, the accuracy of single-trial prediction, under cross-validation, varied from low (near 50%) and not significant to 100% and significant across many sessions (fig. S9).

Because the rat was performing an alternation task, past and future choices were deterministically related on correctly performed trials, and it was not possible to disambiguate their influence on neuronal activity. To distinguish such retrospective and prospective factors (*14–17*), we examined cell-assembly sequences during error trials. Neurons that reliably predicted the behavioral choice of the rat on correct trials continued to predict the choice behavior on error trials (Fig. 5A, fig. S12, and movie S1) (*15*, *24*). Similarly, population sequences that differentiated correct behavioral choices continued to predict behavioral choice errors (Fig. 5, B and C, and fig. S13). Although there were only a few error trials, a majority of them could be predicted from the

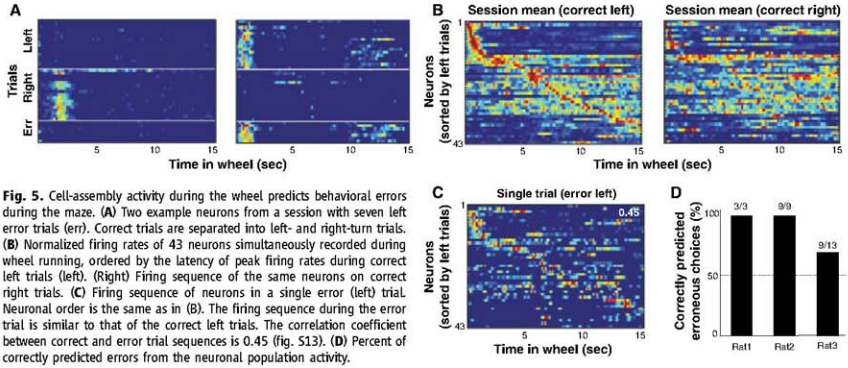

**Fig. 5.** Cell-assembly activity during the wheel predicts behavioral errors during the maze. **(A)** Two example neurons from a session with seven left error trials (err). Correct trials are separated into left- and right-turn trials. **(B)** Normalized firing rates of 43 neurons simultaneously recorded during wheel running, ordered by the latency of peak firing rates during correct left trials (left). (Right) Firing sequence of the same neurons on correct right trials. **(C)** Firing sequence of neurons in a single error (left) trial. Neuronal order is the same as in (B). The firing sequence during the error trial is similar to that of the correct left trials. The correlation coefficient between correct and error trial sequences is 0.45 (fig. S13). **(D)** Percent of correctly predicted errors from the neuronal population activity.

firing patterns of neurons during wheel running (Fig. 5D). Altogether, these observations demonstrate that a particular sequence of neurons was activated in a reliable temporal order from the moment the rat entered the wheel to the time it reached the reward.

Because running speed, head position, and head direction during wheel running before left and right choices were apparently indistinguishable (fig. S1), the above findings indicate that trial differences in hippocampal assembly configurations cannot solely arise from instantaneous environmental inputs or the integration of motion signals.

**Behavioral function of internally generated cell-assembly sequences.** These findings demonstrate that the rat brain can generate continually changing assembly sequences. The patterns of the self-evolving neuronal assembly sequences depend on the initial conditions, and the particular sequences of cell assemblies are predictive of behavioral outcome.

Our results offer new insights into the relationship between hippocampal activity and navigation (*2–7, 14–20, 26–30, 33*). Hippocampal firing patterns during maze navigation were similar to those during wheel running in the delayed alternation memory task with stationary environmental and body cues. Therefore, we suggest that hippocampal networks can produce sequential firing patterns in two possibly interacting ways: under the influence of environmental/idiothetic cues or by self-organized internal mechanisms. The high-dimensional and largely random (nontopographical) connectivity of the CA3 axonal system (*35*) and its inputs makes the hippocampus an ideal candidate for internal sequence generation (*13, 33, 36, 37*). The parameters of cell-assembly dynamics (including their trajectory and lifetimes) are probably affected by a number of factors, including experience-dependent and short-term synaptic plasticity (*34, 38*); asymmetric inhibition (*39*); brain state; and, fundamentally, the character and context of the input. The evolving trajectory can be effectively perturbed, or updated, by external inputs in every theta cycle (*40*). Because of this flexibility in the sources of cell-assembly control, we hypothesize that neuronal algorithms, having evolved for the computation of distances, can also support the episodic recall of events and the planning of action sequences and goals (*19*). During learning, the temporal order of external events is instrumental in specifying and securing the appropriate neuronal representations, whereas during recall, imagination (*35*), or action planning, the sequence identity is determined by the intrinsic dynamics of the network.

### References and Notes

1. J. O'Keefe, J. Dostrovsky, *Brain Res.* **34**, 171 (1971).
2. J. O'Keefe, L. Nadel, *The Hippocampus as a Cognitive Map* (Clarendon, Oxford, UK, 1978).
3. J. Huxter, N. Burgess, J. O'Keefe. *Nature* **425**, 828 (2003).
4. B. L. McNaughton, C. A. Barnes, J. O'Keefe, *Exp. Brain Res.* **52**, 41 (1983).
5. J. O'Keefe, N. Burgess, *Nature* **381**, 425 (1996).
6. R. U. Muller, J. L. Kubie, J. B. Ranck Jr., *J. Neurosci.* **7**, 1935 (1987).
7. B. L. McNaughton *et al.*, *J. Exp. Biol.* **199**, 173 (1996).
8. D. O. Hebb, *The Organization of Behavior: A Neuropsychological Theory* (Wiley, New York, 1949).
9. E. Tulving, *Elements of Episodic Memory* (Clarendon, Oxford, UK, 1983).
10. L. R. Squire, *Psychol. Rev.* **99**, 195 (1992).
11. M. Abeles, *Corticotronics: Neural Circuits of the Cerebral Cortex*, (Cambridge Univ. Press, New York, 1991).
12. M. W. Howard, M. S. Fotedar, A. V. Datey, M. E. Hasselmo, *Psychol. Rev.* **112**, 75 (2005).
13. W. B. Levy, A. B. Hocking, X. Wu, *Neural Netw.* **18**, 1242 (2005).
14. L. M. Frank, E. N. Brown, M. Wilson, *Neuron* **27**, 169 (2000).
15. J. Ferbinteanu, M. L. Shapiro, *Neuron* **40**, 1227 (2003).
16. E. R. Wood, P. A. Dudchenko, R. J. Robitsek, H. Eichenbaum, *Neuron* **27**, 623 (2000).
17. J. A. Ainge, M. A. van der Meer, R. F. Langston, E. R. Wood, *Hippocampus* **17**, 988 (2007).
18. W. E. Skaggs, B. L. McNaughton, M. A. Wilson, C. A. Barnes, *Hippocampus* **6**, 149 (1996).
19. G. Dragoi, G. Buzsáki, *Neuron* **50**, 145 (2006).
20. J. R. Huxter, T. J. Senior, K. Allen, J. Csicsvari, *Nat. Neurosci.* **11**, 587 (2008).
21. G. Buzsáki, *Neuroscience* **31**, 551 (1989).
22. M. A. Wilson, B. L. McNaughton, *Science* **265**, 676 (1994).
23. K. Louie, M. A. Wilson, *Neuron* **29**, 145 (2001).
24. S. A. Deadwyler, T. Bunn, R. E. Hampson, *J. Neurosci.* **16**, 354 (1996).
25. H. Eichenbaum, P. Dudchenko, E. Wood, M. Shapiro, H. Tanila, *Neuron* **23**, 209 (1999).
26. A. Czurko, H. Hirase, J. Csicsvari, G. Buzsáki, *Eur. J. Neurosci.* **11**, 344 (1999).
27. H. Hirase, A. Czurko, J. Csicsvari, G. Buzsáki, *Eur. J. Neurosci.* **11**, 4373 (1999).
28. C. Geisler, D. Robbe, M. Zugaro, A. Sirota, G. Buzsáki, *Proc. Natl. Acad. Sci. U.S.A.* **104**, 8149 (2007).
29. K. M. Gothard, W. E. Skaggs, B. L. McNaughton, *J. Neurosci.* **16**, 8027 (1996).
30. J. O'Keefe, M. L. Recce, *Hippocampus* **3**, 317 (1993).
31. A. P. Maurer, S. L. Cowen, S. N. Burke, C. A. Barnes, B. L. McNaughton, *J. Neurosci.* **26**, 13485 (2006).
32. F. Sargolini *et al.*, *Science* **312**, 758 (2006).
33. B. L. McNaughton, F. P. Battaglia, O. Jensen, E. I. Moser, M. B. Moser, *Nat. Rev. Neurosci.* **7**, 663 (2006).
34. S. Fujisawa, A. Amarasingham, M. T. Harrison, G. Buzsáki, *Nat. Neurosci.* **11**, 823 (2008).
35. X. G. Li, P. Somogyi, A. Ylinen, G. Buzsáki, *J. Comp. Neurol.* **339**, 181 (1994).
36. G. Kreiman, C. Koch, I. Fried, *Nature* **408**, 357 (2000).
37. J. E. Lisman, *Neuron* **22**, 233 (1999).
38. L. F. Abbott, W. G. Regehr, *Nature* **431**, 796 (2004).
39. M. Rabinovich, R. Huerta, G. Laurent, *Science* **321**, 48 (2008).
40. M. B. Zugaro, L. Monconduit, G. Buzsáki, *Nat. Neurosci.* **8**, 67 (2005).

41. We thank H. Hirase for sharing his data and C. Curto, C. Geisler, S. Ozen, S. Fujisawa, K. Mizuseki, A. Sirota, D. W. Sullivan, and R. L. Wright for comments. Supported by NIH (NS34994 and MH54671), NSF (SBE 0542013), the James S. McDonnell Foundation, NSF (A.A.), the Swartz Foundation (V.I.), and the Robert Leet and Clara Guthrie Patterson Trust (E.P.).

### Supporting Online Material

www.sciencemag.org/cgi/content/full/321/5894/1322/DC1
SOM Text
Figs. S1 to S13
Table S1
Movie S1
References

29 April 2008; accepted 29 July 2008
10.1126/science.1159775

# Experimental Test of Self-Shielding in Vacuum Ultraviolet Photodissociation of CO

Subrata Chakraborty,[1] Musahid Ahmed,[2] Teresa L. Jackson,[1] Mark H. Thiemens[1]*

Self-shielding of carbon monoxide (CO) within the nebular disk has been proposed as the source of isotopically anomalous oxygen in the solar reservoir and the source of meteoritic oxygen isotopic compositions. A series of CO photodissociation experiments at the Advanced Light Source show that vacuum ultraviolet (VUV) photodissociation of CO produces large wavelength-dependent isotopic fractionation. An anomalously enriched atomic oxygen reservoir can thus be generated through CO photodissociation without self-shielding. In the presence of optical self-shielding of VUV light, the fractionation associated with CO dissociation dominates over self-shielding. These results indicate the potential role of photochemistry in early solar system formation and may help in the understanding of oxygen isotopic variations in Genesis solar-wind samples.

Isotope-selective photodissociation, or self-shielding, is a process that occurs because of two major parameters: (i) dissociation by isotope-dependent spectral line absorption, and (ii) differential photolysis that depends on the isotopic abundances. As a result, when the spectral line corresponding to the major species $^{16}O$ saturates, the lines corresponding to the minor species ($^{17}O$, $^{18}O$) do not, and equal dissociation of the minor species results with $\delta^{17}O = \delta^{18}O$. CO, the most abundant oxygen-bearing molecule in the nebula, satisfies these criteria, and self-shielding may occur, with equal dissociation rates of the minor isotopes. The consequence is preferential production of $^{17}O$ and $^{18}O$ atomic oxygen species in the region of the disk where self-shielding is effective. Such models assume that there is no other isotope effect associated with the photolysis, a hypothesis that has not been experimentally tested.

Isotopically selective photodissociation of CO is invoked as an important photochemical process in interstellar molecular clouds (*1*–*3*) to explain the observed abundance variation of minor isotopomers of CO ($^{13}C^{16}O$, $^{12}C^{18}O$, $^{12}C^{17}O$). CO self-shielding has been proposed to account for the observed meteoritic oxygen and nitrogen isotopic anomalies (*4*). Recently, this process was proposed to act in a very hot location near the proto-Sun [within 0.6 astronomical unit (AU)], and the heavy atomic oxygen ($^{17}O$ and $^{18}O$) was transported through the "X"-wind to the chondrule-forming zone, whereas calcium-aluminum–rich inclusions (CAIs, the first condensed solids) formed from the residual primordial nebular gas (*5*). To avoid the erasure of the anomaly by isotopic exchange (*6*), it was also suggested that the self-shielding occurred in a low-temperature prenebular molecular cloud (*7*).

Another model invoked a region at low temperatures (~50 K) at 30 AU from the proto-Sun and above the disk midplane as the probable location of CO self-shielding (*8*). Formation of water

**Table 1.** The data obtained for the 14 experimental runs (1 through 4 and 6 through 15) grouped in 6 different experimental configurations. The parameters used in the experiments are also displayed (see supporting online material for blank correction).

| Run # | Column density ($10^{17}$ mol/cm$^2$) | Exposure time (min) | Amount before fluorination (μmol) | Amount after fluorination (μmol) | $N_2$ blank (%) | $O_2$ blank from fluorination (μmol) | Measured $\delta^{17}O$ (‰) | Measured $\delta^{18}O$ (‰) | Blank corrected $\delta^{17}O$ (‰) | Blank corrected $\delta^{18}O$ (‰) | Slope | Ln form: $\delta^{17}O$ (‰) | Ln form: $\delta^{18}O$ (‰) |
|---|---|---|---|---|---|---|---|---|---|---|---|---|---|
| *1. 107.61 nm (11.52 ± 0.25 eV) at room temperature (in order of increasing column density)* | | | | | | | | | | | | | |
| 14 | 6.39 | 190 | 0.09 | 0.27 | 20.7 | 0.12 | 904.9 | 498.8 | 2136.9 | 1155.3 | 1.49 | 1143.2 | 767.9 |
| 15 | 10.6 | 510 | 0.25 | 0.45 | 13.0 | 0.14 | 5167.7 | 2430.0 | 8086.0 | 3792.6 | 1.41 | 2206.7 | 1567.1 |
| *2. 105.17 nm (11.79 ± 0.25 eV) at room temperature (in order of increasing column density)* | | | | | | | | | | | | | |
| 8 | 4.39 | 890 | 0.27 | 0.49 | 12.1 | 0.16 | 1147.1 | 686.2 | 1823.0 | 1081.2 | 1.42 | 1037.8 | 733.0 |
| 2 | 5.87 | 450 | 0.91 | 1.17 | 10.7 | 0.13 | 670.3 | 412.4 | 767.9 | 470.1 | 1.48 | 569.8 | 385.3 |
| 3 | 6.61 | 450 | 0.53 | 0.70 | 12.3 | 0.09 | 1177.9 | 700.2 | 1367.9 | 810.5 | 1.45 | 862.0 | 593.6 |
| 6 | 7.71 | 600 | 1.02 | 1.14 | 13.5 | – | 1809.7 | 1079.3 | 1809.7 | 1079.3 | 1.41 | 1033.1 | 732.1 |
| 7 | 11.9 | 860 | 0.57 | 0.64 | 27.4 | – | 2445.9 | 1407.0 | 2445.9 | 1407.0 | 1.41 | 1237.2 | 878.4 |
| *3. 105.17 nm (11.79 ± 0.25 eV) at dry-ice temperature (–66°C) (in order of increasing column density)* | | | | | | | | | | | | | |
| 4 | 6.09 | 450 | 0.34 | 0.65 | 20.2 | 0.18 | 2031.5 | 1424.0 | 3108.1 | 2170.9 | 1.22 | 1413.0 | 1154.0 |
| 9* | 7.54 | 825 | 0.20 | 35.05 | 0.10 | 34.81 | 43.5 | 43.5 | 5613.9 | 3676.4 | 1.22 | 1889.2 | 1542.5 |
| 11 | 9.37 | 450 | 0.17 | 0.41 | 10.6 | 0.20 | 2908.4 | 1905.3 | 6257.6 | 4081.9 | 1.22 | 1982.0 | 1625.7 |
| *4. 97.03 nm (12.78 ± 0.25 eV) at room temperature* | | | | | | | | | | | | | |
| 12 | 6.81 | 435 | 0.59 | 0.88 | 5.8 | 0.24 | 829.8 | 703.1 | 1161.2 | 978.7 | 1.12 | 805.4 | 717.2 |
| *5. 94.12 nm (13.17 ± 0.25 eV) at room temperature (in order of increasing column density)* | | | | | | | | | | | | | |
| 1 | 3.93 | 290 | 1.46 | 1.54 | 9.9 | – | 159.7 | 258.8 | 159.7 | 258.8 | 0.64 | 148.1 | 230.2 |
| 10† | 7.03 | 430 | 0.49 | 0.56 | 9.3 | 0.02 | 7.7 | 11.7 | 7.6 | 11.3 | 0.67 | 7.6 | 11.3 |
| *6. 94.12 nm (13.17 ± 0.25 eV) at dry-ice temperature (–66°C)* | | | | | | | | | | | | | |
| 13 | 6.81 | 435 | 0.67 | 0.72 | 23.9 | – | 542.9 | 873.7 | 446.1 | 718.6 | 0.69 | 459.6 | 662.1 |

*Air leaked through the oxygen sample tube after fluorination. Condensables are separated cryogenically and the noncondensables ($N_2$) are separated via gas chromatography. From the measured amount of separated $N_2$, the air $O_2$ amount was estimated and used for the blank correction with an air $O_2$ isotopic composition of 12.1 and 23.5‰ for $\delta^{17}O$ and $\delta^{18}O$, respectively. †For unknown reasons, the δ values were quite low compared to those of a similar experiment (#1), though the slope value ($\delta^{17}O/\delta^{18}O$) was the same.

---

[1] Department of Chemistry and Biochemistry, University of California, San Diego, La Jolla, CA 92093–0356, USA. [2] Chemical Sciences Division, Lawrence Berkeley National Laboratory, 1 Cyclotron Road, Berkeley, CA 94720, USA.

*To whom correspondence should be addressed. E-mail: mthiemens@ucsd.edu

ice with anomalous heavy isotopic composition from self-shielded CO dissociation can account for the hydrous minerals of the Allende meteorite (9). Two major assumptions were made: (i) The initial nebular oxygen isotopic composition was considered to be that of CAIs ($\delta^{17}O = \delta^{18}O = -40$‰), and (ii) no isotopic fractionation occurred during CO photodissociation other than via the opacity effect. We test this second assumption through experimental isotopic measurements in the relevant spectral region.

CO absorbs VUV photons at discrete spectral lines, and the excited (Rydberg) states are mostly predissociated through interaction with continuum states (2). Between 90 and 110 nm, there are numerous (~41) strong absorption bands. All bands are not equally effective for photodissociation of CO; the lines assigned to bands with the largest oscillator strength yield the predominant contribution to the rate of photodissociation (2, 10). The lines at 107.61, 94.12, 95.01, 97.03, and 94.01 nm are most effective at lower optical depth, and at higher optical depth (11) the lines at 95.01, 94.01, 96.89, and 92.58 nm are the most effective and contribute substantially to the dissociation rate. Under nebular conditions (in the presence of $H_2$, $H_2/CO \sim 10^4$), CO lines are removed from the absorption lines by $H_2$ and H and do not effectively contribute to dissociation (lines at 91.37, 91.73, 92.87, 93.00, 93.11, 93.17, 94.63, 96.44, 98.56, 100.26, and 106.31 nm are shielded by the absorption lines of $H_2$ and H). Apart from shielding by the $H_2$ and H lines, some lines of minor isotopomers (e.g., $^{13}CO$, $C^{17}O$, and $C^{18}O$) are shielded by CO lines because they lie close to one another and, therefore, there would be no appreciable self-shielding at the lines at 91.57, 91.60, 92.28, 95.62, 97.03, 98.98, and 107.61 nm (11). Hence, the total photodissociation rate is a combination of absorptions associated with many different transitions (table S1).

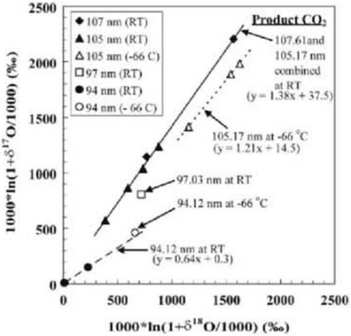

**Fig. 1.** Oxygen isotope composition of product $CO_2$ in a three-isotope plot (in logarithmic form to incorporate the nonlinearity in cross δ-plots for large δ values) showing wavelength-dependent fractionation pattern during CO photodissociation. The RT photolysis products at 107.61 and 105.17 nm [where the upper electronic state is $E^1\Pi$ and associated with "accidental-predissociation" via the channel $C(^3P) + O(^3P)$] are extended over a linear line with a slope value of 1.38 (with an intercept of 37.5‰), whereas the products at −66°C of 105.17 nm are fractionated more than the RT data and follow a relatively lower slope of 1.21 (with an intercept of 14.5‰). The composition of the product of 94.12 nm [which represents a different higher-state ($^1\Pi$) occupancy during VUV absorption and adiabatically dissociates to form $C(^1D)$ and $O(^1D)$] at RT follows a trend line of 0.64. The product of the same wavelength at a lower temperature (−66°C) shows larger fractionation, as observed for 105.17 nm, but has a slope value similar to that at RT. The photolysis product at 97.03 nm [which occupies another electronic state, $C^1\Sigma$, and dissociates through $C(^1D) + O(^3P)$ channel] lies in between the results of 94.12 and 105.17 nm.

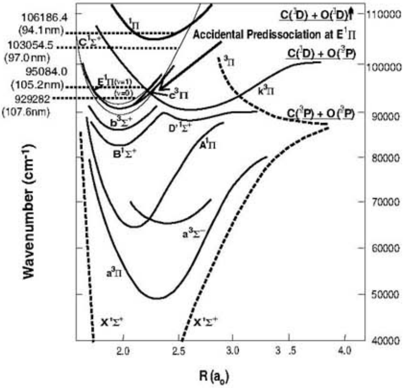

**Fig. 2.** Schematic diagram of the CO potential energy curve, showing the specific upper-level occupations by different VUV photon absorption in this experiment. The upper–electronic state $E^1\Pi$ is associated with "accidental predissociation," and its lower vibrational states are perturbed by another bound triplet state, $k^3\Pi$.

We used a windowless flow chamber with three stages of differential pumping (fig. S1) at the chemical dynamic beamline (9.0.2) located at the Advanced Light Source (ALS), Lawrence Berkeley National Laboratory. Ultrahigh-purity CO was passed through the cylindrical reaction chamber and was exposed to VUV synchrotron photons ($10^{16}$ photons/s) from the beamline to dissociate CO to C and O atoms along the line of CO flow. During the irradiation period, two stainless-steel spirals at the outlet of the reaction chamber were frozen in liquid nitrogen ($LN_2$) and collected the final product $CO_2$, formed by reaction of O atoms and bath gas CO. The $CO_2$ was converted to $O_2$ by means of the fluorination method (12), and the oxygen isotopic ratios were determined by isotope ratio mass spectrometry (see supporting online material for details).

We used four different wavelengths in our experiments—107.61, 105.17, 97.03, and 94.12 nm—to investigate the wavelength and upper electronic excited state–dependent isotopic fractionation in photodissociation. At several wavelengths, we ran the experiment at dry-ice temperatures to evaluate possible temperature dependencies.

Experimental results, conditions, sample amounts (with corresponding blanks), and isotopic compositions (measured and blank-corrected values) for each run are presented in Table 1. Raw data were corrected for fluorination blanks, determined through (measured amount) tank $CO_2$ fluorination of known oxygen isotopic composition. The isotopic composition of initial CO ($\delta^{17}O = 25.5$ and $\delta^{18}O = 51$‰) was determined several times by conversion to $CO_2$ through electric discharge (disproportionation) of CO (complete conversion), followed by fluorination. The heavy isotopes of O in the product $CO_2$ were relatively enriched compared to initial CO in a mass-independent manner (Table 1). The extent of isotopic enrichment was typically a few thousands per mil, depending on experimental conditions (column density and exposure time). This extent of isotopic fractionation is large compared to other known physical or chemical processes.

The oxygen isotopic composition of $CO_2$ is shown in Fig. 1, a three-isotope plot in logarithmic scale [to incorporate the nonlinearity in cross δ-plot for large δ values (13)]. The product $CO_2$ was enriched in heavy O isotopes in all cases compared to the initial CO composition, and the resultant isotopic compositions were wavelength dependent. The range of isotopic composition at particular wavelengths derived from variation of column densities and exposure times. All fractionations, except for photolysis at 94.12 nm, were highly mass independent. The room temperature (RT) photolysis products at 107.61 and 105.17 nm extended over a linear line with a slope of 1.38 (with an intercept of 37‰), whereas the lower-temperature (−66°C) products at 105.17 nm were fractioned to a greater extent than were the RT products and follow a lower slope of 1.21 (with an intercept of 14.5‰). The compositions of the RT product at 94.12 nm define a trend line of 0.64 (with an intercept of 0.3‰). Results for the same wavelength at a lower temperature (−66°C) exhibit a larger fractionation, as observed for 105.17 nm, but define a similar slope value (single points lie over the RT trend line of 94.12 nm). The photolysis product at 97.03 nm (RT) is between the results of 105.17 and 94.12 nm.

Self-shielding occurs as a result of optical shielding of short UV light of the various isotopically substituted CO molecules and, hence, the fractionation is dependent on isotopic abundance and not mass. The models assume that no other isotopic fractionation is associated with photodissociation. CO self-shielding is possible through the band at 105.17 nm, but not through the band at 107.61 nm (*2*), because of line broadening. In contrast, our results show that the dissociation products for the bands at 105.17 and 107.61 nm follow an identical fractionation trend (slope value of 1.38). A similar result (e.g., no self-shielding) was anticipated for the line at 97.03 nm, where we observe a mass-independent fractionated photodissociation product. Self-shielding was predicted at the 94.12-nm line; however, the experimental data display no self-shielding effect. Hence, the different isotope effects during CO dissociation at different wavelengths can derive from the nature of higher electronic states and dissociation dynamics. In a schematic energy-level diagram compiled from (*14*–*19*) for CO (Fig. 2), the upper electronic state $E^1\Pi$ (a bound Rydberg state) is associated with a type of predissociation termed "accidental-predissociation" (*20*). The lower rovibronic states of $E^1\Pi$ are perturbed by the presence of another triplet state, $k^3\Pi$ (*21*). Predissociation from the $E^1\Pi$ state takes place via the bound Rydberg $k^3\Pi$ state, assisted by a repulsive state to a near-resonance dissociative channel $C(^3P) + O(^3P)$. In this experiment, the vibrational energy states $v = 0$ and $v = 1$ of $E^1\Pi$ are populated by VUV photon absorption at 107.61 and 105.17 nm, respectively (Fig. 2), and lead to dissociation through the "accidental-predissociation" pathway, which proceeds via spin-orbit coupling between singlet and triplet states. Accidental predissociation is a well-known near-resonance effect that occurs for narrow ranges of rotational states (*J* states). Cacciani *et al.* (*22*, *23*) showed that for $v = 0$ (107.62 nm), the higher *J*-value states are perturbed by the $k^3\Pi$ state, whereas lower *J*-value states are perturbed for the $v = 1$ (105.17 nm) state. The VUV source used in our experiment is wide (full width at half maximum = 0.25 eV), and the two bands (105.17 and 107.62 nm) slightly overlap, but individually populate high rotational states (*J* states) at RT, which enhances the probability of accidental predissociation. Huge isotope effects have been observed previously as a result of near-resonance spin-orbit coupling between singlet-triplet states. Lim *et al.* (*24*) observed a large effect in Cl isotopes during a fluorescence study of OClO, and Bhattacharya *et al.* (*25*) observed a large isotope effect during $CO_2$ photodissociation and experimentally demonstrated that isotopic selective cross-over occurs between singlet and triplet surfaces due to spin-orbit coupling. A similar type of anomalous isotope-dependent predissociation in the $F^3\Pi_u$ ($v = 1$) state of $O_2$ has also been observed (*26*). At 97.03 nm, the upper electronic state $^1\Sigma$ is populated via another singlet-triplet cross-over and dissociates through the $C(^1D) + O(^3P)$ channel. This singlet-triplet crossing is different from the one associated with the $E^1\Pi$ state and yields a different isotope selectivity. The dissociation at 94.12 nm is relatively straightforward: The $^1\Pi$ state is populated and adiabatically dissociates through the $C(^1D)$ and $O(^1D)$ channel (*15*). Such dissociation usually yields a mass-dependent slope. The wavelength-dependent fractionation pattern (Fig. 1) emphasizes that the observed isotope effect is dominated by a physical-chemical dissociation mechanism of the CO molecule even in the presence of optical shielding of the light source. A mass-independent effect in $CO_2$ formation in the CO + O reaction (slope value close to unity) has been reported (*27*). The observed nonzero intercepts of 37.5 and 14.5‰ (respectively for 107.61 and 105.17 nm combined at RT and for 105.17 nm at −66°C) as shown in Fig. 1 may be explained through this recombination effect as a secondary fractionation step and accounts for the nonzero intercept with the starting isotopic composition, as expected for a multistage fractionation process. The temperature dependence of fractionation is not yet clear, but may arise because the probability of a near-resonance singlet-triplet transition varies inversely with temperature, as was seen for vibrational energy transfer between isotopomers of CO at low temperatures (*28*).

A numerical analysis of absorption and dissociation cross sections of different VUV lines has quantified their differential share at the edge of a molecular cloud in the total absorption cross section (table S1). Van Dishoeck and Black (*2*) estimated that 58% of $C^{18}O$ dissociates through band 31 (105.17 nm) at the center of the cloud; however, this band contributes little to the absorption (1.0%) and dissociation (1.4%) at the edge of the cloud. Other lines used in our experiment—107.61, 97.03, and 94.12 nm—contribute appreciably to the absorption and dissociation. During the exposure of a nebular gas by solar VUV radiation, the lines listed in table S1 are all available for CO dissociation (assuming VUV photodissociation of CO at the outer edge of the disk).

The actual isotopic composition of atomic oxygen is double that of the $CO_2$ that we measured, because $CO_2$ was produced after reaction of an O atom with normal CO. Determination of the O-atom compositions due to self-shielding (calculated through photon absorption by different isotopologs of CO with a fixed set of parameters, e.g., initial photon flux, column density, and exposure time) for all experiments in Table 1 yields a fractionation trend line of slope 1 in a three-isotope oxygen plot (fig. S2). The column density used in our experiments was optically thicker (due to experimental constraint) than that thought to pertain in the solar nebula and may complicate the simple absorption calculation (fig. S2) due to pressure broadening. Nevertheless, a highly enriched anomalously fractionated O-atom reservoir is possible through photodissociation of CO at various wavelengths. Considering the low-temperature data (which are more fractionated and slightly depleted in $^{17}O$ compared to RT experiments), we conclude that CO dissociation at the cold regions of the solar nebula is a potential site for the generation of more O-atom reservoirs with high amounts of $^{17}O$ and $^{18}O$ relative to $^{16}O$, but not via self-shielding.

Water plays a vital role in defining the oxygen isotopic distribution in the solar system as one-third of total oxygen resides in it (*9*, *29*–*32*). Recently, an extremely heavy oxygen isotopic composition (≈180‰ in $\delta^{17,\,18}O$) of nebular water in aqueous altered meteoritic minerals has been reported (*33*). Laboratory experiments have implied that oxygen isotope exchange between water in the gas phase and molten silicates at high temperatures can occur (*34*). Cumulative evidence suggests that there was an anomalous oxygen isotopic reservoir. Our experiments are consistent with the formation of such a reservoir; however, they also indicate that self-shielding is not required, thus eliminating spatial dependencies. The results do not necessarily require the initial isotopic composition of the nebula to be $\delta^{18}O = \delta^{17}O = -40‰$, although this composition is not ruled out.

### References and Notes

1. J. Bally, W. D. Langer, *Astrophys. J.* **255**, 143 (1982).
2. E. F. van Dishoeck, J. H. Black, *Astrophys. J.* **334**, 771 (1988).
3. S. R. Federman *et al.*, *Astrophys. J.* **591**, 986 (2003).
4. M. H. Thiemens, J. E. Heidenreich, *Science* **219**, 1073 (1983).
5. R. N. Clayton, *Nature* **415**, 860 (2002).
6. O. Navon, G. J. Wasserburg, *Earth Planet. Sci. Lett.* **73**, 1 (1985).
7. H. Yurimoto, K. Kuramoto, *Science* **305**, 1763 (2004).
8. J. R. Lyons, E. D. Young, *Nature* **435**, 317 (2005).
9. R. N. Clayton, *Annu. Rev. Earth Planet. Sci.* **21**, 115 (1993).
10. C. Letzelter, M. Eidelsberger, F. Rostas, J. Breton, B. Thieblemont, *Chem. Phys.* **114**, 273 (1987).
11. S. Warin, J. J. Benayoun, Y. P. Viala, *Astron. Astrophys.* **308**, 535 (1996).
12. S. K. Bhattacharya, M. H. Thiemens, *Z. Naturforsch. A* **44a**, 435 (1989).
13. E. D. Young, G. Albert, H. Nagahara, *Geochem. Cosmochim. Acta* **66**, 1095 (2002).
14. S. Wilson, *Int. J. Quantum Chem.* **12**, 609 (1977).
15. D. L. Cooper, K. Kirby, *J. Chem. Phys.* **87**, 424 (1987).
16. K. Kirby, D. L. Cooper, *J. Chem. Phys.* **90**, 4895 (1989).

17. J. Baker *et al.*, *Chem. Phys.* **178**, 569 (1993).
18. A. Mellinger, C. R. Vidal, *J. Chem. Phys.* **101**, 104 (1994).
19. J. Baker, F. Launay, *Chem. Phys. Lett.* **415**, 296 (2005).
20. J. D. Simmons, S. G. Tilford, *J. Mol. Spectrosc.* **49**, 167 (1974).
21. J. Baker, F. Launay, *J. Mol. Spectrosc.* **165**, 75 (1994).
22. P. Cacciani, W. Hogervorst, W. Ubachs, *J. Chem. Phys.* **102**, 8308 (1995).
23. P. Cacciani *et al.*, *Astrophys. J.* **499**, L223 (1998).
24. G. Lim, S. M. Lim, S. K. Kim, Y. S. Choi, *J. Chem. Phys.* **111**, 456 (1999).
25. S. K. Bhattacharya, J. Savarino, M. H. Thiemens, *Geophys. Res. Lett.* **27**, 1459 (2000).
26. B. R. Lewis, S. T. Gibson, J. P. England, G. Stark, J. B. West, *J. Chem. Phys.* **116**, 3286 (2002).
27. A. Pandey, S. K. Bhattacharya, *J. Chem. Phys.* **124**, 234301 (2006).
28. M. L. Turnidge, J. P. Reid, P. W. Barnes, C. J. S. M. Simpson, *J. Chem. Phys.* **108**, 485 (1998).
29. E. Anders, N. Grevesse, *Geochem. Cosmochim. Acta* **53**, 197 (1989).
30. B. Fegley Jr., *Space Sci. Rev.* **92**, 177 (2000).
31. E. D. Young, *Philos. Trans. R. Soc. Lond. A* **359**, 2095 (2001).
32. E. D. Young, *Earth Planet. Sci. Lett.* **262**, 468 (2007).
33. N. Sakamoto *et al.*, *Science* **317**, 231 (2007).
34. Y. Yu, R. H. Hewins, R. N. Clayton, T. K. Mayeda, *Geochem. Cosmochim. Acta* **59**, 2095 (1995).

35. This work was supported by NASA grant NNX07AJ81G under Origins and by the director, Office of Energy Research, Office of Basic Energy Sciences, Chemical Sciences Division of the U.S. Department of Energy under contract DE-AC02-05CH11231. Three reviewers are thanked for helpful suggestions that improved the manuscript.

**Supporting Online Material**
www.sciencemag.org/cgi/content/full/321/5894/1328/DC1
Methods
Figs. S1 and S2
Table S1
References

15 April 2008; accepted 11 July 2008
10.1126/science.1159178

---

# Identification of Active Gold Nanoclusters on Iron Oxide Supports for CO Oxidation

Andrew A. Herzing,[1,2] Christopher J. Kiely,[1]* Albert F. Carley,[3] Philip Landon,[3] Graham J. Hutchings[3]*

Gold nanocrystals absorbed on metal oxides have exceptional properties in oxidation catalysis, including the oxidation of carbon monoxide at ambient temperatures, but the identification of the active catalytic gold species among the many present on real catalysts is challenging. We have used aberration-corrected scanning transmission electron microscopy to analyze several iron oxide–supported catalyst samples, ranging from those with little or no activity to others with high activities. High catalytic activity for carbon monoxide oxidation is correlated with the presence of bilayer clusters that are ~0.5 nanometer in diameter and contain only ~10 gold atoms. The activity of these bilayer clusters is consistent with that demonstrated previously with the use of model catalyst systems.

Gold nanoparticles on oxide supports are being used to catalyze an increasing number of reactions (*1–6*), but there is continuing interest in the relatively simple low-temperature oxidation of CO (*1–3, 7*), especially concerning the nature of the active species. Some proposals emphasize the size and morphology of the gold particle and its interface with the support (*1, 8*), whereas others postulate that the metal oxidation state (*9, 10*) and support material can have strong effects (*1, 11*). Most of the fundamental insights into this reaction have come from well-defined model studies (*12–15*) in which specific structures are tailor-made (*14*). However, the difficulty lies in linking these informative model studies to those carried out on real catalysts, which are inherently more complex. Here, we report a microscopy study of an Au/FeO$_x$ catalyst and demonstrate that, among a number of gold nanostructures present, the origin of the activity is associated uniquely with gold bilayer nanoclusters that are ~0.5 nm in diameter and contain ~10 Au atoms.

Gold supported on FeOOH is a highly active catalyst for the low-temperature oxidation of CO (*16*), and we recently reported a link between catalyst performance and catalyst drying conditions (*10*). A pair of 2.9 atomic % Au/FeO$_x$ samples (denoted samples 1 and 2) were derived from the same coprecipitated precursor. Sample 1 was dried in a tube furnace (static air; furnace was ramped after insertion at 15°C/min to 120°C; 16 hours), whereas sample 2 was dried in a gas chromatography (GC) oven (flowing air; sample inserted into the furnace at 120°C; 16 hours). The Au loading in each was identical, and the underlying disordered FeOOH supports had similar surface areas (~190 m$^2$ g$^{-1}$). X-ray energy-dispersive spectroscopy (XEDS) analysis and high-angle annular dark-field (HAADF) imaging experiments (*10*) indicated that both samples contained 2- to 15-nm Au particles, with mean particle sizes of 5.4 nm for sample 1 and 7.0 nm for sample 2.

If the CO oxidation activity was dictated solely by the Au particle size, as some researchers have suggested (*1, 8*), then these two samples should have exhibited similar activities. In fact, sample 1 would probably be expected to have a slightly better performance by virtue of the Au particles being slightly smaller, on average. However, catalytic testing of these two samples under standard conditions (total flow rate of 66,000 h$^{-1}$; 0.5 volume % CO) revealed that sample 2 achieved 100% CO conversion at 25°C, whereas sample 1 gave only trace CO conversion (<1%). Even at much higher flow rates, sample 2 remained active (i.e., at a total flow rate of 450,000 vol.gas/vol.catalyst.h; the conversion was 25%), whereas sample 1 was totally inactive. Previously (*10*), we were unable to determine the origin of this marked effect because of the resolution and sensitivity limitations of the characterization techniques available. We consider that at least two possibilities exist to explain this difference: (i) There could be highly dispersed Au species present in sample 2 that were beyond the resolution limit of the conventional HAADF and

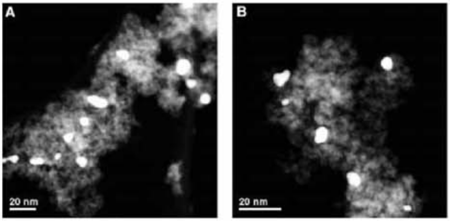

**Fig. 1.** Low-magnification aberration-corrected HAADF-STEM images from **(A)** the inactive, tube furnace catalyst (sample 1) and **(B)** the highly active, GC oven catalyst (sample 2). Au particle size distribution in both samples appears to be very similar at this magnification.

---

[1] Center for Advanced Materials and Nanotechnology, Lehigh University, 5 East Packer Avenue, Bethlehem, PA 18015–3195, USA. [2] National Institute of Standards and Technology, Surface and Microanalysis Science Division, 100 Bureau Drive, Mailstop 8371, Gaithersburg, MD 20899–8371, USA. [3] Cardiff Catalysis Institute School of Chemistry, Cardiff University, Cardiff, CF10 3AT, UK.

*To whom correspondence should be addressed. E-mail: chk5@lehigh.edu (C.J.K.); hutch@cardiff.ac.uk (G.J.H.)

scanning transmission electron microscopy (STEM)–XEDS techniques used previously, or (ii) the active catalyst contained some form of cationic Au species that was absent in the inactive sample. These two possibilities need not be mutually exclusive.

To investigate this unexpected difference in reactivity, we re-examined the samples using a state-of-the-art JEOL 2200FS in STEM mode equipped with a double-hexapole spherical aberration corrector manufactured by CEOS GmbH (*17*). The improvement to the HAADF image resolution, from the use of a 0.1-nm diameter aberration-corrected STEM probe containing 50 pA of current, makes this an ideal instrument to test whether there were Au species present in the highly active sample that were not detected earlier (*10*). Previously, this method has successfully been used to image atomic dispersions in the La/Al$_2$O$_3$, Pt/Al$_2$O$_3$, and Au/TiO$_2$ systems (*18*). The lower-magnification HAADF images for each of the dried Au/FeO$_x$ catalysts (Fig. 1, A and B) confirm the earlier results, with particles between 2 and 15 nm in diameter. However, at higher magnification (Fig. 2, A to D, and figs. S1 and S2), the actual Au particle size distribution and morphology in these samples are quite different. Both samples contain larger (2 to 15 nm) Au particles and a considerable number of individual Au atoms (indicated by white circles) dispersed on the iron oxide surface.

The observation of these individual atoms ensures that we are now resolving all of the types of Au species present. However, in addition a large population of subnanometer Au clusters was found in the active sample 2 (circled in black in Fig. 2, C and D) (see also fig. S1) that was not detected in the inactive sample. These Au clusters, the majority of which were 0.2 to 0.5 nm in diameter, contain at most only a few Au atoms. The contrast level exhibited by the 0.2- to 0.3-nm clusters, which are predominant in Fig. 2D, is similar to that of the individual Au atoms, implying that they are monolayer structures. In comparison, the 0.5-nm clusters highlighted in Fig. 2C exhibit markedly higher contrast in the HAADF image than that of the 0.2- to 0.3-nm clusters, suggesting that these larger clusters are most likely bilayers of Au.

Determination of the exact number of atoms in these various structures is complicated by several factors, including the slight contraction of the Au–Au bond distance known to occur in particles of this size (*19*). However, a rough estimate is still informative, and bilayers of ~0.5-nm lateral dimension would contain ~10 atoms (fig. S3A). In comparison, the 0.2- to 0.3-nm clusters of similar contrast to monolayers could contain about three to four atoms (fig. S3B). In contrast, an estimate based on the volumetric packing density of Au (~59 atoms/nm$^3$) suggests that the larger nanoparticles (5 to 7 nm) would contain 1900 to 5250 atoms if they have a hemispherical geometry. Thus, the subnanometer clusters and individual atoms observed in the highly active sample represent only a very minor fraction of the total Au content.

We used atomic-resolution STEM imaging to estimate the number fraction of the total Au particles represented by both clusters and nanoparticles by surveying several support areas that had ~100 larger nanoparticles, along with their neighboring vicinities (*17*). In terms of their frequency of observation, the individually adsorbed Au atoms represented 44 ± 4.5% of the Au species, whereas 19 ± 3.4% were 0.2- to 0.3-nm clusters, 18 ± 3.0% were 0.3- to 0.5-nm clusters, and 19 ± 3.5% were particles >1 nm (~50% were >5 nm).

However, considering the number of Au atoms in each of these structures (as discussed above) suggests that the individual atoms represent only 0.13 ± 0.07 atomic % and that the monolayer and bilayer subnanometer clusters combined represent only 1.05 ± 0.72 atomic % of the total Au loading (*18*), with the remaining 98.82 ± 0.80 atomic % of Au contained in the larger particles. Because of the very large disparity in the number of atoms they contain, the number of subnanometer clusters would have to exceed that of the 5-nm particles by a margin of nearly four to one for them to represent just 2 atomic % of the total Au loading. Therefore, it is probable that these minority Au species would not be easily detected with traditional "bulk" techniques such as extended x-ray absorption fine structure or Mossbauer spectroscopy, or even by surface analysis techniques such as x-ray photoelectron spectroscopy (XPS), because their contribution to the total signal would be minimal compared with that of the larger nanoparticles (*17*).

The statistical accuracy of the current HAADF analysis must be considered, because undercounting of the subnanometer Au clusters may result from the nature of the STEM imaging process in an aberration-corrected instrument. The ability to detect single atoms on an oxide is highly dependent on the vertical position of the focused electron probe relative to the surface (*20*). Because adsorbed atoms can be present on either the top or bottom surface of the underlying oxide particle, imaging with single-atom resolution is possible only when one of the surfaces is exactly in focus. Practically, this limitation means that in any given image, single atoms are probably only detected on one surface of the support particle, and atoms on the opposite side may not be visible, whereas larger nanoparticles can be detected on either side of the support over a much wider range of defocus values. In the intermediate case of 0.2- to 0.5-nm clusters, it is not clear if the same narrow defocus range required to resolve individual atoms is necessary. However, even if it is pessimistically assumed that our analysis has detected only 50% of the total number of all the individual Au atoms, the atomically dispersed Au would still represent only 61 ± 3.6% of the total number of

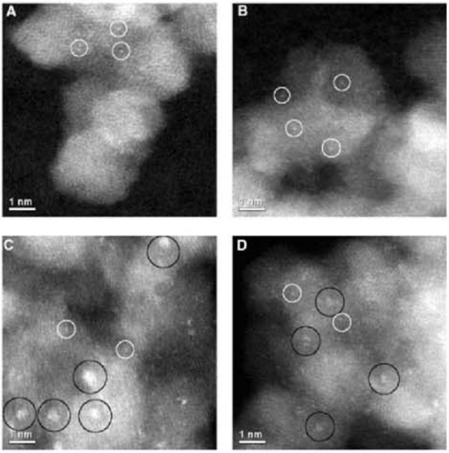

**Fig. 2.** High-magnification aberration-corrected STEM-HAADF images of (**A** and **B**) the inactive (sample 1) and (**C** and **D**) the active (sample 2) Au/FeO$_x$ catalysts acquired with the aberration-corrected JEOL 2200FS. The white circles indicate the presence of individual Au atoms, whereas the black circles indicate subnanometer Au clusters consisting of only a few atoms. Note the presence and image intensity difference of two distinct cluster-types: In (C) there are 0.5 nm higher-contrast clusters, whereas in (D) 0.2- to 0.3-nm low-contrast clusters dominate. This difference indicates that bilayer and monolayer subnanometer Au clusters are present in the active catalyst.

Au species, or ~0.25 ± 0.2 atomic % of the total Au loading.

The observation that the active species in our Au/$FeO_x$ catalysts consist of subnanometer clusters differs from numerous earlier investigations that identified 2- to 5-nm particles as the critical "nanostructure." However, a number of recent experimental and theoretical (*21*–*23*) studies have suggested that the CO oxidation activity should continue to increase as the Au particle size approaches 1 nm because of the presence of a larger fraction of Au atoms with low coordination in the smaller particles. Low-coordination Au atoms possess a d-band that is closer to the Fermi level than their close-packed counterparts, so they can adsorb $O_2$ molecules more readily. More specifically, Falsig *et al.* predicted that adsorption energies for CO and O are ideally suited for maximizing the reaction rate of CO oxidation at sixfold coordinated Au corner atoms, whereas the adsorption energies at close-packed Au faces are inferior for this purpose (*23*). Because clusters smaller than 1 nm should have an even greater fraction of low-coordinated Au atoms, reaching ~90% as a cluster size of 0.5 nm is approached, the role of subnanometer clusters may be crucial. Rashkeev *et al.* (*24*) have recently presented HAADF evidence that subnanometer mono-, bi-, and trilayer Au clusters coexisted in active Au/$TiO_2$ catalysts, although they were unable to isolate the relative importance of each of these subnanometer species and did not report any spectroscopic measurements to determine the possible role of substrate surface chemistry.

Scanning tunneling microscopy studies on model catalysts by Matthey *et al.* (*15*) showed that subtle changes in the chemistry of an oxide surface could alter the energetically favorable Au structures that it stabilized and supported. Specifically, an oxygen-rich $TiO_2$ (110) surface could stabilize a range of Au species from one to seven atoms in size. In contrast, single Au atoms and Au trimers were the only stable configurations on a reduced $TiO_2$ (110) surface, whereas weakly bonded two-dimensional Au raftlike species were the only stable structures on a stoichiometric $TiO_2$ (110) surface. Similar oxygen-rich surfaces to those reported for $TiO_2$ have also been identified for $FeO_x$ (*25*); however, to our knowledge, systematic surface science studies and first-principle calculations of the stable Au structures present on FeOOH or $Fe_2O_3$ have not yet been performed.

On the basis of the observations of the two dried catalysts alone, we are unable to definitively comment on whether the bilayer 0.5-nm clusters, the monolayer 0.2- to 0.3-nm clusters, or both are responsible for the high activity observed or whether some subtle substrate chemistry effect is coming into play. Although individual Au atoms and larger (3 to 5 nm) particles are stable on both catalysts, the subnanometer Au clusters were only stable on the surface of catalyst 2 dried under a flowing air. The critical role played by such slight changes in the catalyst preparation route may help to explain the sometimes radically differing activities reported. We have used XPS to probe the nature of the surface species present in both samples. Analysis of the Au(4f) spectra (fig. S4.1) showed that, in both catalysts, the Au($4f_{7/2}$) binding energy was 85.1 eV, characteristic of $Au^+$ species. The signal from sample 1 shows some broadening to higher binding energy that probably arose from a small amount of $Au^{3+}$, most likely present as AuOOH. The presence of hydroxylated Au species in this inactive sample suggests that the lack of air circulation during the drying process inhibits the removal of the hydroxyl species from the catalyst surface, whereas this process occurs more efficiently under flowing air conditions.

This explanation was confirmed by the O(1s) and C(1s) spectra from these samples (figs. S4.2 and S4.3, respectively). Both catalysts exhibit a main O(1s) component characteristic of oxidic oxygen ($O^{2}$ ) at 530.4 eV, together with a shoulder at 531.8 eV. The latter feature originates from a combination of hydroxyl and carbonate species and is much more pronounced in sample 1. The C(1s) spectra, which show clear evidence of carbonate species, are similar for both. Therefore, the higher intensity of the O(1s) shoulder at 531.8 eV in the inactive catalyst 1 arises from the increased presence of hydroxyl groups relative to the active catalyst 2 dried in flowing air. This higher degree of hydroxylation and reduction of sample 1 seems to enhance the ability of the subnanometer clusters to sinter into larger particles and thus deactivate the catalyst. Hence, on the basis of the evidence presented so far, we are unable to determine whether it is the presence of subnanometer clusters or the differing degree of hydroxylation of the support that is controlling the activity.

Three separate portions of the highly active catalyst 2, denoted 3, 4, and 5, were calcined (3 hours at 400°, 550°, and 600°C, respectively). These heat treatments converted the support material to crystalline $Fe_2O_3$ and progressively reduced the surface area (catalysts 2: 190 $m^2\ g^{-1}$, 3: 45 $m^2\ g^{-1}$, 4: 16 $m^2\ g^{-1}$, and 5: 11 $m^2\ g^{-1}$). Atomic absorption spectroscopy confirmed that all of the Au (2.9 atomic %) was retained. CO conversion decreased from 100% in the fresh, uncalcined state to 91% (400°C), 31% (550°C), and <1% (600°C).

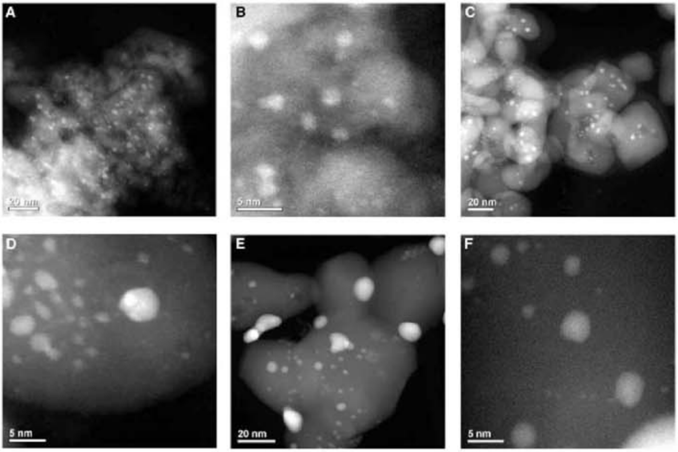

**Fig. 3.** Aberration-corrected STEM-HAADF images of the active 2.9 atomic % Au/$FeO_x$ catalyst 2 calcined for 3 hours at (**A** and **B**) 400°C (sample 3), (**C** and **D**) 550°C (sample 4), and (**E** and **F**) 600°C (sample 5). The heat-treatment procedures have substantially decreased the population of subnanometer Au clusters relative to the highly active, dried catalyst, while at the same time they have increased the population of particles in the 1- to 3-nm range.

Aberration-corrected STEM-HAADF images (Fig. 3, A to F, and figs. S5.1 to 5.3) revealed that, although substantial particle sintering had occurred in all calcined catalysts, each sample also retained a population of the subnanometer clusters and individual Au atoms previously seen in the dried catalyst that had persisted through the various calcination treatments.

The number frequency of the various gold species encountered in samples 2, 3, 4, and 5 is summarized in Fig. 4. The number fraction of atomically dispersed species drops from ~44% to 35% across this sample set, whereas, simultaneously, the number fraction of particles greater than 1 nm progressively increases from 19 to 35%. However, our previous deductions from comparing samples 1 and 2 indicate that the supported subnanometer cluster species (and not the dispersed Au atoms or >1-nm particles) are active for CO conversion. It is also apparent from Fig. 4 that the number population of monolayer clusters remains relatively constant at ~19%, whereas the bilayer cluster frequency gradually drops from 18% to <5% across this same sample set. Hence, the dramatic decrease in catalytic activity exhibited by samples 3, 4 and 5 can be directly correlated to the marked decrease in the number density of the 0.5-nm bilayer clusters as a result of their sintering into less active 1- to 2-nm Au particles.

XPS of samples 3, 4, and 5 (fig. S6) showed no notable difference in either of the Au(4f), Fe(3s), or Fe(2p) profiles (fig. S6.1 and 6.2) associated with this series of calcined catalysts. The O(1s) signals (fig. S6.3) are also all similar, with a high–binding energy tail indicating the presence of some residual hydroxyl and carbonate species, but these are very different from the dried sample (spectra shown in Fig. 5). The presence of carbonate species is confirmed by the weak, high binding feature in the C(1s) spectra (fig. S6.4). This feature is broader for sample 5, possibly reflecting carbonate species in distinct chemical environments, and is consistent with small differences in the high–binding energy tail in the O(1s) spectrum for this sample.

To determine whether the small differences in samples 3 and 4 and the larger differences with the other samples correlate with the catalytic performance, we deconvoluted the O 1s signals into oxide and the higher–binding energy hydroxyl and carbonate species to obtain the relative fractions of each species present. However, the data for either the relative area percent of the higher–binding energy species (samples 2: 60%, 3: 28%, 4: 34%, and 5: 47%) or the hydroxyl/oxide ratio (samples 2: 1.5, 3: 0.4, 4: 0.5, and 5: 0.9) do not correlate with the observed activity trend. Thus, the similarity in the surface chemistry of samples 3 and 4, in particular, and the Au oxidation state in these calcined samples strongly imply that the progressive decrease in catalytic activity upon sintering is attributable to the gradual decrease in the population of the subnanometer bilayer clusters of gold.

Theoretical and model studies (*23*, *26*–*29*) have shown that a critical factor in the catalytic activity of Au is the ability of the clusters to simultaneously adsorb both reactant molecules. Yoon *et al.* and Hakkinen *et al.* (*27*, *28*) showed that the smallest Au cluster on MgO known to be active for CO oxidation is an octamer. Our observations are consistent with these theoretical studies, because the active bilayer subnanometer clusters in our system contain ~10 atoms, whereas the monolayer clusters (which have only three to four atoms) and the isolated Au atoms appear to be essentially inactive for CO oxidation.

Finally, CO oxidation activity of model Au catalysts on $TiO_2$ surfaces is maximized when the Au structures are two atomic layers thick (*14*, *28*, *29*), resulting in turnover frequencies (TOFs) as high as $3.7\ s^{-1}$. In the present case, the TOF of catalyst 2 exhibiting 100% CO conversion was initially calculated to be $0.016\ s^{-1}$ under standard conditions and $0.027\ s^{-1}$ at the higher flow rate where total conversion (which is a more reliable estimate of the catalyst activity) was not observed. However, if the TOF is recalculated assuming that the bilayer clusters are the only active species and using a reasonable estimate of the fraction of the total Au that they contain (0.6 atomic %), the result is a TOF of $2.7\ s^{-1}$ at the standard conditions and $3.5\ s^{-1}$ at the higher–flow rate condition. These re-estimated TOF values are reasonably similar to the value of $3.7\ s^{-1}$ of the model Au/$TiO_2$ catalyst (*14*).

These studies describe the full range of active and inactive Au species that are present within supported Au/$FeO_x$ and Au/$Fe_2O_3$ catalysts. Subtle changes in sample-preparation route and calcination temperature can influence the formation, stability, and relative population of these various Au species. Herein, we have reported that highly active subnanometer Au clusters can be synthesized with a traditional chemical preparation route. Although the highest-activity catalysts correspond to uncalcined materials, experiments involving systematic calcination treatments have allowed us to

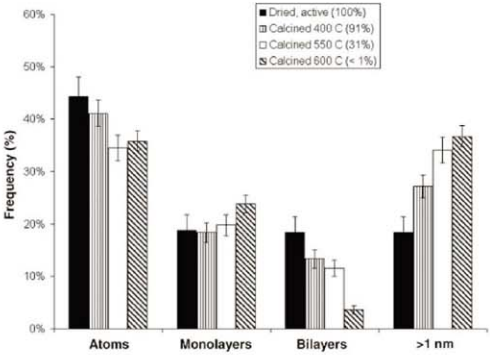

**Fig. 4.** Relative populations of (i) dispersed Au atoms, (ii) 0.2- to 0.3-nm monolayer Au clusters, (iii) 0.5-nm bilayer Au clusters, and (iv) Au nanoparticles >1 nm in diameter, as a function of catalyst calcination temperature and measured CO conversion. The error bars correspond to two SDs on the size measurements.

**Fig. 5.** O(1s) photoemission spectra from the Au/$Fe_2O_3$ catalysts (**A**) dried at 120°C and then calcined at (**B**) 400°C, (**C**) 550°C, and (**D**) 600°C.

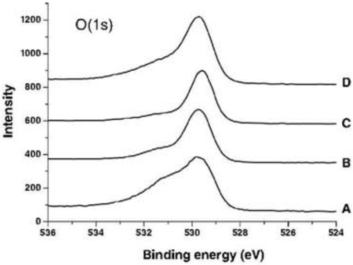

deduce that it is primarily the 0.5-nm bilayer clusters, rather than 0.2- to 0.3-nm monolayer Au clusters, that are active for CO oxidation on $FeO_x$ supports.

### References and Notes

1. M. Haruta, *CATTECH* **6**, 102 (2002).
2. M. Haruta, *Gold Bull.* **37**, 27 (2004).
3. A. S. K. Hashmi, G. J. Hutchings, *Angew. Chem. Int. Ed.* **45**, 7896 (2006).
4. M. D. Hughes *et al.*, *Nature* **437**, 1132 (2005).
5. D. I. Enache *et al.*, *Science* **311**, 362 (2006).
6. A. Corma, P. Serna, *Science* **313**, 332 (2006).
7. J. Guzman, S. Carrettin, A. Corma, *J. Am. Chem. Soc.* **127**, 3286 (2005).
8. J. J. Pietron, R. M. Stroud, D. R. Rolison, *Nano Lett.* **2**, 545 (2002).
9. J. Guzman, B. C. Gates, *J. Am. Chem. Soc.* **126**, 2672 (2004).
10. G. J. Hutchings *et al.*, *J. Catal.* **242**, 71 (2006).
11. M. M. Schubert *et al.*, *J. Catal.* **197**, 113 (2001).
12. R. Meyer, C. Lemire, Sh. K. Shaikhutdinov, H.-J. Freund, *Gold Bull.* **37**, 72 (2004).
13. M. Valden, X. Lai, D. W. Goodman, *Science* **281**, 1647 (1998).
14. M. S. Chen, D. W. Goodman, *Science* **306**, 252 (2004), published online 26 August 2004; 10.1126/science.1102420.
15. D. Matthey *et al.*, *Science* **315**, 1692 (2007).
16. N. A. Hodge *et al.*, *Catal. Today* **72**, 133 (2002).
17. Materials and methods are available as supporting material on *Science* Online.
18. M. Varela *et al.*, *Annu. Rev. Mater. Res.* **35**, 539 (2005).
19. C. W. Mays *et al.*, *Surf. Sci.* **12**, 134 (1968).
20. S. Wang *et al.*, *Nat. Mater.* **3**, 143 (2004).
21. T. V. W. Janssens *et al.*, *Top. Catal.* **44**, 15 (2007).
22. W. Yan *et al.*, *J. Phys. Chem. B* **109**, 10676 (2005).
23. H. Falsig *et al.*, *Angew. Chem. Int. Ed.* **47**, 4835 (2008).
24. S. Rashkeev *et al.*, *Phys. Rev. B* **76**, 035438 (2007).
25. A. Bongiorno, U. Landman, *Phys. Rev. Lett.* **95**, 106102 (2005).
26. M. Abu Haija *et al.*, *Surf. Sci.* **600**, 1497 (2006).
27. B. Yoon *et al.*, *Science* **307**, 403 (2005).
28. H. Hakkinen *et al.*, *Angew. Chem. Int. Ed.* **42**, 1297 (2003).
29. V. A. Bondzie *et al.*, *Catal. Lett.* **63**, 143 (1999).

30. We thank the Athena project of the Engineering and Physical Sciences Research Council, NSF, NASA, and the National Research Council Postdoctoral Associate program for funding this work.

**Supporting Online Material**
www.sciencemag.org/cgi/content/full/321/5894/1331/DC1
Materials and Methods
Figs. S1 to S6

25 April 2008; accepted 23 July 2008
10.1126/science.1159639

---

# Laser Frequency Combs for Astronomical Observations

**Tilo Steinmetz,[1,2] Tobias Wilken,[1] Constanza Araujo-Hauck,[3] Ronald Holzwarth,[1,2] Theodor W. Hänsch,[1] Luca Pasquini,[3] Antonio Manescau,[3] Sandro D'Odorico,[3] Michael T. Murphy,[4] Thomas Kentischer,[5] Wolfgang Schmidt,[5] Thomas Udem[1]***

**A direct measurement of the universe's expansion history could be made by observing in real time the evolution of the cosmological redshift of distant objects. However, this would require measurements of Doppler velocity drifts of ~1 centimeter per second per year, and astronomical spectrographs have not yet been calibrated to this tolerance. We demonstrated the first use of a laser frequency comb for wavelength calibration of an astronomical telescope. Even with a simple analysis, absolute calibration is achieved with an equivalent Doppler precision of ~9 meters per second at ~1.5 micrometers—beyond state-of-the-art accuracy. We show that tracking complex, time-varying systematic effects in the spectrograph and detector system is a particular advantage of laser frequency comb calibration. This technique promises an effective means for modeling and removal of such systematic effects to the accuracy required by future experiments to see direct evidence of the universe's putative acceleration.**

Recent cosmological observations suggest that the universe's expansion is accelerating. Several lines of evidence corroborate this, including results from distant supernovae (*1*, *2*), the cosmic microwave background (*3*), and the clustering of matter (*4*, *5*). However, the current observations are all essentially geometric in nature, in that they map out space, its curvature, and its evolution. In contrast, a direct and dynamical determination of the universe's expansion history is possible by observing the slow drift of cosmological redshifts, *z*, that is inevitable in any evolving universe (*6*). No particular cosmological model or theory of gravity would be needed to interpret the results of such an experiment. However, the cosmological redshift drift is exceedingly small and difficult to measure; for currently favored models of the universe, with a cosmological constant parametrizing the acceleration, the redshifts of objects drift by less than ~1 $\mathrm{cm\,s^{-1}\,year^{-1}}$ (depending on their redshifts).

Nevertheless, the suggestion that the so-called Lyman-α "forest" seen in high-redshift quasar spectra is the best target for this experiment (*7*) was recently supported by cosmological hydrodynamical simulations (*8*). The forest of absorption lines is caused by the Lyman-α transition arising in neutral hydrogen gas clouds at different redshifts along the quasar sight-lines. Detailed calculations with simulated quasar spectra show that the planned 42-m European Extremely Large Telescope (E-ELT), equipped with the proposed Cosmic Dynamics Experiment (CODEX) spectrograph (*9*), could detect the redshift drift convincingly with 4000 hours of observing time over a ~20-year period (*8*). Therefore, as the observation is feasible (in principle), overcoming the many other practical challenges in such a measurement is imperative. Important astrophysical and technical requirements have been considered in detail, and most are not difficult to surmount (*8*, *10*). One (but not the only) extremely important requirement is that the astronomical spectrographs involved must have their wavelength scales calibrated accurately enough to record ~1 $\mathrm{cm\,s^{-1}}$ velocity shifts (~25-kHz frequency shifts) in the optical range. Moreover, this accuracy must be repeatable over ~20-year time scales.

Although the redshift drift experiment requires demanding precision and repeatability, precisely calibrated astronomical spectrographs have several other important applications. For example, Jupiter- and Neptune-mass extrasolar planets have been discovered by the reflex Doppler motion of their host stars (*11*–*13*), but detecting Earth-mass planets around solar-mass stars will require ~5 $\mathrm{cm\ s^{-1}}$ precision maintained over several-year time scales (*14*). Another example is the search for shifts in narrow quasar absorption lines caused by cosmological variations in the fundamental constants of nature (*15*–*17*). Recent measurements (*18*–*21*) achieve precisions of ~20 $\mathrm{m\,s^{-1}}$, but the possibility of hidden systematic effects, and the increased photon-collecting power of future ELTs, warrant much more precise and accurate calibration over the widest possible wavelength range.

Laser frequency combs (LFCs) offer a solution because they provide an absolute, repeatable wavelength scale defined by a series of laser modes equally spaced across the spectrum. The train of femtosecond pulses from a mode-locked laser occurs at the pulse repetition rate, $f_{rep}$, governed by the adjustable laser cavity length. In the frequency domain, this yields a spectrum, $f_n = f_{ceo} + n \times f_{rep}$, with modes enumerated by an integer $n \sim 10^5$ to $10^6$. The carrier envelope offset frequency, $f_{ceo} \le f_{rep}$, accounts for the laser's internal dispersion, which causes the group and phase velocities of the pulses to differ (*22*). Thanks to the large integer *n*, the optical frequencies $f_n$ are at hundreds of THz whereas both $f_{rep}$ and $f_{ceo}$ are radio frequencies and can be handled with simple electronics and stabilized by an atomic clock (*22*). Each mode's absolute frequency is known to a precision limited only by the accuracy of the clock. Even low-cost, portable atomic clocks provide ~1 $\mathrm{cm\,s^{-1}}$ (or 3 parts in $10^{11}$) precision. Because LFC light power is much higher than required, the calibration precision possible is therefore limited by the maximum signal-to-noise

---

[1] Max-Planck Institut für Quantenoptik, Hans-Kopfermann-Strasse 1, D-85748 Garching, Germany. [2] Menlo Systems GmbH, Am Klopferspitz 19, D-82152 Martinsried, Germany. [3] European Southern Observatory, Karl-Schwarzschild-Strasse 3, D-85748 Garching, Germany. [4] Centre for Astrophysics and Supercomputing, Swinburne University of Technology, Mail H39, Post Office Box 218, Victoria 3122, Australia. [5] Kiepenheuer-Institut für Sonnenphysik, Schöneckstr. 6, D-79104 Freiburg, Germany.

*To whom correspondence should be addressed. E-mail: thu@mpq.mpg.de

ratio (SNR) achievable with the detector. For modern astronomical charge-coupled devices (CCDs), the maximum SNR in a single exposure is limited by their dynamic range but is still sufficient to achieve ~1 cm $s^{-1}$ precision (*23*). Furthermore, because LFC calibration is absolute, spectra from different epochs, or even different telescopes, can be meaningfully compared.

The main challenge in reaching ~1 cm $s^{-1}$ calibration accuracy will be the measurement and, eventually, mitigation and/or modeling and removal of systematic effects in astronomical spectrographs and detectors. For typical high-resolution spectrographs, a ~1 cm $s^{-1}$ shift corresponds roughly to the physical size of a silicon atom in the CCD substrate. Only with the statistics of a very large number of calibration lines can the required sensitivity be achieved, provided that systematic effects can be controlled accordingly (*10*). For example, even in a highly stabilized, vacuum-sealed spectrograph, small mechanical drifts will slightly shift the spectrum across the CCD. Although this can easily be tracked to first order, other effects such as CCD intrapixel sensitivity variations will be important for higher precision. Discovering, understanding, and eventually modeling and removing these effects is crucial for the long-term goal of accurate calibration; tests of LFCs on astronomical telescopes, spectrographs, and detectors are therefore imperative.

We have conducted an astronomical LFC test on the German Vacuum Tower Telescope (*24*) (VTT) (Fig. 1). We used a portable rubidium clock with a modest accuracy of 5 parts in $10^{11}$ (or 1.5 cm $s^{-1}$); much more accurate clocks are available if needed. This sets the absolute uncertainty on the frequency of any given comb mode. The VTT can be operated at near-infrared wavelengths, thereby allowing a relatively simple and reliable fiber-based LFC to be used. The erbium-doped fiber LFC used had $f_{\mathrm{rep}} = 250$ MHz which, despite the VTT spectrograph having higher resolving power (resolution of 0.8 GHz or 1.2 km $s^{-1}$) than most astronomical spectrographs, is too low for modes to be resolved apart. Filtering out unwanted modes by using a Fabry-Pérot cavity (FPC) outside the laser (*25*, *26*) was suggested as one solution (*23*, *27*) and has proven effective (*28*, *29*). The FPC comprises two mirrors separated by a distance smaller than the laser cavity length so that all modes, except every *m*th ($m > 1$), are interferometrically suppressed (Fig. 1, lower panel). We used a FPC stabilized to a filter ratio, *m*, by controlling its length with an electronic servo system to generate effective mode spacings, $m \times f_{\mathrm{rep}}$, between 1 and 15 GHz. The degree to which the unwanted modes are suppressed is an important parameter: The FPC transmission function falls sharply away from the transmitted mode frequencies but, because nearby suppressed modes are not resolved from the transmitted ones by the spectrograph, small asymmetries in this function (especially combined with time variations) can cause systematic shifts in the measured line positions. With our setup, we achieve an unwanted mode suppression of more than 46 dB at filter ratios $m \leq 20$. Other possible systematic shifts due to the filtering have been identified (*29*) and need to be controlled.

LFC spectra were recorded with and without the spectrum of a small section of the Sun's photosphere at wavelengths ~1.5 μm. A sample $m \times f_{\mathrm{rep}} =$ 15-GHz recording, superimposed with Fraunhofer and atmospheric lines, is shown in Fig. 2. To estimate our calibration accuracy and to test the spectrograph's stability, we analyzed several exposures of the LFC only. Individual Lorentzian functions were fitted to the recorded modes as a function of pixel position and identified with the absolute comb frequencies, $f_n$, which are referenced to the atomic clock (*10*). The dense grid of modes allows the spectrograph's calibration function (Fig. 3A) to be determined to very high accuracy; even a simple, second-order polynomial fit to the pixel-versus-frequency distribution has only 9 m $s^{-1}$ root mean square (RMS) residual deviations around it (Fig. 3B), and this remains almost unchanged with higher-order polynomial modeling (*10*).

With traditional calibration techniques, such as thorium comparison lamps, $I_2$ gas absorption cells or Earth's atmospheric absorption lines for calibration achieve ~10 m $s^{-1}$ absolute precision per calibration line at best (*30*). Thus, even with these "first light" comb recordings, we already demonstrate superior absolute calibration accuracy. Because more than $10^4$ modes will be available in a larger-bandwidth LFC, the statistical uncertainty would be reduced to the 1 cm $s^{-1}$ regime if the residuals were truly random. However, the theoretical shot noise limit calculated from the number of photons recorded per comb mode is much smaller than 9 m $s^{-1}$; systematic effects from the spectrograph and detector system evidently completely dominate the residuals.

The main reason for testing LFCs at real telescopes, on real astronomical spectrograph and detector systems, is to understand how to measure and then mitigate and/or model and remove such systematics. Because the VTT spectrograph is not stabilized (i.e., temperature-, pressure- and vibration-isolated), instrument drifts are expected and the VTT LFC spectra can already be used to track them accurately. From a time series of exposures, we derive a drift in the spectrograph of typically 8 m $s^{-1}$ $min^{-1}$ (5 MHz $min^{-1}$) (*10*). Much lower drift rates have been demonstrated with suitably stabilized instruments [e.g., ~1 m $s^{-1}$ over months with HARPS (*13*)]; although the VTT is not optimized for stability, this does not affect its usefulness to test calibration procedures. Indeed, different modes are observed to drift at different rates, with neighboring modes having highly correlated drift rates (*10*). Also, as the comb modes drift across the detector, higher-order distortions are evident, which are the combined result of many effects, such as intrapixel

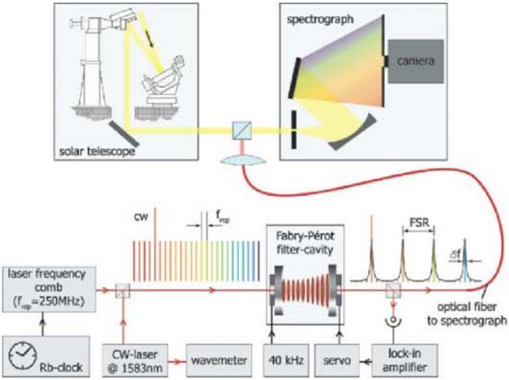

**Fig. 1.** Sketch of our experimental setup at the VTT. By superimposing the frequency comb with light from a celestial body—in this case, the Sun—one can effectively calibrate its emission or absorption spectrum against an atomic clock. An erbium-doped fiber LFC with 250-MHz mode spacing (pulse repetition rate) is filtered with a FPC to increase the effective mode spacing, allowing it to be resolved by the spectrograph. The latter has a resolution of ~0.8 GHz at wavelengths around 1.5 μm, where our LFC tests were conducted. The LFC was controlled by a rubidium atomic clock. A continuous-wave (CW) laser at 1583 nm was locked to one comb line and simultaneously fed to a wavemeter. Even though the wavemeter is orders of magnitude less precise than the LFC itself, it is sufficiently accurate (better than 250 MHz) to identify the mode number, *n*. The FPC length, defining the final free spectral range (FSR), was controlled by feedback from its output. See (*10*) for further details.

sensitivity variations. Thus, the VTT data already show an important advantage of LFC calibration: The dense grid of high SNR calibration information allows the discovery and measurement of complex effects correlated across the chip and in time.

The first light for frequency combs on astronomical spectrographs has delivered calibration precision beyond the state of the art. The key opportunity now is to use LFC spectra to measure and remove systematic effects in order to reach the ~1 cm $s^{-1}$ long-term calibration precision, accuracy, and repeatability required to realize the redshift drift experiment.

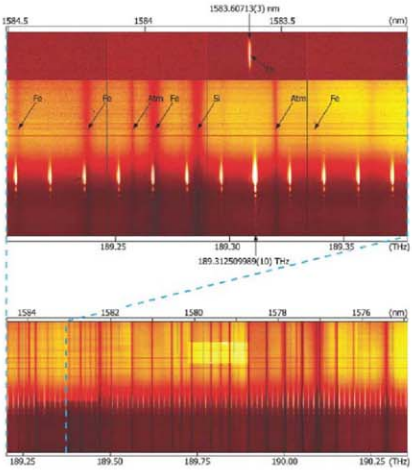

**Fig. 2.** Spectra of the solar photosphere (background image) overlaid by a LFC with 15-GHz mode spacing (white, equally spaced vertical stripes). Spectra are dispersed horizontally, whereas the vertical axis is a spatial cross section of the Sun's photosphere. The upper panel shows a small section of the larger portion of the spectrum below. The brighter mode labeled with its absolute frequency is additionally superimposed with a CW laser used to identify the mode number (Fig. 1). The frequencies of the other modes are integer multiples of 15 GHz higher (right) and lower (left) in frequency. Previous calibration methods would use the atmospheric absorption lines (dark vertical bands labeled "Atm" interleaved with the Fraunhofer absorption lines), which are comparably few and far between. Also shown in the upper panel is the only thorium emission line lying in this wavelength range from a typical hollow-cathode calibration lamp. Recording it required an integration time of 30 min, compared with the LFC exposure time of just 10 ms. Unlike with the LFC, the thorium calibration method cannot be conducted simultaneously with solar measurements at the VTT. The nominal horizontal scale is $1.5 \times 10^{-3}$ nm $pixel^{-1}$ with ~1000 pixels shown horizontally in the upper panel. Black horizontal and vertical lines are artifacts of the detector array.

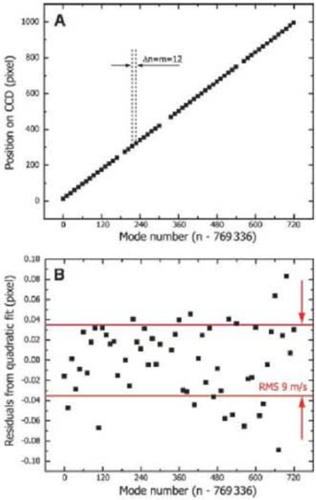

**Fig. 3.** Precision achieved with our calibration with a LFC filtered to 3 GHz ($m = 12$). **(A)** The position of the transmitted modes, derived from a multi-Lorentzian fit, plotted against the mode number. Modes without a corresponding detector position measurement were deemed unsuitable for use in calibration because they fell on large detector artifacts and/or were overlaid with light from the CW laser. The size of one pixel corresponds to 172 MHz at 1583 nm. On this scale, no distortions are visible. **(B)** The residuals from a quadratic fit that gives a RMS residual of 9 m $s^{-1}$. The quadratic fit greatly reduces the residuals compared to a linear model, whereas higher-order polynomials do not improve the performance of the fit significantly (*10*). Even with these first LFC recordings from the VTT, the 9 m $s^{-1}$ RMS residuals here indicate better absolute calibration than is achieved with traditional calibration methods (*30*).

### References and Notes

1. A. G. Riess *et al.*, *Astron. J.* **116**, 1009 (1998).
2. S. Perlmutter *et al.*, *Astrophys. J.* **517**, 565 (1999).
3. D. N. Spergel *et al.*, *Astrophys. J.* **148** (suppl.), 175 (2003).
4. J. A. Peacock *et al.*, *Nature* **410**, 169 (2001).
5. D. J. Eisenstein *et al.*, *Astrophys. J.* **633**, 560 (2005).
6. A. Sandage, *Astrophys. J.* **136**, 319 (1962).
7. A. Loeb, *Astrophys. J.* **499**, L111 (1998).
8. J. Liske *et al.*, *Mon. Not. R. Astron. Soc.* **386**, 1192 (2008).
9. L. Pasquini *et al.*, in *Proceedings of the IAU Symposium*, P. Whitelock, M. Dennefeld, B. Leibundgut, Eds. (Cambridge Univ. Press, Cambridge, 2006), vol. 232, pp. 193–197.
10. Materials and methods are available as supporting material on *Science* Online.
11. M. Mayor, D. Queloz, *Nature* **378**, 355 (1995).
12. G. W. Marcy, R. P. Butler, *Astrophys. J.* **464**, L147 (1996).
13. C. Lovis *et al.*, *Nature* **441**, 305 (2006).
14. C. Lovis *et al.*, in *Proceedings of the SPIE*, I. S. McLean, I. Masanori, Eds. (2006), vol. 6269, pp. 62690P1–62690P9.
15. J. N. Bahcall, E. E. Salpeter, *Astrophys. J.* **142**, 1677 (1965).
16. J. K. Webb, V. V. Flambaum, C. W. Churchill, M. J. Drinkwater, J. D. Barrow, *Phys. Rev. Lett.* **82**, 884 (1999).
17. R. I. Thompson, *Astron. Lett.* **16**, 3 (1975).
18. M. T. Murphy, J. K. Webb, V. V. Flambaum, *Mon. Not. R. Astron. Soc.* **345**, 609 (2003).
19. H. Chand, R. Srianand, P. Petitjean, B. Aracil, *Astron. Astrophys.* **417**, 853 (2004).
20. S. A. Levshakov *et al.*, *Astron. Astrophys.* **449**, 879 (2006).
21. E. Reinhold *et al.*, *Phys. Rev. Lett.* **96**, 151101 (2006).
22. Th. Udem, R. Holzwarth, T. W. Hänsch, *Nature* **416**, 233 (2002).
23. M. T. Murphy *et al.*, *Mon. Not. R. Astron. Soc.* **380**, 839 (2007).
24. E. H. Schröter, D. Soltau, E. Wiehr, *Vistas Astron.* **28**, 519 (1985).
25. T. I. Sizer, *IEEE J. Quantum Electron.* **25**, 97 (1989).
26. Th. Udem, J. Reichert, R. Holzwarth, T. W. Hänsch, *Phys. Rev. Lett.* **82**, 3568 (1999).
27. P. O. Schmidt, S. Kimeswenger, H. U. Kaeufl, *Proc. 2007 ESO Instrument Calibration Workshop*, ESO Astrophysics Symposia series (Springer, in press); available at http://arxiv.org/abs/0705.0763.
28. C.-H. Li *et al.*, *Nature* **452**, 610 (2008).
29. D. A. Braje, M. S. Kirchner, S. Osterman, T. Fortier, S. A. Diddams, *Eur. Phys. J. D* **48**, 57 (2008).
30. C. Lovis, F. Pepe, *Astron. Astrophys.* **468**, 1115 (2007).
31. We thank the Kiepenheuer Institut für Sonnenphysik staff at the Vacuum Tower Telescope and the Instituto de Astrofisica de Canarias (IAC) personnel for their support during the measurements at the VTT. We especially appreciate the efforts of M. Collados (IAC) and F. Kerber (ESO). We thank T. Kippenberg for CW-laser assistance and J. Liske for advice on the manuscript. M.T.M. thanks the Australian Research Council for a QEII Research Fellowship (DP0877998).

### Supporting Online Material

www.sciencemag.org/cgi/content/full/321/5894/1335/DC1
Materials and Methods
Figs. S1 to S4
References

28 May 2008; accepted 25 July 2008
10.1126/science.1161030

# Regional Synthesis of Mediterranean Atmospheric Circulation During the Last Glacial Maximum

J. Kuhlemann,[1]* E. J. Rohling,[2] I. Krumrei,[1] P. Kubik,[3] S. Ivy-Ochs,[4] M. Kucera[1]

Atmospheric circulation leaves few direct traces in the geological record, making reconstructions of this crucial element of the climate system inherently difficult. We produced a regional Mediterranean synthesis of paleo-proxy data from the sea surface to alpine altitudes. This provides a detailed observational context for change in the three-dimensional structure of atmospheric circulation between the Last Glacial Maximum (LGM, ~23,000 to 19,000 years ago) and the present. The synthesis reveals evidence for frequent cold polar air incursions, topographically channeled into the northwestern Mediterranean. Anomalously steep vertical temperature gradients in the central Mediterranean imply local convective precipitation. We find the LGM patterns to be analogous, though amplified, to previously reconstructed phases of enhanced meridional winter circulation during the Maunder Minimum (the Little Ice Age).

Mediterranean climate is determined by an interplay between atmospheric and marine processes and strongly differentiated regional topography (*1*). A wealth of paleoclimate data is available from archives recording conditions at the sea surface and on land at various altitudes, making the Mediterranean one of the few regions in the world where the thermal and dynamical structure of the lower atmosphere could be reconstructed for certain past intervals (*2*). Such reconstructions are invaluable for validation of the atmospheric component in climate models (*3*). Recent attempts to compare model simulations with regional proxy data over Europe during the Last Glacial Maximum (LGM) revealed substantial disagreement, both among the models and between models and paleodata (*4*, *5*), highlighting the need for model-independent constraints on past regional climatic patterns.

The state of the atmosphere in the past is inherently difficult to reconstruct. Proxies from oceanic sediments record mainly large-scale atmospheric patterns (*6*); and terrestrial proxy data, such as those from peat bogs or lake sediments, can be biased by local climate, including temperature inversion and interannual variability (*7*, *8*). The equilibrium line altitude (ELA) of glaciers contains information on the vertical structure of the atmosphere, which can be reconstructed by in situ dating of glacial advances and retreats. Small temperate glaciers in circum-Mediterranean mountain chains are (and were) exposed to well-mixed air masses and are known to have been sensitive to even small changes of the ELA, typically responding by advancing or retreating within periods ranging from several years to decades (*9*, *10*).

The ELA responds to both temperature and precipitation change (*9*, *10*), and it is possible to differentiate between these two factors only in particularly well-studied regions, such as Corsica (data supplement S1 and figs. S2 and S3). For Corsica, we present new information on the LGM ELA, including a deconvolution of the two main controlling processes (fig. S4, B and C). For the ELA depression of LGM glaciers in the wider Mediterranean region, we used previously published information (table S2), which, as a first-order end-member solution, we calculated as pure temperature change, using a standard free atmospheric lapse rate of a 6.5°C decrease per kilometer (6.5°C/km) of increasing elevation. The potential overprint of precipitation changes was then considered where anomalous results were found. The error ranges on the resultant ELA reconstructions (Fig. 1) amount to up to ±100 m in Corsica and ±150 m in other Mediterranean mountains (fig. S1 and Fig. 2). We thus developed a regional synthesis of glacial vertical temperature gradients in the lower atmosphere. Paleoflora-based temperature reconstructions for a variety of terrestrial sites at lower altitudes around the Mediterranean (*7*, *8*) (Fig. 2 and fig. S3) were used to validate and complement our ELA-based temperature reductions and precipitation patterns.

Next, we compared the ELA-based LGM cooling at alpine altitudes with estimates of LGM reduction of Mediterranean sea surface temperatures (SSTs) derived from the difference between long-term instrumental averages (*11*) and glacial SST reconstructions based on foraminiferal assemblages (*12*, *13*) and alkenone data (*14*) (Figs. 1 and 2). Such direct comparison between SST and ELA changes is warranted for the Mediterranean basin, where SSTs generally are closely related to air temperature and the insolation/radiation balance (*15*).

The combination of data on LGM cooling at sea level (SST proxies) and higher altitudes (ELA depression) provides direct constraints on the vertical structure of the LGM atmosphere. When comparing the temperature equivalent of the ELA depression with SST reduction in the LGM relative to the present (Fig. 2), we consider that a shift of similar magnitude would indicate a constant atmospheric lapse rate. Stronger relative reduction of SST would imply a lapse rate of less than 6.5°C/km, supporting more stable atmospheric stratification. A lesser relative SST reduction would imply a lapse rate steeper than 6.5°C/km, potentially enhancing the instability of the atmosphere, driving convection and consequent precipitation.

Our analysis (figs. S1 and S2) reveals an LGM pattern of southward-extending lobes of ELA depression in mountainous regions of Italy

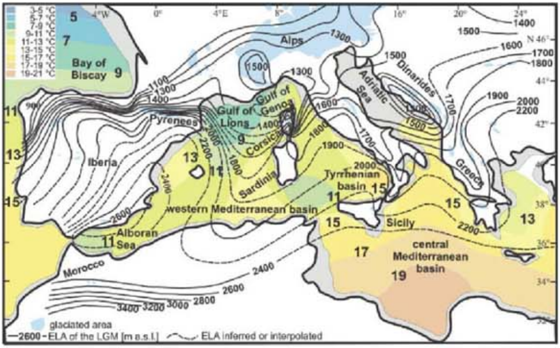

**Fig. 1.** Map of the ELA in the western-central Mediterranean region during the phase of maximum glacier expansion during the LGM (probably at ~23,000 years before the present) and of average annual SSTs and ELA during the LGM. The error range of the ELA estimate is ±150 m for the Mediterranean in general and ±100 m in Corsica.

---

[1] Institute for Geosciences, University of Tuebingen, Sigwartstrasse 10, D-72076 Tuebingen, Germany. [2] School of Ocean and Earth Science, National Oceanography Centre, Southampton SO14 3ZH, UK. [3] Institute of Particle Physics, HPK H30, ETH Zurich, CH-8093 Zurich, Switzerland. [4] Institute of Particle Physics, HPK H27, ETH Zurich, CH-8093 Zurich, Switzerland.

*To whom correspondence should be addressed. E-mail: kuhlemann@uni-tuebingen.de

and the Dinarides, which suggests frequent higher-altitude southward advances of polar air (Fig. 1). Iberia is characterized by a steep gradient from the northern and northwestern coastlines toward the interior and southeast, which probably results predominantly from barrier effects of near-coastal mountain ranges (Fig. 1). The data from Corsica especially identify a lobe of ELA depression that extends over the Gulf of Lions toward the south and east (Fig. 1), indicating a substantial invasion of polar air from the north. The temperature difference inferred from the recent ELA (*16*) and our LGM reconstruction (fig. S3) generally decreases from north (10° to 11°C) to south (6° to 7°C) (Fig. 2), in agreement with previous reconstructions of a steeper glacial meridional temperature gradient (*16*, *17*). The temperature differences calculated from the glacial ELA depression, relative to the present, generally agree with lower-altitude temperature reconstructions from paleofloral data (*7*, *8*) (Fig. 2).

The present-day SST distribution and surface circulation in the western Mediterranean basin are strongly affected by northwesterly winds, particularly in the Gulf of Lions (*15*). As a consequence, cool waters are frequently upwelling in the Gulf of Lions (*11*, *18*). Surface currents are deflected by coastlines, and their strength and flow direction vary seasonally in response to surface winds and the superimposed atmospheric circulation (*11*, *15*). Glacial SST values calculated from foraminiferal assemblages (*12*, *13*) and alkenone data (*14*) display a roughly similar distribution to that of modern SSTs, albeit with a stronger west-east gradient due to stronger cooling in the northwestern Mediterranean than in the central and eastern parts of the basin (*12*) (Fig. 1 and data supplement S3). The extraordinary cooling centered on the Gulf of Lions suggests frequent and/or more persistent northerly incursions of cold polar air, probably channeled through the Rhone valley at low elevation (*14*, *18*), and between the glaciated Alps and the Pyrenees at higher elevation, as suggested by our ELA reconstructions.

Figure 2 compares the spatial pattern of the LGM reduction of SST (relative to the present) with that of atmospheric temperature as derived from our ELA reconstruction. This reveals that both SST and ELA-determined atmospheric temperatures ($T_{\mathrm{ELA}}$) underwent similar (within ±2°C) changes, relative to the present, across the northern Bay of Biscay and the western sector of the western Mediterranean. LGM SST seems less reduced than $T_{\mathrm{ELA}}$ in the Atlantic Ocean offshore of Iberia and Morocco, which probably reflects the southward displacement of the relatively warm Gulf Stream during glacial times (*3*–*6*, *13*, *19*). In the central and (to a lesser extent) eastern Mediterranean, glacial SST appears to have dropped considerably less than $T_{\mathrm{ELA}}$ (Fig. 2). The notable warm anomaly in the central basin can hardly be attributed to the advection of warm surface waters from the western basin because of land barriers. In fact, a notable cool SST anomaly is seen to the southeast of Sardinia, which may reflect leeward upwelling triggered by northwesterly winds (Fig. 1). We propose that the advection of warm desert air from the Sahara and relatively cloud-free subtropical conditions over the central/eastern basin largely account for the minor LGM cooling of SSTs in this region. The fact that glacial SST dropped considerably less than calculated $T_{\mathrm{ELA}}$ over part of the Mediterranean suggests that the atmospheric lapse rate had noticeably steepened: up to ~10°C/km north of Corsica, ~9°C/km in the southern Adriatic Sea, and ~8.5°C/km in the central Mediterranean basin. Given that we applied an initial end-member ELA transformation to (only) temperature changes, using a standard lapse rate of 6.5°C/km, it is clear that increased convective precipitation must be inferred to explain the noticeably steeper rates diagnosed in these specific regions.

The spatial distributions of SST, $T_{\mathrm{ELA}}$, and of the SST-$T_{\mathrm{ELA}}$ difference in the western-central Mediterranean during the LGM are found to be roughly similar to those in the present, although meridional gradients were enhanced during the LGM (Figs. 1 and 2). Hence, it is not unreasonable to expect that cyclones followed similar preferential storm tracks across the basin as well, which contrasts with previous suggestions of northeast-directed cyclone tracks from the Alboran Sea toward the southern flank of the Alps (*20*). During cold periods such as the LGM, cold northerly air outbreaks over the western basin were probably more frequent (*12*, *17*, *18*). The pronounced southward cold (polar air) expansion toward northwest Africa (Figs. 1 and 2) would have triggered cyclogenesis over the relatively warm Mediterranean waters, causing flows of desert air toward the north and northeast, as indicated by the north-extending lobe of the ELA in southeastern Europe (Fig. 1). This would be consistent with observations of enhanced wind-blown dust supply from the Sahara into the eastern Mediterranean during glacial times (*21*).

Even though we compare glacial conditions (the LGM) with interglacial conditions (the present), we observe that the reconstructed property distribution patterns, particularly the preferential flow of polar air masses, are pervasive through time (Figs. 1 and 2). Indeed, these features appear to be strongly fixed by the land/sea distribution and topography, which are virtually invariant on the time scales considered. Outbreaks of polar air masses over the western Mediterranean are typically funneled between the Alps and the Pyrenees, both at present and during the LGM, causing conditions conducive to cyclogenesis over the Gulf of Genoa. The funneling effect may have been stronger with glaciated mountains, as the ice rose several hundreds of meters above the lower watersheds (*20*), and Arctic air masses would also have invaded the western Mediterranean more frequently and/or persistently than today, because of the more southerly position of the polar front during the LGM (*3*–*5*, *19*, *22*). The incursion of cold air masses would have favored the convection of moist air, especially in regions with relatively warm (less reduced) SST, so that we would predict considerable local LGM precipitation in Corsica, the Apennines, the Dinarides, and Greece, especially at the upwind flank of mountain ranges and close to the coast. This would be a suitable mechanism to explain steeper horizontal precipitation gradients during the LGM relative to the present, which indeed are suggested by our data for the steep mountainous margins of northern

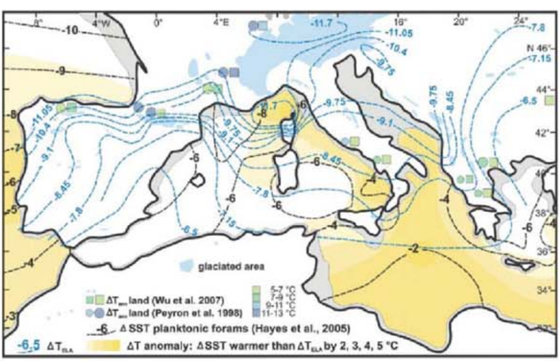

**Fig. 2.** Map of the temperature difference between recent and LGM SSTs (in black) and the temperature equivalent of the ELA depression (6.5°C/km lapse rate; in blue), respectively. The error range of this estimate is ±1°C for the Mediterranean in general and ±0.7°C in Corsica. In orange-colored marine regions, LGM SSTs were lowered significantly less than temperatures in the mid-troposphere, relative to the present. This implies an anomalously steep lapse rate and unstable layering of the lower troposphere. Atmospheric cooling values for low-elevation terrestrial sites based on paleofloral estimates are given for comparison. Small symbols indicate larger error and large symbols lesser error of the temperature estimate. Δ, change in.

Corsica (table S1 and fig. S1). This island's dry northern interior today receives ~30% less precipitation than its margins (fig. S2A), whereas this difference was ~50% during the LGM (fig. S4C). Although this prediction cannot (yet) be confirmed with the data available outside Corsica, it does agree with patterns seen in LGM reconstructions with the high-resolution climate model HadRM (*23*). As mentioned above, locally enhanced precipitation would largely reduce the local lapse rate, so that much of the initially (first-order) inferred temperature anomaly pattern in fact reflects the impact of precipitation anomalies.

Although care must be taken not to simply ascribe past regional property distributions to modern climate oscillation patterns (*24*), it remains useful to consider instrumental records and proxy data in order to develop a sense of realistic analogous climate patterns over the study region (*25*). The contrast between strongly reduced SST in the western basin and much less reduced SST in the central Mediterranean basin during the LGM (Fig. 1) indicates a preferentially meridional geostrophic circulation, with a polar trough that frequently protruded into the western Mediterranean. Such a circulation is favored by northward extension of the Azores High toward Iceland (North Atlantic ridge) or Greenland, blocking moisture supply by the westerlies. It is further enhanced by expansion and intensification of the Siberian High in winter during glacial times (*26*). A similar configuration is thought to have been common during the late Little Ice Age, notably the Maunder Minimum (*2*, *27*). The invasion of polar air as shown by our data, channeled by the topography of mountain ranges and ice sheets in Europe, would have generated cyclone formation in the Gulf of Genoa more frequently than at present, enhancing precipitation along various storm tracks in easterly directions. Our observations do not support a straightforward zonal LGM atmospheric circulation, as inferred from climate models (*19*, *28*). Instead, we propose that frequent meridional circulation during cold seasons (characterized by the LGM ELA pattern) may have alternated with more zonal circulation during warm seasons. A more comprehensive quantitative assessment of the preferential LGM atmospheric circulation requires the use of both nested model simulation and high-resolution global climate model studies (*4*, *5*, *8*, *28*), which should fully resolve the changing topography of glaciated mountain ranges and ice sheets. The validation of such models with our three-dimensional LGM climate proxy data ranging from the sea surface to alpine altitudes is a great future challenge.

### References and Notes

1. E. Xoplaki, J. F. Gonzalez-Rouco, J. Luterbacher, H. Wanner, *Clim. Dyn.* **23**, 63 (2004).
2. J. Luterbacher *et al.*, in *The Mediterranean Climate: An Overview of the Main Characteristics and Issues*, P. Lionello, P. Malanotte-Rizzoli, R. Boscolo, Eds. (Elsevier, Amsterdam, 2006), pp. 27–148.
3. COHMAP Members, *Science* **241**, 1043 (1988).
4. M. Kageyama *et al.*, *Quat. Sci. Rev.* **25**, 2082 (2006).
5. G. Ramstein *et al.*, *Clim. Past* **3**, 331 (2007).
6. G. Bond *et al.*, *Nature* **365**, 143 (1993).
7. O. Peyron *et al.*, *Quat. Res.* **49**, 183 (1998).
8. H. Wu, J. Guiot, S. Brewer, Z. Guo, *Clim. Dyn.* **29**, 211 (2007).
9. H. Kerschner, G. Kaser, R. Sailer, *Ann. Glaciol.* **31**, 80 (2000).
10. D. Steiner *et al.*, *Clim. Change*, 10.1007/s10584-008-9393-1 (2008).
11. M. Conkright *et al.*, *World Ocean Atlas 1998 CD ROM Data Set Documentation* (Technical Report 15, NODC Internal Report, Silver Spring, MD, 1998).
12. A. Hayes, M. Kucera, N. Kallel, L. Sbaffi, E. J. Rohling, *Quat. Sci. Rev.* **24**, 999 (2005).
13. A. Paul, C. Schäfer-Neth, *Palaeoceanography* **18**, 1058 (2003).
14. I. Cacho, J. O. Grimalt, M. Canals, *J. Mar. Syst.* **33-34**, 253 (2002).
15. N. Pinardi, E. Masetti, *Palaeogeogr. Palaeoclimatol. Palaeoecol.* **158**, 153 (2000).
16. B. Messerli, *Geogr. Helv.* **22**, 105 (1967).
17. V. Masson-Delmotte *et al.*, *Clim. Dyn.* **26**, 513 (2006).
18. E. J. Rohling, A. Hayes, D. Kroon, S. De Rijk, W. J. Zachariasse, *Palaeoceanography* **13**, 316 (1998).
19. M. Kageyama, F. D. Andrea, G. Ramstein, P. J. Valdes, R. Vautard, *Clim. Dyn.* **15**, 773 (1999).
20. D. Florineth, C. Schlüchter, *Quat. Res.* **54**, 295 (2000).
21. J. C. Larrasoana, A. P. Roberts, E. J. Rohling, M. Winklhofer, R. Wehausen, *Clim. Dyn.* **21**, 689 (2003).
22. U. Pflaumann *et al.*, *Palaeoceanography* **18**, 10.1029/2002PA000774 (2003).
23. A. Jost *et al.*, *Clim. Dyn.* **24**, 577 (2005).
24. F. Justino, W. R. Peltier, *Geophys. Res. Lett.* **32**, 10.1029/2005GL023822 (2005).
25. C. Cassou, L. Terray, J. W. Hurrell, C. Deser, *J. Clim.* **17**, 1055 (2004).
26. E. J. Rohling, P. A. Mayewski, P. Challenor, *Clim. Dyn.* **20**, 257 (2003).
27. J. Jacobeit, P. Jönsson, L. Bärring, C. Beck, M. Ekström, *Clim. Change* **48**, 219 (2001).
28. A. Laîné *et al.*, *Clim. Dyn.*, 10.1007/s00382-008-0391-9 (2008).

29. We gratefully acknowledge funding by the German Science Foundation (DFG project KU1298/7) and the UK Natural Environment Research Council's thematic program Quantifying the Earth System (QUEST).

**Supporting Online Material**

www.sciencemag.org/cgi/content/full/1157638/DC1
Data Supplements S1 to S3
Figs. S1 to S7
Tables S1 and S2
References

11 March 2008; accepted 21 July 2008
Published online 31 July 2008;
10.1126/science.1157638
Include this information when citing this paper.

---

# Kinematic Constraints on Glacier Contributions to 21st-Century Sea-Level Rise

**W. T. Pfeffer,[1]* J. T. Harper,[2] S. O'Neel[3]**

**On the basis of climate modeling and analogies with past conditions, the potential for multimeter increases in sea level by the end of the 21st century has been proposed. We consider glaciological conditions required for large sea-level rise to occur by 2100 and conclude that increases in excess of 2 meters are physically untenable. We find that a total sea-level rise of about 2 meters by 2100 could occur under physically possible glaciological conditions but only if all variables are quickly accelerated to extremely high limits. More plausible but still accelerated conditions lead to total sea-level rise by 2100 of about 0.8 meter. These roughly constrained scenarios provide a "most likely" starting point for refinements in sea-level forecasts that include ice flow dynamics.**

Eustatic land ice contributions to sea-level change come from surface mass balance (SMB) losses and discharge of ice into the ocean through marine-terminating glaciers. Dynamically forced discharge, via fast flow and calving of marine-terminating glaciers allowing rapid land-to-ocean transfer of ice, is well known from studies of temperate marine-terminating glaciers (*1*–*4*) and is observed in Greenland (*5*–*7*). The consensus estimate of sea-level rise (SLR) by 2100 (0.18 to 0.6 m) that was published in the Intergovernmental Panel on Climate Change (IPCC) Fourth Assessment (*8*) excluded dynamic effects on the grounds that present understanding of the relevant processes is too limited for reliable model estimates. Because modeling (*9*) and paleoclimate comparisons (*10*) have yielded multimeter per century estimates of SLR, similar increases have been inferred as a viable 21st-century scenario. Also argued is that feedbacks unaccounted for in the IPCC estimate could quickly cause several meters of very rapid SLR (*11*, *12*).

Accurate SLR forecasts on the century time scale are imperative for planning constructive and cost-effective responses. Underestimates will prompt inadequate preparation for change, whereas overestimates will exhaust and redirect resources inappropriately. Raising California Central Valley levees only 0.15 m, for example, will cost over $1 billion (*13*); the nonlinearly increasing costs of raising levees 2 m or more without clear and compelling cause would entail enormous expenditures otherwise used for different responses as demanded by a smaller but still significant SLR.

We address the plausibility of very rapid SLR from land ice occurring this century. We give

---

[1] Institute of Arctic and Alpine Research, University of Colorado, Boulder, CO 80309, USA. [2] Department of Geosciences, University of Montana, Missoula, MT 59812, USA. [3] Scripps Institution of Oceanography, University of California San Diego, San Diego, CA 92093, USA.

*To whom correspondence should be addressed. E-mail: pfeffer@tintin.colorado.edu

particular emphasis to Greenland because of its vulnerability to ongoing Arctic warming and meltwater-related feedbacks, recent accelerations of ice motion, and its large volume reductions during the last interglacial (*14*). By using a simple kinematic approach, we determined Greenland and Antarctic outlet glacier velocities required to achieve various magnitudes of SLR by 2100.

To begin, we postulated sea-level increases of 2 and 5 m by 2100 forced solely by Greenland. The total water mass losses required to achieve these targets are $7.24 \times 10^5$ Gt and $1.81 \times 10^6$ Gt, respectively (Table 1). Of this mass, $2.58 \times 10^4$ Gt (less than 4% of the total for 2 m SLR) will be lost as SMB by 2100, which we estimated by integrating present-day values of mass loss forward at present-day rates of change (*15*), with present-day SMB estimated at 30% of total present-day rate of mass loss (*5*). Because future SMB is highly uncertain, we also scaled total SMB losses up by a factor of 10 to investigate the effect of uncertainty in SMB. Adjusting total mass losses for SMB contributions yields the mass to be discharged through marine-based outlets (Table 1). Even when scaled up by an order of magnitude, SMB is a very small fraction of the total loss required to produce the targeted SLR. Thus, even large uncertainties in future SMB have little influence on this calculation.

Rapid, dynamically unstable discharge of ice through calving is restricted to glaciers with beds based below sea level. We identified and calculated the aggregate cross-sectional area of Greenland's marine-terminating outlet glaciers by using surface and bed topography (*16*) and measured ice velocities (*5*) to identify all potential pathways for rapid discharge, including channels presently flowing rapidly as well as potentially unstable channels (Fig. 1 and table S1). Cross-sectional areas (gates) for each outlet were calculated at the point of greatest lateral constriction by bedrock in the glacier's marine-based reach. Ice stream widths in Antarctica can vary in time, but for Greenland outlet glaciers cross-sectional areas are constrained almost entirely by bedrock topography. Of the 290 km$^2$ total aggregate gate cross-sectional area, we identified 170 km$^2$ as the aggregate marine-based gate area where drainage to the ocean is not blocked by near-coastal sills standing above present-day sea level. All dynamic discharge (Table 2) must pass through these gates by 2100 to meet 2- to 5-m SLR targets. We considered four scenarios: velocities were calculated for both the "marine-based" gate (170 km$^2$) and the "total aggregate" gate (290 km$^2$) given both projected SMB and 10× inflated SMB losses. We then considered whether those velocities are realistic.

Coarseness of the digital elevation models (DEMs) used for surface and bed topography (*16*) led to uncertainties in the calculated gate areas, which may be substantial but cannot be evaluated directly. We accounted for a potential underestimate of gate area with a calculation using the total aggregate gate area. The total aggregate area exceeds the more relevant marine-based gate area by 70%. Uncertainties arising from the DEM more likely conceal small unresolved channels than large ones, so the actual gate areas may be smaller than we calculate (thus yielding higher velocities).

The present-day average velocity of all Greenland outlet glaciers is 0.56 km/year when weighted by drainage basin area or 1.23 km/year when weighted by gate cross-sectional area. The two weighted averages are different because gate cross-sectional area does not scale with drainage basin area. Average (present day to 2100) outlet glacier speeds required to meet 2- and 5-m SLR targets

**Table 1.** Fluxes and discharges for SLR targets. $Q$ indicates total discharge to 2100 (Gt); $q$, $Q$ converted to ice flux rate, total to 2100 (km$^3$/year); $Q_1$, total dynamic discharge less SMB to 2100 (Gt); $q_1$, $Q_1$ converted to ice flux rate, total dynamic flux less SMB to 2100 (km$^3$/year); $Q_2$, total dynamic discharge less 10× SMB to 2100 (Gt); and $q_2$, $Q_2$ converted to ice flux rate, total dynamic flux less 10× SMB to 2100 (km$^3$/year).

| SLR target | SLR mm/year | $Q$ | $q$ | $Q_1$ | $q_1$ | $Q_2$ | $q_2$ |
|---|---|---|---|---|---|---|---|
| 2 m | 21.5 | 724,000 | 8,650 | 698,164 | 8,341 | 652,464 | 7,795 |
| 5 m | 53.8 | 1,810,000 | 21,625 | 1,784,165 | 21,317 | 1,738,464 | 20,770 |

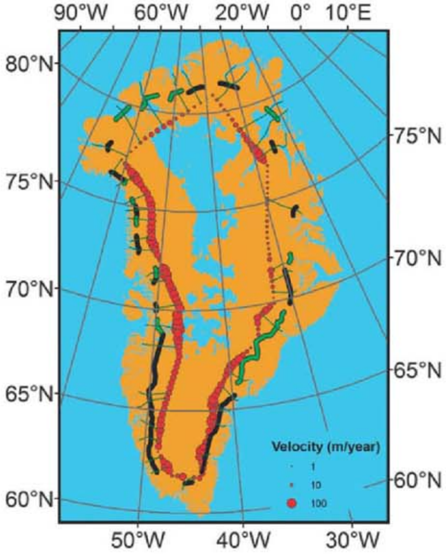

**Fig. 1.** Map showing Greenland and outlet glacier gates; marine-based gates are shown as dark green and nonmarine as black. Regions below sea level are colored blue. Ice velocities at ~2000 m elevation from (*21*) shown by red dots.

**Table 2.** Required velocities of Greenland gates for SLR targets.

| SLR target | Present-day marine-based gates (km/year) 1× SMB | All present-day discharge gates (km/year) 1× SMB | Present-day marine-based gates (km/year) 10× SMB | All present-day discharge gates (km/year) 10× SMB |
|---|---|---|---|---|
| 2 m | 49 | 28.7 | 45.8 | 26.8 |
| 5 m | 125 | 73.4 | 122 | 71.5 |

range from 26.8 km/year to 125 km/year, depending on the scenario considered [Table 2 and supporting online material (SOM)]. These velocities must be achieved immediately on all outlets considered and held at that level until 2100. Delays in the onset of rapid motion increase the required velocity further (fig. S1).

The scenario velocities far exceed the fastest motion exhibited by any Greenland outlet glacier. For example, the near-doubling of ice discharge from Jakobshavn Glacier in 2004–2005 was associated with an acceleration to 12.6 km/year (*7*). Similarly, a temporary 80% increase in the speed near the terminus of Kangerdlugssuaq produced a velocity of 14.6 km/year (*6*). A comparison of calculated (Table 2) and observed (1.23 km/year) average velocities shows that calculated values for a 2-m SLR exceed observations by a factor of 22 when considering all gates and inflated SMB and by a factor of 40 for the marine gates without inflated SMB, which we consider to be the more likely scenario. With the exception of discharge through all gates at inflated SMB (26.8 km/year), none of the velocity magnitudes shown in Table 2 has ever been observed anywhere, even over short time periods. The highest observed velocities have occurred at surging glaciers, including circa (ca.) 70 m/day (25.5 km/year) at Variegated Glacier (*17*) and 105 m/day (38.3 km/year) at Medvezhiy Glacier (*18*), but were held only for brief periods (hours to days). Although no physical proof is offered that the velocities given in Table 2 cannot be reached or maintained over century time scales, such behavior lies far beyond the range of observations and at the least should not be adopted as a central working hypothesis.

Calculations are made only for Greenland because Greenland's outlet glaciers are well constrained by bed topography, which (despite the uncertainties mentioned) is well known in comparison to much of the Antarctic Ice Sheet and the Antarctic Peninsula and virtually all of the marine-terminating glaciers and ice caps (GIC) exclusive of Greenland and Antarctica. In order to estimate how these constraints influence projections of total SLR to 2100, we calculated a zero-order range of eustatic SLR from all land ice sources. Because marine-grounded channels are not well defined in many other locations, we made approximations and scaling arguments to arrive at a range of values for total eustatic SLR and, including reasonable projections of steric SLR, a range of estimates of total SLR to 2100.

**Table 3.** SLR projections based on kinematic scenarios. Thermal expansion numbers are from (*22*).

| | SLR equivalent (mm) | | |
|---|---|---|---|
| | Low 1 | Low 2 | High 1 |
| *Greenland* | | | |
| Dynamics | 93 | 93 | 467 |
| SMB | 71 | 71 | 71 |
| Greenland total | 165 | 165 | 538 |
| *Antarctica* | | | |
| PIG/Thwaites dynamics | 108 | | 394 |
| Lambert/Amery dynamics | 16 | | 158 |
| Antarctic Peninsula dynamics | 12 | | 59 |
| SMB | 10 | | 10 |
| Antarctica total | 146 | 128 | 619 |
| *Glaciers/ice caps* | | | |
| Dynamics | 94 | | 471 |
| SMB | 80 | | 80 |
| GIC total | 174 | 240 | 551 |
| Thermal expansion | 300 | 300 | 300 |
| Total SLR to 2100 | 785 | 833 | 2008 |

Most of the marine-based ice in West Antarctica is held behind the Ross and Filchner-Ronne ice shelves, which we consider unlikely to be removed by climate or oceanographic processes within the next century [e.g., (*19*)]. The Amundson Coast basin [including Pine Island Glacier (PIG) and Thwaites Glacier], however, is not confined by large ice shelves and contains about 1.5 m sea level equivalent ($5.43 \times 10^5$ Gt) (*20*). The aggregate cross-sectional gate area of PIG and Thwaites Glacier is ca. 120 km$^2$ (*20*). The average velocity in this region is 2 km/year (table S2), higher than the average velocity of all Antarctic ice streams [0.65 km/year (*19*)]. An average (present day to 2100) velocity of 53.6 km/year is required to discharge 1.5 m sea-level equivalent through the PIG and Thwaites glacier gates by 2100, again far greater than any observed glacier velocity.

We present three scenarios by combining likely projection methods that we believe roughly bracket the range of potential near-future SLR outcomes (SOM). These are not true limiting cases but give a good sense of the potential variability of total SLR due to dynamic discharge effects.

SLR scenario Low 1 represents a low-range estimate based on specific adjustments to dynamic discharge in certain potentially vulnerable areas. We assumed a doubling of outlet glacier velocities in Greenland and PIG/Thwaites within the first decade and no change from present-day discharge values at Lambert/Amery. SMB for Greenland, the Antarctic Peninsula, and GIC was accelerated at present-day rates of SMB change, and, lacking more directly applicable constraints, dynamic discharge for the Antarctic Peninsula and GIC was calculated by scaling dynamic discharge to SMB by using the ratio of 1.31 as computed for Greenland (SOM). The net result, including thermal expansion, is 785 mm by 2100 (Table 3).

A second low-range scenario (Low 2) shows the effect of varying our assumptions; for this, we simply integrated presently observed rates of change forward in time. We calculated Greenland's contribution as for Low 1 but accelerated the present-day net discharge for Antarctica (East/West/Antarctic Peninsula) forward at the present-day rate of change given by (*19*). The GIC contribution was also calculated by accelerating the present-day net discharge at the current rate of change, with values from (*15*). The net result, including thermal expansion, is 833 mm by 2100 (Table 3).

SLR scenario High 1 combines all eustatic sources taken at high but reasonable values. No firm highest possible value can be determined for SMB or dynamics; the values chosen represent judged upper limits of likely behavior on the century time scale. Greenland SMB was accelerated at present-day rates of change, but dynamic discharge was calculated by accelerating outlet glacier velocities by an order of magnitude in the first decade. In Antarctica, PIG/Thwaites was accelerated from present-day net discharge (*19*) in the first decade and held thereafter to the highest outlet glacier velocity observed anywhere [14.6 km/year (*6*)], and Lambert/Amery was accelerated from present-day net discharge (*19*) in the first decade by an order of magnitude and held thereafter. Antarctic Peninsula and GIC were calculated by scaling dynamic discharge at the dynamics-to-SMB ratio computed for Greenland; this ratio is larger (6.42) than in case Low 1 because Greenland's dynamic discharge is larger. The net result, including thermal expansion, is 2008 mm by 2100 (Table 3).

On the basis of calculations presented here, we suggest that an improved estimate of the range of SLR to 2100 including increased ice dynamics lies between 0.8 and 2.0 m. We emphasize that assumptions made to arrive here contain substantial uncertainties, and many other scenarios and combinations of contributions could be considered. However, the net eustatic SLR from other combinations explored fell within the range given in Table 3. Hence, these values give a context and starting point for refinements in SLR forecasts on the basis of clearly defined assumptions and offer a more plausible range of estimates than those neglecting the dominant ice dynamics term. Certain potentially significant sinks and sources of SLR, such as terrestrial water storage, are still absent altogether. Among the uncertainties explored, the potential for dynamic response from GIC is comparable in magnitude to dynamic response from Greenland or Antarctica but is exceptionally poorly constrained by basic observations. Without better knowledge of the number, size, and catchment areas of marine-based outlet glaciers in the GIC category, improvements on the estimates made here will be very difficult.

### References and Notes

1. S. O'Neel, W. T. Pfeffer, *Geophys. Res. Lett.* **34**, L22502 (2007).
2. M. F. Meier, A. Post, *J. Geophys. Res.* **92**, 9051 (1987).
3. M. Meier *et al.*, *J. Geophys. Res.* **99**, 15219 (1994).
4. B. Kamb *et al.*, *J. Geophys. Res.* **99**, 15231 (1994).
5. E. Rignot, P. Kanagaratnam, *Science* **311**, 986 (2006).
6. I. M. Howat, I. Joughin, T. A. Scambos, *Science* **315**, 1559 (2007); published online 7 February 2007 (10.1126/science.1138478).
7. I. Joughin, W. Abdalati, M. Fahnestock, *Nature* **432**, 608 (2004).
8. IPCC, *Climate Change 2007: The Physical Science Basis. Contribution of Working Group I to the Fourth Assessment Report of the Intergovernmental Panel on Climate Change*, S. Solomon *et al.*, Eds. (Cambridge Univ. Press, Cambridge, 2007).

9. B. L. Otto-Bliesner *et al.*, *Science* **311**, 1751 (2006).
10. J. T. Overpeck *et al.*, *Science* **311**, 1747 (2006).
11. J. Hansen, *Environ. Res. Lett.* **2**, 024002 (2007).
12. J. Hansen *et al.*, *Philos. Trans. R. Soc. London Ser. A* **365**, 1925 (2007).
13. J. Mount, R. Twiss, *San Francisco Estuary Watershed Sci.* **3**, 1 (2005).
14. E. Bard *et al.*, *Nature* **382**, 241 (1996).
15. M. F. Meier *et al.*, *Science* **317**, 1064 (2007); published online 18 July 2007 (10.1126/science.1143906).
16. J. L. Bamber, R. L. Layberry, S. Gogineni, *J. Geophys. Res.* **106**, 33773 (2001).
17. B. Kamb *et al.*, *Science* **227**, 469 (1985).
18. E. R. Hope, "English translation T409R," Defense Research Board, Ottawa, Canada, 1963 [translation from L. D. Dolgushin, S. A. Yevteyev, A. N. Krenke, K. P. Rototayev, N. M. Svatkov, *Priroda* **11**, 84 (1963)].
19. E. Rignot *et al.*, *Nat. Geosci.* **1**, 106 (2008).
20. E. Rignot, personal communication (2007).
21. R. Thomas *et al.*, *Science* **289**, 426 (2000).
22. G. A. Meehl *et al.*, in (*8*).
23. This work was supported by NSF grants OPP-0327345 and OPP-0622351 and a University of Colorado Faculty Fellowship (W.T.P.), NSF grants OPP-0612506 and OPP-0454789 (J.T.H.), and the Greens Foundation at Scripps Institution of Oceanography (S.O.). E. Rignot generously supplied Greenland surface velocity data.

**Supporting Online Material**

www.sciencemag.org/cgi/content/full/321/5894/1340/DC1
Materials and Methods
Fig. S1
Tables S1 and S2
References

14 April 2008; accepted 18 July 2008
10.1126/science.1159099

---

# *Apobec3* Encodes *Rfv3*, a Gene Influencing Neutralizing Antibody Control of Retrovirus Infection

Mario L. Santiago,[1] Mauricio Montano,[1]* Robert Benitez,[1]* Ronald J. Messer,[2] Wes Yonemoto,[1] Bruce Chesebro,[2] Kim J. Hasenkrug,[2]† Warner C. Greene[1,3,4]†

Recovery from Friend virus 3 (*Rfv3*) is a single autosomal gene encoding a resistance trait that influences retroviral neutralizing antibody responses and viremia. Despite extensive research for 30 years, the molecular identity of *Rfv3* has remained elusive. Here, we demonstrate that *Rfv3* is encoded by *Apobec3*. *Apobec3* maps to the same chromosome region as *Rfv3* and has broad inhibitory activity against retroviruses, including HIV. Not only did genetic inactivation of *Apobec3* convert *Rfv3*-resistant mice to a susceptible phenotype, but *Apobec3* was also found to be naturally disabled by aberrant messenger RNA splicing in *Rfv3*-susceptible strains. The link between *Apobec3* and neutralizing antibody responses highlights an *Apobec3*-dependent mechanism of host protection that might extend to HIV and other human retroviral infections.

The study of viral resistance factors has provided important insights into the evolutionary strategies of defense used by mammalian hosts (*1*–*5*). Recovery from Friend virus (FV) gene 3 (*Rfv3*) was first identified as a resistance trait in 1978 (*6*, *7*), and later genetic studies showed that the phenotypes of decreased viremia and FV-specific neutralizing antibody responses segregated as a single gene (*8*). Because the generation of neutralizing antibodies is critical for recovery from FV infection (*1*, *9*) and a desired but often unrealized outcome in various retroviral infections, including HIV-1, we have focused our efforts on identifying the gene encoding *Rfv3*. The *Rfv3* locus maps to a 0.83-centimorgan region of chromosome 15 (fig. S1A) (*10*–*12*), which contains at least 61 annotated genes (table S1), one of which is murine *Apobec3* (*mA3*), a member of a family of deoxycytidine deaminases with antiretroviral and antiretroelement activity [as reviewed in (*13*)]. This fact, along with the presence of substantial polymorphism in *mA3* (table S1), led us to consider *mA3* as a prime candidate for *Rfv3*.

Because *Rfv3* has no described in vitro phenotype, our investigation required the generation of *mA3*-deficient mice (*14*). First, an inactivated *mA3* gene (fig. S1B) was introduced into the *Rfv3*$^{r/r}$ C57BL/6 (B6) background to test its ability to act as a defective *Rfv3* allele in matings with *Rfv3*$^{s/s}$ mice (Table 1). Because the *Rfv3* resistance trait is dominant over susceptibility (*7*), *Rfv3*$^{r/s}$ $F_1$ offspring should control viremia and mount effective neutralizing antibody responses. Conversely, if *mA3* encodes *Rfv3*, then the gene from a *mA3*$^{-/-}$ parent will be null, and the resultant $F_1$ offspring with an *Rfv3*$^{-/s}$ genotype are predicted to exhibit higher levels of viremia and weaker neutralizing antibody responses. To test this possibility, B6 x BALB/c $F_1$ offspring were infected with FV and plasma viremia levels were measured. At 7 days post infection (dpi), the $F_1$ mice containing an inactivated *mA3* gene exhibited levels of viremia 15 times as high as their congenic partners carrying the wild-type *mA3* allele (Fig. 1A). These high viral loads in *mA3*$^{-}$ $F_1$ mice were comparable to FV levels found in fully susceptible *Rfv3*$^{s/s}$ BALB/c parental mice. Thus, *mA3* is a restriction factor contributing to the

**Table 1.** FV infection characteristics of various mouse strains used in this study.

| Type | Strain | General FV susceptibility | Viremia | *Rfv3* | Neutralizing antibody | *H-2** | Cell-mediated immunity | *Fv2*† | Splenomegaly induction |
|---|---|---|---|---|---|---|---|---|---|
| Wild-type | C57BL/6 (B6) | Resistant | Resistant | *r/r* | High | *b/b* | High | *r/r* | No |
| | BALB/c | Susceptible | Chronic | *s/s* | Low | *d/d* | Very low | *s/s* | Yes |
| | A.BY | Susceptible | Chronic | *s/s* | Low | *b/b* | High | *s/s* | Yes |
| | 129/Ola‡ | Resistant | Resistant | *r/r* | High | *b/b* | High | *r/r* | No |
| $F_1$ hybrids | B6 x BALB/c | Susceptible | Acute | *r/s* | High | *b/d* | Low | *r/s* | Yes |
| | B6 x A.BY | Susceptible | Acute | *r/s* | High | *b/b* | High | *r/s* | Yes |

**H-2* is the murine major histocompatibility complex that dictates cell-mediated immunity against FV (*5*, *15*). †*Fv2* is a dominant FV susceptibility gene that facilitates splenomegaly induction through aberrant signaling in erythroblasts (*4*). ‡FV susceptibility data on 129/Ola were based on results from this study (Fig. 2C) (*14*). The cell-mediated immune response of this strain was inferred from its *H-2* haplotype.

---

[1] Gladstone Institute of Virology and Immunology, San Francisco, CA 94158, USA. [2] Laboratory of Persistent Viral Diseases, Rocky Mountain Laboratories, National Institute of Allergy and Infectious Diseases, Hamilton, MT 59840, USA. [3] Department of Medicine, University of California, San Francisco, CA 94143–1230, USA. [4] Department of Microbiology and Immunology, University of California, San Francisco, CA 94143–1230, USA.

*These authors contributed equally to this work.

†To whom correspondence should be addressed. E-mail: khasenkrug@nih.gov (K.J.H.); wgreene@gladstone.ucsf.edu (W.C.G.)

early control of FV infection in adult immunocompetent mice.

*Rfv3*-mediated recovery from FV infection correlates strongly with FV-specific neutralizing antibody responses at 28 dpi (*7*). Thus, $mA3^+$ and *mA3* F$_1$ congenic strains were monitored for up to 1 month after FV infection. However, F$_1$ mice lacking the B6 *mA3* allele suffered a markedly higher rate of FV-induced death (Fig. 1B), indicating that, like $Rfv3^s$ susceptibility, *mA3* inactivation compromised recovery from FV disease. Compared with $mA3^+$ F$_1$ mice, the three surviving *mA3* F$_1$ mice exhibited mean viremia higher by a factor of 14 (fig. S2A) and low FV-specific neutralizing antibody titers at 28 dpi (fig. S2B), but the small number of surviving animals precluded obtaining statistically significant data. Therefore, separate cohorts of mice were studied for FV-specific antibodies at 14 dpi, before the steep decline in survival of *mA3* F$_1$ mice. The *mA3* F$_1$ mice exhibited significantly less FV binding antibody than $mA3^+$ F$_1$ mice, and the low levels of FV antibodies in *mA3* F$_1$ mice proved comparable to levels detected in the parental $Rfv3^{s/s}$ BALB/c mice (Fig. 1C). These findings indicated that *mA3* influenced FV-specific antibody responses.

To better assess FV-specific neutralizing antibody responses in mice expressing or lacking *mA3*, these studies were repeated in high-recovery B6 x A.BY F$_1$ mice, which generally survive more than 1 month after FV infection because of protective cell-mediated immune responses associated with the $H$-$2^{b/b}$ haplotype (Table 1) (*5*, *15*). Plasma samples obtained at 28 dpi revealed significantly lower FV-specific neutralizing antibody titers in *mA3* F$_1$ mice compared with $mA3^+$ F$_1$ mice (Fig. 1D). These findings confirmed that *mA3* influenced FV-specific neutralizing antibody responses and demonstrated that this effect operated independently of *H-2*, a known property of *Rfv3* (*7*).

Purebred B6 mice are highly resistant to FV infection (Table 1), but their resistance can be overcome by inoculating aged mice with high doses of FV (*16*) or by using immunodeficient mice, including those that fail to produce specific antibodies (*9*). Genetic inactivation of *mA3* in B6 mice might therefore recapitulate the $Rfv3^s$ susceptible phenotype without a requirement for outcrossing to susceptible strains. To test this possibility, >16-week-old B6 $mA3^{+/+}$ and $mA3^{-/-}$ mice were infected with FV. Plasma viremia was 6.2 times as high in $mA3^{-/-}$ mice as in $mA3^{+/+}$ mice at 8 dpi (Fig. 2A). Furthermore, $mA3^{-/-}$ mice exhibited significantly lower neutralizing antibody titers than wild-type mice by 28 dpi (Fig. 2B). Thus, *mA3* inactivation was sufficient both to enhance viremia and to diminish neutralizing antibody production even in the highly resistant B6 genetic background. These results were confirmed in a second highly resistant strain of mice, 129/Ola (Table 1 and Fig. 2C) (*14*). Together, these findings demonstrate that genetic inactivation of *mA3* recapitulates the $Rfv3^s$ phenotype and indicate that *Rfv3* is encoded by *mA3*.

Both resistant and susceptible mouse strains contain the *mA3* gene and express *mA3* mRNA. Cloning of splenocyte *mA3* mRNA from the $Rfv3^{r/r}$ 129/Ola strain revealed the predominant expression of a full-length *mA3* transcript, whereas most mRNA transcripts from $Rfv3^{r/r}$ B6 mice lacked exon 5 sequences (figs. S3 and S4) (*17*). *mA3* transcripts from both $Rfv3^{s/s}$ strains BALB/c and A.BY were distinguished by the absence of exon 2 sequences (Fig. 3A and fig. S4). Quantitative reverse transcription polymerase chain reaction (RT-PCR) revealed similar levels of total *mA3* mRNA in both the $Rfv3^{r/r}$ and $Rfv3^{s/s}$ strains but a level lower by a factor of 17 of Exon2-containing transcripts in both $Rfv3^{s/s}$ mouse strains (Fig. 3B). Thus, the presence of an alternatively spliced *mA3* mRNA lacking exon 2 correlated with the $Rfv3^s$-susceptible phenotype.

Translational read-through of the *mA3* mRNA lacking exon 2 predicts two possible outcomes: no mA3 protein expression or a truncated mA3 protein (Fig. 3A and fig. S5). Without suitable mA3 antibodies, these outcomes cannot be distinguished. We investigated the antiviral activity of this latter Δexon 2 mA3 protein by cloning it as a fusion with an N-terminal triple FLAG epitope tag. NIH3T3 cells were cotransfected with the expression construct and an FV molecular clone (pLRB302) (*18*) to test the infectivity of the resulting FV virions. For comparison, cotransfections were performed with a FLAG-tagged expression construct containing the *mA3* cDNA from B6 mice lacking exon 5. When standardized for relative mA3 expression levels, the BALB/c Δexon 2 mA3 protein was at least 3 to 5 times less potent at inhibiting FV infectivity than was the B6 Δexon 5 mA3 protein (Fig. 3C). In control experiments, the full-length mA3 protein from 129/Ola also potently inhibited FV (fig. S6). These data indicated that, even if a truncated mA3 protein were expressed in $Rfv3^{s/s}$ mice, its antiviral activity would be significantly impaired.

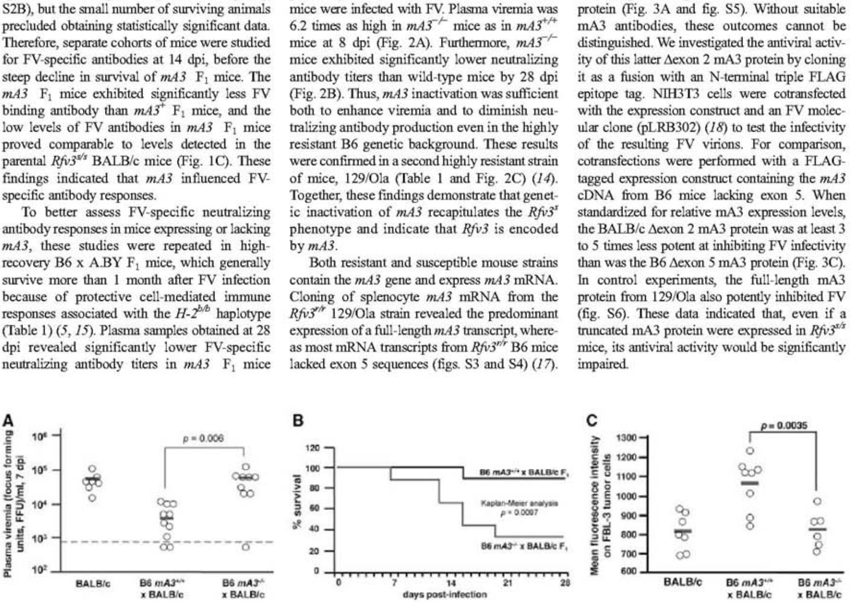

**Fig. 1.** The *Rfv3* genetic restriction is mediated by *mA3* in vivo. (**A** to **C**) *mA3* confers the *Rfv3* phenotype in low-recovery $H$-$2^{b/d}$ mice. Congenic $mA3^+$ and $mA3^-$ (B6 x BALB/c) F$_1$ mice were infected with 140 spleen focus-forming units (SFFU) of FV. (A) *mA3* is required for viremic control at an early time point (7 dpi); (B) *mA3* inactivation compromises *Rfv3*-associated survival from FV-induced disease; (C) *mA3* influences FV-specific immunoglobulin G (IgG) production 14 dpi. FV binding IgG was measured by flow cytometry using FV antigen-expressing FBL-3 cells. (**D**) *mA3* confers the *Rfv3* phenotype in high-recovery $H$-$2^{b/b}$ mice. Congenic (B6 x A.BY)F$_1$ mice were infected with 1400 SFFU of FV. Mean 28 dpi neutralizing antibody (NAb) titers (75% inhibitory concentration, IC$_{75}$) are significantly lower in $mA3^-$ F$_1$ mice. Open circles indicate individual mice data, gray bars indicate means, and dashed lines refer to the assay detection limit. Statistical analyses were performed with two-tailed Student's *t* test.

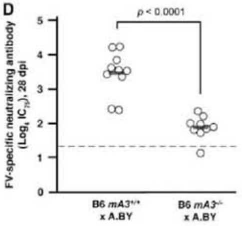

The involvement of *mA3* in the control of FV viremia before the onset of adaptive anti-FV immune responses confirms its stature as a bona fide innate immune factor in vivo. In addition, *mA3* influences the development of virus-specific neutralizing antibody responses, perhaps by (i) limiting the early viral antigenic load and evading a form of "high-zone tolerance" (*19*–*21*) or (ii) inhibiting early FV-induced injury of critical cell types, such as B cells, T cells, or antigen-presenting cells, required for the development of FV-specific humoral immunity. However, mA3 is expressed in B cells and is evolutionarily related to activation-induced deaminase, an enzyme that controls somatic hypermutation and class-switch recombination in these cells (*22*). Thus, mA3 may conceivably be involved in shaping the antibody repertoire.

The human *Apobec3* family has been implicated in the control of HIV-1 infection, but HIV-1 encodes Vif, which thwarts the actions of Apobec3G (A3G) and Apobec3F (A3F) (*23*–*26*). Compromised A3G/A3F antiviral activity may therefore contribute to the generally poor neutralizing antibody response observed in HIV-1 infection (*27*). Vif antagonists, if and when they are available, may enhance the generation of effective humoral immune responses against HIV-1. Finally, studies exploring the apparent intrinsic resistance of individuals who are extensively exposed to HIV-1, yet remain uninfected, have genetically mapped this phenotype to chromosome 22q12-13 (*12*), a location distinguished by a tandem array of the seven human *Apobec3* family members. Genome-wide studies of the entire human *Apobec3* locus, with particular emphasis on functional differences induced by alternative splicing, are clearly merited to fully explore the potential contribution of this gene family to HIV resistance, neutralizing antibody production, and disease progression.

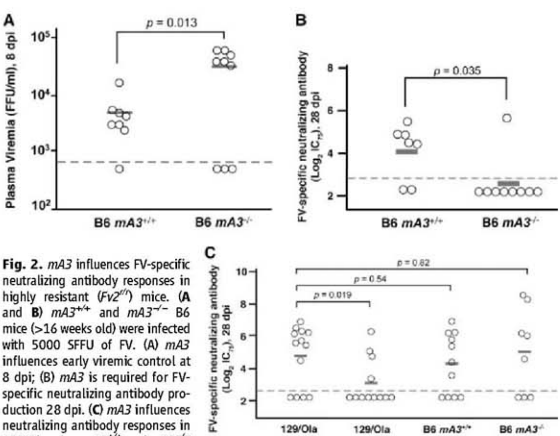

**Fig. 2.** *mA3* influences FV-specific neutralizing antibody responses in highly resistant ($Fv2^{r/r}$) mice. (**A** and **B**) $mA3^{+/+}$ and $mA3^{-/-}$ B6 mice (>16 weeks old) were infected with 5000 SFFU of FV. (A) *mA3* influences early viremic control at 8 dpi; (B) *mA3* is required for FV-specific neutralizing antibody production 28 dpi. (**C**) *mA3* influences neutralizing antibody responses in 129/Ola mice. $mA3^{+/+}$ and $mA3^{-/-}$ 129/Ola mice were crossed with $mA3^{+/+}$ and $mA3^{-/-}$ B6 mice to generate $F_1$ offspring. FV-specific neutralizing antibody titers ($IC_{75}$) at 28 dpi with 5000 SFFU of FV are shown. Additional information is found in SOM text and (*14*). Statistical analysis was performed using a two-tailed Student's *t* test.

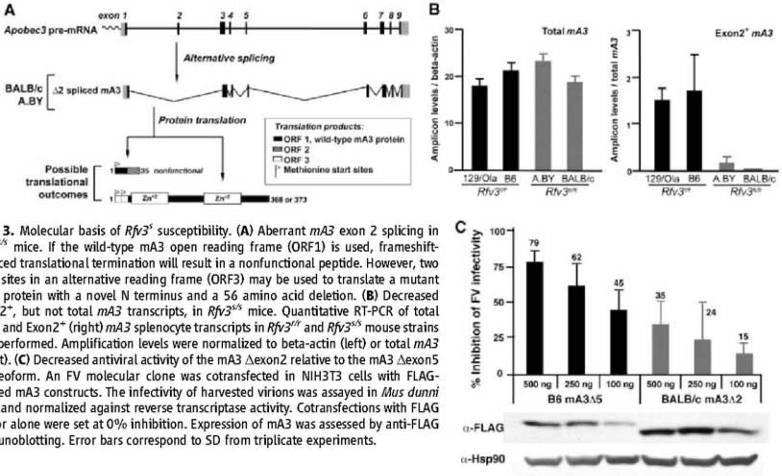

**Fig. 3.** Molecular basis of $Rfv3^s$ susceptibility. (**A**) Aberrant *mA3* exon 2 splicing in $Rfv3^{s/s}$ mice. If the wild-type mA3 open reading frame (ORF1) is used, frameshift-induced translational termination will result in a nonfunctional peptide. However, two start sites in an alternative reading frame (ORF3) may be used to translate a mutant mA3 protein with a novel N terminus and a 56 amino acid deletion. (**B**) Decreased Exon2$^+$, but not total *mA3* transcripts, in $Rfv3^{s/s}$ mice. Quantitative RT-PCR of total (left) and Exon2$^+$ (right) *mA3* splenocyte transcripts in $Rfv3^{r/r}$ and $Rfv3^{s/s}$ mouse strains was performed. Amplification levels were normalized to beta-actin (left) or total *mA3* (right). (**C**) Decreased antiviral activity of the mA3 Δexon2 relative to the mA3 Δexon5 spliceoform. An FV molecular clone was cotransfected in NIH3T3 cells with FLAG-tagged mA3 constructs. The infectivity of harvested virions was assayed in *Mus dunni* cells and normalized against reverse transcriptase activity. Cotransfections with FLAG vector alone were set at 0% inhibition. Expression of mA3 was assessed by anti-FLAG immunoblotting. Error bars correspond to SD from triplicate experiments.

### References and Notes

1. K. J. Hasenkrug, B. Chesebro, *Proc. Natl. Acad. Sci. U.S.A.* **94**, 7811 (1997).
2. W. Li, W. R. Green, *J. Virol.* **80**, 5777 (2006).
3. S. Best, P. Le Tissier, G. Towers, J. P. Stoye, *Nature* **382**, 826 (1996).
4. D. A. Persons *et al.*, *Nat. Genet.* **23**, 159 (1999).
5. W. J. Britt, B. Chesebro, *J. Exp. Med.* **157**, 1736 (1983).
6. B. Chesebro, K. Wehrly, in *Advances in Comparative Leukemia Research*, P. Bentvelzen, Ed. (North-Holland Biomedical Press, Elsevier, 1978), pp. 69–73.
7. B. Chesebro, K. Wehrly, *Proc. Natl. Acad. Sci. U.S.A.* **76**, 425 (1979).
8. D. Doig, B. Chesebro, *J. Exp. Med.* **150**, 10 (1979).
9. K. J. Hasenkrug, *J. Virol.* **73**, 6468 (1999).
10. K. J. Hasenkrug *et al.*, *J. Virol.* **69**, 2617 (1995).
11. H. J. Super *et al.*, *J. Virol.* **73**, 7848 (1999).
12. Y. Kanari *et al.*, *AIDS* **19**, 1015 (2005).
13. Y. L. Chiu, W. C. Greene, *Annu. Rev. Immunol.* **26**, 317 (2008).
14. Materials and methods are available as supporting material on *Science* Online.
15. B. Chesebro, K. Wehrly, *J. Exp. Med.* **143**, 73 (1976).
16. H. C. Van der Gaag, A. A. Axelrad, *Virology* **177**, 837 (1990).
17. S. J. Rulli Jr. *et al.*, *J. Virol.* **82**, 6566 (2008).
18. J. L. Portis, F. J. McAtee, S. C. Kayman, *J. Acquir. Immune Defic. Syndr.* **5**, 1272 (1992).
19. J. G. Monroe, A. Lowy, R. D. Granstein, M. I. Greene, *Immunol. Rev.* **80**, 103 (1984).
20. A. Gonzalez-Fernandez, C. Milstein, *Immunology* **93**, 149 (1998).
21. Y. T. Kim, G. W. Siskind, *Clin. Exp. Immunol.* **17**, 329 (1974).
22. M. Muramatsu *et al.*, *Cell* **102**, 553 (2000).
23. K. Stopak, C. de Noronha, W. Yonemoto, W. C. Greene, *Mol. Cell* **12**, 591 (2003).
24. M. Marin, K. M. Rose, S. L. Kozak, D. Kabat, *Nat. Med.* **9**, 1398 (2003).
25. A. M. Sheehy, N. C. Gaddis, M. H. Malim, *Nat. Med.* **9**, 1404 (2003).
26. Y. H. Zheng *et al.*, *J. Virol.* **78**, 6073 (2004).
27. D. R. Burton *et al.*, *Nat. Immunol.* **5**, 233 (2004).

28. We thank the Transgenic Core Laboratory, the Animal Facility, and S. Espineda at the J. David Gladstone Institutes for technical assistance; L. Evans, J. Portis, R. Gallo, R. Locksley, and members of the Greene and Hasenkrug Laboratory for helpful discussions; and R. Givens, S. Cammack, and G. Howard for manuscript preparation. This work was supported by the NIAID Division of Intramural Research at NIH to K.J.H. and B.C., an NIH R01 AI065329 to W.C.G., and an NIH facility grant to the J. David Gladstone Institutes. Sequences are deposited in GenBank, with accession numbers EU707568 to EU707571.

### Supporting Online Material

www.sciencemag.org/cgi/content/full/321/5894/1343/DC1
Materials and Methods
SOM Text
Figs. S1 to S6
Table S1
References

29 May 2008; accepted 24 July 2008
10.1126/science.1161121

---

# Human-Specific Gain of Function in a Developmental Enhancer

**Shyam Prabhakar,[1]* Axel Visel,[1] Jennifer A. Akiyama,[1] Malak Shoukry,[1] Keith D. Lewis,[1]† Amy Holt,[1] Ingrid Plajzer-Frick,[1] Harris Morrison,[2] David R. FitzPatrick,[2] Veena Afzal,[1] Len A. Pennacchio,[1,3] Edward M. Rubin,[1,3]‡ James P. Noonan[1]‡§**

Changes in gene regulation are thought to have contributed to the evolution of human development. However, in vivo evidence for uniquely human developmental regulatory function has remained elusive. In transgenic mice, a conserved noncoding sequence (*HACNS1*) that evolved extremely rapidly in humans acted as an enhancer of gene expression that has gained a strong limb expression domain relative to the orthologous elements from chimpanzee and rhesus macaque. This gain of function was consistent across two developmental stages in the mouse and included the presumptive anterior wrist and proximal thumb. In vivo analyses with synthetic enhancers, in which human-specific substitutions were introduced into the chimpanzee enhancer sequence or reverted in the human enhancer to the ancestral state, indicated that 13 substitutions clustered in an 81–base pair module otherwise highly constrained among terrestrial vertebrates were sufficient to confer the human-specific limb expression domain.

Genome sequence changes that altered the molecular machinery of development likely facilitated the evolution of uniquely human morphological traits (*1*, *2*). Although these genetic modifications remain largely unidentified, it has long been thought that they included changes in gene expression due to positive selection for nucleotide substitutions that altered the activity of cis-regulatory elements (*3*). Several cases of putatively adaptive sequence change, including polymorphisms among human populations and apparently fixed differences between humans and other primates, have been shown to affect in vitro promoter or enhancer function in cell line reporter assays (*4*–*7*). However, the impact of human-specific nucleotide substitutions on the in vivo activity of developmental regulatory elements remains obscure.

In vivo analyses of evolutionarily conserved noncoding sequences have revealed them to be enriched in cis-regulatory transcriptional enhancers that confer specific expression patterns during development (*8*–*11*). Recent efforts have identified conserved noncoding sequences that evolved rapidly on the human lineage, but it is not known whether these sequences include regulatory elements with altered activities in humans (*12*–*15*). Here, we focus on functionally characterizing the most rapidly evolving human noncoding element yet identified, which we termed human-accelerated conserved noncoding sequence 1 (*HACNS1*) (*12*). Although this 546–base pair (bp) element is highly constrained in all sequenced terrestrial vertebrate genomes, it has accumulated 16 human-specific sequence changes in the ~6 million years since the human-chimpanzee split (Fig. 1A). We evaluated the significance of this evolutionary acceleration by means of a test statistic that represents the log-likelihood, or information theoretic "surprisal," of observing the human sequence given the orthologous sequences from multiple terrestrial vertebrates. Assuming *HACNS1* is under functional constraint in humans, its rapid divergence is highly unexpected given its strong conservation in these other species [surprisal test $P$ value = $9.2 \times 10^{12}$ (*16*)]. This divergence also significantly exceeds the ~4 substitutions expected if *HACNS1* were evolving at the neutral substitution rate in humans [surprisal test $P$ value = $1.3 \times 10^{6}$ (*16*)]. One explanation for this marked acceleration is that *HACNS1* has undergone several instances of positive selection during human evolution that may have altered its function.

To test this hypothesis, we evaluated the ability of *HACNS1* and its orthologs from chimpanzee and rhesus macaque to function as transcriptional enhancers during development, using a transgenic mouse enhancer assay in which the activity of each sequence is assessed through a β-galactosidase (*lacZ*) reporter gene coupled to a minimal *Hsp68* promoter (*17*). We initially examined the potential enhancer activity of *HACNS1* at embryonic day 11.5 (E11.5). We tested a 1.2-kb DNA fragment encompassing *HACNS1* that also contained nonconserved sequences flanking the element, in order to include possible functional sequences near *HACNS1* not detected by conservation (table S1). At E11.5, the human element drove strong and reproducible reporter gene expression in the anterior limb bud, pharyngeal arches, and developing ear and eye, which suggests that *HACNS1* acts as a robust enhancer during development (Fig. 1, B and C, and fig. S1). In striking contrast to the highly reproducible staining driven by the human enhancer, which extended into the most distal region of the anterior limb bud in five of six lacZ-positive embryos (Fig. 1C and *HACNS1* embryos

---

[1] Genomics Division, Lawrence Berkeley National Laboratory, Berkeley, CA 94720, USA. [2] MRC Human Genetics Unit, Western General Hospital, Edinburgh EH4 2XU, UK. [3] United States Department of Energy Joint Genome Institute, Walnut Creek, CA 94598, USA.

*Present address: Computational and Mathematical Biology, Genome Institute of Singapore 138672, Singapore.
†Present address: Division of Biology, California Institute of Technology, Pasadena, CA 91125, USA.
‡To whom correspondence should be addressed. E-mail: emrubin@lbl.gov (E.M.R.); james.noonan@yale.edu (J.P.N.)
§Present address: Department of Genetics, Yale University School of Medicine, New Haven, CT 06520, USA.

1 to 5 in fig. S1), the chimpanzee and rhesus orthologs failed to drive reproducible reporter gene expression in the distal limb bud, although they did drive moderately reproducible expression at the base of the limb (Fig. 1, B and C; chimpanzee enhancer embryos 1, 2, 6, 7, and 8 and rhesus enhancer embryos 1 to 4, 6 to 8, and 10 in fig. S1).

Two of the embryos that were transgenic for the chimpanzee ortholog and showed this pattern also exhibited diffuse, low-level staining that extended into the anterior limb, which suggests that the chimpanzee enhancer may possess a weak capacity to drive expression in this structure (embryos 6 and 7 in fig. S1). However, this infrequent pattern was in stark contrast to the strong and highly reproducible pattern of the human enhancer. Furthermore, pharyngeal arch, eye, and ear expression was less reproducible and, where present, generally weaker in multiple positive embryos for both nonhuman orthologs; these findings suggest additional sites of reduced overall enhancer activity relative to the human ortholog.

To assess the *HACNS1* limb expression pattern at higher resolution, we sectioned *HACNS1* transgenic embryos and found that staining in the forelimb was restricted to the mesenchyme, forming a continuous expression domain that extended deep into the limb bud along the anteroposterior axis at the handplate and shoulder while remaining more anterior in between (fig. S3). These results provide evidence that the human-specific sequence changes in *HACNS1* have resulted in a gain of function in this otherwise highly conserved enhancer, increasing its overall robustness and producing a strong human-specific expression domain in the anterior limb bud mesenchyme at E11.5. Because the chimpanzee and rhesus orthologs yield similar patterns to each other and show consistent differences relative to *HACNS1*, a parsimonious conclusion would be that the chimpanzee and rhesus patterns reflect the ancestral primate state from which the human-specific pattern has evolved.

To explore the activity of *HACNS1* at a more advanced stage of limb development, we compared the expression patterns of the human, chimpanzee, and rhesus enhancers in E13.5 transgenic mouse embryos. At this stage, the human element continued to drive reproducible reporter gene expression in the anterior developing forelimb, particularly in the shoulder and the anterior junction of the forearm and handplate, in 11 of 12 positive embryos (Fig. 2, A to C; embryos 1 to 10 and 12 in fig. S2). In four of these embryos, the reporter gene activity extended into the future anterior-most digit of the forelimb (Fig. 2B). Similar expression, although with weaker staining, was also observed in the corresponding structures in the hindlimb. Imaging of lacZ staining in a representative *HACNS1* transgenic embryo by means of optical projection tomography [OPT (*18*)] revealed that the anterior expression evident in the whole mount extended deep inside the limb at the forearm-handplate junction (fig. S4). The orthologous chimpanzee and rhesus elements failed to drive reproducible expression in the distal limbs at this time point, although a subset of positive embryos in each case (4 of 10 for chimpanzee; 3 of 12 for rhesus) showed reporter gene expression in the shoulder region of the limb bud, thus recapitulating the proximal tip of the expression domain of the human enhancer (Fig. 2A; chimpanzee enhancer embryos 2 to 5 and rhesus enhancer embryos 1, 5, and 6 in fig. S2). OPT imaging confirmed the absence of reproducible lacZ staining inside the distal limb in representative embryos transgenic for the rhesus and chimpanzee enhancers (fig. S4). These results indicate that the human-specific enhancer activity persists across multiple developmental stages. Moreover, they suggest that the robust anterior limb expression pattern of *HACNS1* evolved from a weaker ancestral pattern that is largely confined to the base of the limb bud, as evident in the

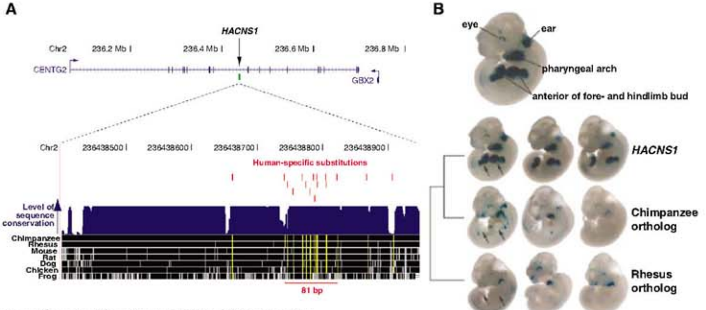

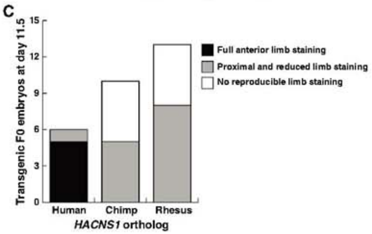

**Fig. 1.** Human-specific gain of function in *HACNS1*. (**A**) Top: Location of *HACNS1* in NCBI build 36.1 of the human genome assembly. Bottom: Sequence alignment of *HACNS1* with orthologs from other vertebrate genomes; positions identical to human are shown in black. A quantitative plot of sequence conservation is shown in blue above the alignment (*26*–*28*). The location of each human-specific substitution is indicated by a vertical red line, and the depth of nonhuman evolutionary conservation at human-substituted positions is shown by a vertical yellow line that indicates whether each sequence is identical to chimpanzee and rhesus at that position. The cluster of 13 human-specific substitutions in 81 bp is also indicated. (**B**) Expression patterns obtained from the *HACNS1* enhancer and orthologous sequences from chimpanzee and rhesus driving expression of a *lacZ* reporter gene in E11.5 mouse embryos. Arrows indicate positions in the anterior limb bud where reproducible reporter gene expression is present or absent. A representative *HACNS1* embryo is shown at top to illustrate the relevant anatomical structures. Three embryos resulting from independent transgene integration events are shown for each orthologous sequence tested. (**C**) Number of embryos transgenic for each sequence displaying the limb expression patterns described in the text.

activities of the chimpanzee and rhesus enhancers at both time points.

We next sought to identify human-specific sequence changes responsible for the functional change in the human enhancer. Although the 16 human-specific substitutions within the 546-bp conserved region corresponding to *HACNS1* are the most striking feature of the 1.2-kb orthologous segments we initially tested for enhancer function, these segments also included ~650 bp of nonconserved DNA containing additional human-chimpanzee sequence differences. To isolate the effect of the substitutions within *HACNS1* on enhancer function, we synthesized a chimeric 1.2-kb enhancer in which we transferred all 16 substitutions into the chimpanzee sequence background (*16*). This "humanized" chimpanzee enhancer produced an E11.5 expression pattern nearly identical to that of the native human enhancer; this finding suggests that the human-specific sequence changes within *HACNS1* are responsible for the gain of function we observed (8 of 8 embryos; Fig. 3D and fig. S1). Strikingly, these human-specific substitutions were significantly clustered: 13 of 16 substitutions occurred within an 81-bp region of the 546-bp conserved element [permutation test *P* value = $1.7 \times 10^{7}$ (*16*)], which suggests that this region may be particularly relevant to the human-specific function of *HACNS1* (Figs. 1A and 3A).

To test this hypothesis, we synthesized a chimeric 1.2-kb enhancer in which the 13 clustered human substitutions were introduced into the chimpanzee sequence background (table S2). At E11.5, this element produced an anterior limb bud pattern highly similar to the *HACNS1* pattern (6 of 6 positive embryos; Fig. 3 and fig. S1). We also performed the reciprocal experiment, synthesizing a complementary chimeric enhancer where we replaced the 13 human-specific nucleotides in the human enhancer sequence with their putatively ancestral orthologs from chimpanzee. This "reverted" enhancer yielded a pattern very similar to the chimpanzee and rhesus enhancer patterns shown in Fig. 1B, with expression in the anterior limb bud greatly reduced or absent (Fig. 3 and fig. S1). These results confirm the robustness of the functional differences we observed between *HACNS1* and its chimpanzee and rhesus orthologs, and they indicate that the *HACNS1* anterior limb bud pattern is largely attributable to one or more of the 13 clustered human-specific substitutions we identified. To further dissect the functional contribution of these substitutions, we introduced independent groups of six substitutions and three substitutions into the chimpanzee enhancer sequence (fig. S5). These enhancers drove variable expression in the anterior limb bud, which suggests that at least two human-specific substitutions are required for the gain of function in *HACNS1*.

The precise molecular mechanism by which the substitutions in *HACNS1* confer the human-specific expression pattern remains to be determined. Computational analysis of predicted transcription factor binding sites in *HACNS1* and its nonhuman orthologs suggested that multiple sites have been gained and lost in this enhancer during human evolution (fig. S6). Predicted human-specific binding sites for the developmental transcription factors PAX9 and ZNF423 may contribute to *HACNS1* enhancer activity, given that the known expression pattern of *PAX9* in the mouse limb overlaps the human-specific limb domain of *HACNS1* at E11.5 and E13.5, and *ZNF423* is expressed in the mouse handplate mesenchyme from E10.5 through E12.5 (*19–21*).

Multiple lines of evidence suggest that the functional changes in *HACNS1* are due to adaptive evolution. The rate of human-specific accelerated evolution in *HACNS1* is more than 4 times the local neutral rate. Moreover, this rapid evolution cannot be explained purely on the basis of biased gene conversion (BGC), a neutral mechanism postulated to cause hotspots of accelerated evolution in the genome by increasing the local fixation rate of AT → GC substitutions (*22*, *23*). Under the neutral BGC hypothesis, one would expect an increase in the overall substitution rate across the entire region of increased AT → GC substitution (*23*). An excess of AT → GC substitutions is indeed present in *HACNS1* [binomial test *P* value = $1.1 \times 10^{4}$ (*16*)], and the element lies in a ~5-kb genomic region enriched in such substitutions (Fig. 4). However, the human-specific substitution rate is elevated only in the narrow 81-bp region in *HACNS1* described above and is close to the local average outside of this window (Fig. 4). These data, coupled with the human-specific functional changes in *HACNS1*, argue against a purely neutral explanation for the rapid evolution of this element in humans.

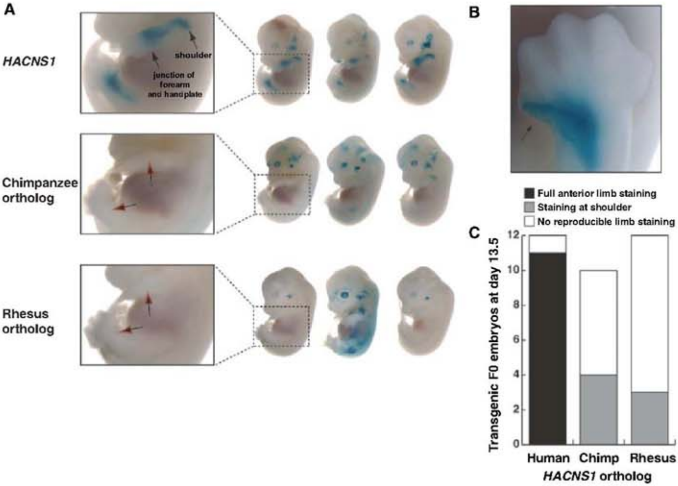

**Fig. 2.** Gain of function in *HACNS1* persists at E13.5. **(A)** Expression patterns obtained from *HACNS1* and its chimpanzee ortholog in E13.5 mouse embryos. Three embryos resulting from independent transgene integration events are shown for each construct. Close-up views of forelimb and hindlimb expression in a representative embryo for each construct are shown at left, and arrows indicate positions where limb expression is present or absent. **(B)** Dorsal view of reporter gene expression in the distal anterior forelimb of a *HACNS1* E13.5 transgenic embryo. Arrow indicates the most anterior digit. **(C)** Number of embryos transgenic for each construct that display the limb expression patterns described in the text.

Our results evoke the hypothesis that human-specific adaptive evolution in *HACNS1* has contributed to uniquely human aspects of digit and limb patterning. The dexterity of the human hand is due to morphological differences compared with other primates that include rotation of the thumb toward the palm and an increase in the length of the thumb relative to the other digits (*1*). Human-specific changes in hindlimb morphology, such as the characteristic inflexibility and shortened digits of the human foot, facilitated habitual bipedalism. The gain of function in *HACNS1* may have influenced the evolution of these or other human limb features by altering the expression of nearby genes during limb development. *HACNS1* is located within an intron of *CENTG2*, which encodes a guanosine triphosphatase activating protein involved in the regulation of endosome function. The next-closest gene is *GBX2*, which is located ~300 kb downstream of *HACNS1* and encodes an essential developmental transcription factor (*24*, *25*). The role of *CENTG2* in limb development has not been evaluated. Mouse *Gbx2* is expressed in the developing limb, but *Gbx2* null mice have not been described as showing abnormal limbs (*25*). The potential impact of human-specific changes in the expression of these genes on limb development thus remains to be explored. We also note that the *HACNS1* expression pattern in transgenic mice may not entirely recapitulate the precise *HACNS1* expression pattern in the human embryo. We therefore cannot rule out the possibility that the accelerated evolution of *HACNS1* reflects selection for changes in structures other than, or in addition to, the limb. Elucidating the role of *HACNS1* in human morphological evolution requires further lines of evidence, including the analysis of *GBX2* and *CENTG2* expression during human development and the generation of *HACNS1* targeted replacement mice. Independent of these considerations, our study suggests that adaptive nucleotide substitution altered the function of a developmental enhancer in humans, and illustrates a strategy that could be used across the genome to understand at a molecular level how human development evolved through cis-regulatory change.

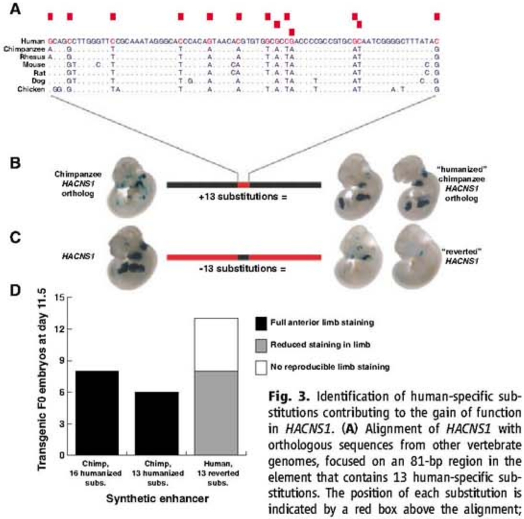

**Fig. 3.** Identification of human-specific substitutions contributing to the gain of function in *HACNS1*. (**A**) Alignment of *HACNS1* with orthologous sequences from other vertebrate genomes, focused on an 81-bp region in the element that contains 13 human-specific substitutions. The position of each substitution is indicated by a red box above the alignment; each human-specific nucleotide is highlighted in red. Positions in the nonhuman genomes that are identical to the human sequence are displayed as dots. (**B**) Expression pattern of a synthetic enhancer in which the 13 human-specific substitutions (red box) are introduced into the orthologous 1.2-kb chimpanzee sequence background (black bar). (**C**) Expression pattern of a synthetic enhancer obtained by reversion of these substitutions (black box) in the human sequence (red bar) to the nucleotide states in chimpanzee and rhesus. (**D**) Number of embryos transgenic for each synthetic enhancer that show full, partial, or no expression in the limb at E11.5.

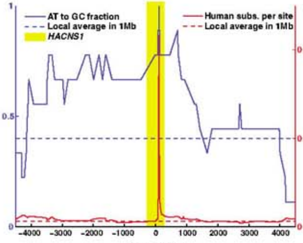

**Fig. 4.** Human-specific substitution rate and proportion of AT → GC substitutions in *HACNS1* and flanking genomic region. The rate of human-specific substitutions (solid red line) and the fraction of human substitutions that are AT → GC events (solid blue line) were estimated in sliding windows across a 9-kb interval around *HACNS1*. The average values of each metric for 1 Mb of genomic sequence centered on *HACNS1* are shown for reference (dashed lines). The 546-bp interval corresponding to *HACNS1* is highlighted in yellow.

### References and Notes

1. E. Trinkaus, in *The Cambridge Encyclopedia of Human Evolution*, S. Jones, R. Martin, D. Pilbeam, Eds. (Cambridge Univ. Press, New York, 1993), pp. 346–349.
2. S. B. Carroll, *Nature* **422**, 849 (2003).
3. M. C. King, A. C. Wilson, *Science* **188**, 107 (1975).
4. C. Tournamille *et al.*, *Nat. Genet.* **10**, 224 (1995).
5. M. V. Rockman *et al.*, *PLoS Biol.* **3**, e387 (2005).
6. S. A. Tishkoff *et al.*, *Nat. Genet.* **39**, 31 (2007).
7. G. A. Wray, *Nat. Rev. Genet.* **8**, 206 (2007).
8. D. Boffelli, M. A. Nobrega, E. M. Rubin, *Nat. Rev. Genet.* **5**, 456 (2004).
9. M. A. Nobrega, I. Ovcharenko, V. Afzal, E. M. Rubin, *Science* **302**, 413 (2003).
10. L. A. Pennacchio *et al.*, *Nature* **444**, 499 (2006).
11. A. Visel *et al.*, *Nat. Genet.* **40**, 158 (2008).
12. S. Prabhakar, J. P. Noonan, S. Pääbo, E. M. Rubin, *Science* **314**, 786 (2006).
13. K. S. Pollard *et al.*, *Nature* **443**, 167 (2006).
14. C. P. Bird *et al.*, *Genome Biol.* **8**, R118 (2007).
15. E. C. Bush, B. T. Lahn, *BMC Evol. Biol.* **8**, 17 (2008).
16. See supporting material on *Science* Online.
17. R. Kothary *et al.*, *Development* **105**, 707 (1989).
18. J. Sharpe *et al.*, *Science* **296**, 541 (2002).
19. A. Neubüser, H. Koseki, R. Balling, *Dev. Biol.* **170**, 701 (1995).
20. H. Peters, A. Neubüser, K. Kratochwil, R. Balling, *Genes Dev.* **12**, 2735 (1998).
21. S. Warming, T. Suzuki, T. P. Yamaguchi, N. A. Jenkins, N. G. Copeland, *Oncogene* **23**, 2727 (2004).
22. K. S. Pollard *et al.*, *PLoS Genet.* **2**, e168 (2006).
23. N. Galtier, L. Duret, *Trends Genet.* **23**, 273 (2007).
24. Z. Nie *et al.*, *J. Biol. Chem.* **277**, 48965 (2002).
25. K. M. Wassarman *et al.*, *Development* **124**, 2923 (1997).
26. M. Blanchette *et al.*, *Genome Res.* **14**, 708 (2004).
27. A. Siepel *et al.*, *Genome Res.* **15**, 1034 (2005).
28. W. J. Kent *et al.*, *Genome Res.* **12**, 996 (2002).

29. We thank members of the Pennacchio and Rubin laboratories for critical comments on the manuscript. Research was done under Department of Energy Contract

DE-AC02-05CH11231, University of California, E. O. Lawrence Berkeley National Laboratory, and supported by National Heart, Lung and Blood Institute grant HL066681 and National Human Genome Research Institute grant HG003988 (L.A.P.); the Agency for Science, Technology, and Research of Singapore (S.P.); an American Heart Association postdoctoral fellowship (A.V.); and NIH National Research Service Award fellowship 1-F32-GM074367 and the Department of Genetics, Yale University School of Medicine (J.P.N.).

**Supporting Online Material**
www.sciencemag.org/cgi/content/full/321/5894/1346/DC1
Materials and Methods
Figs. S1 to S6
Table S1
References

2 May 2008; accepted 7 July 2008
10.1126/science.1159974

---

# Wnt3a-Mediated Formation of Phosphatidylinositol 4,5-Bisphosphate Regulates LRP6 Phosphorylation

**Weijun Pan,[1]* Sun-Cheol Choi,[2]* He Wang,[3]* Yuanbo Qin,[3] Laura Volpicelli-Daley,[4] Laura Swan,[4] Louise Lucast,[4] Cynthia Khoo,[5] Xiaowu Zhang,[6] Lin Li,[3] Charles S. Abrams,[5] Sergei Y. Sokol,[2] Dianqing Wu[1]†**

The canonical Wnt–β-catenin signaling pathway is initiated by inducing phosphorylation of one of the Wnt receptors, low-density lipoprotein receptor-related protein 6 (LRP6), at threonine residue 1479 ($\text{Thr}^{1479}$) and serine residue 1490 ($\text{Ser}^{1490}$). By screening a human kinase small interfering RNA library, we identified phosphatidylinositol 4-kinase type II α and phosphatidylinositol-4-phosphate 5-kinase type I (PIP5KI) as required for Wnt3a-induced LRP6 phosphorylation at $\text{Ser}^{1490}$ in mammalian cells and confirmed that these kinases are important for Wnt signaling in *Xenopus* embryos. Wnt3a stimulates the formation of phosphatidylinositol 4,5-bisphosphates [PtdIns $(4,5)P_2$] through frizzled and dishevelled, the latter of which directly interacted with and activated PIP5KI. In turn, PtdIns $(4,5)P_2$ regulated phosphorylation of LRP6 at $\text{Thr}^{1479}$ and $\text{Ser}^{1490}$. Therefore, our study reveals a signaling mechanism for Wnt to regulate LRP6 phosphorylation.

Members of the Wnt family of secretory glycoproteins have important roles in various physiological and pathophysiological processes, including embryonic development, bone development, neuronogenesis, adipogenesis, myogenesis, organogenesis, lipid and glucose metabolism, and tumorigenesis (*1*–*5*). Canonical Wnt binds to two receptors, lipoprotein receptor-related protein 6 (LRP6) and frizzled (Fz) proteins, leading to phosphorylation of LRP6 at $\text{Thr}^{1479}$ by casein kinase 1γ and at $\text{Ser}^{1490}$ by glycogen synthase kinase 3 (GSK3) (*6*–*10*). Wnt appears to regulate $\text{Thr}^{1479}$ phosphorylation by inducing the formation of LRP6 aggregates (*9*), whereas it regulates $\text{Ser}^{1490}$ phosphorylation through GSK in an axin-dependent manner (*10*). To determine whether there are other kinases that take part in the regulation of LRP6 phosphorylation, we screened a human kinase small in-

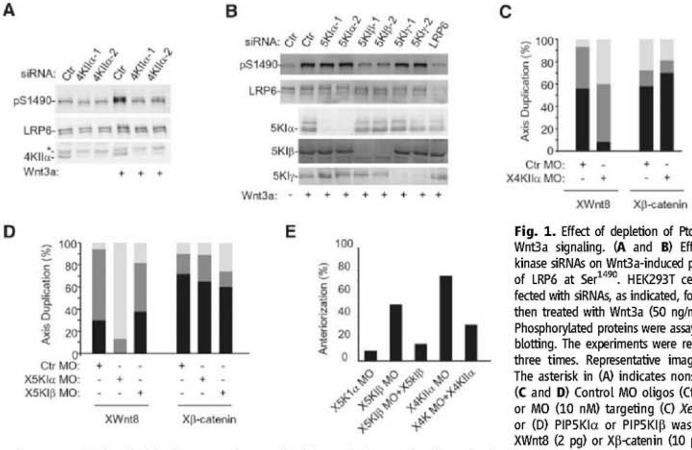

**Fig. 1.** Effect of depletion of PtdIns kinases on Wnt3a signaling. (**A** and **B**) Effects of PtdIns kinase siRNAs on Wnt3a-induced phosphorylation of LRP6 at $\text{Ser}^{1490}$. HEK293T cells were transfected with siRNAs, as indicated, for 48 hours and then treated with Wnt3a (50 ng/ml) for 30 min. Phosphorylated proteins were assayed by Western blotting. The experiments were repeated at least three times. Representative images are shown. The asterisk in (A) indicates nonspecific bands. (**C** and **D**) Control MO oligos (Ctr MO, 10 nM) or MO (10 nM) targeting (C) *Xenopus* PI4KIIα or (D) PIP5KIα or PIP5KIβ was injected with XWnt8 (2 pg) or Xβ-catenin (10 pg) mRNA into four-cell stage embryos. $n > 40$ for all of the *Xenopus* embryo studies (where $n$ is the number of examined embryos). Open bars, no double axis; light gray bars, incomplete double axis; black bars, complete double axis. (**E**) Four-cell stage embryos were injected with XPIP5KIβ MO (40 ng), XPI4KIIα MO (40 ng), or XPIP5KIα MO (40 ng) with or without XPIP5KIβ (10 pg) or XPI4KIIα (5 pg) RNA in the dorsal region and cultured to tailbud stages. XPIP5KIα MO, $n = 30$; XPIP5KIβ MO, $n = 45$; XPIP5KIβ MO+XPIP5KIβ, $n = 29$; XPI4KIIα MO, $n = 55$; and XPI4KIIα MO+XPI4KIIα, $n = 30$.

---

[1]Department of Pharmacology, Yale University School of Medicine, New Haven, CT 06510, USA. [2]Department of Developmental and Regenerative Biology, Mount Sinai School of Medicine, New York, NY 10029, USA. [3]State Key Laboratory of Molecular Biology and Center of Cell Signaling, Institute of Biochemistry and Cell Biology, Shanghai Institutes for Biological Sciences, Chinese Academy of Sciences, Shanghai 200031, China. [4]Department of Cell Biology and Howard Hughes Medical Institute, Yale University School of Medicine, New Haven, CT 06510, USA. [5]Department of Medicine, University of Pennsylvania, Philadelphia, PA 19104, USA. [6]Cell Signaling Technology, Danvers, MA 01923, USA.

*These authors contribute equally to this work.

†To whom correspondence should be addressed. E-mail: dan.wu@yale.edu

terfering RNA (siRNA) library from Applied Biosystems for effects on Wnt-induced accumulation of cytosolic β-catenin detected by an enzyme-linked immunosorbent assay (ELISA) and on phosphorylation of Ser$^{1490}$ of LRP6 detected by protein immunoblotting in human embryonic kidney (HEK) 293T cells (*11*). Multiple phosphatidylinositol (PtdIns) kinase siRNAs inhibited cytosolic β-catenin accumulation (fig. S1A and table S1) and the phosphorylation of LRP6 at Ser$^{1490}$ (Fig. 1, A and B) in response to purified Wnt3a protein. Among the tested PtdIns kinase siRNAs, siRNAs for phosphatidylinositol 4-kinase type II α (PI4KIIα) and phosphatidylinositol-4-phosphate 5-kinase type I β (PIP5KIβ) had the strongest inhibitory effects (Fig. 1, A and B, and fig. S1A). These siRNA also inhibited Wnt3a-induced reporter gene activity (fig. S1B). Additional siRNAs for both PI4KIIα and PIP5KIβ directed against different targeting sequences were also tested (Fig. 1, A and B, and fig. S1, B and C). To further verify that the effects of these siRNAs were specific, we restored Wnt signaling by expressing the kinases knocked down by the siRNAs (fig. S1, D to G). PI4KIIα and PIP5KIβ siRNAs did not inhibit lithium- and axin1/2 siRNA–induced accumulation of β-catenin, but β-catenin siRNA did (fig. S1, C and H). Thus, these siRNAs appeared to affect Wnt signaling by affecting LRP6 phosphorylation rather than Wnt signaling downstream components.

PIP5KIγ siRNAs also showed a weak inhibitory effect, whereas PIP5KIα siRNAs had no effect in HEK293T cells (Fig. 1B). However, treatment of the cells with combinations of the PIP5KI siRNAs showed that the combination targeting all three PIP5KI isoforms reduced Wnt3a-indcued accumulation of β-catenin and phosphorylation of LRP6 almost to basal levels (fig. S1, C and I), suggesting that PIP5KIα and Iγ may also contribute to Wnt signaling in these cells.

We next examined the roles of the PtdIns kinases in Wnt signaling with the use of *Xenopus* embryos. A morpholino (MO) targeting *Xenopus* PI4KIIα inhibited XWnt8-induced, but not β-catenin–induced, axis duplication in *Xenopus* embryos (Fig. 1C and fig. S2A). Although PIP5KIβ MO showed little effect, a MO targeting its close homolog PIP5KIα inhibited XWnt8-induced, but not β-catenin–induced, axis duplication (Fig. 1D). Consistent with the phenotypes, PIP5KIα and PI4KIIα MOs reduced phosphorylation of LRP6 (fig. S2B). In addition, the expression of catalytically inactive PIP5KIα and PI4KIIα mutants suppressed axial duplication induced by XWnt8, but not by β-catenin (fig. S2C), further confirming the importance of these kinases in Wnt signaling.

Inhibition of zygotic Wnt–β-catenin signaling induces anteriorized phenotypes that include enlarged cement glands and head structures (*12*). PI4KIIα MO that was injected into the dorsal regions of *Xenopus* embryos induced strong anteriorized phenotypes in more than 70% of embryos. This effect could be partially reversed by coinjection of *Xenopus* PI4KIIα mRNA (Fig. 1E and fig. S2D). Although PIP5KIα MO had little effect on the phenotype, PIP5KIβ MO induced anteriorized phenotypes in ~50% of the treated embryos. The PIP5KIβ MO effect could be almost completely reversed by the injection of XPIP5KIβ mRNA (Fig. 1E and fig. S2D). Together, these results indicate that PtdIns kinases regulate endogenous Wnt signaling in *Xenopus* embryos.

Because sequential phosphorylation of PtdIns lipids by PI4KII and PIP5KI constitutes the major pathway for PtdIns (4,5)P$_2$ production in most cells (*13*, *14*), we suspected that PtdIns (4,5)P$_2$ might regulate the phosphorylation of LRP6 at Ser$^{1490}$. To test this hypothesis, we delivered PtdIns, plus all of the seven possible isoforms of PtdIns phosphates at equal molar concentrations, into HEK 293T cells in a lipid carrier. PtdIns (4,5)P$_2$ showed the strongest stimulatory effect on Wnt3a-induced phosphorylation of Ser$^{1490}$ (Fig. 2A). In addition, the delivery of PtdIns (4)P (but not PtdIns) rescued the effect of PI4K siRNA, whereas the delivery of PtdIns (4,5)P$_2$ (but not PtdIns (4)P) rescued the effect of PIP5K siRNA on Wnt3a-induced phosphorylation of LRP6 (Fig. 2, B and C) and β-catenin accumulation (fig. S3). These results suggest that PtdIns (4,5)P$_2$ may be the primary PtdIns lipid involved in the regulation of Ser$^{1490}$ phosphorylation.

We used a rapidly inducible PtdIns (4,5)P$_2$ hydrolysis system to further investigate the role of PtdIns (4,5)P$_2$ in regulating phosphorylation of LRP6. In this system, rapamycin induces the heterodimerization of membrane-targeted FRP (fragment of mammalian target of rapamycin that binds FKBP12) and FKBP12 (FK560–binding protein 12) fused with a truncated form of type IV phosphoinositide 5-phosphatase, leading to activation of the phosphatase (*15*, *16*). As shown in Fig. 2D, rapamycin reduced the amount of PtdIns (4,5)P$_2$ in cells expressing both FRP and phosphatase-fused FKBP12, but not in those expressing FRP and FKBP12 alone. Rapamycin also attenuated phosphorylation of LRP6 only in cells expressing both FRP and phosphatase-fused FKBP12 (Fig. 2E).

To determine whether Wnt3a can stimulate PtdIns (4,5)P$_2$ production, we established a PtdIns (4,5)P$_2$ ELISA and detected significant Wnt3a-induced formation of PtdIns (4,5)P$_2$ (more than two-fold increases) in HEK293T, Hela, and NIH3T3 cells (fig. S4A). We confirmed these results by high-performance liquid chromatography (HPLC) and thin-layer chromatography (TLC) (Fig. 3A and fig. S4, B and C). Together with the findings that the PI4KIIα siRNA abolished (and the PIP5KIβ siRNA

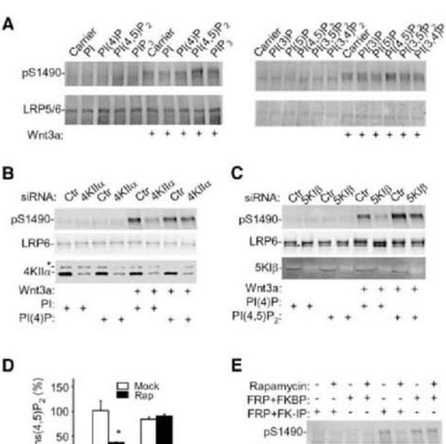

**Fig. 2.** Effect of PtdIns (4,5)P$_2$ on Wnt3a signaling. **(A)** Effect of exogenous PtdIns (4,5)P$_2$ on Wnt3a-induced phosphorylation of LRP6 at Ser$^{1490}$. HEK293T cells were treated with various PtdIns lipids in a lipid carrier for 10 min and incubated with Wnt3a (20 ng/ml) for an additional 20 min before being assayed by immunoblotting. **(B** and **C)** Rescuing the effects of PI kinase siRNAs by direct delivery of PtdIns lipids. The asterisk in (B) indicates nonspecific bands. **(D** and **E)** Reduction in PtdIns (4,5)P$_2$ levels decreases LRP6 Ser$^{1490}$ phosphorylation. HEK293T cells transfected with FRB (PM-FRB-CFP), FKBP (mRFP-FKBP12), or FK-IP (mRFP-FKBP12-5-ptase-dom) were treated with Wnt3a (20 ng/ml) in the presence or absence of rapamycin (100 nM) for 30 min before they were collected for the lipid assay (D) and immunoblotting analysis (E). $^*P < 0.01$ compared with the same transfection in the absence of rapamycin (Student's *t* test). Error bars indicate SDs.

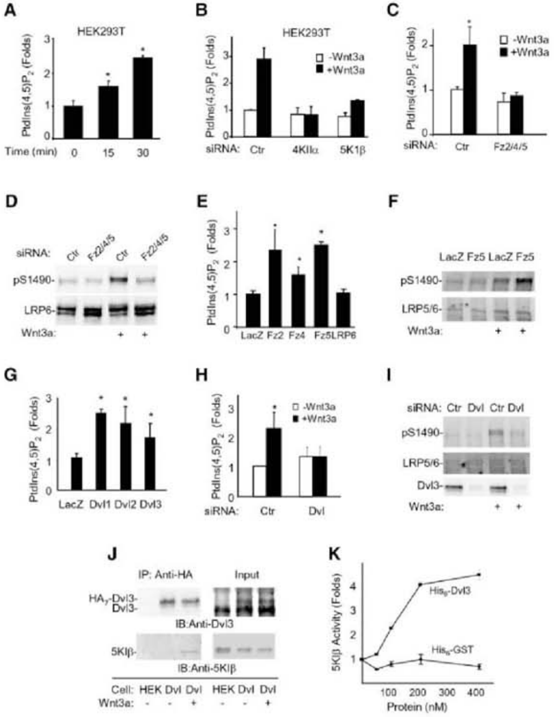

**Fig. 3.** Stimulation of PtdIns (4,5)P$_2$ formation by Wnt3a through Fz and Dvl. **(A)** Effect of Wnt3a treatment on PtdIns (4,5)P$_2$ content. HEK293T Cells were stimulated with Wnt3a protein (50 ng/ml) before lipid extraction. PtdIns (4,5)P$_2$ content was determined by HPLC. $*P < 0.01$ compared with time 0 (Student's *t* test). **(B)** Requirement of PI4KIIα and PIP5KIβ for Wnt3a-induced formation of PtdIns (4,5)P$_2$. Cells were transfected with siRNAs, as indicated, for 48 hours and then treated with Wnt3a (50 ng/ml) for 30 min. PtdIns (4,5)P$_2$ were detected by ELISA. **(C)** Effect of Fz siRNAs on Wnt3a-induced formation of PtdIns (4,5)P$_2$. Cells were transfected with control siRNA or a combination of Fz2, Fz4, and Fz5 siRNAs for 48 hours and then treated with Wnt3a (50 ng/ml) for 30 min before assays. $*P < 0.01$ compared with control siRNA transfection in the absence of Wnt3a (Student's *t* test). **(D)** Effect of Fz siRNAs on Wnt3a-induced phosphorylation of LRP6 at Ser$^{1490}$. Cells were transfected as in (C) for 48 hours and then treated with Wnt3a (50 ng/ml) for 30 min. **(E)** Effect of Fz overexpression on accumulation of PtdIns (4,5)P$_2$. HEK293T cells were transfected with the LacZ, Fz5, or LRP6 expression plasmids for 18 hours, and PtdIns (4,5)P$_2$ levels were determined by ELISA. $*P < 0.01$ compared with the sample expressing LacZ (Student's *t* test). **(F)** Effect of Fz5 expression on phosphorylation of LRP6 at Ser$^{1490}$. Cells were transfected with Fz5 expression plasmid for 18 hours and then treated with Wnt3a (20 ng/ml) for 20 min. **(G)** Effect of Dvl expression on the PtdIns (4,5)P$_2$ levels. HEK293T cells were transfected with the mouse Dvl1, 2, or 3 expression plasmid for 18 hours before the PtdIns (4,5)P$_2$ ELISA assay. $*P < 0.01$ compared with the sample expressing LacZ (Student's *t* test). **(H and I)** Effect of Dvl siRNAs on formation of PtdIns (4,5)P$_2$ and phosphorylation of LRP6 at Ser$^{1490}$. HEK293T cells were transfected with control siRNA or Dvl siRNA mixture targeting Dvl1, 2, and 3 for 48 hours and then treated with Wnt3a (50 ng/ml) for 30 min. $*P < 0.01$ compared with control siRNA transfection in the absence of Wnt3a (Student's *t* test). **(J)** Interaction of Dvl3 with endogenous PIP5KIβ. HEK293T cells (Dvl) stably expressing Dvl3-HA$_7$ were used in immunoprecipitation by an antibody against HA (anti-HA). The parent HEK293T cells (HEK) were used as a control. Immunocomplexes were detected by the anti-Dvl3 and anti-PIP5KIβ antibodies. **(K)** Effect of purified recombinant Dvl3 protein on kinase activity of purified recombinant PIP5KIβ protein. PIP5KIβ (50 nM) was incubated with the GST (glutathione *S*-transferase)or Dvl3 proteins for 2 hours at room temperature. One-tenth of the samples was taken for Western blotting, and the rest was subjected to in vitro kinase assay with PtdIns (4)P as a substrate. The product PtdIns (4,5)P$_2$ is separated by TLC, detected, and quantified by a phosphoimager. Error bars indicate SDs in all panels.

reduced) Wnt3a-induced accumulation of PtdIns (4,5)P$_2$ (Fig. 3B), we conclude that Wnt3a stimulates PtdIns (4,5)P$_2$ production via these PtdIns kinases.

We next investigated whether Fz is required for Wnt3a-induced formation of PtdIns (4,5)P$_2$ and detected expression of Fz2, 3, 4, 5, and 6 in HEK293T cells by reverse transcription polymerase chain reaction (table S2). We made and validated two sets of siRNAs for each of these Fz genes (table S2). Fz5 siRNA showed the strongest inhibition of Wnt3a-induced accumulation of β-catenin, whereas Fz2 and Fz4 siRNAs also had some inhibitory effect (fig. S5B and table S2). The combination of Fz2, 4, and 5 siRNAs virtually abolished Wnt3a-induced accumulation of β-catenin (table S2). This combination also abrogated Wnt3a-induced formation of PtdIns (4,5)P$_2$ (Fig. 3C) and phosphorylation of LRP6 at Ser$^{1490}$ (Fig. 3D, fig. S5C, and table S2). On the other hand, expression of Fz5, 2, and 4 stimulated the formation of PtdIns (4,5)P$_2$ (Fig. 3E) and Wnt3a-induced phosphorylation of Ser$^{1490}$ (Fig. 3F, and fig. S5, D and E). These results together indicate that Wnt3a acts through Fz to stimulate PtdIns (4,5)P$_2$ formation in HEK293T cells and regulates LRP6 phosphorylation.

Because dishevelled (Dvl) is required for the phosphorylation of LRP6 (*9*, *10*), we questioned whether Dvl might have a role in the formation of PtdIns (4,5)P$_2$. Expression of Dvl1-3 increased the amount of PtdIns (4,5)P$_2$ in HEK293T cells (Fig. 3G and fig. S6A). When HEK293T cells were transfected with a mixture of three Dvl siRNAs targeting each of the three Dvl isoforms (*17*), both Wnt3a-induced formation of PtdIns (4,5)P$_2$ and phosphorylation of Ser$^{1490}$ were inhibited (Fig. 3, H and I, and fig. S6B). Dvl is a scaffold protein with no known enzymatic domains. We tested whether Dvl and PIP5KIβ interacted and found that they coimmunoprecipitated when overexpressed in HEK293T cells (fig. S6C). We mapped Dvl interaction site to the N-terminal half of PIP5KIβ kinase domain (fig. S6D) and PIP5KI-binding sites to two fragments of Dvl1 that contain the DIX and PDZ domain, respectively (fig. S6E). The interaction of Dvl3 and PIP5KIβ was also examined in a HEK293T cell line that stably expressed Dvl3 carrying seven hemagglutinin (HA) tags at its C terminus at a level lower than that of endogenous Dvl3

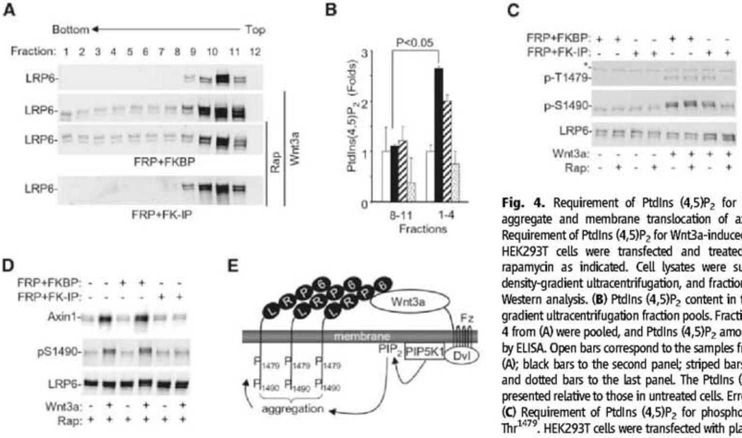

**Fig. 4.** Requirement of PtdIns $(4,5)P_2$ for formation of LRP6 aggregate and membrane translocation of axin and GSK3. **(A)** Requirement of PtdIns $(4,5)P_2$ for Wnt3a-induced LRP6 aggregation. HEK293T cells were transfected and treated with Wnt3a and rapamycin as indicated. Cell lysates were subjected to sucrose density-gradient ultracentrifugation, and fractions were analyzed by Western analysis. **(B)** PtdIns $(4,5)P_2$ content in two sucrose density-gradient ultracentrifugation fraction pools. Fractions 8 to 11 and 1 to 4 from (A) were pooled, and PtdIns $(4,5)P_2$ amounts were measured by ELISA. Open bars correspond to the samples from the top panel in (A); black bars to the second panel; striped bars to the third panel; and dotted bars to the last panel. The PtdIns $(4,5)P_2$ amounts are presented relative to those in untreated cells. Error bars indicate SDs. **(C)** Requirement of PtdIns $(4,5)P_2$ for phosphorylation of LRP6 at $Thr^{1479}$. HEK293T cells were transfected with plasmids, as indicated, for 20 hours and then treated with Wnt3a (20 ng/ml) for 30 min in the presence or absence of rapamycin (100 nM) before they were collected for immunoblotting analysis. The asterisk indicates nonspecific bands. **(D)** Requirement of PtdIns $(4,5)P_2$ for Wnt3a-induced membrane recruitment of axin1. HEK293T cells were transfected and treated as indicated. The membrane fractions were prepared and analyzed by Western analysis. **(E)** Model for Wnt3a cross-membrane signaling.

(upper right panel in Fig. 3J). Although we did not observe coimmunoprecipitation in the absence of Wnt3a, an interaction of Dvl3-HA with endogenous PIP5KIβ was detected in the presence of Wnt3a (Fig. 3J), suggesting that Wnt3a may regulate the interaction. In a pull-down assay with recombinant proteins prepared in *E. coli*, Dvl1 interacted with PIP5KIβ and Iα in vitro (fig. S6F). We then tested whether Dvl could directly regulate PIP5KI kinase activity. Using the recombinant Dvl3 and PIP5KIβ prepared from *E. coli*, we found that, in an in vitro kinase assay, Dvl directly stimulated PIP5KIβ in a dose-dependent manner (Fig. 3K and fig. S6G). Together with the knowledge that Fz can interact with Dvl and recruit it to the membranes (*9, 18–23*), the above data suggest that Wnt3a may induce (through Fz) Dvl to bind and activate PIP5KI.

We next tested whether PtdIns $(4,5)P_2$ is required for Wnt3a-induced formation of LRP6 aggregates (referred to as "signalosomes"), which precedes phosphorylation of LRP6 at $Thr^{1479}$ (*9*). We used sucrose density-gradient centrifugation to detect LRP6 aggregates (Fig. 4A). Fractions that contained LRP6 aggregates also had a higher PtdIns $(4,5)P_2$ content than did fractions containing nonaggregated LRP6 (Fig. 4B). Notably, the aggregation was sensitive to the elimination of PtdIns $(4,5)P_2$ through rapamycin-induced PtdIns $(4,5)P_2$ hydrolysis (Fig. 4A). We also examined LRP6 aggregation using confocal microscopy in Hela cells expressing LRP6-YFP (*9*). We observed the aggregates in control cells but not in cells transfected with the PIP5KI siRNAs (fig. S7). Elimination of PtdIns $(4,5)P_2$ also led to decreased phosphorylation of $Thr^{1479}$ (Fig. 4C) (*9*). Therefore, we conclude that PtdIns $(4,5)P_2$ is required for Wnt-induced LRP6 aggregation and $Thr^{1479}$ phosphorylation.

Because LRP6 aggregates appear to have a high affinity for axin (*9*) and because axin membrane translocation is required for GSK3-mediated phosphorylation of $Ser^{1490}$ (*10*), we examined if PtdIns $(4,5)P_2$ is involved in Wnt-induced axin membrane translocation. Elimination of PtdIns $(4,5)P_2$ using the rapamycin-inducible PtdIns $(4,5)P_2$ hydrolysis system abrogated Wnt3a-induced axin translocation (Fig. 4D). Putting all of these results together, we propose a model (Fig. 4E) to suggest that Wnt3a regulates the activity of PIP5KI through Fz and Dvl and induces the formation of PtdIns $(4,5)P_2$. PtdIns $(4,5)P_2$ is required, but not sufficient, for LRP6 aggregation and phosphorylation at both $Thr^{1479}$ and $Ser^{1490}$, as well as for axin translocation. Precise mechanisms by which PtdIns $(4,5)P_2$ regulates these Wnt signaling events, however, need to be investigated further.

### References and Notes

1. C. Y. Logan, R. Nusse, *Annu. Rev. Cell Dev. Biol.* **20**, 781 (2004).
2. T. Reya, H. Clevers, *Nature* **434**, 843 (2005).
3. H. Clevers, *Cell* **127**, 469 (2006).
4. R. T. Moon, A. D. Kohn, G. V. De Ferrari, A. Kaykas, *Nat. Rev. Genet.* **5**, 691 (2004).
5. A. Mani *et al.*, *Science* **315**, 1278 (2007).
6. G. Davidson *et al.*, *Nature* **438**, 867 (2005).
7. R. Nusse, *Nature* **438**, 747 (2005).
8. X. Zeng *et al.*, *Nature* **438**, 873 (2005).
9. J. Bilic *et al.*, *Science* **316**, 1619 (2007).
10. X. Zeng *et al.*, *Development* **135**, 367 (2007).
11. Materials and methods are available as supporting material on *Science* Online.
12. R. Harland, J. Gerhart, *Annu. Rev. Cell Dev. Biol.* **13**, 611 (1997).
13. J. J. Hsuan, S. Minogue, M. dos Santos, *Adv. Cancer Res.* **74**, 167 (1998).
14. R. L. Doughman, A. J. Firestone, R. A. Anderson, *J. Membr. Biol.* **194**, 77 (2003).
15. W. D. Heo *et al.*, *Science* **314**, 1458 (2006), published online 8 November 2006; 10.1126/science.1134389.
16. P. Varnai, B. Thyagarajan, T. Rohacs, T. Balla, *J. Cell Biol.* **175**, 377 (2006).
17. L. Li, J. Mao, L. Sun, W. Liu, D. Wu, *J. Biol. Chem.* **277**, 5977 (2002).
18. J. D. Axelrod, J. R. Miller, J. M. Shulman, R. T. Moon, N. Perrimon, *Genes Dev.* **12**, 2610 (1998).
19. H. C. Wong *et al.*, *Mol. Cell* **12**, 1251 (2003).
20. W. Chen *et al.*, *Science* **301**, 1391 (2003).
21. F. Cong, L. Schweizer, H. Varmus, *Development* **131**, 5103 (2004).
22. W. J. Pan *et al.*, *Cell Res.* **14**, 324 (2004).
23. N. Yokoyama, D. Yin, C. C. Malbon, *J. Mol. Signal.* **2**, 11 (2007).
24. We thank P. De Camilli for making available resources from his lab in connection to this work, discussion, and critical reading of the manuscript; Z. Li, M. Orsulak, Y. Zhang, L. Tang, W. Liu, Y. Xi, F. Nie, Y. Wu, and X. Gan for technical assistance; and D. Sussman, C. Carpenter, R. Grosschedl, T. Balla, B. Williams, M. F. Roussel, X. He, C. Niehrs, R. Nusse, and J. Nathans for providing experimental materials. This work was supported by grants from NIH (AR051476, CA132317, HL080706, NS36251, and DA018343), the National Institute on Drug Abuse to Yale Neuroproteomics Center, the Ministry of Science and Technology of China (2002CB513000), and the National Science Foundation of China (30521005).

**Supporting Online Material**

www.sciencemag.org/cgi/content/full/321/5894/1350/DC1
Materials and Methods
Figs. S1 to S7
Tables S1 to S4
References

20 May 2008; accepted 4 August 2008
10.1126/science.1160741

# Helical Structures of ESCRT-III Are Disassembled by VPS4

Suman Lata,[1] Guy Schoehn,[1,2] Ankur Jain,[3]* Ricardo Pires,[1] Jacob Piehler,[3] Heinrich G. Göttlinger,[4] Winfried Weissenhorn[1]†

During intracellular membrane trafficking and remodeling, protein complexes known as the ESCRTs (endosomal sorting complexes required for transport) interact with membranes and are required for budding processes directed away from the cytosol, including the budding of intralumenal vesicles to form multivesicular bodies; for the budding of some enveloped viruses; and for daughter cell scission in cytokinesis. We found that the ESCRT-III proteins CHMP2A and CHMP3 (charged multivesicular body proteins 2A and 3) could assemble in vitro into helical tubular structures that expose their membrane interaction sites on the outside of the tubule, whereas the AAA-type adenosine triphosphatase VPS4 could bind on the inside of the tubule and disassemble the tubes upon adenosine triphosphate hydrolysis. CHMP2A and CHMP3 copolymerized in solution, and their membrane targeting was cooperatively enhanced on planar lipid bilayers. Such helical CHMP structures could thus assemble within the neck of an inwardly budding vesicle, catalyzing late steps in budding under the control of VPS4.

ESCRT (endosomal sorting complexes required for transport) complexes 0, I, II, and III and accessory proteins regulate cell surface receptor sorting into intralumenal endosomal vesicles, generating multivesicular bodies (MVBs) (*1*–*3*). ESCRTs are also recruited during budding of some enveloped viruses (*4*) and cytokinesis (*5*, *6*), processes that are topologically similar to vesicle budding into endosomes.

Yeast expresses six ESCRT-III–like proteins (*7*), whereas mammalian cells express 10, known as charged multivesicular body protein (CHMP) 1 to 6 (*8*). C-terminally truncated CHMP3 has a four helical bundle core and two regions that are important for CHMP polymerization and membrane targeting (*9*). CHMPs exist in an auto-inhibited state in the cytosol (*10*, *11*); removal of autoinhibition induces membrane targeting (*9*, *12*, *13*) and ESCRT-III assembly into a putative protein lattice (*1*, *2*). Overexpression of SNF7/CHMP4 in mammalian cells produces filaments that induce outward buds in the presence of catalytically inactive VPS4 (*14*), but little is known about heteromeric polymerization by ESCRT-III proteins.

The recruitment of the AAA-type adenosine triphosphatase (ATPase) VPS4 is essential for the termination of the budding process and catalyzes disassembly of the complex (*2*, *15*, *16*). The central role of ESCRT-III and VPS4 in all known ESCRT-catalyzed budding events is further underlined by the inhibitory effects of dominant negative mutants of ESCRT-III (*8*, *9*, *17*, *18*) and VPS4 (*2*, *5*, *18*) on MVB formation, HIV-1 budding, and cytokinesis.

Yeast Vps2p (CHMP2) and Vps24p (CHMP3) form a subcomplex (*7*) consistent with the heterodimerization potential suggested by the CHMP3 crystal structure (*9*). Such subcomplexes may thus represent the building blocks for polymerization. We set out to study the interactions and polymerization mode of CHMP2 and CHMP3 in vitro. Interactions between full-length autoinhibited CHMP3 and CHMP2A could not be detected, and so both proteins were produced as C-terminal truncations (fig. S1A; CHMP2AΔC and CHMP3ΔC) in their proposed activated forms (*9*, *10*, *13*). Whereas CHMP3ΔC was monodisperse in solution (*9*), CHMP2AΔC fused to the maltose binding protein (MBP) formed monomers and concentration-dependent aggregates (fig. S1B). Co-incubation of monomeric CHMP2AΔC and CHMP3ΔC led to the formation of oligomers, migrating to the bottom fraction of a sucrose gradient (Fig. 1A). CHMP2AΔC and CHMP3ΔC assembled into long tubular structures (Fig. 1B), with the majority of the particles revealing a di-

---

[1] Unit for Virus Host Cell Interaction, UMR 5233 UJF (Université Joseph Fourier)-EMBL (European Molecular Biology Laboratory)-CNRS, 6 rue Jules Horowitz, 38042 Grenoble Cedex 9, France. [2] Institut de Biologie Structurale UMR 5075 CEA (Comissariat à l'Énergie Atomique)-CNRS-UJF, 41 rue Jules Horowitz, 38027 Grenoble Cedex 1, France. [3] Institute of Biochemistry, Johann Wolfgang Goethe University, Max-von-Laue Straße 9, 60438 Frankfurt am Main, Germany. [4] Program in Gene Function and Expression, Program in Molecular Medicine, University of Massachusetts Medical School, Worcester, MA 01605, USA.

*Present address: Department of Physics, University of Illinois at Urbana-Champaign, 1110 West Green Street, Urbana, IL 61801–3080, USA.

†To whom correspondence should be addressed. E-mail: weissenhorn@embl.fr

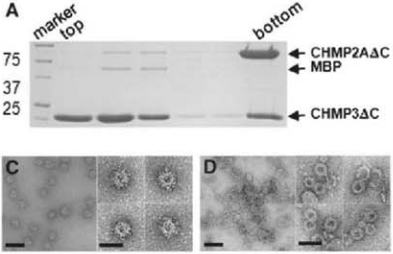

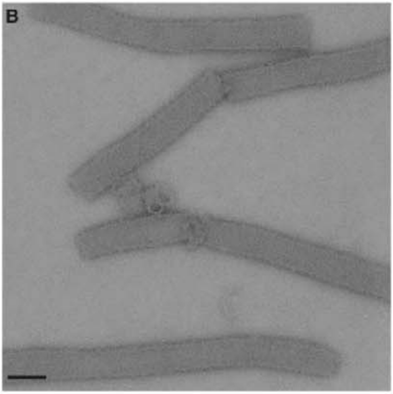

**Fig. 1.** CHMP2AΔC-CHMP3ΔC polymer formation. (**A**) Sucrose density gradient analysis of CHMP2AΔC-CHMP3ΔC complex formation. (**B**) Negative staining EM of tubular structures formed by CHMP2AΔC and CHMP3ΔC. Negative staining EM (**C**) of CHMP2AΔC and (**D**) of CHMP2AΔC after removal of MBP. Scale bars indicate 100 nm; inset scale bars, 50 nm.

**Fig. 2.** Cryo EM of CHMP2ΔC-CHMP3ΔC (**A**) tubes and (**B**) tubes after removal of MBP from CHMP2AΔC. Scale bars, 100 nm. (**C**) The EM reconstruction model showing the 45 Å width of the helical structure produced by the CHMP lattice (top view).

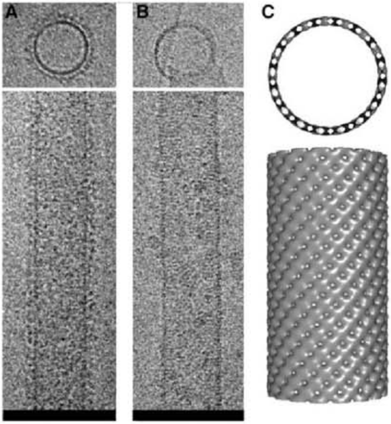

**Fig. 3.** CHMP2AΔC-CHMP3 tube disassembly by VPS4B. (**A**) Negative staining EM of tubes formed by CHMP2AΔC and CHMP3. Sucrose gradient analysis of (**B**) CHMP2AΔC, (**C**) CHMP3, (**D**) VPS4B, (**E**) CHMP2AΔC-CHMP3-VPS4B complex formation, and (**F**) CHMP2AΔC-CHMP3-VPS4B complexes after incubation with ATP $Mg^{2+}$. (**G**) Negative staining EM of CHMP2AΔC-CHMP3 tubes revealing VPS4B on the inside. Radial density profile (**H**) of a CHMP2AΔC-CHMP3-VPS4B and (**I**) of CHMP2AΔC-CHMP3 tubes calculated across the cross section of the tube. (**J**) Negative staining EM after adding ATP $Mg^{2+}$ to CHMP2AΔC-CHMP3-VPS4B tubes. (**K**) Disassembly of fluorescein-labeled CHMP2AΔC-CHMP3 tubes measured by change in emission intensity upon addition of HBS (magenta), 10 μM VPS4B (blue), 10 μM VPS4B plus 100 μM AMP-PNP $Mg^{2+}$ (green), 5 μM VPS4B plus 50 μM ATP $Mg^{2+}$ (black), and 10 μM VPS4B plus 100 μM ATP $Mg^{2+}$ (red). (Inset) The fluorescein-labeled CHMP2AΔC and CHMP3 visualized on an SDS–polyacrylamide gel. Scale bars, 100 nm.

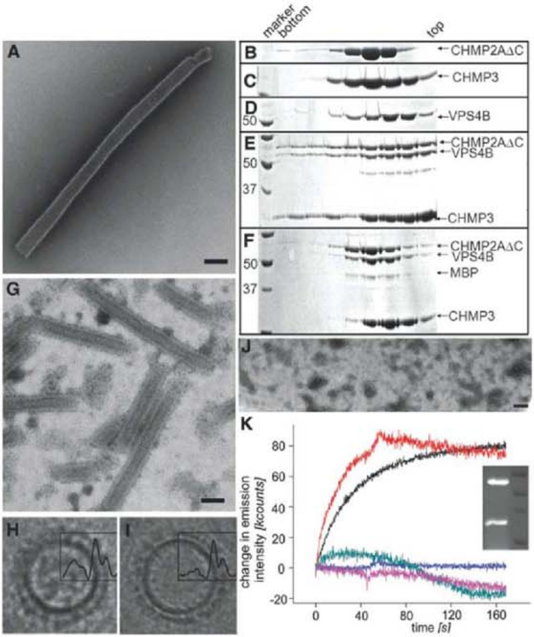

ameter of ~40 nm and a small fraction showing deviations up to 70 nm in negative staining electron microscopy (EM).

Although neither CHMP3, CHMP3ΔC, nor CHMP2A formed higher-order oligomers on their own, CHMP2AΔC sedimented in a sucrose gradient (fig. S1C) and formed ringlike structures (Fig. 1C). Removal of MBP produced particles with inner and outer diameters of ~12 nm and ~30 nm, respectively. Increased aggregation upon MBP cleavage and the exclusive face-up orientations (Fig. 1D) hindered determination of the ring thickness.

Cryo-EM of the CHMP2AΔC-CHMP3ΔC polymer showed tubes with a fuzzy surface (Fig. 2A). Removal of MBP from CHMP2AΔC rendered the surface smooth, revealing striations perpendicular to the longitudinal axis of the tube (Fig. 2B). Because image analyses of MBP-cleaved tubes was hindered by their aggregation, we applied the iterative helical real space reconstruction algorithm (*19*) to reconstruct volumes from the tubes containing MBP attached to CHMP2AΔC (*20*). The 32 Å pitch of the helical assembly was determined by the Fourier transform of the images (*20*). The calculated helical structure contains 16.57 repeating units per turn, with inner and outer diameters of 43 nm and 52 nm, respectively (Fig. 2C). The CHMP2A-CHMP3 dimer model could fit into the repeating unit of the EM map (*20*) (fig. S2, A to D), exposing the membrane targeting surface to the outside and the VPS4B interaction site toward the inside of the tube (fig. S2, D and E).

The organization of the CHMP2AΔC-CHMP3ΔC polymer did not indicate how other CHMPs could participate in the same polymer. In fact, monomeric CHMP4BΔC did not integrate into CHMP2AΔC-CHMP3ΔC tubes (fig. S3) despite similarities in polymerization (*14*). Although CHMP4 may participate in CHMP2A-CHMP3 tube formation as a CHMP4-CHMP6 subcomplex (*7*), different ESCRT-III complexes may be formed in vivo that interact (*7*) and act sequentially.

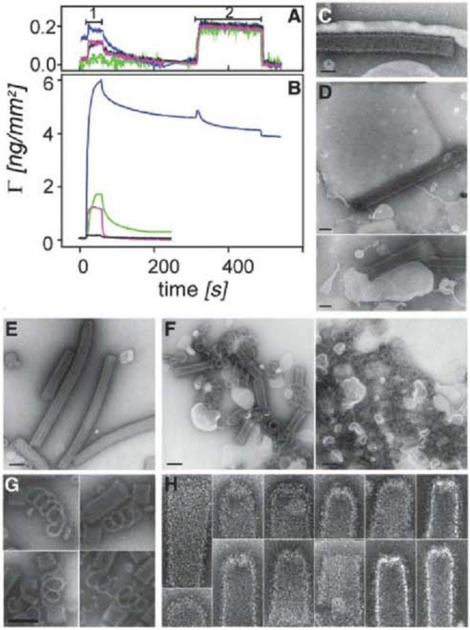

**Fig. 4.** CHMP protein membrane interaction. **(A)** Binding curves measured by RIfS on a SOPC bilayer: MBP (black), CHMP3ΔC (magenta), CHMP2AΔC (green), and CHMP2AΔC-CHMP3ΔC (blue). **(B)** Binding curves measured by RIfS on a DOPS:SOPC bilayer: MBP (black), CHMP3ΔC (magenta), CHMP2AΔC (green), and CHMP2AΔC-CHMP3ΔC (blue). Protein injections were followed by injection of 1 M NaCl in HBS. CHMP2AΔC-CHMP3ΔC tubes **(C)** with and **(D)** without MBP attached to CHMP2AΔC. **(E)** CHMP2AΔC-CHMP3ΔC tubes assembled in the presence of SOPC LUVs. **(F)** CHMP2AΔC-CHMP3ΔC tubes assembled in the presence of 0.5 mg ml$^{-1}$ (left) and 1.5 mg ml$^{-1}$ (right). SOPC:DOPS LUVs are shorter, **(G)** reveal single helical coils, and **(H)** are often cone-shaped. Scale bars, 100 nm.

Because the VPS4B-CHMP interaction requires an intact C terminus (*21*, *22*), we used full-length proteins for tube formation. Whereas CHMP2AΔC and CHMP3 formed similar tubes to those formed with CHMP3ΔC (Figs. 1B and 3A), combinations of CHMP2A and CHMP3 and CHMP2A and CHMP3ΔC did not polymerize. In sucrose gradient centrifugation, isolated forms of CHMP2AΔC, CHMP3, and VPS4B floated at similar positions (Fig. 3, B to D), consistent with monomeric or dimeric VPS4B in the absence of adenosine triphosphate (ATP) (*23*). Mixing all three proteins recruited them to the pellet fraction, corroborating the CHMP3-VPS4B interaction (Fig. 3E). Negative staining EM of the CHMP2AΔC-CHMP3 tubes assembled in the presence of VPS4B revealed additional electron-dense material along the longitudinal axis of the tubes (Fig. 3G). Radial density profiles of cross sections obtained by cryo-EM (fig. S4B) showed a broad central peak, confirming the VPS4B presence inside the tubes, followed by a sharp peak corresponding to the CHMP lattice and a smaller peak corresponding to MBP attached to CHMP2AΔC (Fig. 3H and fig. S4D). In contrast, in cross sections of tubes without VPS4B (fig. S4A), the central peak of the density profile did not rise above the background signal (Fig. 3I and fig. S4C). Thus, VPS4B used CHMP2AΔC-CHMP3 tubes as a scaffold for assembly, which apparently produced disordered VPS4B oligomers in the absence of ATP. Addition of ATP and $Mg^{2+}$ to the CHMP2AΔC-CHMP3-VPS4B tubular structures induced disassembly of the tubes (Fig. 3, F and J). Incubation of fluorescein-labeled tubes (fig. S5) with buffer, VPS4B, or VPS4B plus adenylyl-imidodiphosphate (AMP-PNP) $Mg^{2+}$ showed no change in emission intensity as a function of time (Fig. 3K). In contrast, dequenching, indicating disassembly, was measured as an increase in emission intensity when the tubes were incubated with VPS4B plus ATP $Mg^{2+}$ (Fig. 3K). Thus, VPS4B induced tube disassembly in vitro.

CHMPs are selectively targeted to cellular membranes (*7*, *13*, *24*), which requires an extended basic surface in case of CHMP3 (*9*). With reflectometric interference spectroscopy (RIfS) (*20*), CHMP2AΔC, CHMP3ΔC, and their complex showed no notable mass deposition (<0.10 ng mm$^{-2}$) on silica-supported bilayers composed of 1-stearoyl-2-oleoyl-*sn*-glycero-3-phosphocholine (SOPC) lipids (Fig. 4A). However, CHMP3ΔC bound to 1,2-dioleoyl-*sn*-glycero-3-phosphoserine (DOPS):SOPC bilayers (fig. S6) with an equilibrium binding amplitude ($\Gamma_{eq}$) of 1.08 ng mm$^{-2}$ and dissociated with a rate of ($k_d$) ~ 0.3 s$^{-1}$, whereas CHMP2AΔC (4 μM) showed a $\Gamma_{eq}$ of

$1.36\ \mathrm{ng\ mm^{-2}}$ and a $k_d$ of $0.081\ \mathrm{s^{-1}}$ (Fig. 4B). When the two proteins were mixed, a $\Gamma_{eq}$ of $5.95\ \mathrm{ng\ mm^{-2}}$ was reached. An apparent $k_d > 0.0008\ \mathrm{s^{-1}}$ was determined by fitting a monoexponential function to the dissociation phase, which is 3 and 2 orders of magnitude lower as compared with the single proteins (fig. S7). Both SOPC and DOPS:SOPC bilayers showed no interaction with the control protein MBP (Fig. 4, A and B). Dissociation of bound CHMP2AΔC and CHMP3ΔC in Hepes buffered saline (HBS) containing 1 M NaCl revealed a $k_d \geq 1\ \mathrm{s^{-1}}$, which was much faster than dissociation in HBS alone. In contrast, the CHMP2AΔC-CHMP3ΔC polymer did not dissociate with a higher rate ($k_d \leq 0.00046\ \mathrm{s^{-1}}$) in the presence of 1 M NaCl (fig. S7), indicating resistance to change in ionic strength. Once assembled on membranes, CHMP2AΔC-CHMP3ΔC did not exchange with soluble or membrane-bound CHMP3ΔC (fig. S8). Thus, CHMP2A-3 complexes assembled on membranes in vitro in the absence of CHMP4-6 subcomplexes, even though yeast Snf7-Vps20 (CHMP4-6) complexes may recruit Vps2-Vps24 (CHMP2A-3) complexes to membranes in vivo (*7*).

To assess the influence of CHMP2AΔC-CHMP3ΔC tubes on membrane shapes, we used large unilamellar vesicles (LUVs) composed of DOPS:SOPC. LUV incubation with either CHMP2AΔC or CHMP3ΔC had no effect on their floatation in sucrose gradients (fig. S9, A and B), whereas preformed CHMP2AΔC-CHMP3ΔC tubes restricted LUV floatation to the middle of the gradient (fig. S9, C and D). Negative staining EM confirmed CHMP2AΔC-CHMP3ΔC tube membrane interaction via their outer surfaces (Fig. 4, C and D). However, no systematic remodeling of the LUV membranes was observed. Potential membrane remodeling by the CHMP copolymer or vice versa was further explored by assembling the polymer in the presence of LUVs. Although CHMP2AΔC-CHMP3ΔC assembly in the presence of SOPC LUVs had no effect on tube morphology (Fig. 4E), the presence of DOPS:SOPC LUVs produced shorter tubes (Fig. 4F), displaying loose helical coils (Fig. 4G) and cone-shaped tubes that appeared closed at the narrower end (Fig. 4H). Thus, this suggests a mechanism where lipid interaction affects CHMP polymerization.

Because modified VPS4 and CHMP3 exert dominant negative effects on HIV-1 budding (*8*, *9*, *17*, *25*) and cytokinesis (*6*, *18*), CHMP2A-CHMP3-VPS4 complexes may catalyze a common step such as membrane fission. The CHMP2A-CHMP3 polymer presents a membrane binding topology that is inverse to that of dynamin membrane complexes (*26*), which catalyze endocytotic vesicle abscission (*27*). ESCRT-III coupled to VPS4 may exert a similar role in budding processes directed away from the cytosol. Thus, we propose that a helical CHMP2A-CHMP3 polymer assembles on the inside of a membrane bud, which may induce membrane deformation, leading to constriction and eventually abscission when coupled to VPS4 activity, the only energy-providing candidate in the pathway (*2*, *15*) (fig. S10).

### References and Notes

1. R. L. Williams, S. Urbe, *Nat. Rev. Mol. Cell Biol.* **8**, 355 (2007).
2. S. Saksena, J. Sun, T. Chu, S. D. Emr, *Trends Biochem. Sci.* **32**, 561 (2007).
3. J. H. Hurley, *Curr. Opin. Cell Biol.* **20**, 4 (2008).
4. P. D. Bieniasz, *Virology* **344**, 55 (2006).
5. J. G. Carlton, J. Martin-Serrano, *Science* **316**, 1908 (2007); published online 6 June 2007 (10.1126/science.1143422).
6. E. Morita *et al.*, *EMBO J.* **26**, 4215 (2007).
7. M. Babst, D. J. Katzmann, E. J. Estepa-Sabal, T. Meerloo, S. D. Emr, *Dev. Cell* **3**, 271 (2002).
8. U. K. von Schwedler *et al.*, *Cell* **114**, 701 (2003).
9. T. Muziol *et al.*, *Dev. Cell* **10**, 821 (2006).
10. A. Zamborlini *et al.*, *Proc. Natl. Acad. Sci. U.S.A.* **103**, 19140 (2006).
11. S. Lata *et al.*, *J. Mol. Biol.* **378**, 816 (2008).
12. Y. Lin, L. A. Kimpler, T. V. Naismith, J. M. Lauer, P. I. Hanson, *J. Biol. Chem.* **280**, 12799 (2005).
13. S. Shim, L. A. Kimpler, P. I. Hanson, *Traffic* **8**, 1068 (2007).
14. P. I. Hanson, R. Roth, Y. Lin, J. E. Heuser, *J. Cell Biol.* **180**, 389 (2008).
15. M. Babst, B. Wendland, E. J. Estepa, S. D. Emr, *EMBO J.* **17**, 2982 (1998).
16. N. Bishop, P. Woodman, *Mol. Biol. Cell* **11**, 227 (2000).
17. B. Strack, A. Calistri, E. Popova, H. Göttlinger, *Cell* **114**, 689 (2003).
18. J. D. Dukes, J. D. Richardson, R. Simmons, P. Whitley, *Biochem. J.* **411**, 233 (2008).
19. E. H. Egelman, *Ultramicroscopy* **85**, 225 (2000).
20. Materials and methods are available as supporting materials on *Science* Online.
21. M. D. Stuchell-Brereton *et al.*, *Nature* **449**, 740 (2007).
22. T. Obita *et al.*, *Nature* **449**, 735 (2007).
23. A. Scott *et al.*, *EMBO J.* **24**, 3658 (2005).
24. P. Whitley *et al.*, *J. Biol. Chem.* **278**, 38786 (2003).
25. J. Martin-Serrano, A. Yarovoy, D. Perez-Caballero, P. D. Bieniasz, *Proc. Natl. Acad. Sci. U.S.A.* **100**, 12414 (2003).
26. S. M. Sweitzer, J. E. Hinshaw, *Cell* **93**, 1021 (1998).
27. K. Takei, P. S. McPherson, S. L. Schmid, P. De Camilli, *Nature* **374**, 186 (1995).
28. We thank X. Siebert (Institut de Biologie Structurale) for advice on UROX. This work was supported by Deutsche Forschungsgemeinschaft (SPP 1175) (W.W.), the Agence Nationale de la Recherche sur le SIDA (W.W.), Université Joseph Fourier (W.W.), the Agence Nationale de la Recherche (G.S.), the CNRS (G.S.), the NIH (grant AI29873, H.G.), and by postdoctoral fellowships from the European Molecular Biology Organization (S.L.) and the International Human Frontier Science Program Organization (S.L.). The EM map has been deposited at the European Bioinformatics Institute, accession code EMD-1536.

**Supporting Online Material**
www.sciencemag.org/cgi/content/full/321/5894/1354/DC1
Materials and Methods
Figs. S1 to S10
References

28 May 2008; accepted 24 July 2008
Published online 7 August 2008;
10.1126/science.1161070
Include this information when citing this paper.

---

# A Neoplastic Gene Fusion Mimics Trans-Splicing of RNAs in Normal Human Cells

**Hui Li,[1] Jinglan Wang,[1] Gil Mor,[2] Jeffrey Sklar[1]***

Chromosomal rearrangements that create gene fusions are common features of human tumors. The prevailing view is that the resultant chimeric transcripts and proteins are abnormal, tumor-specific products that provide tumor cells with a growth and/or survival advantage. We show that normal endometrial stromal cells contain a specific chimeric RNA joining 5′ exons of the *JAZF1* gene on chromosome 7p15 to 3′ exons of the Polycomb group gene *JJAZ1/SUZ12* on chromosome 17q11 and that this RNA is translated into JAZF1-JJAZ1, a protein with anti-apoptotic activity. The *JAZF1-JJAZ1* RNA appears to arise from physiologically regulated trans-splicing between precursor messenger RNAs for *JAZF1* and *JJAZ1*. The chimeric RNA and protein are identical to those produced from a gene fusion found in human endometrial stromal tumors. These observations suggest that certain gene fusions may be pro-neoplastic owing to constitutive expression of chimeric gene products normally generated by trans-splicing of RNAs in developing tissues.

Recurrent, specific gene fusions arising from chromosomal rearrangements are characteristic features of many neoplasms, especially those having hematopoietic and mesenchymal origins (*1*–*6*). In most fusions, recombination occurs within introns that interrupt the coding sequences, giving rise to the expression of chimeric proteins (*2*). The prevailing view is that the chimeric proteins resulting from chromosomal rearrangements are entirely abnormal and have neoplastic effects leading to the growth and/or survival advantage of cells containing them.

An observation that seems at odds with this view is that chimeric mRNAs identical to those derived from fusion genes can often be detected in low abundance by reverse transcription–

---

[1] Department of Pathology, Yale University School of Medicine, New Haven, CT 06520, USA. [2] Department of Obstetrics and Gynecology, Yale University School of Medicine, New Haven, CT 06520, USA.

*To whom correspondence should be addressed. E-mail: jeffrey.sklar@yale.edu

polymerase chain reaction (RT-PCR) of RNA from healthy tissues (*7*). The explanation generally offered for this finding is that specific chromosomal rearrangements occur within small numbers of cells in healthy tissues but that the chimeric proteins generated by them are alone insufficient to drive substantial clonal expansion.

We have previously described a gene fusion due to a (7;17)(p15;q21) chromosomal translocation found in about 50% of human endometrial stromal sarcomas (ESSs) (*8*, *9*). The fusion joins the first three exons (from a total of five) in the gene *JAZF1* to the last 15 (from 16) in the Polycomb group gene *JJAZ1/SUZ12*. Expression of the chimeric JAZF1-JJAZ1 protein in cultured human embryonic kidney (HEK) 293 cells confers resistance to apoptosis and, when accompanied by suppression of the unrearranged *JJAZ1* allele, increased rates of proliferation (*9*).

We examined normal human endometrial tissues for possible chimeric *JAZF1-JJAZ1* RNA, beginning with endometrial stromal cell lines. RNA extracted from the immortalized, normal human endometrial stromal cell line (HESC) (*10*) was analyzed for the presence of *JAZF1-JJAZ1* chimeric RNA by RT-PCR with primers containing sense and antisense sequence flanking the site of joining between *JAZF1* and *JJAZ1* (*11*). A single amplification product generated by this reaction was identical in size to that amplified from human ESSs carrying a *JAZF1-JJAZ1* gene fusion due to the presence of a t(7;17)(p15;q21) (Fig. 1A). RT-PCR for the *JAZF1-JJAZ1* RNA in two additional, nonimmortalized primary cell lines derived from the normal endometrial stroma of two other patients amplified similarly sized products. Nucleotide sequence analysis of the RT-PCR products from each cell line yielded the same sequence of nucleotides at the *JAZF1-JJAZ1* junction as was found in RNA of tumors with the gene fusion. RT-PCR for *JAZF1-JJAZ1* RNA failed to amplify products from the RNA extracted from a variety of other epithelial and mesenchymal cell lines, all of which contained *JAZF1* and *JJAZ1* RNA (fig. S1).

To investigate the specificity of the junction between *JAZF1* and *JJAZ1* RNA sequences in the HESC cell line, we carried out detailed RT-PCR studies on RNA from the HESC cell line using antisense primers for *JJAZ1* exon 3 sequence paired with six different sense primers for five exons of *JAZF1*. With primers for the first three exons of *JAZF1*, single products were obtained matching the sizes predicted for the joining of *JAZF1* exon 3 to *JJAZ1* exon 2 (Fig. 1B). Similar results were achieved when the sense primer for *JAZF1* exon 3 was paired with six different antisense primers distributed among the 16 exons of *JJAZ1*. These results are consistent with the *JAZF1-JJAZ1* RNA joined at exon 3 and exon 2 of the respective genes being the only abundant *JAZF1-JJAZ1* RNA in HESC cells.

To determine whether the *JAZF1-JJAZ1* RNA is translated into protein, we performed Western blot analysis with JJAZ1-specific antibody on protein extracts prepared from HESC cells. This analysis detected a protein identical in size to JAZF1-JJAZ1 protein detected in ESSs (Fig. 1C and supporting online text).

The detection of *JAZF1-JJAZ1* RNA in endometrial stromal cell lines was duplicated by RT-PCR analysis of RNA extracted from formalin-fixed, paraffin-embedded tissues from normal human uteri. *JAZF1-JJAZ1* RNA was detected primarily in endometrium from late secretory and early proliferative phases of the menstrual cycle (Fig. 2A). No *JAZF1-JJAZ1* RNA sequences were amplified from normal myometrium at any phase of the cycle (fig. S2).

Because of the general association of the *JAZF1-JJAZ1* RNA with endometrium from particular phases of the menstrual cycle, we investigated the effects of steroid hormones on the production of the chimeric transcript in HESC cells. Low concentrations of progesterone seemed to slightly increase amounts of the *JAZF1-JJAZ1* RNA seen in the absence of added hormone, whereas both estrogen and, at higher concentrations, progesterone suppressed detection of the chimeric RNA (Fig. 2B). These findings are consistent with the results of analyses on endometrial tissue, showing that *JAZF1-JJAZ1* RNA is present predominantly at the beginning and end of the menstrual cycle, when hormone concentrations are low.

Because normal endometrium is subjected to hypoxia and undergoes apoptosis during the late secretory phase of the menstrual cycle, we investigated whether hypoxia can induce production of *JAZF1-JJAZ1* RNA in HESC cells by treatment with desferroximine (DFO), which simulates hypoxic conditions. HESC cells treated with 250 μM DFO for 8 hours showed increased amounts of *JAZF1-JJAZ1* RNA (Fig. 2C). Another,

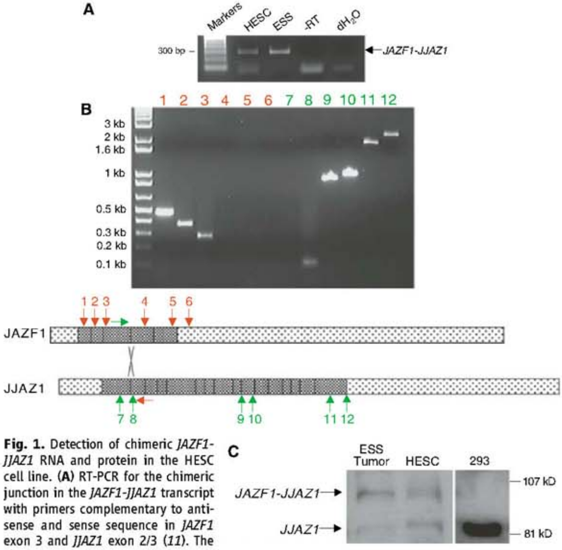

**Fig. 1.** Detection of chimeric *JAZF1-JJAZ1* RNA and protein in the HESC cell line. **(A)** RT-PCR for the chimeric junction in the *JAZF1-JJAZ1* transcript with primers complementary to antisense and sense sequence in *JAZF1* exon 3 and *JJAZ1* exon 2/3 (*11*). The figure shows the results of agarose gel electrophoresis of amplification products. Results of RT-PCR with RNA from an ESS containing the t(7;17)(p15;q21) are shown in the lane labeled ESS; results of the RT-PCR procedure with RNA from the HESC cell line omitting reverse transcriptase are shown in the lane labeled RT; results without template RNA are shown in the lane labeled $dH_2O$. **(B)** Analyses by RT-PCR for the specificity of exon joining between *JAZF1* and *JJAZ1* RNAs in HESC cells. Lanes 1 to 6 used six different forward primers at the positions of the downward orange arrows above the diagram of the *JAZF1* transcript, paired with a reverse primer indicated by the orange arrow below the *JJAZ1* transcript. Lanes 7 to 12 used the forward primer indicated in green above the *JAZF1* transcript, paired with six different reverse primers at the positions of the upward green arrows below the *JJAZ1* transcript. **(C)** Western blot of protein extracts from ESS tissue, the HESC cell line, and HEK 293 cells (as a negative control) for JJAZ1 and JAZF-JJAZ1 protein with JJAZ1-specific antibody.

nonimmortalized normal endometrial stromal cell line, HESC-597, also showed up-regulation of *JAZF1-JJAZ1* RNA when treated with DFO. Cultures of cells derived from tissue other than endometrial stroma showed no detectable chimeric RNA with DFO treatment. Analysis of the RNA in DFO-treated HESC cells by a nuclease protection assay (fig. S3) indicated that somewhat less chimeric RNA was produced in these cells than in tumor cells containing the *JAZF1-JJAZ1* fusion, consistent with relative amounts of 10 to 35% detected by quantitative RT-PCR. The nuclease protection assay also confirmed that detection of chimeric RNA was not a methodologic artifact associated with RT-PCR. Quantitative RT-PCR revealed that treatment of HESC cells with DFO did not appreciably change the amount of either *JAZF1* or *JJAZ1* RNA (fig. S4), suggesting that DFO raises the levels of *JAZF1-JJAZ1* RNA by a mechanism independent of increased transcription of the two genes.

To investigate whether *JAZF1-JJAZ1* RNA is produced from a t(7;17)(p15;q21) in HESC cells, we first showed that this cell line, which had not intentionally been cloned, had in fact originated from a single cell immortalized in culture (fig. S5). We then performed Southern blot analyses of HESC DNA by using probes that had previously detected t(7;17)(p15;q21) rearrangements in ESSs. No rearranged bands were detected. Cytogenetic analysis of numerous metaphase spreads from HESC cells revealed no abnormalities in chromosomes 7, 17, or any other chromosome (Fig. 3A). Similarly, analysis by fluorescence in situ hybridization (FISH) with pairs of bacterial artificial chromosome (BAC) probes for DNA flanking on either side the chromosome 7p15 breakpoint and separately the 17q21 breakpoint detected no breakage in these regions of the genome (fig. S5). Additionally, a probe consisting of a yeast artificial chromosome (YAC) that contains DNA spanning the 7p15 breakpoint showed no splitting of the fluorescent signal (Fig. 3B). Finally, no superimposition of signals was observed when probes for chromosomes 7p15 and 17q21 were used together in FISH studies.

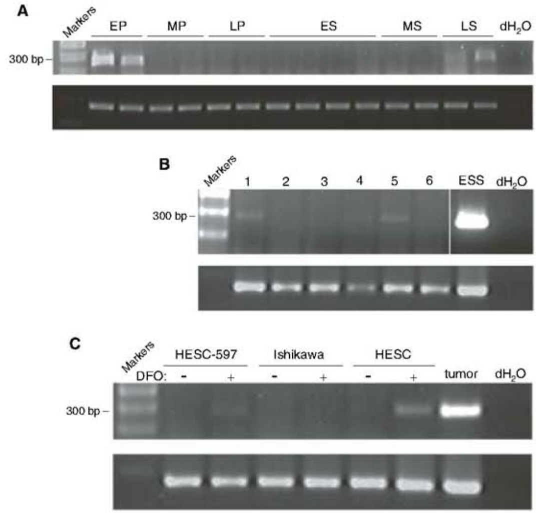

**Fig. 2.** Detection of *JAZF1-JJAZ1* RNA in endometrial tissues and effects of hormones and hypoxia on amounts of *JAZF1-JJAZ1* RNA in cultured cells. Analyses were performed by RT-PCR, as in Fig. 1A. Unlabeled panels show results of RT-PCR for β-actin RNA as a control for input RNA. (**A**) Detection of *JAZF1-JJAZ1* RNA in total RNA extracted from endometrial samples representing various phases of the menstrual cycle: EP, early proliferative; MP, mid-proliferative; LP, late proliferative; ES, early secretory; MS, mid-secretory; LS, late secretory. At least two separate uteri were tested for each phase. (**B**) Effect of hormone treatment on *JAZF1-JJAZ1* RNA in HESC cells. After 2 days of serum starvation, medium containing serum and no drug (lane 1), 17 β-estradiol at $5 \times 10^{-8}$ M (lane 2), progesterone at $1 \times 10^{-6}$ M, $1 \times 10^{-7}$ M, or $1 \times 10^{-8}$ M (lanes 3 to 5), or 17 β-estradiol at $5 \times 10^{-8}$ M plus progesterone at $1 \times 10^{-7}$ M (lane 6) was added to the cells for 24 hours. (**C**) Effect of DFO treatment on *JAZF1-JJAZ1* RNA in HESC and HESC-597 cells. No chimeric transcript could be detected in Ishikawa cells, an endometrial carcinoma line.

To investigate the possibility that (7; 17)(p15;q21) translocations or their equivalents arose in cells in culture at some point after immortalization, we subcloned HESC cells by limiting dilution. Thirty-seven subclones derived on average from half a cell per culture were tested for the production of *JAZF1-JJAZ1* RNA. RT-PCR of RNA from these subclones detected *JAZF1-JJAZ1* RNA in all clones examined, and for most subclones, the amount of *JAZF1-JJAZ1* RNA increased when DFO was added to the culture (Fig. 3C). Furthermore, analyses of all clones examined were negative for rearrangements at the chromosome 7p15 site by FISH with flanking probes (Fig. 3D). Ten of these subclones were also tested for rearrangements at the 17q12 site by FISH, and none of these showed abnormalities.

Given the evidence against DNA recombination in HESC cells and the precise joining of sequences at exon boundaries in *JAZF1-JJAZ1* RNA, we reasoned that the mechanism most likely responsible for production of this RNA is trans-splicing of pre-mRNAs for the *JAZF1* and *JJAZ1* genes. To test this hypothesis, we prepared in vitro splicing extracts from the nuclei of HESC cells. Samples of this extract were mixed with samples of a nuclear extract from a primary rhesus fibroblast cell line RF (*12*). RT-PCR of *JJAZ1* intron 1 RNA sequence revealed that unspliced pre-mRNA was present in the HESC and RF nuclear extracts (fig. S7). Nucleotide sequence analysis of exon 3 in the *JAZF1* gene of RF cells showed two single base-pair sequence differences from the human *JAZF1* gene that permitted both selective RT-PCR of any RNA containing either rhesus or human exon 3 and the ability to distinguish between the products amplified from these RNAs. With selective primers and conditions, amplification of RNA after incubation of mixed extracts yielded products in which RF *JAZF1* exon 3 was joined to exon 2 of *JJAZ1* (Fig. 4B). Sequence analysis of the RT-PCR products confirmed that the amplified *JAZF1-JJAZ1* sequences contained exon 3 of RF *JAZF1* (Fig. 4C). The amount of product generally increased when the HESC extract was prepared from cells cultured with DFO, although the extent of increase varied considerably among experiments. No product was obtained from extracts of HESC cells or RF cells alone, or when adenosine 5′-triphosphate (ATP), an obligate cofactor for splicing, was omitted from the splicing reaction. Similar results were obtained with extracts from the nonimmortalized endometrial stromal cell line, HESC-597 (Fig. 4D).

To study the mechanism further and to rule out the possibility of polymerase switching during transcription, we carried out the in vitro trans-splicing assay with HESC nuclear extract mixed with purified RF RNA. The amount of trans-spliced product detected was similar to that in the assay performed with a mixture of HESC and RF nuclear extracts (Fig. 4E). Elimination of all PCR-detectable traces of DNA from the RF RNA preparation by treatment with deoxyribonuclease I did not affect the production of the trans-spliced product (figs. S7 and S8).

The data presented here are consistent with trans-splicing of the pre-mRNAs transcribed from the *JAZF1* and *JJAZ1* genes in normal

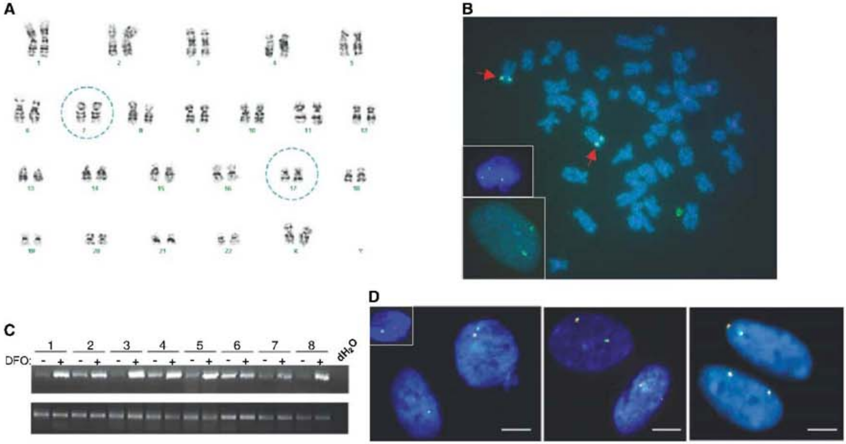

**Fig. 3.** Absence of the t(7;17)(p15;q21) in HESC cells. **(A)** Cytogenetic analysis of HESC cells. Normal chromosomes 7 and 17 are circled. **(B)** FISH analysis of HESC cells with a YAC probe containing DNA spanning the *JAZF1* locus. Arrows point to the intact YAC signal in metaphase chromosomes. (Lower inset) A representative interphase HESC nucleus; (upper inset) an ESS control showing splitting of the probe signal. **(C)** RT-PCR analysis for *JAZF1-JJAZ1* RNA in representative subclones of the HESC cell line with and without DFO treatment. **(D)** FISH analysis of three HESC subclones with two BAC probes, labeled red or green and each containing DNA sequences that flank the *JAZF1* locus on one side or the other. The juxtaposition of red and green signals indicates no separation of these sequences. (Inset) Separation of signals in an ESS control. Bars, ~10 μm.

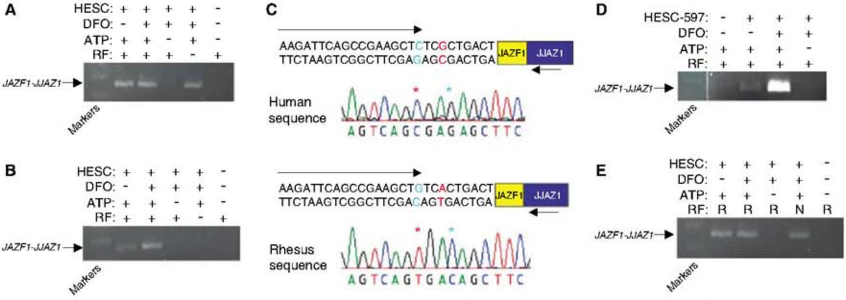

**Fig. 4.** In vitro trans-splicing reactions. **(A)** RT-PCR analysis for *JAZF1-JJAZ1* RNA with a human-specific primer. RT-PCR products from chimeric RNA were amplified only when ATP was supplied, and the amount of product increased when the HESC nuclear extracts were prepared from cells pretreated with DFO. **(B)** RT-PCR analysis for *JAZF1-JJAZ1* RNA with a rhesus-specific primer. No band was detected in HESC or RF extracts alone, but products were observed when the two kinds of nuclear extracts were mixed. The amount of product increased when the HESC extract was prepared from the cells pretreated with DFO. **(C)** Sequence analysis of the RT-PCR products amplified with antisense human- or rhesus-specific primers. Aqua-colored bases and stars indicate the interspecies sequence differences included in the species-specific primers; red bases and stars indicate the species-specific sequence differences detected in the products. **(D)** RT-PCR analysis for *JAZF1-JJAZ1* RNA in nuclear extracts of the HESC-597 and RF cells with rhesus-specific primers. Mixed extracts produced detectable signal in the presence of ATP. **(E)** RT-PCR analysis for *JAZF1-JJAZ1* RNA in HESC nuclear extracts mixed with purified RF RNA by means of amplification with the rhesus-specific primer. R, RNA; N, nuclear extract.

endometrial stromal cells and tissues to yield chimeric products identical to those produced by a recurrent gene fusion in endometrial stromal tumors. Trans-splicing of noncoding, leader exons to separately transcribed pre-mRNAs is common in certain lower eukaryotes, such as protozoa and nematodes (*13–16*). However, in vertebrates, only a few examples of trans-splicing have been described (*17–25*), and most of these involve splicing between pre-mRNAs of the same gene to generate mRNAs with duplicated exons (*17–20*). For these reasons, trans-splicing in vertebrates has sometimes been regarded as a nonfunctional by-product of a somewhat sloppy splicing system (*26*). This conclusion seems inapplicable to *JAZF1-JJAZ1* RNA because the *JAZF1-JJAZ1* fusion gene is a recurrent finding in a high fraction of endometrial stromal tissues, and fusion genes associated with chromosomal translocations in cancer have repeatedly been shown to contribute to the neoplastic phenotype of the tumors containing them (*27*, *28*). Additionally, the expression of the *JAZF1-JJAZ1* coding sequences in cultured cells has demonstrated effects on cell survival and proliferation (*9*). Whether JAZF1-JJAZ1 protein in tissues provides protection from hypoxia, to which endometrium is subjected during the late secretory phase and possibly the early proliferative phase of the menstrual cycle, remains to be determined.

The mechanisms involved in the trans-splicing of RNAs and the regulation of this process are unclear. Juxtaposition of the loci encoding the RNAs that participate in trans-splicing would not seem essential because in vitro splicing in nuclear extracts of RNAs at physiological concentrations was found to be efficient. These results also indicate that cotranscriptional splicing is not an absolute requirement for trans-splicing. Whether in vivo trans-splicing of RNA transcribed from loci that participate in chromosomal rearrangements predisposes DNA at those sites to recombination with or without prior intranuclear colocalization of the loci will require further investigation.

In view of the regulated trans-splicing between *JAZF1* and *JJAZ1* pre-mRNAs in normal endometrium, the t(7;17)(p15;q21) found in ESSs might be considered a mutation that leads to constitutive production of the *JAZF1-JJAZ1* mRNA and its protein product. This relation is similar to that seen in other oncogenic mutations associated with tumor development, namely, that mutations lead to overproduction or irreversible activation of gene products rather than to creation of "new" genes, as the fusion genes resulting from many chromosomal translocations and other DNA rearrangements have generally been thought to be.

If RNA products of fusion genes other than *JAZF1-JJAZ1* also mimic normal products resulting from trans-splicing of pre-mRNAs, it would explain the ability to frequently amplify from healthy tissues chimeric RNAs associated with chromosomal rearrangements in tumors. Considering the large number of recurrent gene fusions found in tumors, it would further suggest that trans-spliced RNAs may be relatively common in normal cells and tissues (supporting online text). At a minimum, the finding of the trans-spliced *JAZF1-JJAZ1* RNA in normal cells implies a risk to inferring the presence of chromosomal rearrangements in tissue specimens for the diagnosis and detection of cancer, especially in the context of minimal disease. Additionally, it is possible that drugs designed to target chimeric proteins produced by neoplastic gene fusions may have toxicities due to inhibited function of similar proteins in normal cells.

### References and Notes

1. M. A. Pierotti *et al.*, *Proc. Natl. Acad. Sci. U.S.A.* **89**, 1616 (1992).
2. F. Mitelman, B. Johansson, F. Mertens, *Nat. Rev. Cancer* **7**, 233 (2007).
3. O. Bernard *et al.*, *Oncogene* **6**, 1477 (1991).
4. P. J. Kourlas *et al.*, *Proc. Natl. Acad. Sci. U.S.A.* **97**, 2145 (2000).
5. A. Pardanani *et al.*, *Blood* **102**, 3093 (2003).
6. S. A. Tomlins *et al.*, *Science* **310**, 644 (2005).
7. S. Janz, M. Potter, C. S. Rabkin, *Genes Chromosomes Cancer* **36**, 211 (2003).
8. J. I. Koontz *et al.*, *Proc. Natl. Acad. Sci. U.S.A.* **98**, 6348 (2001).
9. H. Li *et al.*, *Proc. Natl. Acad. Sci. U.S.A.* **104**, 20001 (2007).
10. G. Krikun *et al.*, *Endocrinology* **145**, 2291 (2004).
11. Materials and methods are available as supporting material on *Science* Online.
12. R. C. Desrosiers *et al.*, *J. Virol.* **71**, 9764 (1997).
13. L. Bonen, *FASEB J.* **7**, 40 (1993).
14. M. Krause, D. Hirsh, *Cell* **49**, 753 (1987).
15. N. Agabian, *Cell* **61**, 1157 (1990).
16. R. E. Sutton, J. C. Boothroyd, *Cell* **47**, 527 (1986).
17. C. Caudevilla *et al.*, *Proc. Natl. Acad. Sci. U.S.A.* **95**, 12185 (1998).
18. A. N. Akopian *et al.*, *FEBS Lett.* **445**, 177 (1999).
19. S. A. Frantz *et al.*, *Proc. Natl. Acad. Sci. U.S.A.* **96**, 5400 (1999).
20. T. Takahara, S. I. Kanazu, S. Yanagisawa, H. Akanuma, *J. Biol. Chem.* **275**, 38067 (2000).
21. C. Finta, P. G. Zaphiropoulos, *J. Biol. Chem.* **277**, 5882 (2002).
22. G. Flouriot, H. Brand, B. Seraphin, F. Gannon, *J. Biol. Chem.* **277**, 26244 (2002).
23. C. Fitzgerald *et al.*, *J. Biol. Chem.* **281**, 38172 (2006).
24. Z. Jehan *et al.*, *Genome Res.* **17**, 433 (2007).
25. C. Zhang *et al.*, *DNA Cell Biol.* **22**, 303 (2003).
26. T. Maniatis, B. Tasic, *Nature* **418**, 236 (2002).
27. C. S. Huettner, P. Zhang, R. A. Van Etten, D. G. Tenen, *Nat. Genet.* **24**, 57 (2000).
28. A. T. Look, *Science* **278**, 1059 (1997).

29. Supported by the National Cancer Institute (grant R01 CA85995) and a generous gift from the Burnstein-Turnbull family. We thank M. Martel for assistance in the histologic evaluation of tissue samples; R. Means for providing the rhesus fibroblast cell line RF; P. Li for cytogenetic analysis; V. Patriub for technical assistance; and H. Taylor, J. Steitz, D. Mishler, E. Ullu, and A. Krensky for helpful discussion.

**Supporting Online Material**

www.sciencemag.org/cgi/content/full/321/5894/1357/DC1
Materials and Methods
SOM Text
Figs. S1 to S8
References

20 February 2008; accepted 7 July 2008
10.1126/science.1156725

---

# Germline Allele-Specific Expression of *TGFBR1* Confers an Increased Risk of Colorectal Cancer

Laura Valle,[1] Tarsicio Serena-Acedo,[1] Sandya Liyanarachchi,[1] Heather Hampel,[1] Ilene Comeras,[1] Zhongyuan Li,[1] Qinghua Zeng,[2] Hong-Tao Zhang,[2] Michael J. Pennison,[2] Maureen Sadim,[2] Boris Pasche,[2]* Stephan M. Tanner,[1]* Albert de la Chapelle[1]*

Much of the genetic predisposition to colorectal cancer (CRC) in humans is unexplained. Studying a Caucasian-dominated population in the United States, we showed that germline allele-specific expression (ASE) of the gene encoding transforming growth factor–β (TGF-β) type I receptor, *TGFBR1*, is a quantitative trait that occurs in 10 to 20% of CRC patients and 1 to 3% of controls. ASE results in reduced expression of the gene, is dominantly inherited, segregates in families, and occurs in sporadic CRC cases. Although subtle, the reduction in constitutive *TGFBR1* expression alters SMAD-mediated TGF-β signaling. Two major *TGFBR1* haplotypes are predominant among ASE cases, which suggests ancestral mutations, but causative germline changes have not been identified. Conservative estimates suggest that ASE confers a substantially increased risk of CRC (odds ratio, 8.7; 95% confidence interval, 2.6 to 29.1), but these estimates require confirmation and will probably show ethnic differences.

The annual worldwide incidence of colorectal cancer (CRC) exceeds 1 million, being the second to fourth most common cancer in industrialized countries (*1*). Although diet and lifestyle are thought to have a strong impact on CRC risk, genes have a key role in the predisposition to this cancer. A positive family history of CRC occurs in 20 to 30% of all probands. Highly penetrant autosomal dominant and recessive hereditary forms of CRC account for at most 5% of all CRC cases (*2*). Although additional high- and low-penetrance alleles have been proposed, much of the remaining predisposition to CRC remains unexplained (*3*).

Aberrations in the transforming growth factor–β (TGF-β) pathway are heavily involved in CRC carcinogenesis (*4*). Although mutations in the TGF-β type II receptor gene have been explicitly associated with CRC (*5*), the type I receptor gene (*TGFBR1*) has received less attention, although there is evidence that a common variant may be associated with cancer risk (*6*, *7*). We hypothesized that *TGFBR1* is a notable candidate for a gene that, when mutated, causes predisposition to CRC or acts as a modifier of other genes, resulting in a predisposition. Our study was undertaken to test this assumption.

Given the previously existing evidence that inherited allele-specific expression of *APC* acts as a mechanism of predisposition to familial adenomatous polyposis (*8*) and of an analogous mechanism involving *DAPK1* in chronic lymphocytic leukemia (*9*), we searched for a similar association of *TGFBR1* with CRC. We hypothesized that the putative change might be subtle; for instance, lowered rather than extinguished expression of one allele referred to here as ASE, for allele-specific expression. To test for ASE in *TGFBR1*, we chose three single-nucleotide polymorphisms (SNPs) (rs334348, rs334349, and rs1590) in the 3′ untranslated region (3′UTR), to which primer extension with fluorescent nucleotides (SNaPshot) (*10*) was applied. These three SNPs are separated by 1916 and 1778 base pairs (bp), respectively, yet they exhibit total linkage disequilibrium.

Among a total of 242 patients with microsatellite instability (MSI)–negative CRC (*10*), 96 (39.7%) were heterozygous for the three 3′UTR SNPs, of whom 12 showed ASE variation ratios higher than 1.5, whereas no patient showed ratios below 0.67. Forty-nine additional cases were heterozygous for one further SNP (rs7871490) located in the 3′UTR that was not in strong linkage disequilibrium with the above three markers, and 17 out of 49 (17/49) had ASE values higher than 1.5. Thus, 29 out of 138 (21%) informative CRC patients showed ASE in the *TGFBR1* gene. Three additional cases had borderline values (fig. S1 and table S1).

DNA samples from the blood of healthy Columbus, Ohio–area controls (195 individuals) (*10*) were genotyped for the four SNPs. One hundred and nine (55.9%) were heterozygous, and ASE analysis in 105 of them revealed ratios ranging between 0.72 and 3.25 (fig. S1). Only three controls showed ratios above 1.5. Our results in both the CRC patients and controls suggest that the degree of ASE is a quantitative trait (Fig. 1). Differences in the degree of ASE between patients and controls showed a *P* value of 0.1208 when a Wilcoxon rank sum test was applied and a *P* value of 0.0207 when a permutation test (100,000 permutations) was applied.

At this stage, it is not possible to determine whether the degree of predisposition to CRC is proportional to the degree of ASE or whether there is a threshold value that separates "abnormal" values that predispose to CRC from "normal" values that do not. A ratio of 1 means that both alleles are equally expressed, whereas a ratio of 1.5 means a 33% difference, as does a ratio of 0.67. To define a cutoff point, we applied receiver operating characteristic (ROC) analysis, which estimates the sensitivity and specificity of cutoff points. As shown in table S2, the value of 1.5 maximizes both characteristics, providing the highest Youden's index. When a cutoff of 1.5 was used, the *P* value comparing cases and controls was $7.655 \times 10^{-5}$. Although there is no overall need to define a firm cutoff point, we used the value of 1.5 to categorize CRC cases and controls into ASE and non-ASE. In order to determine whether the observed ratios falling outside this range represent an increase or decrease in the transcript of one allele, a reverse transcription polymerase chain reaction (RT-PCR) experiment was performed, taking advantage of hybrid clones monoallelic for chromosome 9 created from two individuals with ASE (patients 1 and 26, table S1). Each of the four hybrid clones contained either the maternal or paternal copy of chromosome 9, plus the mouse genome (*10*). As shown in Fig. 2A, ASE determination in the diploid samples indicated that the expression of one allele (a) was reduced as compared to that of the other allele (b). In the four monoallelic hybrid clones, the densitometric values of the RT-PCR of human *TGFBR1* were compared with the corresponding values for mouse *Gpi* (*10*). One allele (a) showed reduced expression in both patients. These experiments support the notion of lowered expression of one allele, and in both patients the same allele was affected (Fig. 2, A and B).

To assess the effect of ASE on TGF-β signaling, lymphoblastoid cell lines from four ASE patients and four non-ASE healthy controls were exposed to TGF-β (*10*), which binds TGFBR2 and leads to the formation of the TGFBR2/TGFBR1/TGF-β heteromeric complex. We observed differences in levels of phosphorylated SMAD2 (pSMAD2), an important downstream effector and surrogate marker of TGF-β signaling (*11*, *12*). There were constitutive differences in pSMAD2 expression between ASE patients and non-ASE controls in the absence of exogenously added TGF-β (time 0; Fig. 3A). Differences in pSMAD2 levels became more pronounced upon exposure to TGF-β. These differences were observed at low TGF-β concentrations (<5 pM) (Fig. 3B) and occurred in four out of four ASE cases as compared to non-ASE controls.

It has been shown that phosphorylation of SMAD3 is an essential step in signal transduction by TGF-β for the inhibition of cell proliferation (*13*). Furthermore, *Smad3*-deficient mice are prone to developing colon cancer (*14*, *15*). To assess the impact of *TGFBR1* ASE on the phosphorylation of SMAD3, we used an antibody targeting the $\mathrm{Ser}^{423/425}$ site in SMAD3 (*10*, *16*). Constitutive levels of pSMAD3 were detectable in the lymphoblastoid cell lines of three non-ASE controls, whereas pSMAD3 was barely detectable in one ASE case (Fig. 3C). Exposure to TGF-β did not result in any detectable increase in pSMAD3 in the lymphoblastoid cell lines of the ASE patients. The pSMAD2 and pSMAD3 results indicate that patients with ASE exhibit decreased SMAD-mediated signaling when compared with non-ASE controls.

A GCG trinucleotide variable number of tandem repeat polymorphism occurs in exon 1 of *TGFBR1*. The most common allele contains nine repeats leading to a stretch of nine alanines (9A) in the signal peptide of the receptor protein. The second most common allele has six repeats (6A) and occurs in approximately 14% of all individuals in most Caucasian populations (*6*). The 6A allele has been associated with a low-level but statistically significant predisposition to sev-

**Fig. 1.** *TGFBR1* ASE distribution in 138 CRC patients and 105 controls studied by SNaPshot. The ASE cutoff value of 1.5 chosen to categorize the cases is indicated, together with its associated *P* value obtained from comparing the proportions of cases (29/138) and controls (3/105) above the indicated value.

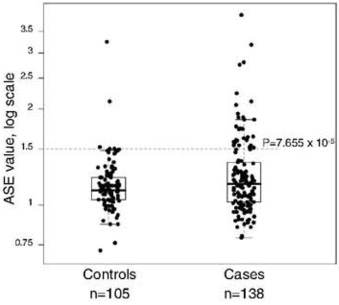

---

[1]Human Cancer Genetics Program, Comprehensive Cancer Center, The Ohio State University, Columbus, OH 43210, USA. [2]Cancer Genetics Program, Division of Hematology/Oncology, Department of Medicine and Robert H. Lurie Comprehensive Cancer Center, Feinberg School of Medicine, Northwestern University, Chicago, IL 60611, USA.

*To whom correspondence should be addressed. E-mail: b-pasche@northwestern.edu (B.P.); Stephan.Tanner@osumc.edu (S.M.T.); Albert.delaChapelle@osumc.edu (A.d.l.C.)

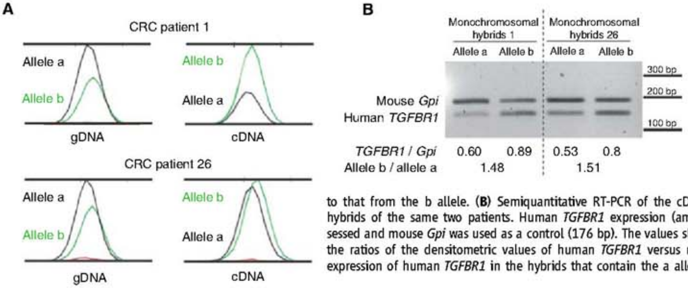

**Fig. 2.** ASE determination in two ASE CRC probands. **(A)** ASE detection in blood DNA by SNaPshot. The ASE ratio was calculated by normalizing the ratio between the peak areas of the two alleles in cDNA with the same parameters in genomic DNA (gDNA). In both examples, the transcript from the a allele is reduced with respect to that from the b allele. **(B)** Semiquantitative RT-PCR of the cDNA from monochromosomal hybrids of the same two patients. Human *TGFBR1* expression (amplicon size 135 bp) was assessed and mouse *Gpi* was used as a control (176 bp). The values shown below the gel represent the ratios of the densitometric values of human *TGFBR1* versus mouse *Gpi*, showing reduced expression of human *TGFBR1* in the hybrids that contain the a allele.

eral forms of cancer (*17*–*20*). Recent studies suggest that the association of 6A with colon cancer is either weak [odds ratio (OR) 1.2, 95% confidence interval (CI) 1.01 to 1.43] (*17*) or borderline significant (OR 1.13, CI 0.98 to 1.30) (*21*). We typed this polymorphism in all 242 CRC cases studied by us and found 9A/9A in 197, 9A/6A in 40, 6A/6A in 4, and 1 failed (table S3). There were clearly more 9A/6A heterozygotes among the patients with ASE (14/29) than in those without ASE (22/108) ($P = 0.0052$, chi-square test). We tentatively concluded from these data that the 6A allele is probably in linkage disequilibrium with one of the putative mutations that causes ASE, but 6A is not in itself causative of ASE.

All 29 patients showing ASE and three patients with borderline ASE values (1.49, 1.49, and 1.46) ($n = 32$ patients) were studied for genetic changes occurring in the germ line. By sequencing of all nine exons, 2 kb upstream of exon 1, and the entire 3′UTR (*10*), a single sequence change in the coding exons was identified in patient 30, consisting of a coding DNA 1204 T→A (c.1204T>A) missense change in exon 7 that changes a tyrosine to asparagine (p.Tyr401Asn). Its pathogenicity is currently being assessed. Several changes, all previously reported as polymorphic, were identified in the 3′UTR and promoter regions. In three patients, a deletion (del) of two bases (c.1-1782_1783delCA) at 1783 bp upstream of exon 1 was identified in a repetitive sequence of short interspersed nuclear elements. Multiplex ligation-dependent probe amplification (*10*) did not suggest any large rearrangements, deletions, or duplications of exons. In a study of promoter methylation, none of the comparisons of germline methylation status between ASE and non-ASE cases and ASE cases versus controls were significant (supporting online material text and table S4). Thus, germline promoter methylation is unlikely to play a role in ASE.

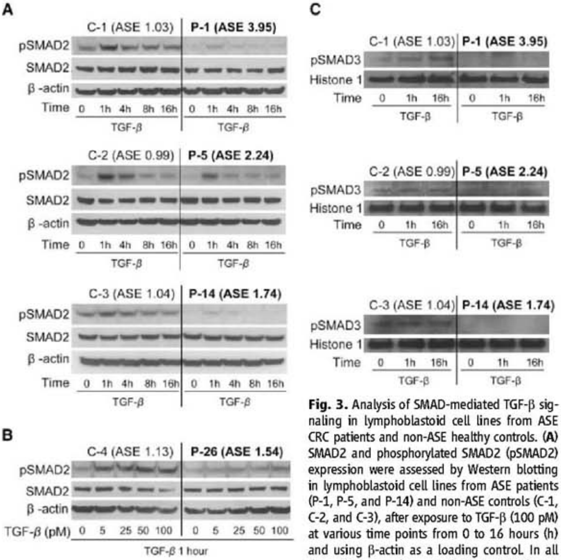

**Fig. 3.** Analysis of SMAD-mediated TGF-β signaling in lymphoblastoid cell lines from ASE CRC patients and non-ASE healthy controls. **(A)** SMAD2 and phosphorylated SMAD2 (pSMAD2) expression were assessed by Western blotting in lymphoblastoid cell lines from ASE patients (P-1, P-5, and P-14) and non-ASE controls (C-1, C-2, and C-3), after exposure to TGF-β (100 pM) at various time points from 0 to 16 hours (h) and using β-actin as a loading control. In all three ASE cases, less constitutive pSMAD2 was observed than in non-ASE controls. The differences in pSMAD2 expression between ASE and non-ASE cell lines were further enhanced after exposure to TGF-β. **(B)** SMAD2 and p-SMAD2 expression 1 hour after exposure to different TGF-β concentrations. The effect shown in (A) also occurs at low concentrations of TGF-β (5 pM). **(C)** pSMAD3 detection in nuclear extracts from three ASE patients and three non-ASE controls after exposure to TGF-β1. The three non-ASE lymphoblastoid cell lines had pSMAD3 expression in the nucleus, whereas nuclear pSMAD3 expression was undetectable in two ASE cases (P-1 and P-14) and barely detectable in one case (P-5).

We hypothesized that changes occurring in noncoding regions of the gene could be responsible for the reduction in expression. To fully study this possibility, overlapping fragments of 1.7 to 10 kb were amplified by long-range PCR, cloned, and sequenced. In all, approximately 96.5 kb covering the whole gene and 3′UTR (49 kb), 35 kb upstream of exon 1 (up to the next gene *COL15A1*), and 12.5 kb downstream of the 3′UTR (Fig. 4) were fully sequenced in the four monochromosomal hybrids (patients

1 and 26) and in diploid DNA from four other ASE patients (patients 5, 11, 14, and 21) (*10*). Our sequencing strategy allowed us to determine the phase of every change within each amplicon and over larger regions when at least one change occurred in the overlapping fragments. In all, 25 and 104 changes were identified in the down-regulated alleles of patients 1 and 26, respectively, whereas 31 and 6 changes were detected in their wild-type counterparts. Diploid DNA from the four patients harbored 61, 37, 33, and 135 changes, respectively.

Excluding changes known to be present in the wild-type alleles, 140 changes were identified in the down-regulated alleles. Only the c.1-1782_1783delCA change stood out as a candidate mutation. It occurred in 3/29 (10.3%) ASE patients, in 0/3 ASE controls, in 1/51 (2%) non-ASE CRC patients, and 1/81 (1.2%) non-ASE controls. In summary, these investigations did not uncover the genetic changes causing ASE.

Genotyping of most changes identified by sequencing was carried out in all available ASE CRC patients, including borderline cases ($n$ = 31), and in 55 non-ASE CRC patients. Construction of haplotypes from the available genotype and haplotype data was performed with PHASE v.2.1.1 (*10*). In all, 60 polymorphisms covering 73.5 kb (from 12 kb upstream of exon 1 to 12.5 kb downstream of the 3′UTR) were used for haplotype inference (table S5). For all ASE and non-ASE patients, the program was run with 1000 permutations with overlapping 10-SNP sliding windows. Haplotype frequency distributions in ASE and non-ASE populations showed significant differences in a genomic region covering the area between the 3′ end of intron 3 to ~5 kb downstream of the 3′ end of the UTR (Fig. 4).

The group of patients carrying the minor allele for the three 3′UTR SNPs in linkage disequilibrium (group 1) was very different from the other group derived from the study of SNP rs7871490 (group 2). Haplotype analysis was performed separately in the two groups, using 50 and 21 SNPs, respectively. In group 1 ($n$ = 53), one major haplotype for the affected alleles was present in 11/14 (78.6%) of ASE but also in 22/39 (56.4%) non-ASE patients (Fig. 4). For group 2 ($n$ = 33), another major haplotype for the affected allele was present in 14/17 (82.4%) of ASE and in 1/16 (6.3%) of non-ASE patients (Fig. 4). Fisher's exact test to compare haplotype proportions showed $P$ values of 0.2031 and $1.260 \times 10^{-5}$ for groups 1 and 2, respectively. The 6A allele of the 9A/6A polymorphism occurred in the ASE haplotype in all 14 cases of group 2, but not in group 1, where all ASE cases except one were homozygous for the 9A allele.

In search of somatic changes in line with Knudson's two-hit hypothesis, loss of heterozygosity (LOH) analyses as well as a search for somatic mutations in the coding sequences of the gene were performed in DNA from the tumors of 26 ASE patients. Using the described threshold (*10*), 6 cases out of 26 showed LOH. In three of these six cases, the wild-type allele, the one with normal expression in blood, was lost or reduced, whereas in the other three cases, the allele showing germline ASE was lost. Exon-by-exon sequencing of the entire gene in tumors from 26 ASE patients revealed somatic changes in three tumors that were not found in blood DNA. The mutations were: c.634G>A (p.Gly212Asp) in one tumor and c.682_685delAAG (p.Glu228del) in two tumors. These mutations occurred in exon 4, which encodes the kinase domain of the protein. LOH analyses and exon 4 sequencing in 49 tumors of CRC patients without ASE showed that none of these tumors had evidence of somatically acquired mutations, and five showed LOH (table S3). Fisher's exact test comparing proportions of LOH and mutations between ASE and non-ASE cases showed $P$ values of 0.1708 and 0.0355, respectively. The occurrence of somatic mutations in ASE cases but not in controls supports the role of *TGFBR1* as a tumor suppressor gene. On the other hand, the fact that

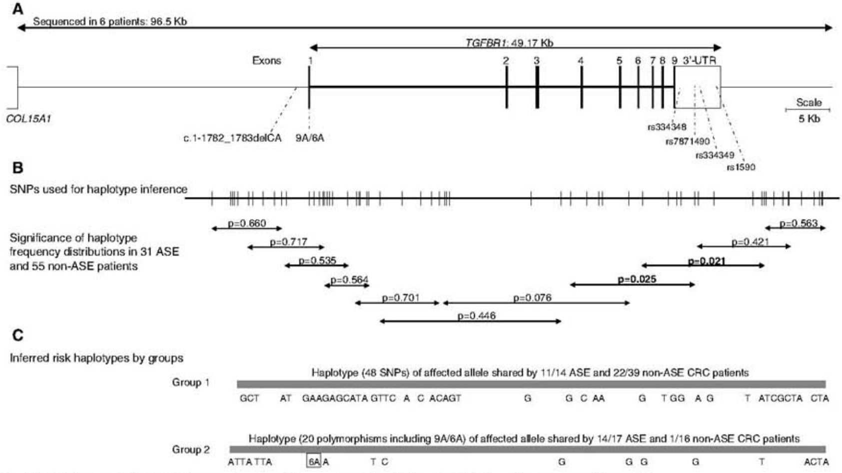

**Fig. 4.** (**A**) Diagram of the *TGFBR1* genomic region. The uppermost line depicts the 96.5-kb region sequenced in six ASE patients (four monochromosomal hybrids and four diploid DNAs). Shown are the locations of the 2-bp CA deletion upstream of exon 1, the 9A/6A polymorphism in exon 1, and the four SNPs in the 3′UTR used for ASE determinations. (**B**) Locations of the 60 SNPs used for haplotype inference in ASE ($n$ = 31) and non-ASE ($n$ = 55) CRC patients. The arrowed shorter lines each depict a 10-SNP overlapping window. $P$ values indicate the significance of differences in haplotype distribution between ASE and non-ASE individuals. (**C**) Two major haplotypes identified in ASE patients are shown.

☐ 6A allele of the 9A/6A polymorphism

LOH affected the ASE allele as often as the wild-type allele could indicate random losses.

The cohort of MSI-negative CRC patients had been deliberately enriched in familial cases (*10*). In the cohort of 138 patients with available ASE values, 59 out of 136 (43.4%) were familial according to the criteria indicated above, and family information was not available in two cases. Among the cases showing ASE, 53.6% were familial (table S3). The proportion of ASE was higher among familial than nonfamilial cases: 15/59 (25.4%) familial cases versus 13/77 nonfamilial cases (16.9%). A chi-square test to compare proportions showed that this difference was not statistically significant ($P = 0.314$).

The above data suggest that ASE contributes somewhat more to familial than to sporadic CRC but do not allow its inheritance to be assessed. If ASE is regularly inherited as a dominant trait, the expectation is that 50% of first-degree relatives (FDRs) also have ASE. Data from four families that are informative in this regard are shown in fig. S2. In all, among 11 FDRs, ASE was greater than 1.5 in 4, borderline in 2 (ASE values 1.40 and 1.44), and low in 5. There was no instance of ASE being incompatible with Mendelian dominant inheritance. In all four families, co-segregation of ASE with the inferred risk haplotype, representing the down-regulated allele, occurred. The highest Kong and Cox nonparametric LOD score was 1.25, with a $P$ value of 0.008 (nonparametric $z$ score = 4.12; $P$ value = 0.00002). Among the four to six ASE-positive FDRs, two had CRC, one had endometrial cancer and a tubular colonic adenoma, one had prostate cancer, and another had multiple polyps in the colon and rectum (table S6). Although fragmentary, these data suggest dominant inheritance of ASE with incomplete penetrance of CRC in ASE carriers.

There is indirect evidence to support the notion that ASE of *TGFBR1* contributes to CRC development. The TGF-β pathway is strongly involved in the carcinogenesis of colon and other cancers, and its signaling is dependent on the integrity of both of its receptors (TGFBR1 and TGFBR2) (*22*, *23*). In a comprehensive study of CRC tumors, somatic mutations occurred with high frequency in 69/13,023 genes. Among these 69 genes were *TGFBR2*, *SMAD4*, *SMAD2*, and *SMAD3*, attesting to the importance of the TGF-β pathway in CRC (*24*). There is rapidly increasing evidence that subtle variations in gene expression play central roles not only in development in various organisms but also in human disease (*8*, *9*, *25*). Linkage analysis of a cohort of sibling pairs concordant or discordant for colorectal carcinoma or adenoma highlighted a region in chromosome 9q22-31 (*26*). Subsequently, borderline significant linkage to the same region was observed in families segregating colorectal cancer or adenoma without microsatellite instability (*27*, *28*). This evidence is compatible with, but in no way proves, a role for *TGFBR1*.

We were unable to determine what mechanism causes ASE. The haplotype data support the implication of ancestral mutations for most ASE patients. Moreover, the elusive genomic change causing ASE is likely to occur in cis, but the data do not exclude the possibility that ASE arises as a result of trans-acting genes that preferentially affect the risk haplotypes. Such genes could well be RNA genes as predicted earlier (*29*). Very recently, the existence of extensive quantitative trait loci for gene expression was documented in two large studies (*30*, *31*).

How common is ASE of *TGFBR1*? Using our definition, it occurred in 29/138 tested CRC patients (21%) and in 3/105 tested controls (3%). In the extreme, if none of the non-informative CRC cases had ASE, the frequency would be 29/242 (12%), and for the controls, 3/195 (1.5%). Because not all individuals are informative (heterozygous for a transcribed SNP), the true frequency in cases and controls cannot be precisely assessed at present. Using the above alternative numbers, we can calculate the OR of CRC in carriers of ASE. In the first scenario, the OR is 9.0 (CI 2.7 to 30.6), and in the conservative one, OR is 8.7 (CI 2.6 to 29.1).

What proportion of all CRC is attributable to ASE of *TGFBR1*? From the available data of the present case-control study, we estimated the population attributable risk (PAR). If ASE occurs in 21% of cases and 3% of controls, the estimated PAR is 18.7% (CI 10.8 to 25.8). If ASE occurs in 12% of cases and 1.5% of controls, the estimated PAR is 10.6% (CI 6.0 to 14.9). These numbers are estimates, representing the Caucasian-dominated population of central Ohio, and are heavily dependent on the relevant allele frequencies, which may show strong inter-ethnic variation. We nevertheless conclude that ASE of *TGFBR1* is a major contributor to the genetic predisposition to CRC.

### References and Notes

1. D. M. Parkin, F. Bray, J. Ferlay, P. Pisani, *CA Cancer J. Clin.* **55**, 74 (2005).
2. A. de la Chapelle, *Nat. Rev. Cancer* **4**, 769 (2004).
3. N. M. Lindor *et al.*, *JAMA* **293**, 1979 (2005).
4. P. M. Siegel, J. Massague, *Nat. Rev. Cancer* **3**, 807 (2003).
5. S. Markowitz *et al.*, *Science* **268**, 1336 (1995).
6. B. Pasche *et al.*, *Cancer Res.* **58**, 2727 (1998).
7. Y. Xu, B. Pasche, *Hum. Mol. Genet.* **16**, R14 (2007).
8. H. Yan *et al.*, *Nat. Genet.* **30**, 25 (2002).
9. A. Raval *et al.*, *Cell* **129**, 879 (2007).
10. Materials and methods are available as supporting material on *Science* Online.
11. J. Massague, R. R. Gomis, *FEBS Lett.* **580**, 2811 (2006).
12. J. Massague, *Mol. Cell* **29**, 149 (2008).
13. X. Liu *et al.*, *Proc. Natl. Acad. Sci. U.S.A.* **94**, 10669 (1997).
14. Y. Zhu, J. A. Richardson, L. F. Parada, J. M. Graff, *Cell* **94**, 703 (1998).
15. N. M. Sodir *et al.*, *Cancer Res.* **66**, 8430 (2006).
16. G. Sekimoto *et al.*, *Cancer Res.* **67**, 5090 (2007).
17. B. Pasche *et al.*, *J. Clin. Oncol.* **22**, 756 (2004).
18. B. Pasche *et al.*, *Cancer Res.* **59**, 5678 (1999).
19. B. Pasche *et al.*, *JAMA* **294**, 1634 (2005).
20. Y. Bian *et al.*, *J. Clin. Oncol.* **23**, 3074 (2005).
21. J. Skoglund *et al.*, *Clin. Cancer Res.* **13**, 3748 (2007).
22. B. Bierie, H. L. Moses, *Cytokine Growth Factor Rev.* **17**, 29 (2006).
23. J. Massague, S. W. Blain, R. S. Lo, *Cell* **103**, 295 (2000).
24. T. Sjoblom *et al.*, *Science* **314**, 268 (2006).
25. H. Yan, W. Zhou, *Curr. Opin. Oncol.* **16**, 39 (2004).
26. G. L. Wiesner *et al.*, *Proc. Natl. Acad. Sci. U.S.A.* **100**, 12961 (2003).
27. Z. E. Kemp *et al.*, *Cancer Res.* **66**, 5003 (2006).
28. J. Skoglund *et al.*, *J. Med. Genet.* **43**, e7 (2006).
29. M. Morley *et al.*, *Nature* **430**, 743 (2004).
30. H. H. Goring *et al.*, *Nat. Genet.* **39**, 1208 (2007).
31. B. E. Stranger *et al.*, *Nat. Genet.* **39**, 1217 (2007).

32. We thank H. He, K. Sotamaa, and W. Frankel for help. This work was supported by NIH grants CA67941, CA16058, CA112520, and CA108741; grants from the Walter S. Mander Foundation, Chicago, IL; and the Jeannik M. Littlefield–American Association for Cancer Research Grant in Metastatic Colon Cancer Research. L.V. was supported by a fellowship from the Fundación Ramón Areces.

### Supporting Online Material

www.sciencemag.org/cgi/content/full/1159397/DC1
Materials and Methods
SOM Text
Figs. S1 and S2
Tables S1 to S6
References

21 April 2008; accepted 5 August 2008
Published online 14 August 2008;
10.1126/science.1159397
Include this information when citing this paper.

# New Products Focus: Mass Spectrometry

Thermo Fisher Scientific
For information 800-532-4752
www.thermo.com/tsqvantage

## LC-MS/MS System

The TSQ Vantage is a new liquid chromatography-mass spectrometry/mass spectrometry (LC-MS/MS) system that offers increased sensitivity without increased noise for better reproducibility, accuracy, and precision in quantitative analysis. Technical breakthroughs have improved the TSQ Vantage's signal-to-noise performance, providing better reproducibility and precision in the quantitative analysis of small molecules, biomolecules, and peptides. The instrument offers up to 10 times the signal-to-noise ratio compared with the TSQ Quantum series. The TSQ Vantage's new S-Lens ion optics system features a novel electrostatic field technology to capture virtually every ion and efficiently transfer it into the HyperQuad quadrupole mass analyzer. The S-Lens design is an advance over high-pressure, skimmer-based ion source designs because it eliminates mass discrimination and lowers the gas load on the expensive turbo-molecular pumps.

## Glycopeptide Analysis Software

The new version of the innovative mass spectrometry (MS) data analysis tool, SimGlycan, can analyze glycopeptides in addition to released glycans. SimGlycan matches MS/MS spectra with its own comprehensive, robust, and annotated database to predict the structure of glycans. It generates a list of all the probable glycans that are close to the experimental data, saving time and laborious work. Each structure is scored to help the user judge which results closely match the experimental data. Alongside the probable glycan structure, the software makes available information such as the glycan class, reaction, pathway, and enzyme. Users can resolve glycan structures in glycopeptide molecules by specifying the sequence or mass of the attached peptide moiety.

Premier Biosoft International
For information 650-856-2703
www.PremierBiosoft.com

## Surfactant

ProteasMAX Surfactant is designed to enhance the enzymatic performance of trypsin and other proteases in preparation for analysis by mass spectrometry or liquid chromatography. The surfactant provides a more complete digestion prior to protein analysis, resulting in more accurate data in a shorter time and reduced risk of sample degradation. The new surfactant exposes cleavage sites usually inaccessible because of secondary or tertiary structure and can increase sample recovery from gels. It can reduce standard protein digestion time from overnight to just three hours. It also enhances protein solubilization at room temperature, which means that high temperatures and precipitation can be avoided, even for complex proteins. Because ProteasMAX degrades during the digestion reaction, researchers can proceed directly to analysis of peptides by mass spectrometry without additional deactivation steps.

Promega
For information 608-274-4330
www.promega.com

## Cell Lysis Kit

The ProteaPrep Cell Lysis Kit, Mass Spec Grade, is designed for the efficient recovery of purified protein lysates from biological samples. The kit is a proprietary mixture of salts, glycerol, and an acid-labile surfactant optimized for efficient solubilization, extraction, and recovery of proteins during cell lysis. Because the kit contains no lysozyme or harsh detergents, it permits recovery of cell lysates free from artifactual protein contaminants and promotes efficient sample protein solubilization. It is optimal for mass spectrometry, enzymatic digestions, two-dimensional gel electrophoresis, and protein quantitation procedures.

Protea Biosciences
For information 877-776-8321
www.proteabio.com

## Tandem Quadrupole MS

The Waters Xevo TQ MS System is an advanced tandem quadrupole mass spectrometer that allows scientists with varying levels of mass spectrometry (MS) expertise to quickly produce high quality data. The system features IntelliStart, a new technology that simplifies instrument setup and troubleshooting. It automatically ensures the system is ready for use by performing mass calibration, setting MS resolution, generating compound-specific MS methods, and optimizing source conditions. The instrument is equipped with a unique collision cell that can be operated in conventional T-Wave-1 enabled mode or in a new ScanWave-enabled mode. ScanWave improves the duty cycle and enhances the full-scan capability to meet the demands of complex analyses, allowing users to more easily confirm the identities and structures of targeted analytes.

Waters
For information 508-482-2614
www.waters.com

## High-Resolution Time-of-Flight MS

The maXis electrospray ultrahigh-resolution time-of-flight mass spectrometer offers high resolution of 40,000–60,000 FWHM over a broad mass range and mass accuracy typically between 600 and 800 parts per billion, at speeds of up to 20 full spectra per second. The maXis offers 20 Hz full spectra acquisition at high mass resolution for high-speed liquid chromatography, a high dynamic range of five orders of magnitude for trace detection in complex mixtures, and sub-parts-per-million mass accuracy in both mass spectrometry (MS) and MS/MS mode. The instrument makes high-resolution mass spectrometry over a broad mass range compatible with ultra performance liquid chromatography.

Bruker Daltonics
For information 978-667-9580
www.bdal.com

Electronically submit your new product description or product literature information! Go to **www.sciencemag.org/products/newproducts.dtl** for more information.